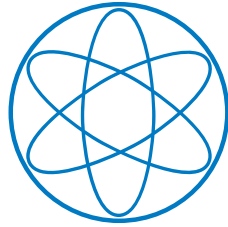# Scintillating CaWO$_4$ Crystals for the Direct Dark Matter Search Experiments CRESST and EURECA

Dissertation
von

Moritz von Sivers

Technische Universität München

Technische Universität München

Lehrstuhl E15 für Experimentalphysik und Astroteilchenphysik

Scintillating CaWO$_4$ Crystals for the Direct Dark Matter Search Experiments CRESST and EURECA

Moritz von Sivers

Vollständiger Abdruck der von der Fakultät für Physik der Technischen Universität München zur Erlangung des akademischen Grades eines

Doktors der Naturwissenschaften (Dr. rer. nat.)

genehmigten Dissertation.

Vorsitzender: Univ.-Prof. Dr. B. Garbrecht

Prüfer der Dissertation:

1. Univ.-Prof. Dr. L. Oberauer

2. Priv.-Doz. Dr. H. Kroha

Die Dissertation wurde am 07.07.2014 bei der Technischen Universität München eingereicht und durch die Fakultät für Physik am 17.07.2014 angenommen.

"There is a theory which states that if ever anyone discovers exactly what the Universe is for and why it is here, it will instantly disappear and be replaced by something even more bizarre and inexplicable. There is another theory which states that this has already happened."

Douglas Adams, *The Restaurant at the End of the Universe*

Abstract

There is compelling evidence for the existence of non-baryonic Cold Dark Matter (CDM) from many astrophysical observations. A well motivated candidate that can account for the Dark Matter abundance is the so called Weakly Interacting Massive Particle (WIMP). Several experiments aim at the direct detection of WIMPs in our galaxy with earthbound detectors. An example is the Cryogenic Rare Event Search with Superconducting Thermometers (CRESST) which presently uses a multi-element target consisting of in total $\sim$5 kg of scintillating $CaWO_4$ crystals. To reach a better sensitivity the future EUropean Rare Event Calorimeter Array (EURECA) project aims at a multi-material target comprising $CaWO_4$ and Ge with a total mass of up to 1 tonne. In the past, $CaWO_4$ crystals for the CRESST experiment have been supplied by external institutes. Recently, we started the production of $CaWO_4$ crystals with a dedicated Czochralski furnace at the crystal laboratory of the Technische Universität München (TUM). The motivation has been to have a direct influence on the whole production process and thereby ensure the availability of crystals with the required properties. These include, in particular, a high light output and extremely low amounts of radioactive impurities.

In the course of this work we have successfully produced several scintillating $CaWO_4$ detector crystals ($\sim$250-300 g each) for the CRESST experiment. We have investigated the influence of high-temperature oxygen annealing, different crystal shapes and surface roughening on the scintillation properties of the crystals. By optimization of these treatments it was possible to increase the light output by up to $\sim$50% and significantly improve the detector resolution by $\sim$35%.

As CRESST detectors operate at low temperatures in the mK range we have also studied the temperature dependence of the scintillation properties. We have observed a new scintillation component at low temperatures with a long decay time of $\sim$2 ms. In addition, the temperature dependence of the α/γ-ratio of the light yield was investigated for the first time. We have found that this ratio is about $\sim$10% smaller at low temperatures as compared to room temperature.

Furthermore, the optical and scintillation properties as well as the radiopurity of the produced crystals were compared to those from external suppliers. The light output of the TUM-grown crystals was found to be $\sim$30% lower than that of the best crystals from other suppliers. The cause was found in a lower attenuation length which requires further optimization of the crystal growth process, e.g., by lowering the growth speed.

To determine the radioactive contamination of the produced crystals a setup for low-background scintillation spectroscopy was designed and constructed. With this setup it is possible to determine activities of individual isotopes in the µBq/kg range.

The raw materials for crystal production were selected by trace impurity analysis and low-background γ-ray spectrometry. Using these methods we have reached a radiopurity which is about a factor of 10 better than that of previously available crystals from other suppliers.

Several of the crystals were installed as detectors in the current data-taking campaign of the CRESST experiment. With these detectors an unprecedented background count rate of $\sim 3\,\mathrm{cpd/kg/keV}$ was achieved. This is about one order of magnitude lower than the typical count rate of other detectors and about a factor of 2 better than the best rate achieved so far. With one of these detectors CRESST has been able to set the current best limit on spin-independent WIMP-nucleon scattering for WIMP masses below $\sim 3\,\mathrm{GeV/c^2}$.

Zusammenfassung

Es gibt überzeugende Hinweise auf die Existenz von nicht-baryonischer Kalter Dunkler Materie durch eine Vielzahl an astrophysikalischen Beobachtungen. Das sogenannte Weakly Interacting Massive Particle (WIMP) ist ein wohlmotivierter Kandidat, um die beobachtete Häufigkeit der Dunklen Materie zu erklären. Mehrere Experimente versuchen WIMPs aus unserer Galaxie mit Detektoren auf der Erde nachzuweisen. Ein Beispiel ist das Cryogenic Rare Event Search with Superconducting Thermometers (CRESST) Experiment welches ein mehrelementiges Target bestehend aus szintillierenden $CaWO_4$ Kristallen mit einer gesamten Masse von $\sim 5\,kg$ verwendet. Um die Sensitivität zu verbessern, strebt das zukünftige EUropean Rare Event Calorimeter Array (EURECA) Projekt ein Target mit einer gesamten Masse von bis zu einer Tonne an, welches sich aus $CaWO_4$ und Ge zusammensetzt. In der Vergangenheit wurden die $CaWO_4$ Kristalle für CRESST von externen Instituten bezogen. Seit kurzem werden die Kristalle mit einer eigenen Czochralski Anlage im Kristalllabor der Technischen Universität München (TUM) produziert. Die Motivation dafür war einen direkten Einfluss auf den gesamten Produktionsprozess zu haben, um damit die Verfügbarkeit von Kristallen mit den gewünschten Eigenschaften zu sichern. Dies betrifft im Besonderen eine hohe Lichtausbeute und eine extrem geringe Menge an radioaktiven Verunreinigungen.

Im Zuge dieser Arbeit wurden erfolgreich mehrere szintillierende $CaWO_4$ Kristalle (jeweils ~ 250-$300\,g$) für das CRESST Experiment hergestellt. Wir untersuchten den Einfluss von Tempern unter Sauerstoff Atmosphäre, verschiedenen Kristallformen und Aufrauen der Kristalloberflächen auf die Szintillationseigenschaften. Durch die Optimisierung dieser Behandlung ist es uns gelungen die Lichtausbeute um $\sim 50\%$ zu steigern, und damit die Detektorauflösung um $\sim 35\%$ zu verbessern.

Da CRESST Detektoren bei tiefen Temperaturen im mK Bereich betrieben werden, wurde die Temperaturabhängigkeit der Szintillationseigenschaften untersucht. Dabei haben wir eine neue Szintillationskomponente bei tiefen Temperaturen mit einer langen Abfallszeit von $\sim 2\,ms$ beobachtet. Darüber hinaus wurde zum ersten mal die Temperaturabhängigkeit des α/γ Verhältnisses der Lichtausbeute untersucht. Dieses Verhältnis ist bei tiefen Temperaturen ca. 10% kleiner als bei Raumtemperatur.

Weiterhin wurden die optischen und Szintillationseigenschaften sowie die Reinheit bezüglich radioaktiver Isotope der hier produzierten Kristalle mit denen von anderen Instituten stammenden verglichen. Die Lichtausbeute der an der TUM produzierten Kristalle ist $\sim 30\%$ kleiner als die der besten Kristalle von anderen Herstellern. Der Grund dafür wurde in einer kleineren Abschwächlänge gefunden, welche einer weiteren Optimierung des Züchtungsverfahrens bedarf, z.B. durch Verlangsamung der Ziehgeschwindigkeit.

Um die radioaktiven Verunreinigungen der produzierten Kristalle zu messen, wurde ein Aufbau für Untergrundarme Szintillationsspektroskopie entworfen und realisiert. Mit diesem Aufbau ist es möglich die Häufigkeit von einzelnen Isotopen auf dem µBq/kg Level zu messen.

Die Rohmaterialien für die Kristallproduktion wurden durch Spurenanalyse und Untergrundarme Gammaspektrometrie ausgewählt. Durch diese Maßnahmen ist es uns

gelungen die radioaktiven Verunreinigungen um ca. einen Faktor 10 gegenüber bisher verfügbaren Kristallen zu reduzieren.

Mehrere der produzierten Kristalle wurden als Detektoren in der momentan laufenden Messkampagne des CRESST Experiments eingebaut. Mit diesen Detektoren ist eine bisher unerreichte Untergrundrate von $\sim 3\,\mathrm{cpd/kg/keV}$ erreicht worden. Dies ist eine Größenordnung besser als die typische Untergrundrate von anderen Detektoren und ca. einen Faktor 2 besser als die bisher niedrigste erreichte Untergrundrate. Mit einem der TUM Detektoren ist es CRESST möglich das momentan beste Limit für die spin-unabhängige WIMP-Nukleon Streuung für WIMP Massen kleiner $\sim 3\,\mathrm{GeV/c^2}$ aufzustellen.

Contents

Chapter 1

Introduction

1.1 Dark Matter

1.1.1 Evidence for Dark Matter

There is compelling evidence for the existence of Dark Matter on all cosmological scales. The first indications for Dark Matter were found in the 1930s by Fritz Zwicky from the observation of the dynamics in the Coma galaxy cluster. In his famous paper published in 1933 he found that "the average density in the Coma system would have to be at least 400 times larger than that derived on the grounds of observations of luminous matter. If this would be confirmed we would get the surprising result that dark matter is present in much greater amount than luminous matter." [1]. In the 1960s the dominant presence of Dark Matter was supported by measurements of the rotation curves of galaxies. At large distances from the galactic center the radial velocity of stars was expected to decrease as $\propto 1/\sqrt{r}$ according to Kepler's law. However, it was observed that the velocities stay approximately constant which could be explained by an additional spherical halo of Dark Matter (see Fig. 1.1). Further evidence for non-baryonic Dark Matter is provided by the observation of colliding galaxy clusters such as the "Bullet Cluster" [2]. These objects show that the main mass is separated from the cluster gas that makes up the main baryonic component (see Fig. 1.2). This supports the presence of collisionless Dark Matter and disfavors theories of Modified Newtonian Gravity (MOND). Moreover, CDM is believed to be responsible for the formation of large scale structures. Observed structures from, e.g., the Sloan Digital Sky Survey can be explained by the hierarchical growth through gravitational forces provided by Cold Dark Matter (see Fig. 1.3) [3].
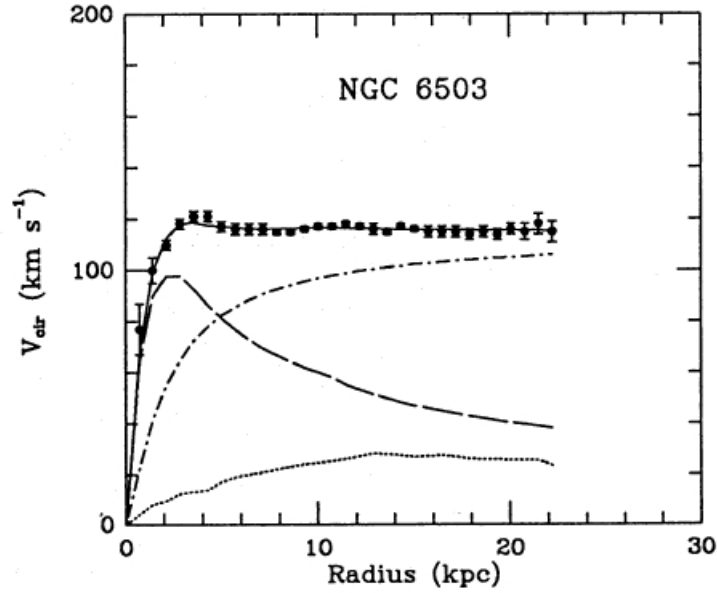
Fig. 1.1: The measured rotation curve (points) of the galaxy NGC 6503 with a Dark-halo model fit (solid line). The rotation curves of the individual components are also shown: visible component (dashed line), gas (dotted line) and dark halo (dash-dot line). Figure adapted from Ref. [4].
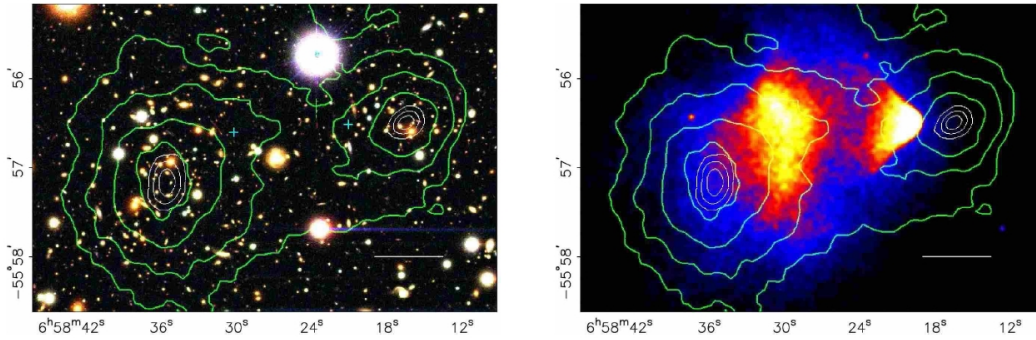
Fig. 1.2: The so called "Bullet Cluster" (1E0657-558) was formed by the collision of two smaller galaxy clusters. The white bar indicates a distance of $200\,\mathrm{kpc}$. The contour lines show the mass density derived by gravitational lensing. In the right panel also the X-ray emitting intracluster plasma is depicted. The difference between the centers of mass derived by lensing (white contours) from those of the plasma (blue "+"-signs in left panel) is a strong indication for a collisionless form of Dark Matter. Figure adapted from Ref. [2].

2
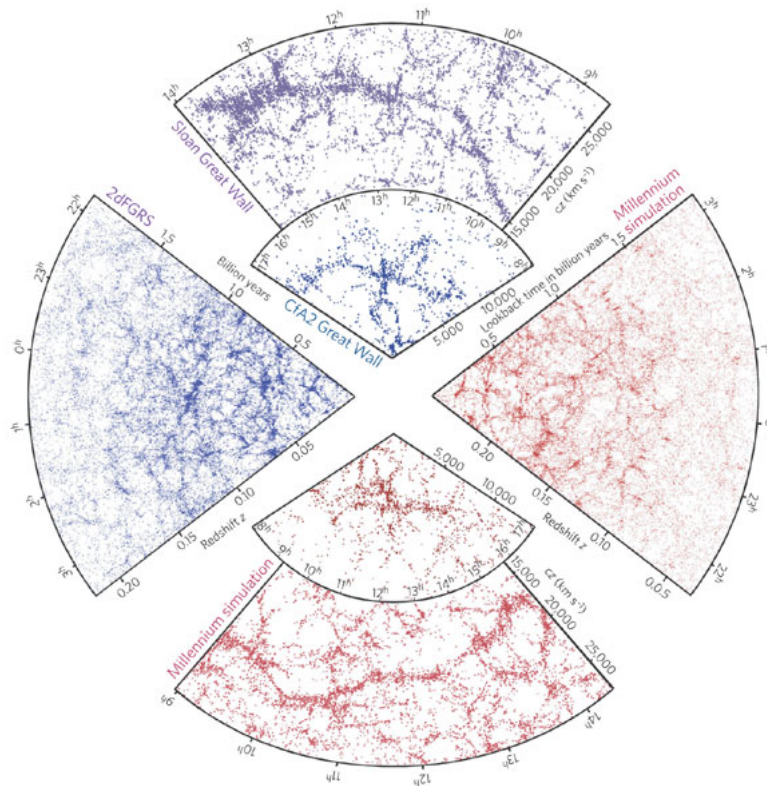
Fig. 1.3: The figure shows large scale structures observed by the Sloan Digital Sky Survey (large blue slice at top), Cf2A (small blue slice at top) and 2dFGRS (left blue slice). In comparison predictions by the "Millennium" simulation are shown (red bottom and right slice) which simulates the growth of structures due to the gravitational interaction of CDM. Figure adapted from Ref. [3]. Reprinted by permission from Macmillan Publishers Ltd: Nature 440, 1137-1144, copyright (2006).

The total amount of Dark Matter in the universe can be obtained from measurements of temperature fluctuations in the cosmic microwave background (CMB). The most precise measurement of the CMB was carried out by the Planck satellite which has derived the following values for the parameters of the standard Λ-CDM model[1] of cosmology [5]:

---

[1]The model is named after Cold Dark Matter and the cosmological constant Λ describing Dark Energy.

$$H_0 = 67.4 \pm 1.4 \, \mathrm{km \, s^{-1} \, Mpc^{-1}}$$

$$\Omega_\Lambda = 0.686 \pm 0.020$$

$$\Omega_\mathrm{b} h^2 = 0.02207 \pm 0.00033$$

$$\Omega_\mathrm{c} h^2 = 0.1196 \pm 0.0031$$

Here H_0 is the Hubble constant, Ω_Λ is the Dark Energy density divided by the critical density, $\Omega_b h^2$ is the baryonic matter density, $\Omega_c h^2$ is the density of CDM and h is the Hubble constant normalized to $100 \, \mathrm{km \, s^{-1} \, Mpc^{-1}}$. These values imply that the universe consists of $\sim 68\%$ of Dark Energy, $\sim 27\%$ of Dark Matter and $\sim 5\%$ of baryonic matter.
One has to point out that not all astrophysical observations are fully consistent with the existence of CDM [6]. Examples are the overprediction of rotation speeds near the galactic center and the number of dwarf galaxy satellites of the milky way. These discrepancies could be solved by self-interacting Dark Matter or Warm Dark Matter (WDM). It also has to be mentioned that theories of modified gravity like MOND do not require the existence of Dark Matter [7]. This theory provides a good description of the dynamics on small scales like galaxy rotation curves. However, it does not provide a satisfactory description of galaxy clusters and the CMB power spectrum [8]. In addition, MOND is a rather empirical theory while the existence of Dark Matter particles is well motivated from theories beyond the standard model of particle physics.

1.1.2 Dark Matter Candidates

There are many particle candidates for non-baryonic CDM the most promising one is the so called Weakly Interacting Massive Particle (WIMP). The motivation for the existence of WIMPs is that under the assumption that Dark Matter is produced as a thermal relic from the early universe the correct abundance is produced for an annihilation cross section of $3 \times 10^{-26} \mathrm{cm^3/s}$ which is typical for the weak interaction [9]. In addition, well motivated extensions of the standard model of particle physics like Supersymmetry (SUSY) predict the existence of such particles. An example is the neutralino which is usually the lightest supersymmetric particle (LSP) [10]. As it is stable[2], electrically neutral and has a mass $\mathcal{O}(100 \, \mathrm{GeV/c^2})$ it is an ideal candidate for Cold Dark Matter.
Other well motivated Dark Matter candidates are, e.g., axions and sterile neutrinos [11].

1.1.3 Dark Matter Search

There are three different approaches towards the detection of Dark Matter particles the indirect detection, direct detection and production at colliders.

---

[2]This is valid for most models where a quantum number called R-parity is conserved.

Search at Colliders

A confirmation of the existence of Dark Matter particles should ultimately be provided by colliders such as the LHC. Searches for new particles beyond the standard model that can account for Dark Matter like the neutralino are carried out by the CMS [12] and ATLAS experiments [13]. Since such a particle would not directly be detected due to its rare interaction the data is searched for events with large missing energy. So far ATLAS and CMS have put constraints on the parameter space of WIMP mass versus WIMP-nucleon scattering cross section. In the case of spin dependent scattering these limits are superior to direct detection experiments while for spin independent scattering they are competitive for low WIMP masses (see Fig. 1.4). However, as the collider experiments do not directly measure the scattering cross section but the production cross section these exclusion limits are strongly model dependent.
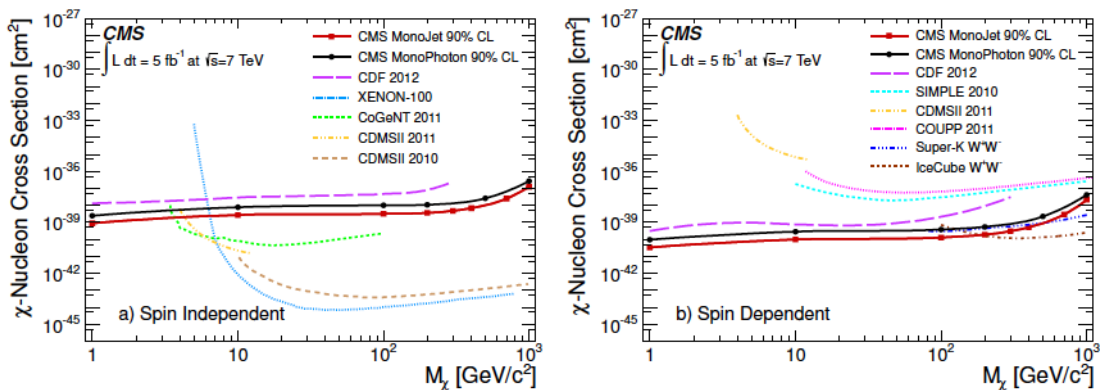
Fig. 1.4: Exclusion limits for the spin independent (a) and spin dependent (b) WIMP-nucleon cross section derived from the CMS experiment. Figure adapted from Ref. [12]. Reprinted with permission under the Creative Commons Attribution license.

Indirect Detection

The method of indirect detection concerns the decay or annihilation of Dark Matter particles. The goal is the detection of an excess of, e.g., neutrinos, γ-rays or positrons that originate from Dark Matter annihilation (or decay). Indirect detection experiments are carried out with satellite missions (e.g. Fermi, PAMELA) or ground based telescopes (e.g. IceCube, HESS). These experiments preferably observe regions with a high Dark Matter density like the galactic center or dwarf galaxies which have a high ratio of Dark Matter to luminous matter.

Interestingly, there are some signals from these experiments that could be explained by Dark Matter. An example is the positron excess first measured by PAMELA and Fermi-LAT which was recently confirmed by AMS02 (see Fig. 1.5). This excess can be fitted by

the annihilation of Dark Matter particles with masses between $500\,\mathrm{GeV/c^2}$-$100\,\mathrm{TeV/c^2}$ but requires very high annihilation cross sections of $>10^{-24}\,\mathrm{cm^3/s}$ [14]. However, the signal can also be explained by known astrophysical sources like nearby pulsars [15].

Probably the most compelling signal from indirect detection is the excess of γ-rays from the galactic center observed by the Fermi satellite [16]. This excess is well fitted by a 20-40 $\mathrm{GeV/c^2}$ dark matter particle with an annihilation cross section of $(1\text{-}2)\times10^{-26}\,\mathrm{cm^3/s}$ (see Fig. 1.6) which is very close to the thermal annihilation cross section [17]. In addition, the signal has a large statistical significance and its spatial distribution matches that expected for a standard Dark Matter profile.

Yet another excess is that observed at $3.5\,\mathrm{keV}$ in the X-ray spectrum of several galaxy clusters by the XMM Newton satellite [18, 19]. This line can not be accounted for by any known atomic emission lines and would be consistent with the decay of sterile neutrino Dark Matter with a mass of $7\,\mathrm{keV}$. However, the line is very weak and could be an instrumental effect or an atomic emission with anomalous brightness and has yet to be confirmed by other experiments.

Finally, the IceCube observatory has recently detected two PeV neutrino events of astrophysical origin [20]. These events could potentially originate from the decay of heavy PeV Dark Matter [21].

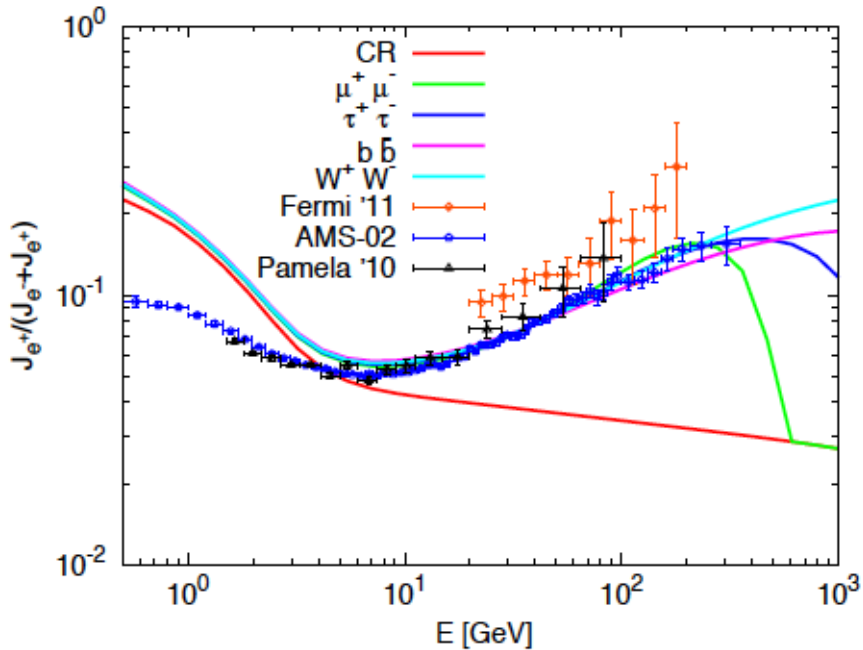**Fig. 1.5:** Positron fraction measured by the PAMELA, Fermi and AMS02 experiments. The solid lines show fits including the cosmic ray (CR) background plus a Dark Matter component for different annihilation channels. Figure adapted from Ref. [14].
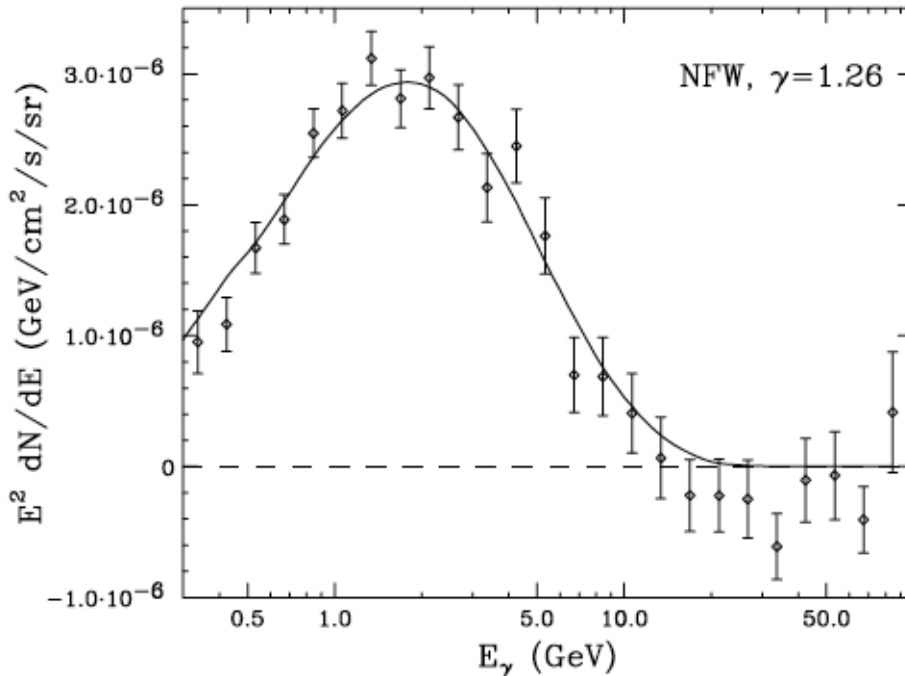
Fig. 1.6: Spectrum of γ-rays in the inner galaxy as measured by the Fermi satellite. The solid line shows the spectrum predicted for a $35.25\,\text{GeV}/\text{c}^2$ Dark Matter particle annihilating to $b\bar{b}$ with a cross section of $1.7\times10^{-26}\,\text{cm}^3/\text{s}$. Figure adapted from Ref. [17].

Direct Detection

Direct detection experiments are mainly focussed on WIMP Dark Matter. The idea is to detect the elastic WIMP-nucleus scattering from the Dark Matter halo in our galaxy with earth based detectors. Since the event rate of such an interaction is very small ($<0.1\,\text{event/kg/day}$) these experiment are located in deep underground laboratories to be shielded from cosmic radiation. In addition, they have to be well shielded against background from natural radioactivity. Most direct detection experiments use either scintillation detectors based on liquid noble gases or solid state detectors with ionization, scintillation or phonon read out. Most of the current generation of experiments use two read-out channels which provides a method of active background discrimination.

Also in the field of direct detection there are several hints for positive signals. The most long-standing claim comes from the DAMA/LIBRA experiment which has measured an annual modulation of the rate that is consistent with a Dark Matter interpretation [22]. Because of the movement of the earth around the sun the WIMP flux modulates annually with an expected maximum at June 2nd. If the DAMA result is explained by elastic

WIMP-nucleus scattering off Na[3] it would correspond to a WIMP mass of $\sim 10\,\text{GeV}/\text{c}^2$ and a scattering cross section of $\sim 2\times 10^{-40}\text{cm}^2$ [23]. The CoGeNT experiment has observed an excess of events at low-energies which can be explained by a light $\sim 8\,\text{GeV}/\text{c}^2$ WIMP [24]. CoGeNT also observes an annual modulation of the event rate with a phase compatible with a Dark Matter interpretation, however, with a small significance of 2.2σ and an amplitude that is not consistent with the standard WIMP halo [25]. The CDMS-Si experiment has observed three events with a 0.19% probability for the known-background-only hypothesis. These events are best fitted by a $8.6\,\text{GeV}/\text{c}^2$ WIMP with a WIMP-nucleon cross section of $1.9\times 10^{-41}\,\text{cm}^s$ [26]. Finally, also the CRESST-II experiment has observed an excess of events compatible with $\sim 12\text{-}25\,\text{GeV}/\text{c}^2$ WIMPs [27]. Even though the parameter space of all these experiments does not fully overlap they all point towards light $\sim 10\,\text{GeV}/\text{c}^2$ WIMPs with a scattering cross section of $(10^{-40}\sim 10^{-41})\,\text{cm}^2$ (see Fig. 1.7). A well motivated model for light WIMPs is that of Asymmetric Dark Matter [28]. It assumes that the baryon and Dark Matter abundance have a common origin in the asymmetry of number densities for particles and antiparticles.

In contradiction to these positive signals are the null results of several other experiments. In particular, the LUX [29], XENON100 [30] and SuperCDMS [31] experiments exclude the parameter space derived from the positive signals (see Fig. 1.7). This tension can partially be avoided by non-standard Dark Matter interactions like Isospin Violating Dark Matter, Exothermic Dark Matter or Inelastic Dark Matter [32, 33, 34]. However, even under extreme assumptions it is not possible to bring all experiments in agreement. The current status of Dark Matter direct detection demands clarification of this low-mass WIMP scenario. In this regard the current data taking campaign of the CRESST-II experiment will provide crucial information as it will either confirm the signal seen in the previous run with a high significance or rule out the relevant parameter space.

---

[3]The DAMA experiment uses NaI(Tl) crystals as target material, therefore, WIMPs can either scatter off Na or I.
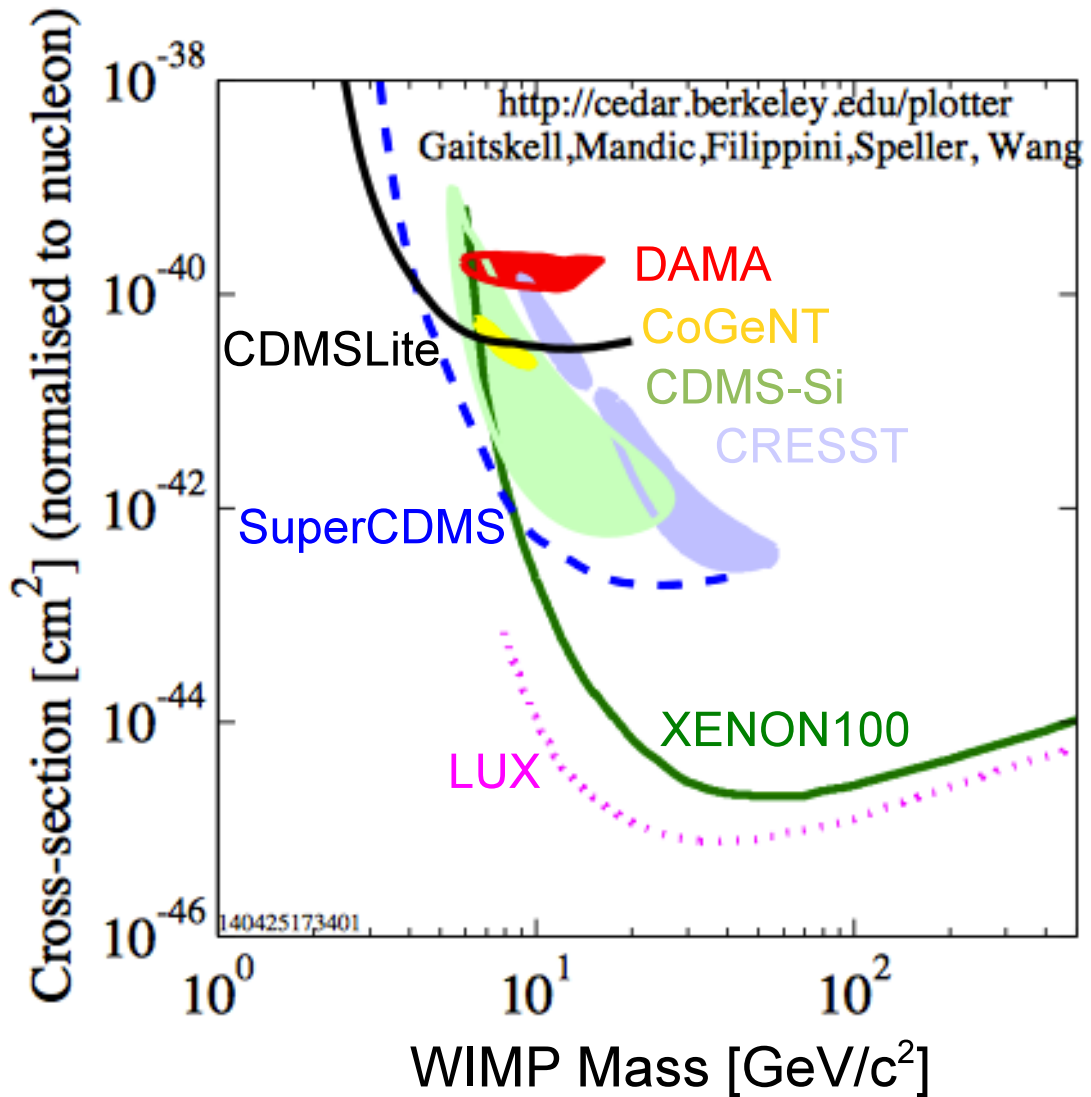
Fig. 1.7: The plot shows the results of different direct detection experiments in the plane of WIMP mass versus WIMP-nucleon cross section. The filled regions mark the signals measured by the experiments DAMA [23], CoGeNT [25], CRESST [27] and CDMS-Si [26]. Also shown are the exclusion limits by CDMSLite [35], SuperCDMS [31], XENON100 [30] and LUX [29].

9

1.2 The CRESST-II Experiment

1.2.1 Setup

The CRESST-II experiment located at the Laboratori Nazionali del Gran Sasso (LNGS) in Italy aims at the direct detection of WIMP Dark Matter. It uses low-temperature detectors based on scintillating $CaWO_4$ crystals.

The location at the Gran Sasso underground laboratory provides a shielding of ~3500 m.w.e. (meters water equivalent) which reduces the muon flux by six orders of magnitude to a flux of ~$1\,m^{-2}h^{-1}$ [36]. In addition, the detectors are shielded against ambient radioactivity by copper and lead as well as polyethylene to moderate neutrons (see Fig. 1.8). Plastic scintillator panels are used as active muon veto.

Cooling of the detectors is provided by $^3He/^4He$ dilution refrigerator which is kept outside the shielding while the heat is transferred with a cold finger made of copper. The cryostat can house up to 33 detector modules. A single detector module consists of a ~$300\,g$ scintillating $CaWO_4$ crystal (phonon detector) that serves as target and a silicon-on-sapphire waver (light detector) that detects the scintillation light (see Fig. 1.9). Both detectors are operated at mK temperatures and measure the temperature rise by a particle interaction. This is achieved by transition edge sensors (TESs) which consist of a thin tungsten film that is deposited onto the crystal. The TES is then stabilized around $15\,mK$ in the transition between normal and superconducting phase. A small rise in temperature ΔT leads to a relatively large change of the resistance ΔR which is read out by a SQUID circuit (see Fig. 1.10).
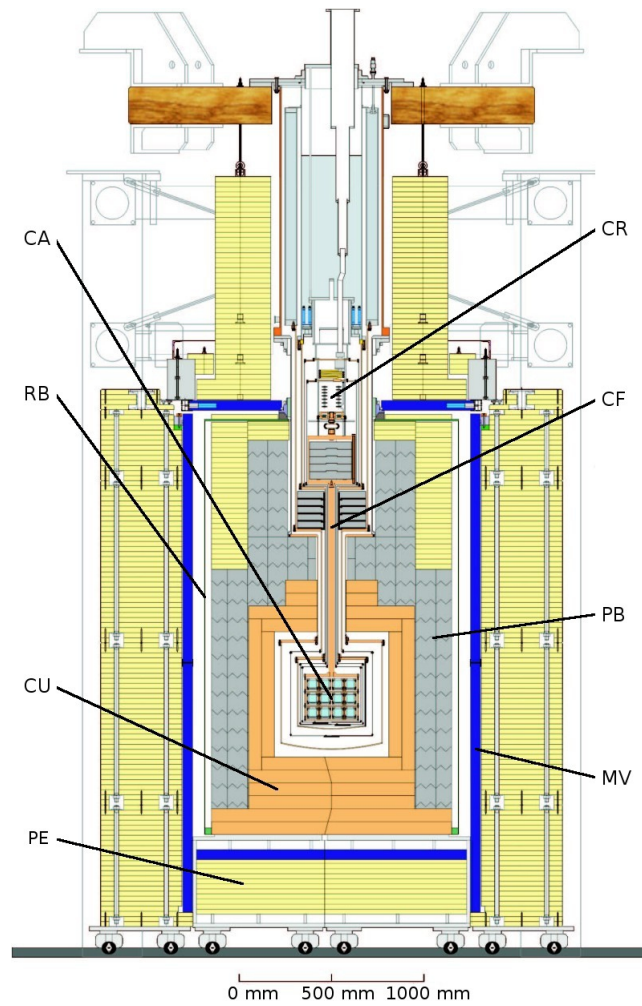
Fig. 1.8: Experimental setup of the CRESST-II experiment: detector carousel (CA), mixing chamber of the cryostat (CR), cold finger (CF), lead shield (PB), muon veto (MV), polyethylene shield (PE), copper shield (CU) and radon box (RB).

11

(a)

(b)
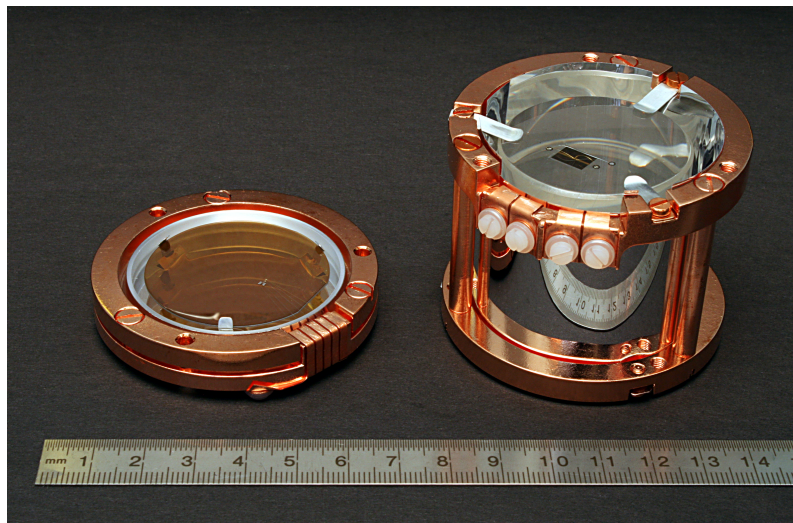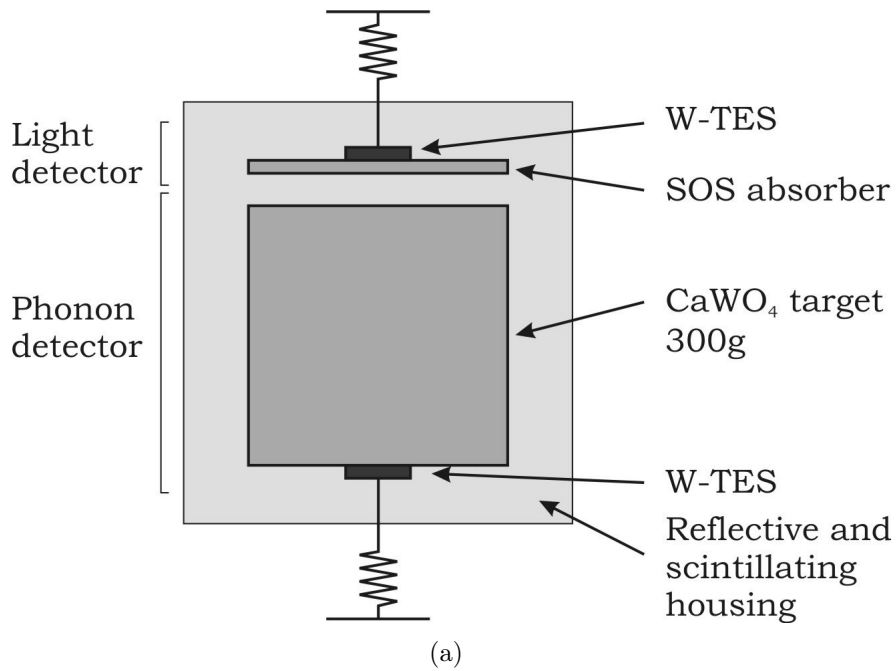
Fig. 1.9: Schematic drawing (a) and photograph of a CRESST-II detector module (b). The module consists of a 300 g scintillating $CaWO_4$ crystal ($\varnothing$=40 mm, h=40 mm) equipped with a tungsten TES to measure the phonon signal and a silicon-on-sapphire (SOS) light detector ($\varnothing$=40 mm, d=0.4 mm) for the simultaneous detection of the scintillation light. The light and phonon detector are enclosed together in a reflective and scintillating housing.
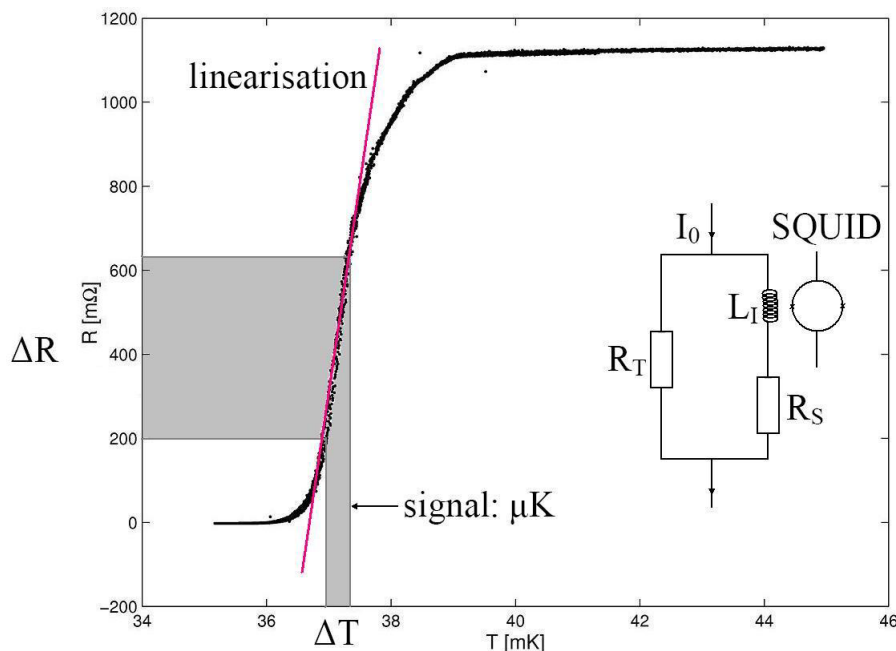
Fig. 1.10: Working principle of a TES. In a superconducting film operated at its transition temperature a small change in temperature causes a steep approximately linear rise in resistance R_T. The whole circuit is biased with a constant current I_0. A change of R_T causes a change of the current in the superconducting coil L_I which is then picked up by a Superconducting Quantum Interference Device (SQUID). Figure adapted from Ref. [37].

1.2.2 Active Background Discrimination

The simultaneous detection of the signal from the phonon detector and light detector provides a method of active background discrimination. The phonon signal corresponds to ~95% of the total deposited energy and is in good approximation independent of the type of interacting particle while the light signal is largely dependent on the type of recoil. This effect is known as scintillation quenching and has its origin in the different ionization densities of different particles. Recently, a detailed model was developed that describes this effect on a microscopic level by the interaction between excitons [38]. The ratio of the phonon and light signal is called "Light Yield" (LY)[4] and is defined as 1 for

---

[4]The term "Light Yield" is often used to describe different properties. In Sec. 3.2.2, e.g., we use a different definition of the light yield.

122 keV γ-quanta:

$$LY_x(E) = \frac{E_x^{light}(E)}{E_x^{phonon}(E)} \tag{1.1}$$

$$LY_\gamma(122\,\text{keV}) := 1 \tag{1.2}$$

For other types of particles the Light Yield is reduced to a certain fraction which is described by quenching factors. The quenching factor QF_x is hereby defined as the ratio of the LY for the particle x to a γ event of the same energy E:

$$QF_x(E) = \frac{LY_x(E)}{LY_\gamma(E)} \tag{1.3}$$

The values and energy dependence of the quenching factors for different types of nuclear recoils have been recently precisely measured at mK temperatures [39]. Because of this quenching effect different types of recoil events show up at different bands in the LY versus energy plane (see Fig. 1.11). Since WIMPs are expected in the nuclear recoil bands this can be used to discriminate the dominant background that consists of electron and γ events.

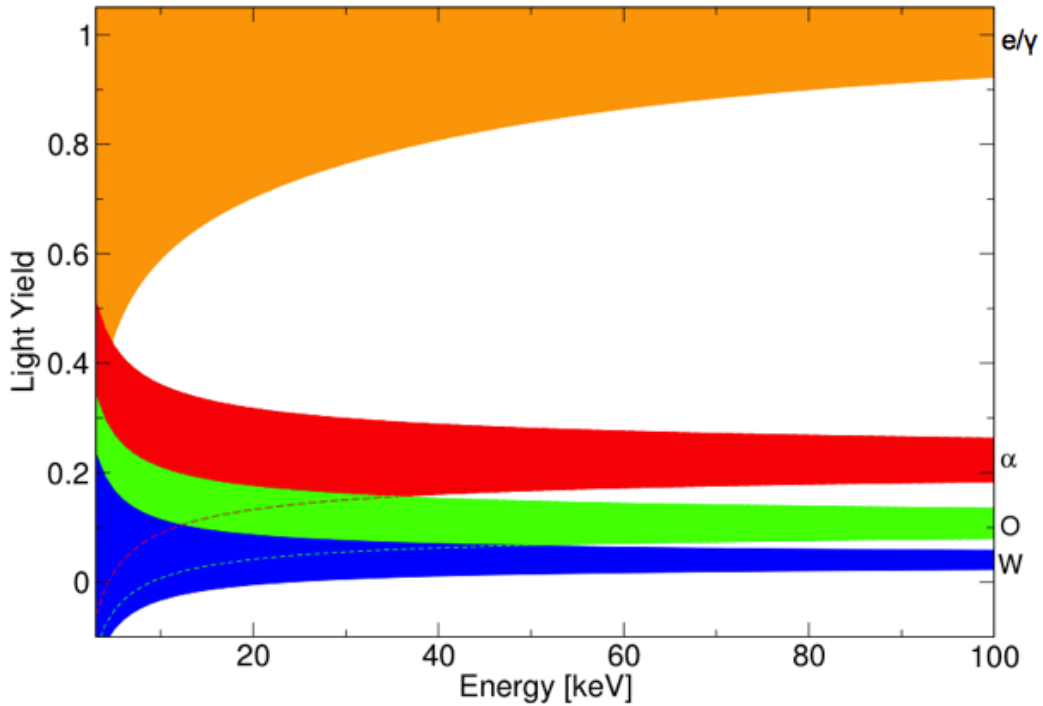**Fig. 1.11:** Schematic picture of a Light Yield versus energy plot. Shown are the different recoil bands for electrons/γ-rays (e/γ), alpha particles (α) and nuclear recoils on oxygen (O) and tungsten (W). The calcium recoil band is left out for clarity.

1.3 The EURECA Experiment

The goal of the EURECA (European Underground Rare Event Calorimeter Array) project is to develop a tonne-scale cryogenic direct Dark Matter search experiment [40]. The experiment will use $CaWO_4$ detectors with phonon-light read out as well as Ge detectors based on the phonon-ionization technique [41]. The advantage of a multi-element target is that it is sensitive to wide range of WIMP-masses and different scattering mechanisms. In case of a positive signal it will also put tighter constraints on the WIMP parameter space. The experiment is foreseen to be hosted at the DOMUS extension of the Laboratoire Souterrain de Mondane (LSM) in France at a depth of $\sim$4800 m.w.e. There is also a collaboration with the SuperCDMS project that will be constructed at SNO Lab (Canada) which serves as an alternative location for a common experiment.

Cooling of the detectors will be achieved by a ^{3}He/^{4}He dilution refrigerator installed inside a water tank that provides a shielding of 3 m water in each direction against ambient radioactivity and neutrons (see Fig. 1.12(a)). An additional shielding consisting of copper, Polymethylmethacrylat (PMMA) and polyethylene (PE), is needed to protect detectors from still prevailing internal radioactivity. The water tank can also be equipped with $\sim$100 photomultipliers to serve as water Cherenkov veto for muons. If enough space is available an alternative design of the experiment includes two identical water tanks and cryostats (see Fig. 1.12(b)). A building between the two tanks can provide the necessary infrastructure such as cleanrooms. The advantage of this design would be that one system is available for science runs while the other can be used for R&D and comissioning of the detectors.

The experiment is divided into two phases: In phase I a total target mass of 150 kg will be operated for 1 year to reach sensitivities of 3×10^{-10} pb. In the second phase the maximum sensitivity of 2×10^{-11} pb will be reached after 3 years with a total target mass of 1 tonne (see Fig. 1.13).

Projects with similar target mass are also being pursued by liquid noble gas experiments such as XENON1T [42] or DEAP3600 [43] which are already in construction and will probably explore this parameter region before EURECA. However, cryogenic detectors offer an complementary technique that is needed for confirmation in case of a positive signal. Furthermore, the low threshold and good energy resolution will allow a better sensitivity for low-mass WIMPs.
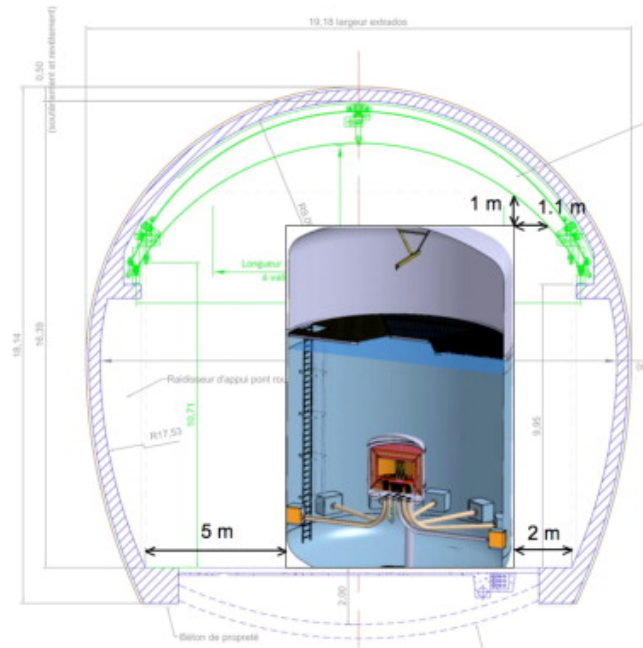
(a)
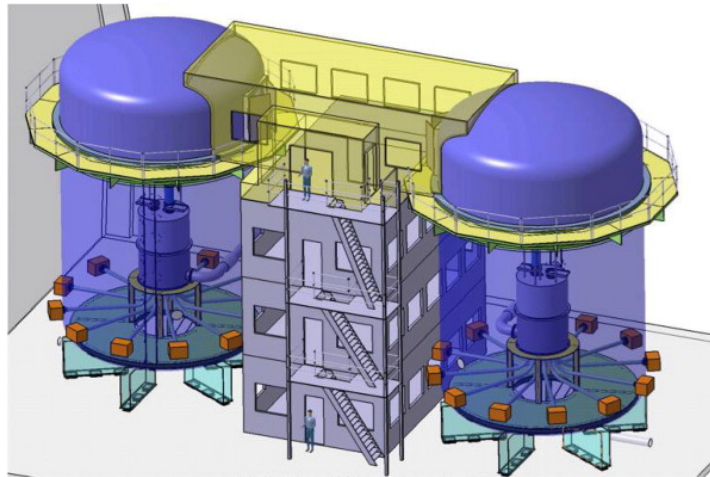
(b)

Fig. 1.12: (a): Schematic picture of the EURECA setup within the DOMUS laboratory. The cryostat will be housed inside a water tank that provides shielding and can be used as a water Cherenkov veto. (b): Alternative design with two identical cryostats and a building that provides the necessary infrastructure between them. Figures adapted from Ref. [40]. Reprinted with permission under the Creative Commons Attribution license.
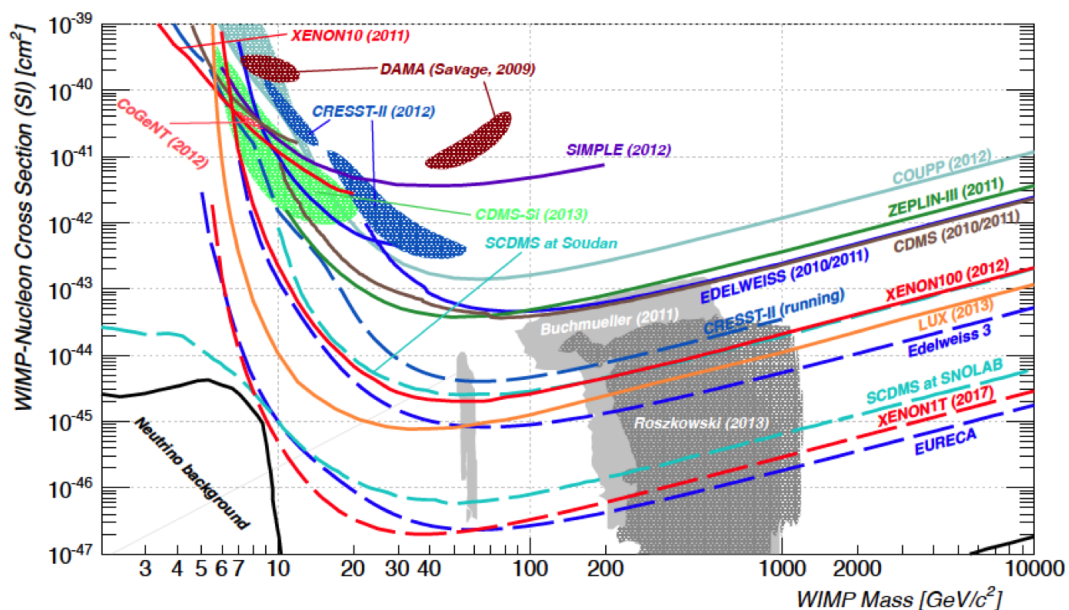
Fig. 1.13: Projected sensitivity of the EURECA experiment in comparison to other current and future direct Dark Matter searches. The solid black line shows the ultimate sensitivity that can be achieved due to the background from coherent nucleus scattering of solar and atmospheric neutrinos.

1.4 Scintillating CaWO$_4$ Crystals

The main topic of this thesis is the production and characterization of CaWO$_4$ crystals for the CRESST-II and EURECA experiments. The following section will explain the relevance of the material for rare event searches and give an overview of its crystal and scintillation properties.

1.4.1 Relevance for Rare Event Searches

CaWO$_4$ is a multi-element target and interesting for different rare event searches. For Dark Matter search the presence of W (A=184) provides a good sensitivity to coherent scattering where the cross section is proportional to A^2 [44]. The isotope ^{184}W with a natural abundance of 14% has a nuclear spin which provides also some sensitivity to spin-dependent scattering. In addition, the lighter elements Ca (A=40) and O (A=16) lead to detectable recoil energies also for light WIMPs (see Fig. 1.14).

It is also possible to use CaWO$_4$ to study double beta decay and double electron capture processes (see Tab. 1.1). The most interesting process to study would be the neutrinoless double beta decay ($0\nu2\beta$) which has not yet been observed [45]. This decay is forbidden

in the standard model and would proof the Majorana nature of the neutrino. Limits on the half life of this decay can be used to constrain the effective neutrino mass. Double electron capture (2EC) has been observed only indirectly for ^{130}Ba in a geochemical experiment [46]. There is also the possibility for a neutrinoless mode ($0\nu2EC$) which can be used to study neutrino properties similar to $0\nu2\beta$ [47].

The isotope ^{48}Ca is the candidate for double beta decay with the highest Q-value. Experiments to search for the $0\nu2\beta$ of ^{48}Ca with CaWO$_4$ scintillators have already been proposed [48]. The problem is the small natural abundance of 0.18% which would require enriched detectors. However, the enrichment of ^{48}Ca is problematic as there are no gaseous calcium compounds at room temperature [49]. The isotope ^{40}Ca is interesting as it is the candidate for 2EC with the highest natural abundance of 96.9%. Finally, ^{180}W is a promising candidate for $0\nu2EC$ because there is the possibility of a resonant enhancement [50].

CRESST detectors with their good resolution and low background are well suited to search for these double beta processes. In fact, it could be shown that world-leading limits on most of these processes can be derived from CRESST data [51]. A dedicated analysis for double beta processes using the latest CRESST data is currently ongoing.
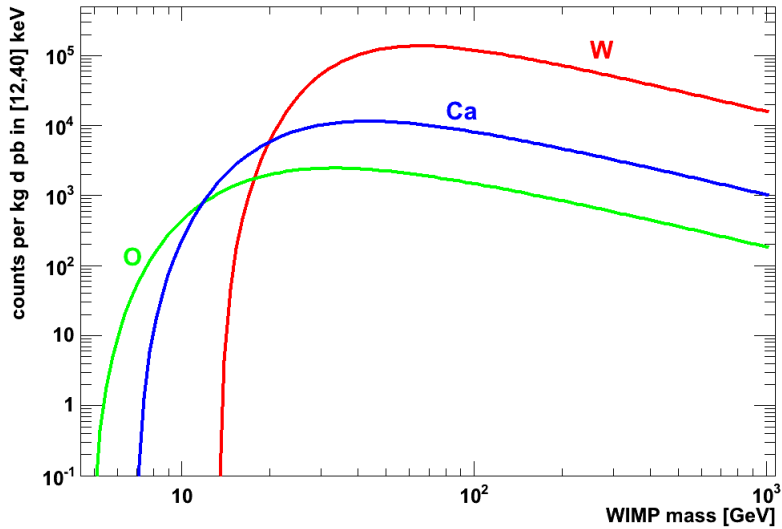
Fig. 1.14: The plot shows the expected rate of WIMP events in CaWO$_4$ for the different target nuclei in the energy range 12-40 keV in dependence of the WIMP mass. For WIMP masses $\gtrsim 11\,\text{GeV}/\text{c}^2$ the rate is dominated by tungsten while for smaller masses only oxygen and calcium recoils are above the assumed detector threshold of 12 keV.

isotope	natural abundance (%)	decay mode	Q-value [keV]
^{48}Ca	0.18	$2\beta^-$	4274
^{46}Ca	0.004	$2\beta^-$	988
^{40}Ca	96.9	2EC	194
^{180}W	0.13	2EC	144
^{186}W	28.4	$2\beta^-$	490

Tab. 1.1: Isotopes in CaWO$_4$ that can be used to study double beta processes.

1.4.2 Crystal Properties

Calcium tungstate (CaWO$_4$) is a mineral also known as Scheelite named after Swedish chemist C. W. Scheele. Scheele who is famous for the discovery of several elements including oxygen could show that CaWO$_4$ also contains a new element, namely tungsten. The crystal properties of CaWO$_4$ are summarized in Tab. 1.2. The crystal lattice has a body-centered tetragonal structure (space group: I4$_1$/a) [52]. The unit cell is shaped like a rectangular prism with a square base and is built of Ca^{2+} ions surrounded by WO$_4^{2-}$ tetrahedra (see Fig. 1.15). One important property is the occurrence of natural cleavage planes which requires to minimize mechanical and thermal stresses during crystal production. The rather high melting point of 1600 °C limits the choice of a suited crucible material for crystal growth to the noble metals rhodium, iridium and platinum.
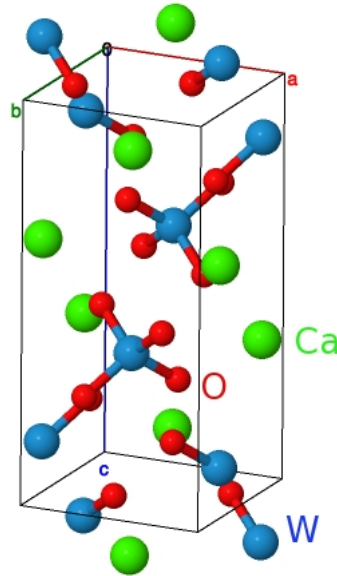
Fig. 1.15: Crystal structure of CaWO$_4$. The unit cell is shaped like a square prism and is built of Ca^{2+} ions and WO$_4^{2-}$ tetrahedra.

density	$6.1\,\mathrm{g/cm^3}$
melting point	$1600°C$
hardness	$4.5\text{-}5\,\mathrm{Mohs}$
cleavage planes	distinct on $\{101\}$, indistinct on $\{001\}$
space group	$I4_1/a$
cell parameters	a=b=5.24$\mathring{A}$, c=11.37$\mathring{A}$

Tab. 1.2: Crystal properties of $CaWO_4$ [52].

1.4.3 Scintillation Properties

The scintillation of $CaWO_4$ was discovered by Thomas Edison in 1896 only one year after Röntgen's discovery of X-rays [53]. Therefore, it belongs to the oldest known scintillators and has been well studied (see Ref. [54] and references therein). Recently, a microscopic model of the scintillation mechanism in $CaWO_4$ has been developed within the framework of the CRESST experiment [38]. The scintillation mechanism is of intrinsic nature and ascribed to the recombination of self-trapped excitons. Electron-hole pairs are created by ionizing particles or radiation. The holes can then be trapped at an oxygen anion of a WO_4 complex which causes an attractive potential for electrons (see Fig. 1.16). Electrons that come by can fall into this potential leading to the formation of a so called self-trapped exciton (STE). The recombination of this self-trapped exciton then causes the emission of scintillation light.

The optical and scintillation properties of $CaWO_4$ are summarized in Tab. 1.3. It has a rather high refractive index of 1.95 [55] which can lead to large trapping of scintillation light due to total internal reflection [56]. It is also weakly birefringent [52]. The absolute light yield corresponds to about 40% of that of NaI(Tl) [57]. It has a rather long decay time of $\sim9\,\mathrm{\mu s}$ [58] which makes it less attractive for high energy physics. The emission maximum is at $\sim420\,\mathrm{nm}$ [59] which is well matched to the sensitivity of most photomultipliers.

It has to be noted that these properties all refer to room temperature. At mK temperatures where CRESST-II detectors are operated most of these properties especially the light yield and decay time can change which will be discussed in Sec. 3.2.3.
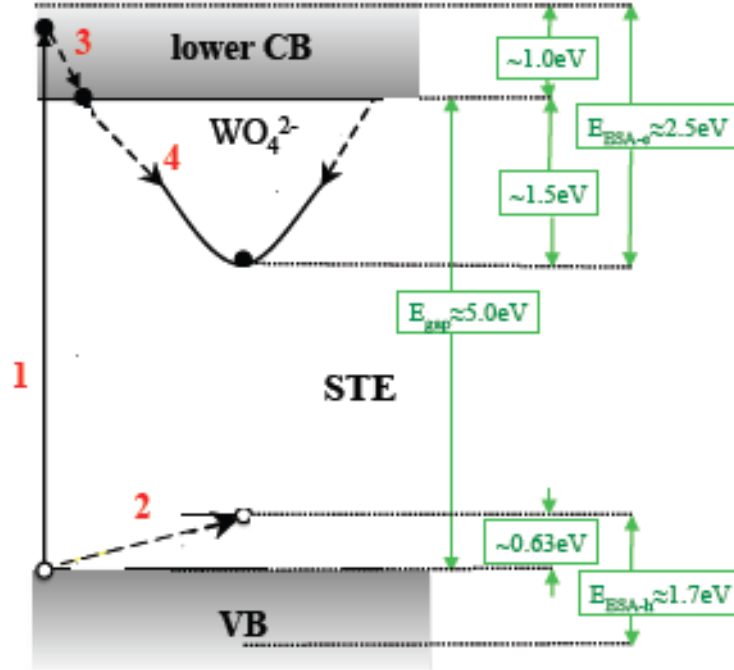
Fig. 1.16: Band structure and scintillation mechanism in CaWO$_4$. (1) excitation of an electron from the valence band (VB) into the lower conduction band (CB); (2) self-trapping of the hole leading to an attractive potential for electrons within the band gap; (3) relaxation of the electron to the band edge; (4) the electron falls into the potential well, thus, forming a self-trapped exciton. Figure adapted from Ref. [38].

refractive index	1.95 [55]
birefringence	0.017 [52]
light yield	16,000-20,000 ph/MeV [57, 60, 61]
scintillation decay time	9 µs [58]
emission maximum	420 nm [59]

Tab. 1.3: Optical and scintillation properties of CaWO$_4$.

Chapter 2

CaWO$_4$ Crystal Production

Up to now all CaWO$_4$ crystals that were used in CRESST were provided by different institutes like the General Physics Institute of the Russian Academy of Science (GPI RAS) in Moscow or the Scientific Research Company (SRC) "Carat" in Lviv (Ukraine). In 2008, we started the production of CaWO$_4$ crystals within the collaboration using a dedicated Czochralski furnace at the Crystal Laboratory of the Technische Universität München (TUM) [62]. The aim of this effort was to have direct influence on the selection of the raw materials, the crystal growth and the after-growth treatment in order to improve radiopurity and scintillation properties as, e.g., the light output of the crystals. In this chapter an overview of the crystal growth process is given and the post-growth treatment is described.

2.1 Crystal Growth

The Czochralski process [63] is a method of crystal growth to obtain large cylindrical single crystals. Coincidentally, the first reported oxide material grown using the Czochralski technique was CaWO$_4$ [64].
In the Czochralski method a seed crystal with a well-defined orientation is mounted on a rod and lowered into the melt. This rod with the seed crystal is then pulled upwards and rotated at the same time (see Fig. 2.1). The crystallization takes place at the crystal-melt interface and the seed crystal's crystallographic orientation is transferred so that finally a large cylindrical single crystal can be extracted from the melt. The diameter d$_s$ of the crystal during growth is directly related to the mass growth rate G of the crystal by [65]:

$$G = \frac{\pi}{4} d_s{}^2 \rho_s P \left(1 + \frac{d_s{}^2}{\frac{\rho_l}{\rho_s} d_l{}^2 - d_s{}^2} \right) \tag{2.1}$$

Here P is the pulling rate, d$_l$ the crucible diameter and ρ_l the liquid density. The growth rate is influenced by the temperature gradient at the phase boundary. This temperature gradient and therefore the growth rate and the crystal diameter are controlled by the

heating power. An increase of the heating power leads to a smaller crystal diameter and vice versa.
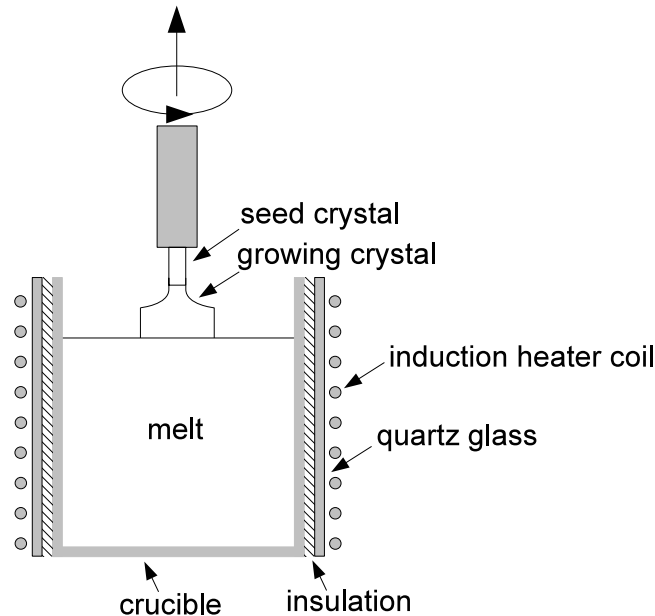
Fig. 2.1: Schematic drawing of the Czochralski setup. A seed crystal mounted on a rod is lowered into the melt. This rod is then pulled upwards and rotated at the same time. The crystallization takes place at the crystal-melt interface and the seed crystal's crystallographic orientation is transferred. Finally, a large cylindrical single crystal is extracted from the melt.

2.1.1 Czochralski Furnace

Figure. 2.2 depicts the Cyberstar Oxypuller 20-04 Czochralski furnace installed at the crystal laboratory of the TUM. The pulling rod of the furnace is connected to a scale which is continuously weighing the crystal during the growth process. The derivative of the weight measurement gives the current growth rate. This allows the automatic adjustment of the heating power by a PI controller [66] so that the current crystal diameter calculated from Eq. (2.1) matches previously specified dimensions of the crystal. The growth is carried out in rhodium crucibles with a diameter of 80mm or 120mm. The high oxidation resistance of rhodium allows to grow crystals under an atmosphere containing a small percentage of oxygen. The crucible is surrounded by thermal insulation made from ZrO$_2$ followed by a quartz-glass cylinder (see Fig. 2.3(a)) and an induction coil which is connected to a RF generator. The quartz glass avoids sparks between the induction coil and the crucible and also supports a resistive after-heater located above the crucible (see Fig. 2.3(b)). The latter lowers the risk of cleavage of the crystals due to thermal stress

caused by temperature gradients that are induced after the crystal is separated from the melt. During the growth a constant flow ($\sim$25 l/h) of a mixture of 99% Ar and 1% O_2 is maintained inside the furnace. The furnace is connected to a computer interface and the rotation and pulling speed as well as the heating power can be controlled by software.
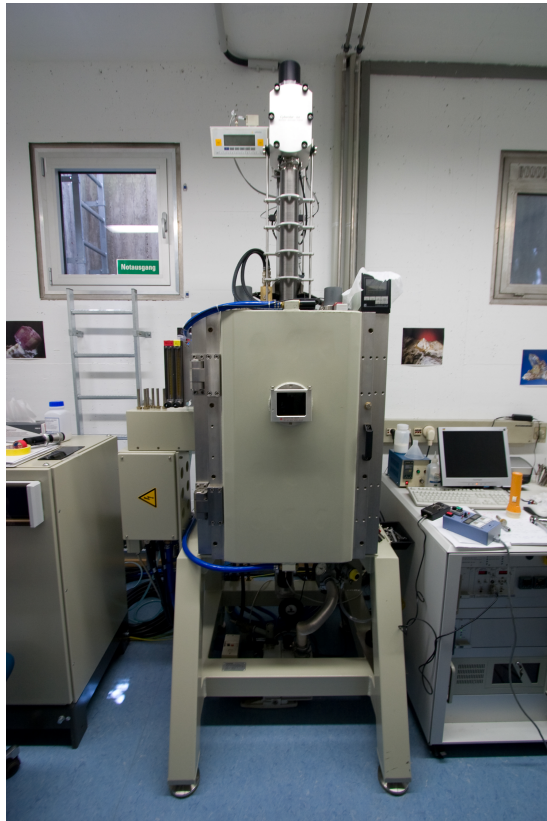
Fig. 2.2: Cyberstar Oxypuller 20-04 Czochralski furnace at the crystal laboratory of the TUM. Visible is the scale which is connected to the pulling rod. It allows an automatic diameter control through continuous weighing of the crystal during growth.

(a)
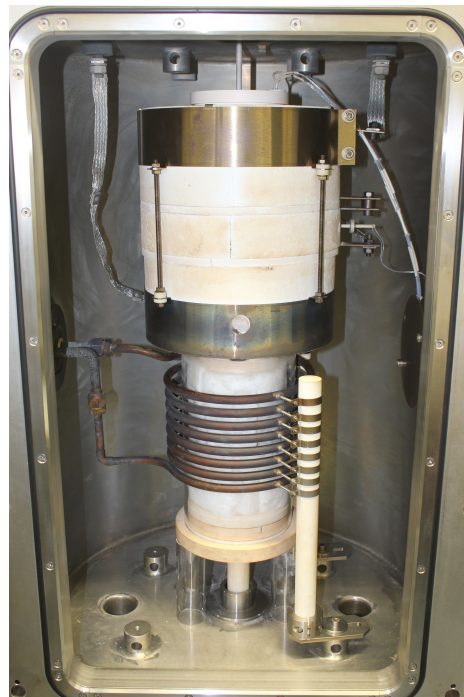
(b)

Fig. 2.3: (a): Rhodium crucible with the residual melt. The crucible is surrounded by thermal insulation and a quartz-glass cylinder to avoid sparks between the induction coil and the crucible. (b): View inside the Czochralski furnace showing the induction coil surrounding the crucible. A resistive after-heater located above the crucible lowers the risk of cleavage of the crystals due to thermal stress originating from temperature gradients during cooling.

2.1.2 Growth Procedure

The following paragraph describes the growth process in more detail.

The $CaWO_4$ powder for the melt is prepared by a solid state reaction between $CaCO_3$ and WO_3 under air at 1250°C:

$$CaCO_3 + WO_3 \rightarrow CaWO_4 + CO_2 \tag{2.2}$$

The reaction is carried out in Al_2O_3 crucibles with intermediate grinding of the powders. Completeness of the reaction can be monitored by the weight loss from the CO_2. As starting materials $CaCO_3$ and WO_3 with a high purity of 5N and 4N8 are used (see Sec. 3.3.1), respectively. One has to point out that there are also alternative synthesis reactions like the chemical precipitation from a solution which may be more advantageous (see Sec. 3.3.1).
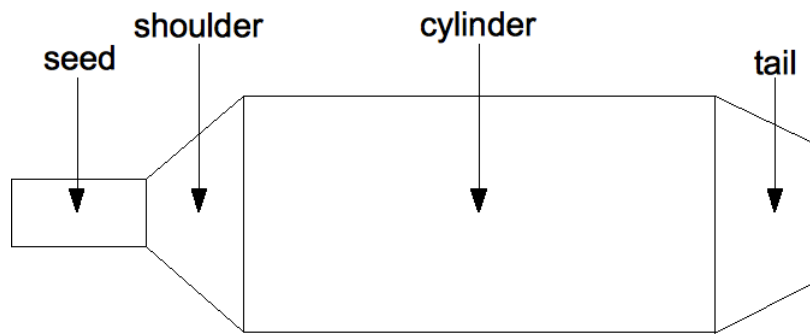
Fig. 2.4: Schematic picture of a grown crystal. The crystal is divided into four parts: the seed, the shoulder, the cylinder and the tail. In the growth software the dimensions for each part as well as a set of growth parameters at the beginning and end of each part have to be specified.

Before the growth the crystal geometry and growth parameters have to be entered into the growth software. In the software the crystal is divided into four parts: The seed, shoulder, cylinder and tail (see Fig. 2.4). For every part the length and diameter as well as a parameter that determines the shoulder angle have to be specified (see Tab. 2.1). Furthermore, the crystal and liquid densities and the crucible diameter have to be entered into the software which allows the calculation of the crystal diameter from the measured growth rate via Eq. (2.1).

The parameters controlled during growth are the rotation speed of the pulling rod and the growth speed[1] which have to be specified at different positions along the crystal (see Tab. 2.2). The proportional and integral terms for the automatic control of the heating

---

[1]The pulling speed is then calculated from the growth speed and the liquid level drop.

power have also to be defined for the different positions. All values are changed linearly in between these positions. To find the right set of growth parameters can be difficult and is mainly based on experience.

Starting the growth, the rhodium crucible containing the raw material is heated via the induction coil to a temperature slightly above the melting point T$_m$ ≈1600°C. After it is ensured that all of the CaWO$_4$ has melted the temperature is decreased and stabilized at ∼1620°C. Then the seed crystal is manually lowered and dipped into the melt. The seeding procedure is very critical as it has to be done at just the right temperature. A too low temperature will lead to a sudden solidification when the seed crystal touches the melt while a too high temperature will melt the seed crystal. If the seeding was successful and the crystal is slowly gaining weight the control of the growth process can be handed over to the software. The parameters of a typical growth which are constantly measured and controlled by the software are shown in Fig. 2.5. The error of the growth rate is used to adjust the heating power as described above. It indicates the stability of the growth process and is usually ≲10 g/h for a ∼730 g crystal.

When the growth process is finished the crystal is manually pulled up into the after-heater which is then stabilized at a temperature of 1200°C. After the crystal has been annealed for 24 h the after-heater is slowly cooled down at a rate of 50°C/h. Thereafter the raw crystal, so called ingot, can be extracted from the furnace and is ready for further processing. The seed crystal can be cut from the ingot and used again.

crystal mass [g]	737.4
growth duration [h]	10.3
crystal length [mm]	130
covered height [mm]	106.6
seed length [mm]	5
shoulder length [mm]	55
R2/R1	0.3
angle [deg]	68
cylinder length [mm]	45
tail length [mm]	25
crucible diameter [mm]	80
solid density [g/cm^3]	6.28
liquid density [g/cm^3]	6.28
seed diameter [mm]	7
cylinder diameter [mm]	45.5
tail diameter [mm]	80
max. generator setpoint [%]	28
max. growth rate [g/h]	500
growth rate warning [g/h]	250
extraction height [mm]	65
extraction speed [mm/min]	60
cooling program [h]	3

Tab. 2.1: Standard parameters to grow a $\sim$730 g crystal with $\sim$45 mm diameter and 130 mm length (e.g. growth number 40 in Tab. 2.3). The parameters in the first section are implicitly determined by the other growth parameters. The values in the second section define the geometry of the crystal. The third section contains safety values that limit certain growth parameters. In the last section values for the extraction of the crystal and cooling of the generator are defined.

29

position [mm]	growth speed [mm/h]	rotation speed [rpm]	P	I
0	20	15	5	20
5	15	15	5	25
23.3	12	20	5	35
41.7	12	25	4	40
60	12	25	3.5	55
75	12	25	3	55
90	12	25	3	55
105	12	25	3	55
130	15	20	4	40

Tab. 2.2: Control parameters for the growth of a crystal as defined in Tab. 2.1. The table shows the growth and rotation speed and parameters for the PI controller of the heating power along different positions of the crystal.
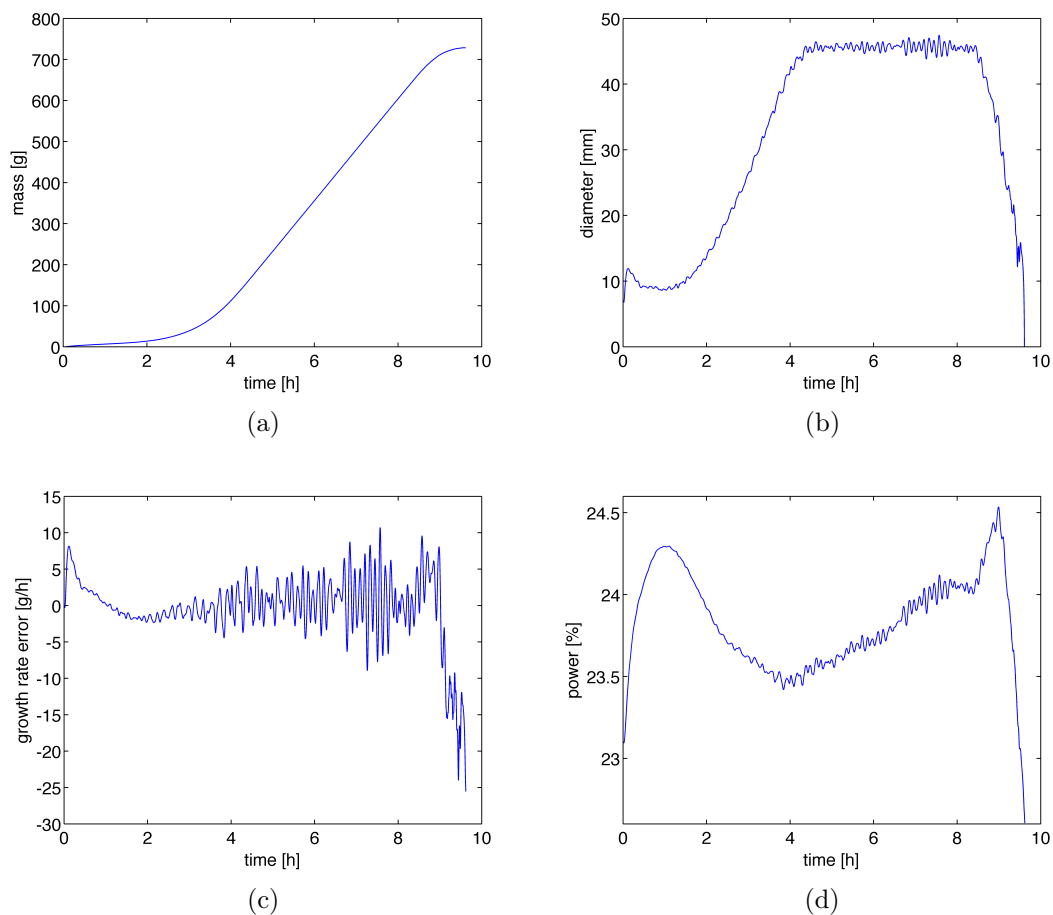
Fig. 2.5: Control parameters measured during growth number 40 (see Tab. 2.3). Shown are the crystal mass (a), the crystal diameter (b), the error of the growth rate (c) and the heating power (d).

2.1.3 Grown Crystals

Figure 2.6(a) shows a typical grown ingot. The properties of all crystals grown in the scope of this work are summarized in Tab. 2.3. All crystals were grown in [001] direction. The first crystal grown with the furnace had a mass of just 58 g while the largest crystal weighed ~1.6 kg. The growth speed varied between 6-20 mm/h. Crystals up to 45 mm diameter were grown in the 80 mm diameter crucible while for larger crystals the 120 mm crucible was used.

The raw materials for crystal growth ($CaCO_3$ and WO_3 powders) were obtained from Alfa Aesar (AA) and MV Laboratories (MV) (see also Sec. 3.3.1). All crystals were grown from stoichiometric melt except for growth numbers 55 and 56 where 1% excess WO_3

was added to eliminate scattering centers (see Sec. 3.1.3).

While the first crystals were grown under N$_2$ atmosphere it was then changed to 99% Ar with 1% O$_2$. This reduces grey coloring due to an oxygen deficiency of the crystals (see Fig. 2.7). To test if the oxygen deficiency can be further reduced growth number 50 was carried out with 3% O$_2$. However, this resulted in a crystal with pink colored inclusions (see Fig. 2.8(a)) which may come from the incorporation Rh caused by an oxidation of the crucible material. Furthermore, these inclusions also appeared in the two subsequent growths carried out with only 1% O$_2$ until the crucible was cleaned. This suggests that the melt was contaminated with some impurity.

Some crystals especially the largest ones showed cracks when they were extracted from the furnace (see Fig. 2.8(b)) while some crystals also cracked during handling. These problems are related to the natural cleavage planes of CaWO$_4$ (see Sec. 1.4.2) and to internal stresses resulting, e.g., from temperature gradients during cooling.

For each growth the melt has to reach a certain level because the pulling rod can only be lowered to a certain extend and because the crystal grower has to be able to visually inspect the dipping procedure. Therefore the 80 mm and 120 mm crucibles have to be charged with, respectively, ~1.6 kg and ~4.5 kg of CaWO$_4$ for each growth. After each growth the crucible is then refilled with CaWO$_4$ powder as well as parts of former growths that could not be used for detector crystals like e.g. the shoulder and tail. In this way about 5-10 crystals with each ~800 g can be grown before they show some coloration or inclusions (see Fig. 2.9). This is related to the fact that most impurities are segregated during crystal growth and accumulate in the melt (see Sec. 3.3.2).

In some cases the growth was aborted by the software which happens when the deviation of the growth rate from the current set point exceeds a certain limit (see Tab. 2.1). This can happen when e.g. the crystal touches either the crucible or a solid chunk of CaWO$_4$ in the melt.

| growth number	name	date	mass [g]	length [mm]	diameter [mm]	crucible diameter [mm]	growth speed [mm/h]	raw materials	growth atmosphere	comments
1	Hermann I	02.04.2008	58	125	10	80	20	AA	N_2	-
2	Hermann II	?	243	100	25	80	15	AA	N_2	grey coloration
3	Hermann III	?	247	105	25	80	15	AA	99%Ar/1%O_2	-
4-5	*growth aborted*									
6	Hermann IV	06.07.2009	252	110	25	80	15	AA	99%Ar/1%O_2	-
7-8	*growth aborted*									
9	Hermann V	26.10.2010	337	135	25	80	15	AA	99%Ar/1%O_2	-
10	*growth aborted*									
11	Hermann VI	?	328	135	25	80	15	AA	99%Ar/1%O_2	cracks
12	Friedrich I	04.02.2010	253	120	25	80	10	AA	99%Ar/1%O_2	-
13	Rudolf I	23.04.2010	359	120	30	80	10	AA	99%Ar/1%O_2	cracks
14-15	*growth aborted*									
16	Hesso	22.06.2010	786	120	44	80	10	AA	99%Ar/1%O_2	coloration
17	Rudolf III	29.10.2010	765	120	44	80	10	AA	99%Ar/1%O_2	coloration
18	*crucible emptied*									
120 mm crucible installed										
19	*growth aborted*									
20	Friedrich II	16.03.2011	1112	150	46	120	10	AA	99%Ar/1%O_2	cracks
21	*growth aborted*									
22	Hermann VIII	13.04.2011	1589	155	54	120	10	AA	99%Ar/1%O_2	pink coloration, cracks
23	Rudolf Hesso	14.06..2011	944	135	47	120	10	AA	99%Ar/1%O_2	-
24	Hermann IX	27.07.2011	1235	155	47	120	10	AA	99%Ar/1%O_2	cracks
25	Friedrich III	09.09.2011	1274	170	47	120	10	AA	99%Ar/1%O_2	cracks
26	Rudolf V	20.09.2011	349	105	30	120	10	AA	99%Ar/1%O_2	-
80 mm crucible installed										
27	Rudolf VI	30.09.2011	827	130	42	80	12	AA	99%Ar/1%O_2	-
28	*growth aborted*									
29	Bernhard I	18.10.2011	889	150	44	80	10	AA	99%Ar/1%O_2	-
30	Jakob I	02.11.2011	886	150	44	80	12	AA	99%Ar/1%O_2	cracks, inclusions
31	Georg	06.11.2011	1138	175	44	80	12	AA	99%Ar/1%O_2	cracks, cloudy
crucible cleaned										
32-34	*growth aborted*									
35	Jakob II	19.02.2012	838	145	44	80	12	AA	99%Ar/1%O_2	-
36	Bernhard III	24.02.2012	830	145	44	80	12	AA	99%Ar/1%O_2	-
37	Philibert	29.02.2012	835	145	44	80	12	AA	99%Ar/1%O_2	-
38	Philipp II	26.03.2012	923	155	44	80	12	AA	99%Ar/1%O_2	-
39	Eduard F.	17.04.2012	836	135	47	80	12	AA	99%Ar/1%O_2	-
40	Wilhelm	27.04.2012	722	130	45.5	80	12	AA	99%Ar/1%O_2	-
41	-	20.05.2012	724	130	45.5	80	12	AA	99%Ar/1%O_2	-
42	-	14.06.2012	735	130	45.5	80	12	AA	99%Ar/1%O_2	-
43	-	18.07.2012	734	130	45.5	80	12	AA	99%Ar/1%O_2	-
44	*growth aborted*									
45	Ludwig W.	08.08.2012	736	130	45.5	80	12	AA	99%Ar/1%O_2	-
46	Ludwig G. S.	12.09.2012	732	130	45.5	80	12	AA	99%Ar/1%O_2	-
47	August G. S.	18.10.2012	730	130	45.5	80	12	AA	99%Ar/1%O_2	-
crucible cleaned										
48	Ernst	14.03.2013	737	130	45.5	80	12	MV	99%Ar/1%O_2	-
49	Karl II	19.03.2013	735	130	45.5	80	6	MV	99%Ar/1%O_2	-
50	-	05.04.2013	734	130	45.5	80	12	MV	97%Ar/3%O_2	pink coloration, inclusions
51	-	16.04.2013	720	130	45.5	80	12	MV	99%Ar/1%O_2	pink coloration, inclusions
52	-	25.04.2013	734	130	45.5	80	12	MV	99%Ar/1%O_2	pink coloration, inclusions
crucible cleaned										
53	*growth aborted*									
54	Ernst F.	04.11.2013	735	130	45.5	80	12	MV	99%Ar/1%O_2	-
55	Georg F.	11.11.2013	739	130	45.5	80	12	MV 1% excess WO_3	99%Ar/1%O_2	-
56	Friedrich V	18.11.2013	737	130	45.5	80	12	MV 1% excess WO_3	99%Ar/1%O_2	-

Tab. 2.3: Properties of all ingots grown with the Czochralski furnace in the scope of this work. For details see text.

(a)
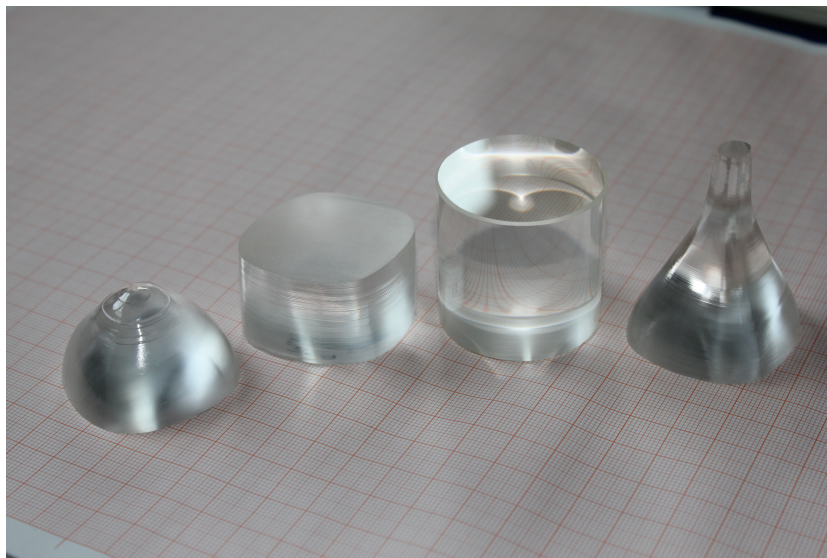
(b)

Fig. 2.6: Picture of the ingot "Rudolf VI" after extraction from the Czochralski furnace (a) and after cutting and polishing (b). The ingot in (a) has a mass of 827 g, a maximum diameter of 43 mm and a total length of 130 mm. The cylindrical detector crystal in (b) has a mass of 300 g, a diameter of 40 mm and a height of 40 mm.

34

(a)
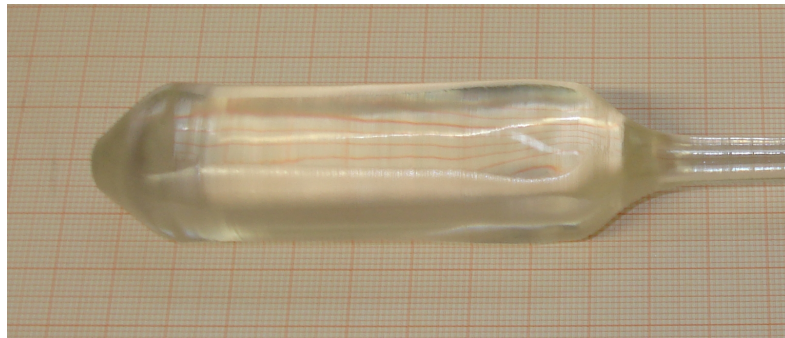
(b)

Fig. 2.7: (a) Crystal "Hermann II" grown under pure N_2 atmosphere. (b) Crystal "Friedrich I" grown in 99% Ar with 1% O_2. The lack of atmospheric oxygen leads to a reduction and grey coloring of the crystal while with a small oxygen content a clear crystal is obtained.

After growth the ingots were annealed in oxygen (see Sec. 2.2) before further treatment. Thereafter they can be sawed, lapped and polished to obtain a regular shaped crystal (see Fig. 2.6(b)). The influence of the crystal shape on the detector properties such as light collection will be discussed in Sec. 2.3. All detector crystals produced from the grown ingots are summarized in Tab. 2.4. From the 4 crystals "Bernhard I", "Philipp II", "Wilhelm" and "Ludwig W." low-temperature detectors were built that were installed in run33 of the CRESST-II experiment (see Sec. 3.4).

name	shape	dimensions	mass [g]
Rudolf VI (TUM-27)	cylinder	d=40mm, h=40mm	300
Bernhard I (TUM-29)	cylinder	d=40mm, h=40mm	300
Jakob II (TUM-35)	cylinder	d=38mm, h=40mm	275
Philibert (TUM-37)	cylinder	d=40mm, h=40mm	300
Wilhelm (TUM-40)	square prism	s=32mm, h=40mm	250
Ludwig W. (TUM-45)	square prism	s=32mm, h=40mm	250
Ludwig G. S. (TUM-46)	cylinder	d=40mm, h=40mm	300
Ernst (TUM-48)	square prism	s=32mm, h=40mm	250
Karl II (TUM-49)	cylinder	d=40mm, h=40mm	300

Tab. 2.4: Properties of all detector crystals produced from the grown ingots described in Tab. 2.3. For the CRESST detector database crystals are denoted by the label "TUM" followed by their growth number. The 4 crystals "Bernhard I", "Philipp II", "Wilhelm" and "Ludwig W." were installed as low-temperature detectors in run33 of the CRESST-II experiment.

(a)

(b)

Fig. 2.8: (a): The crystal from growth number 50 was grown with 3% O_2 which resulted in pink colored inclusions. These may come from the incorporation of Rh caused by an oxidation of the crucible material. (b): The crystal "Friedrich III" showing cracks that are related to internal stresses during cooling and the natural cleavage planes of $CaWO_4$.

37

Fig. 2.9: The crystal "Georg" was grown as the 5th crystal without intermittent cleaning of the crucible. The cloudiness that is visible and increasing towards the tail comes from impurities which have accumulated in the melt after each growth.

2.2 Oxygen Annealing

It is known that the thermal annealing under oxygen atmosphere can ameliorate the mechanical, optical and luminescent properties of $CaWO_4$ crystals [67, 68, 69]. Oxygen annealing is also used to improve the properties of other tungstate scintillators like $ZnWO_4$ and $PbWO_4$ [70, 71]. High-temperature annealing results in relief of internal stresses. In addition, oxygen annealing can reduce the oxygen deficiency which is present after growth due to the high growth temperature ($\sim 1600\,°C$) and the reduced oxygen partial pressure in the growth atmosphere (see Sec. 2.1.1). It is expected that during annealing oxygen diffuses inside the crystal and fills vacancies [67]:

$$V_O^{\bullet\bullet} + \frac{1}{2}O_2 \rightarrow O_O^{\times} + 2h^{\bullet} \tag{2.3}$$

Hereby $V_O^{\bullet\bullet}$ denotes the oxygen vacancy with charge 2^+, $O_O^{\times}$ denotes the electrically neutral vacancy after it has been refilled with an oxygen atom and $h^{\bullet}$ denotes the positively charged holes produced in the reaction.

2.2.1 Influence on Optical and Scintillation Properties

In this section we investigate the influence of oxygen annealing on the room temperature optical and scintillation properties of a $CaWO_4$ crystal. For the measurements a cubic crystal with $18\times18\times18mm^3$ size that was produced from the ingot "Friedrich I" (see Tab. 2.3) was used. All surfaces of the crystal were polished to optical quality. The annealing was carried out at a temperature of $1450\,°C$ under constant flow of pure oxygen and lasted $48\,h$. The crystal was heated up and cooled down at a rate of $100\,°C/h$.

Transmission Measurement

At first the transmittance of the crystal was measured before and after annealing. A detailed description of the setup for the transmission measurements can be found in Sec. 3.1.2. Figure 2.10 shows the measured transmittance T (see Eq. 3.5) of the crystal before and after annealing in dependence of the photon wavelength λ. It can be seen that the transmittance is considerably increased after the annealing process. Table 2.5 summarizes the values of the attenuation coefficient at a photon wavelength of $430\,nm$ which corresponds to the approximate peak position of the $CaWO_4$ scintillation spectrum at room temperature [59].
The error for the attenuation coefficient is given at 95% CL and was calculated from the data of four independent transmission measurements. However, it has to be pointed out that, in addition, there are some systematic uncertainties in the value of α_{att} because the refractive index of the crystal was not directly measured. Furthermore, surface irregularities can cause errors in the measured transmittance in the order of $\sim20\%$ [72].
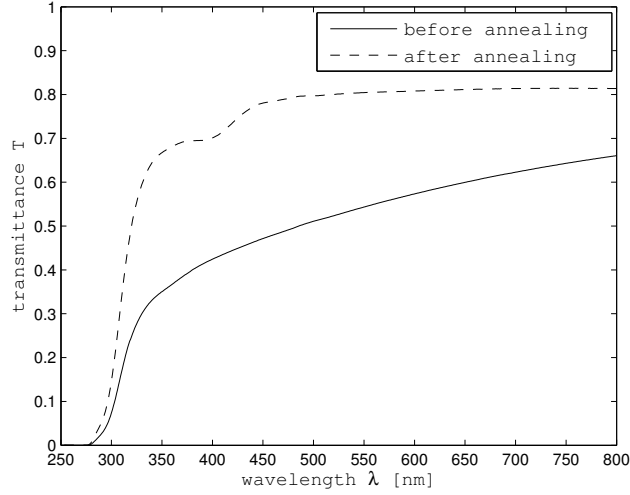
39

Fig. 2.10: Transmittance T of the CaWO$_4$ crystal before and after annealing versus photon wavelength λ. The pronounced absorption around 400 nm in the annealed crystal is probably caused by O$^-$ hole centers. Reprinted from Ref. [60], Copyright (2012), with permission from Elsevier.

	α_{att} [cm^{-1}] at 430 nm
before annealing	0.335±0.026
after annealing	0.039±0.010

Tab. 2.5: Value of the attenuation coefficient α_{att} at 430 nm of the CaWO$_4$ crystal before and after annealing. The wavelength corresponds to the approximate peak position of the scintillation spectrum at room temperature. The errors are given at 95 % CL and were determined from the data of four independent transmission measurements. Reprinted from Ref. [60], Copyright (2012), with permission from Elsevier.

Tab. 2.5 shows that the attenuation coefficient at 430 nm is decreased by a factor of ~ 8 after the annealing procedure. This can be attributed to the removal of crystal defects which otherwise cause scattering or absorption of the photons. It is believed that this is mostly caused by the filling of oxygen vacancies during annealing. In addition, there may also be other reasons for the observed reduction of the attenuation coefficient. Dislocations that are present in the crystal can act as dielectric inhomogeneities and hence also scatter light [73]. During annealing dislocations become mobile and can be removed from the crystal or form low-angle boundaries [74, 75].

In Fig. 2.10 one can observe a pronounced absorption around 400 nm in the annealed crystal. According to Ref. [68] oxygen can also be incorporated on interstitial sites during annealing which leads to absorption bands at ~ 400 nm and ~ 310 nm. However, it is also known that for $PbWO_4$ an absorption band at ~ 420 nm can be induced after oxygen annealing [76, 77]. This absorption band is commonly ascribed to O^- hole centers [76]. The filling of oxygen vacancies during annealing might lead to the creation of O^- centers to maintain local charge balance. It is known that for $CaWO_4$ the localization of holes at one oxygen of the WO_4 tetrahedron is the dominant trapping mechanism [54]. In this way the O^- hole center may be a more natural explanation for the observed absorption band. This absorption band often gives the crystal a slight green coloration that can e.g. be seen in Fig. 2.11.

The vanishing transmittance below ~ 300 nm in both curves of Fig. 2.10 is due to intrinsic absorption corresponding to the excitation of electrons from the valence band to the conduction band of $CaWO_4$ [59].

The large improvement of the crystal's transmittance after annealing can also be observed by eye. This is especially true for large crystals which still show some grey coloration after growth that vanishes after annealing (see Fig. 2.11).

Fig. 2.11: The picture shows the influence of oxygen annealing on the grown crystals. After growth large crystals show a grey coloration due to an oxygen deficiency (left and right crystals). This can be compensated by annealing them in pure oxygen resulting in clear crystals (middle crystal).

MCRIM Technique

In this section we use the Monte-Carlo Refractive Index Matching (MCRIM) technique to determine the influence of annealing on the intrinsic light yield L$_0$ as well as on the ratio B of the scattering coefficient α_{scat} and the absorption coefficient α_{abs}:

$$B = \alpha_{scat}/\alpha_{abs} \tag{2.4}$$

Since the already determined attenuation coefficient is the sum of the scattering and absorption coefficients,

$$\alpha_{att} = \alpha_{abs} + \alpha_{scat} \tag{2.5}$$

One can then calculate the values for the scattering and absorption coefficients using Eqs.(2.4) and (2.5). A detailed description of the MCRIM technique is given in Refs. [61, 56].

The results for the intrinsic light yield L$_0$, the absorption coefficient α_{abs} and the scattering coefficient α_{scat} are summarized in Tab. 2.6. All errors are given at 95% CL and were determined from the data of four independent light-yield measurements and the uncertainty of the attenuation coefficient (see Tab. 2.5).

	L$_0$ [ph/MeV] at 59.5 keV	α_{abs} [cm^{-1}]	α_{scat} [cm^{-1}]
before annealing	24800±3300	0.231±0.051	0.104±0.048
after annealing	20600±900	0.036±0.010	0.004±0.003

Tab. 2.6: Results of the MCRIM technique for the intrinsic light yield L$_0$ at 59.5 keV, the absorption coefficient α_{abs} and the scattering coefficient α_{scat}. All errors are given at 95 % CL and were determined from the data of four independent light-yield measurements and the uncertainty of the attenuation coefficient (see Tab. 2.5). Reprinted from Ref. [60], Copyright (2012), with permission from Elsevier.

The values show that the annealing procedure leads to a decrease of the absorption coefficient of the crystal by a factor of ∼6 and an even larger reduction of the scattering coefficient. The measurements also suggest that the attenuation of scintillation light in the annealed crystal is dominated by absorption. However, as the errors of the scattering and absorption coefficients are rather large no definitive statements can be made.
The value of the intrinsic light yield L$_0$ shows a small, although not significant, decrease after the annealing procedure. This may result from the formation of defects which act as quenching centers, i.e. they are responsible for energy absorption followed by non-radiative decay.
We note that the values of the intrinsic light yield from Tab. 2.6 are comparable to the value of 22700±1100 ph/MeV which was determined in Ref. [61] using the same technique

for a CaWO$_4$ crystal produced by the Institute of Materials SRC "Carat" (Ukraine).[2] However, it is a bit higher than the light yield of 15000 ph/MeV which was determined for another CaWO$_4$ crystal in Ref. [57] by comparison to a NaI(Tl) crystal.

Light-Yield Measurements

To investigate the influence of the annealing procedure on the performance of the crystal as a scintillator additional light-yield measurements were performed at room temperature. The setup for these measurements is described in Sec. 3.2.2 (see Fig. 3.10). In the measurements the crystal surface that is facing the PMT was roughened using silicon carbide powder with a grain size of $\sim$9 μm as it is done for CRESST-II detectors (see Sec. 2.4).[3] The crystal was again irradiated with a ^{241}Am gamma source (59.5 keV). Fig. 2.12 shows two ^{241}Am spectra measured with the CaWO$_4$ crystal before and after annealing. In Tab. 2.7 we show the mean values and errors (95 % CL) for the measured light yield L_m as determined from the peak position, and for the energy resolution as derived from the ratio of the peak width (FWHM) and peak position. The results were calculated from the data of four independent light-yield measurements.
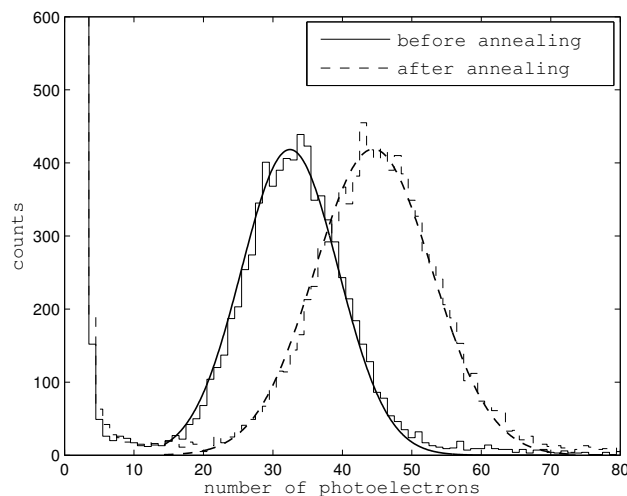
Fig. 2.12: Spectra of ^{241}Am gamma rays (59.5 keV) measured with the roughened CaWO$_4$ crystal before and after annealing. The measured light yield (peak position) and energy resolution (FWHM/peak position) were determined from a Gaussian fit to the photopeak. Reprinted from Ref. [60], Copyright (2012), with permission from Elsevier.

---

[2]In the past the "Carat" institute was one of the suppliers for CRESST-II detector crystals.

[3]The roughening procedure was also reapplied after annealing.

	L_m [p.e.] at 59.5 keV	resolution [%] at 59.5 keV
before annealing	31.0 ± 0.6	52.2 ± 0.6
after annealing	43.3 ± 0.5	46.0 ± 1.0

Tab. 2.7: Measured light yield L_m in photoelectrons (p.e.) and energy resolution at 59.5 keV of the roughened crystal before and after annealing. The mean values and errors (95 % CL) were determined from the data of four independent light-yield measurements. Reprinted from Ref. [60], Copyright (2012), with permission from Elsevier.

The measured light yield L_m is increased by $\sim 40\%$ and the energy resolution is improved by $\sim12\%$ after annealing. The observed improvement can be explained by the reduction of the absorption coefficient (see Tab. 2.6). We note that a similar result was found for ZnWO₄ crystals which have shown an improvement of the measured light yield in a similar setup by $\sim30\%$ after oxygen annealing [71].

2.2.2 Various Annealing Procedures

Since it was shown that high temperature annealing in oxygen can improve the transmittance of as grown CaWO₄ crystals it was tested if further improvement can be achieved by multiple annealing. Furthermore, different annealing temperatures were tested.

As a first test the ingot "Friedrich II" was cut in two parts where one part was annealed in oxygen at 1000°C for 150 h with 50°C/h heating and cooling. Another part was annealed with the same procedure but at 1450°C for 120 h. Figure 2.13 shows both parts of the ingot in comparison. It is obvious that the annealing at higher temperature even for a shorter duration leads to a larger improvement of the transmittance. This is also what would be expected assuming the improvement is caused by the diffusion of oxygen into the crystal since the diffusion coefficient inside a solid does exponentially increase with increasing temperature [78]:

$$D \propto \exp\left(-\frac{E}{R \cdot T}\right) \tag{2.6}$$

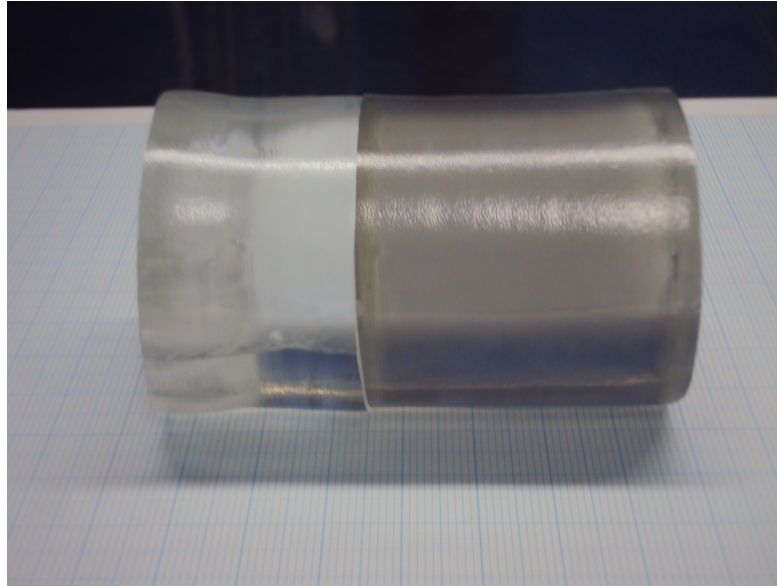where E is an energy barrier and R is the ideal gas constant.

Fig. 2.13: The picture shows the influence of different annealing temperatures on the transmittance. The left part of the ingot was annealed in oxygen at 1450°C for 120 h while the right part was annealed at 1000°C for 150 h. Only the annealing at higher temperature can eliminate the grey coloration of the crystal.

For another test the crystals "Bernhard I", "Philibert" and "Jakob II" were used. All crystals were of cylindrical shape with ∼40 mm diameter and 40 mm height (see Tab. 2.4). All crystal surfaces were optically polished except for one planar surface which was roughened using 600SiC powder as it is usually done for CRESST-II detectors (see Sec. 2.4). The ingots of all three crystals were already annealed in oxygen at 1450 °C for 72 h with 50 °C/h heating and cooling. This was done immediately after growth before the crystals were cut and polished which is also necessary to lower the risk of cleavage during cutting. For the tests a second (and third) annealing was applied after cutting and polishing similar to the first one but at different temperatures. The crystals "Philibert" and "Jakob II" were annealed at 800 °C while the crystal "Bernhard I" was annealed twice at 1500 °C. Before and after annealing the light yield of the crystals was measured at room temperature in a setup resembling the geometry of a CRESST-II detector module (see Fig. 3.10). The crystals were excited with a ^{137}Cs source and read out by a PMT. The results are summarized in Tab. 2.8. For the crystals "Philibert" and "Jakob II" a small degradation of the normalize light yield (NLY)[4] was observed after the second annealing at 800 °C. In contrast the crystal "Bernhard I" which was annealed twice at a higher temperature of 1500 °C shows a ∼3% increase of the NLY after each annealing. This contradictory behaviour at different temperatures might be explained by the simultaneous formation

---

[4]The normalized light yield is measured relative to the reference crystal "Boris" (see Sec. 3.2.2).

and reduction of different defects during annealing. As already shown above annealing at high temperatures removes defects that can otherwise lower the crystal's transmittance and thus improves the light output. However, it was also hinted that there is a small decrease of the intrinsic light yield (see Tab. 2.6) probably caused by the additional creation of defects which act as quenching centers. At low temperatures the formation of such defects may dominate over the reduction of defects that improve the transmittance while it is opposite for high temperatures.

crystal	annealing	NLY [%]	Res. [%]
Philibert	1st annealing after growth at 1450 °C	95.0±0.1	12.7±0.3
Philibert	2nd annealing after cutting/polishing at 800°C	92.2±0.1	12.6±0.3
Jakob II	1st annealing after growth at 1450 °C	103.3±0.1	11.6±0.2
Jakob II	2nd annealing after cutting/polishing at 800 °C	100±0.1	11.8±0.2
Bernhard I	1st annealing after growth at 1450 °C	93.0±0.2	13.9±0.5
Bernhard I	2nd annealing after cutting/polishing at 1500 °C	96.8±0.2	13.2±0.4
Bernhard I	3rd annealing after cutting/polishing at 1500 °C	100.0±0.2	14.7±0.5

Tab. 2.8: Influence of multiple annealing at different temperatures on the resolution (FWHM) and the normalized light yield (NLY) measured relative to the reference crystal "Boris".

Summary

It was shown that oxygen annealing at high temperatures leads to an improvement of the transmittance and therefore the light output. It was also observed that this improvement is larger for higher temperatures while for an annealing at lower temperatures of 800°C even a small decrease of the light output was observed. It was also shown that multiple annealing can further improve the light output, however, this improvement is only small compared to that after the first annealing step.
Based on these findings the following annealing procedure was applied to all ingots after they were extracted from the Czochralski furnace:

- Heating with 200°C/h to 1400°C

- Annealing at 1400°C for 20 h

- Cooling at 5°C/h to 1200°C

- Cooling at 50°C/h to room temperature

2.3 Crystal Shaping

The CaWO$_4$ detectors used in CRESST-II up to now were cylindrically shaped with 40 mm diameter and 40 mm height. Here we consider also different shapes which may be more advantageous. In general, the crystal geometry should meet the following requirements. It should allow a close packing of the detector modules which becomes even more important for the future EURECA experiment where a high target mass of up to 1 tonne has to be housed in the cryostat. Secondly, the material loss when the crystal is produced from the ingot should be minimized. Furthermore, the manufacturing process should be not too complex which is again especially important for the large scale EURECA project. Finally, the shape should have good light collection properties. To study the latter simulations and light yield measurements at room temperature (RT) were performed with differently shaped crystals in Ref. [56]. It was found that a crystal shaped like a square prism has a similar light collection efficiency compared to the cylinder. In addition, it shows a smaller position dependence of the light collection which does improve its resolution as a scintillation detector. This can be seen in Fig. 2.14 showing the position dependence of the light collection in a CRESST-like detector module with a cylindrical crystal and a crystal shaped like a square prism (both with the surface facing the light detector roughened) that was simulated using Geant4 (see App. A.2). In the cylindrical crystal there is a higher collection efficiency for light generated in the center due to a radial position dependence of the fraction of trapped photons [79]. This position dependence degrades the resolution as shown in Fig. 2.15 where room temperature measurements with a ^{60}Co gamma source (1173 keV, 1332 keV) are shown. The measurements were done using a cylindrical and a cubic crystal (both with one surface roughened) with each $\sim$30 g mass that were cut from the same ingot [80]. In both crystals the gamma lines appear at approximately the same pulse height which means that they have a similar collection efficiency. However, in the cylindrical crystal it is difficult to distinguish both gamma lines while they are well separated in the cubic crystal. The same two crystals were also measured at mK temperatures using a cryogenic light detector. Here the measurements showed an increased light yield of the cubic crystal by $\sim$20% compared to the cylinder [80]. Finally, a standard CRESST-II detector module with a 300 g cylindrical crystal (40 mm height, 40 mm diameter) and a 250 g crystal shaped like a square prism ($32 \times 32 \times 40$ mm^3) (both produced from different ingots) were both measured at mK in the CRESST test cryostat at Gran Sasso. It was found that the light yield of the square prism was $\sim$20-40% (depending on the number of roughened surfaces) higher than that of the cylinder [39].
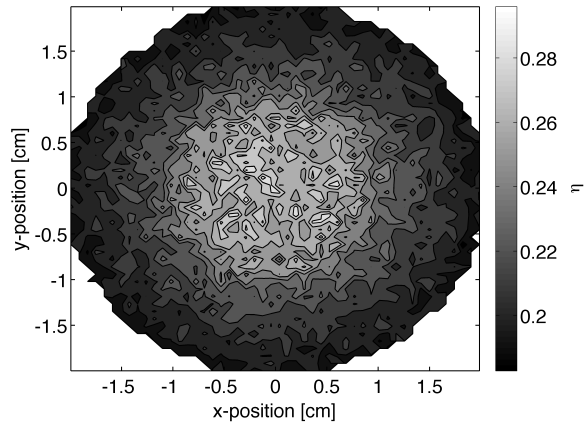
(a)
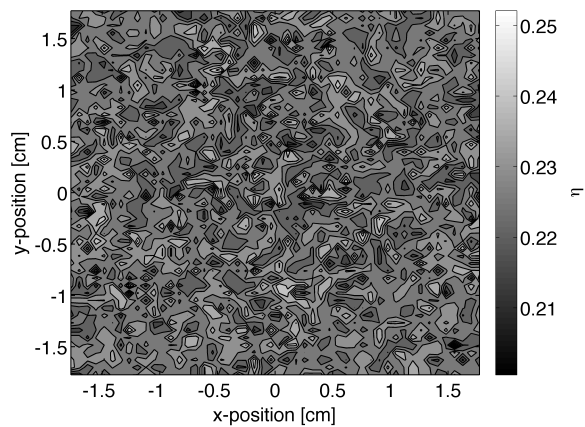
(b)

Fig. 2.14: Simulated position dependence of the light collection efficiency η in a cryogenic detector module with a cylindrical crystal (a) and a crystal shaped like a square prism (b). In the cylinder there is larger probability for photons generated near the center to escape the crystal and be detected. In the cubic crystal this position dependence is absent.
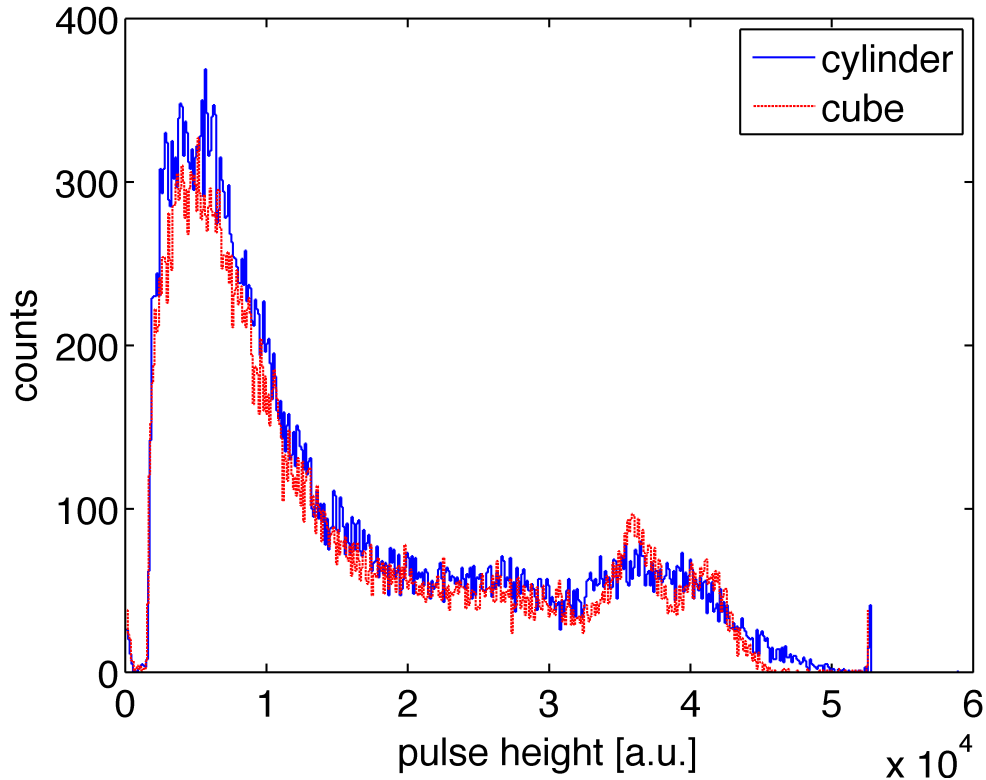
Fig. 2.15: ^{60}Co spectrum measured at RT with a cylindrical and cubic crystal cut from the same ingot. While both crystals show about the same light collection the resolution is better in the cubic crystal resulting from the smaller position dependence of the light collection.

In summary, a crystal shaped like a cube or square prism is preferred compared to the cylinder as it shows a smaller position dependence and possibly also a higher light collection in a cryogenic detector module. Furthermore, a higher close packing can be achieved with a rectangular crystal, it is easy to produce and only little material is lost during production. Two crystals with this geometry and a new (fully scintillating) holder design were installed in run33 of CRESST-II (see Sec. 3.4).

2.4   Surface Roughening

It is known that surface roughening can improve the light output of a scintillator especially when there is no optical coupling to the light detector [81, 56]. In measurements at CRESST-II a significant improvement of the resolution was achieved after roughening of the crystal surface that is facing the light detector [82]. Roughening reduces the probability that photons travel infinite paths inside the crystal and thus reduces the fraction of trapped light. Furthermore, a rough surface can transmit light for angles of incidence larger than the critical angle where no transmitted light would be observed at a specular surface [83]. In this section we investigate the effects of different surface treatments on the light collection by numerical calculations, Monte-Carlo (MC) simulations and light yield measurements. The goal is to find the optimal surface treatment that will lead to the largest increase of the light collection in a detector module.

2.4.1   Description of a Surface Profile

In general there are two approaches for the theoretical modeling of a surface profile which use either the distribution of its height or its slope with respect to a mean value. In the following we consider only uniform surfaces and thus limit the description of our surface profile to a single spatial coordinate x. The descriptions given here follow closely the ones that are given in [84].

Height Distribution Model

The height h of a surface can be expressed as a function of the spatial coordinate x. The shape of the surface is then described by the probability distribution of h. If h is normally distributed with a mean value of $\langle h \rangle = 0$ and standard deviation σ_h its probability distribution can be written as:

$$p_h(h) = \frac{1}{\sqrt{2\pi}\sigma_h} e^{-\frac{h^2}{2\sigma_h^2}} \tag{2.7}$$

The surface is not uniquely described by the statistical distribution of h, however, as it contains no information about the distances between the hills and valleys of the surface profile. Therefore, the model can be complemented by an autocorrelation coefficient $c(\tau)$ which determines the correlation between the random values assumed by the height h at two surface points x_1 and x_2 separated by a distance τ. The autocorrelation coefficient is calculated by the following equation:

$$c(\tau) = \frac{1}{\sigma_h^2} \langle h(x)h(x+\tau) \rangle \tag{2.8}$$

We chose the following function to describe the autocorrelation coefficient:

$$c(\tau) = e^{-\frac{\tau^2}{l^2}} \tag{2.9}$$

where l is the correlation distance for which c(τ) drops to the value e^{-1}. By varying the parameters σ_h and l of our surface model one can generate surfaces that match in appearance almost any rough surface met in practice.

Slope Distribution Model

It is sometimes convenient to think of a surface as a collection of micro-facets. Each micro-facet has its own orientation which deviates from the mean surface orientation by an angle α. The surface can then be modeled by the statistical distribution of the micro-facet slopes. For example, the surface may be modeled by assuming a normal distribution for the facet slope α with mean value $\langle\alpha\rangle$=0 and standard deviation σ_α:

$$p_\alpha(\alpha) = \frac{1}{\sqrt{2\pi}\sigma_\alpha}e^{-\frac{\alpha^2}{2\sigma_\alpha^2}} \tag{2.10}$$

Unlike the height distribution model which requires two parameters, the surface model in this case is determined by the single parameter σ_α. Larger values of σ_α may be used to model rougher surfaces. The advantages of using a single parameter come with the cost of a weaker model when compared to the height model. However, the slope distribution model is popular in the analysis of surface reflection, as the scattering of light rays has been found to be dependent on the local slope of the surface and not the local height of the surface.

2.4.2   Light Yield and Surface Profile Measurements

In this section we investigate the influence of mechanical roughening with different grain sizes on the surface profile the measured light yield and resolution of a CaWO$_4$ crystal at RT. In addition, the roughening of different surfaces is tested.

For the measurements we used a cylindrical crystal with a diameter of 18 mm and 18 mm height that was produced from the ingot "Friedrich II" (see Tab. 2.3). At first all surfaces of the crystal were optically polished. The light yield at RT and the surface profile were measured after mechanical roughening of one or more surfaces using silicon carbide (SiC) or boron carbide (B$_4$C) powders of different grain sizes.
The surface profile was measured with a stylus probe (TENCOR P10 Surface Profiler) over a length of 500 μm with a horizontal resolution of 0.1 μm (see Fig. 2.16). The value of σ_h was then determined by a Gaussian fit to the histogram of the surface height h (see Fig. 2.16). The correlation length l was obtained from the autocorrelation function which in turn was calculated from the surface profile by Eq.(2.8). From the differentiation of the surface profile in steps of 2 μm the distribution of the micro-facet slopes α was obtained (see Fig. 2.16). The value of σ_α was then determined by a Gaussian fit to this distribution. For the light yield measurements the crystal was mounted in a reflective housing coupled to a PMT (see Fig. 3.10) and irradiated by a ^{241}Am gamma source (59.5 keV). The setup for these measurements is described in detail in Sec. 3.2.2.
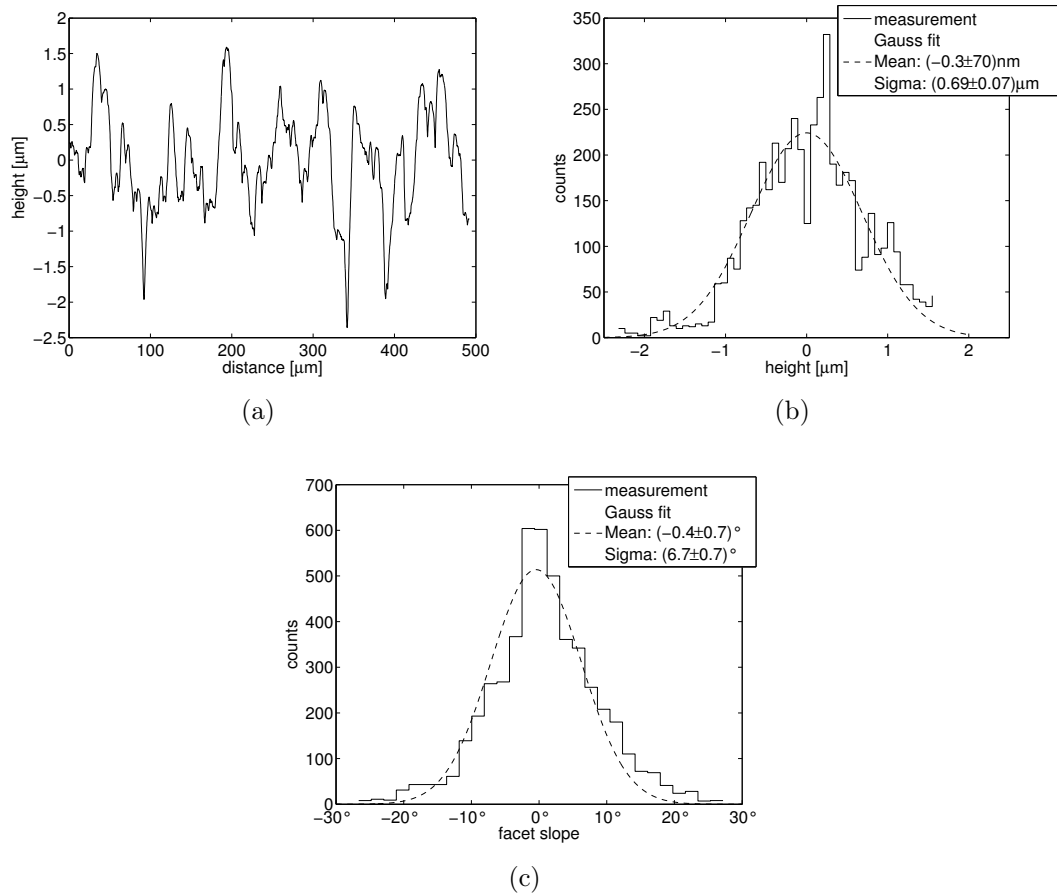
(a)

(b)

(c)

Fig. 2.16: (a) Surface profile of a $CaWO_4$ crystal roughened with $800B_4C$ powder; (b) Distribution of the surface height together with a Gaussian fit; (c) Distribution of the micro-facet slope obtained from the differentiation of the surface profile together with a Gaussian fit.

Roughening with Different Grain Sizes

In CRESST-II crystals are currently roughened using 600SiC or $800B_4C$ powder. In this section we investigate if a further improvement can be achieved using different grain sizes. Table 2.9 shows the height distribution σ_h, correlation length l and slope distribution σ_α that were determined from the measured surface profile after roughening of the crystal using different abrasives. The grain sizes of the abrasives that were used for the roughening, as stated by the supplier, are also summarized in table 2.9. It can be observed that the values of σ_h, l and σ_α increase with increasing grain size of the abrasive that was used for roughening.

surface treatment	grain size [µm]	σ_h [µm]	l [µm]	σ_α [°]	LY (%)	FWHM (%)
polished	-	$(1.4\pm0.05)\times10^{-3}$	0.0	0.06±0.004	100.0±0.6	64.7±1.7
1200B$_4$C	∼3	0.28±0.02	4.3	5.0±0.3	160.6±0.8	47.8±1.2
800B$_4$C	∼7	0.69±0.07	9.1	6.7±0.7	158.9±0.8	47.0±1.2
600B$_4$C	∼9	0.84±0.07	10.9	6.8±0.6	161.6±0.7	46.2±1.1
600SiC	∼ 9	0.74±0.06	9.0	8.1±0.6	166.1±0.8	45.7±1.1
400B$_4$C	∼17	1.23±0.08	37.5	9.6±0.7	169.5±0.9	43.5±1.1
280B$_4$C	∼37	3.95±0.2	37.2	11.7±0.9	171.0±0.9	42.1±1.2
180B$_4$C	53∼90	7.06±0.5	57.2	13.8±0.9	168.6±0.8	43.1±1.1

Tab. 2.9: Results of the surface profile and light yield measurements after roughening of the crystal using silicon carbide (SiC) and boron carbide (B$_4$C) abrasives with different grain sizes. The table shows the correlation length l, height distribution σ_h and slope distribution σ_α of the surface profile. In addition, the light yield (LY) normalized to the value of the polished crystal and the resolution (FWHM) at 59.5 keV after roughening of the planar surface that is facing the PMT is given. In CRESST-II crystals are currently roughened using 600SiC or 800B$_4$C.

The last two columns in Tab. 2.9 show the light yield (LY) normalized to the value of the polished crystal and the resolution (FWHM) at 59.5 keV after roughening of the surface that is facing the PMT. It can be seen that roughening leads to an increase of the light yield by ∼60-70% and to an improvement of the resolution by ∼25-35%. It is also observed that the improvement is larger for a larger grain size of the powder used for roughening, however, the differences are only small.

Roughening of Different Surfaces

Figure 2.17 shows the measured ^{241}Am spectra after subsequent roughening of all surfaces of the cylindrical crystal using 600SiC. The values for the light yield and resolution (FWHM) normalized to that of the polished crystal can be found in Tab. 2.10. At first only the bottom surface of the crystal (facing the PMT) was roughened. As already shown above this leads to a large improvement of the light yield and resolution. If in addition the curved side surface is roughened a further improvement of the light yield by ∼10% and an even larger improvement of the resolution by ∼20% is achieved. This shows that in particular the position dependency of the light collection can be further reduced by roughening the curved surface. If all surfaces are roughened there is a small decrease of the light yield compared to the crystal with just the curved and bottom surface roughened.
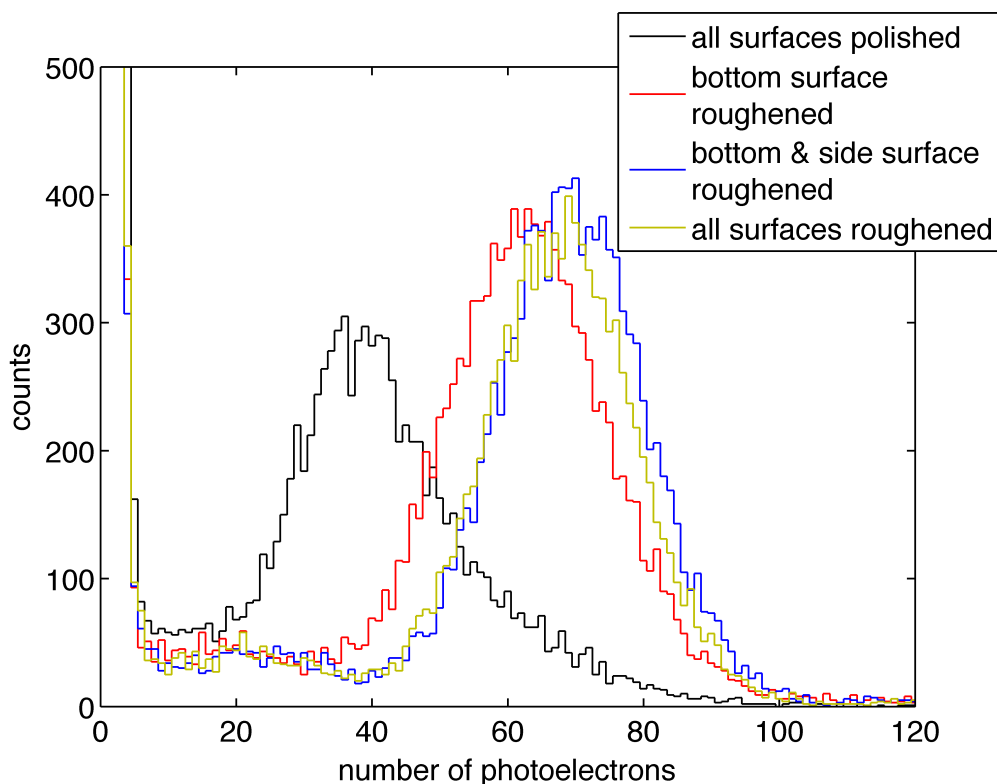
Fig. 2.17: [241]Am spectra measured after subsequent roughening of all surfaces of a cylindrical crystal. From the spectra the measured light yield and resolution were determined by Gaussian fits to the photopeak at 59.5 keV (see Tab. 2.10).

	LY (%)	FWHM (%)
all surfaces polished	100.0±0.6	64.7±1.7
bottom surface roughened	166.1±0.8	45.7±1.1
bottom & side surface roughened	184.0±0.9	37.5±0.9
all surfaces roughened	181.6±0.9	37.8±0.9

Tab. 2.10: Results for the light yield measurements after subsequent roughening of all surfaces of a cylindrical crystal. The values show the light yield (LY) normalized to the value of the polished crystal and the resolution (FWHM). The values were determined from Gaussian fits to the photopeaks at 59.5 keV in the measured [241]Am spectra (see Fig. 2.17).

The roughening of different surfaces was also tested at low temperatures with cryogenic detector modules operated at the CRESST test cryostat at LNGS. Figure 2.18(a)

shows a spectrum measured with the cylindrical detector "Rudolf VI" (see Tab. 2.4) where the surface facing the light detector was roughened. The plot shows that position dependencies are still present in the crystal which lead to a non-Gaussian light yield distribution. While for most crystals that were obtained from other suppliers these position dependencies are usually already removed by roughening one surface they are more pronounced in TUM-grown crystals which is related to their rather small absorption length (see Sec. 3.1.2). However, Fig. 2.18(b) shows that these position dependencies can be removed by additional roughening of the curved surface. Furthermore, the additional roughening leads also to an improvement of the light yield by ∼20% [39].

A similar measurement was carried out with the crystal "Wilhelm" which is shaped like a square prism (see Tab. 2.4). Here it was also observed that position dependencies are still present when only one surface is roughened but that they can be removed by additional roughening the side surfaces. However, the additional roughening lead to no significant increase of the light yield [39].
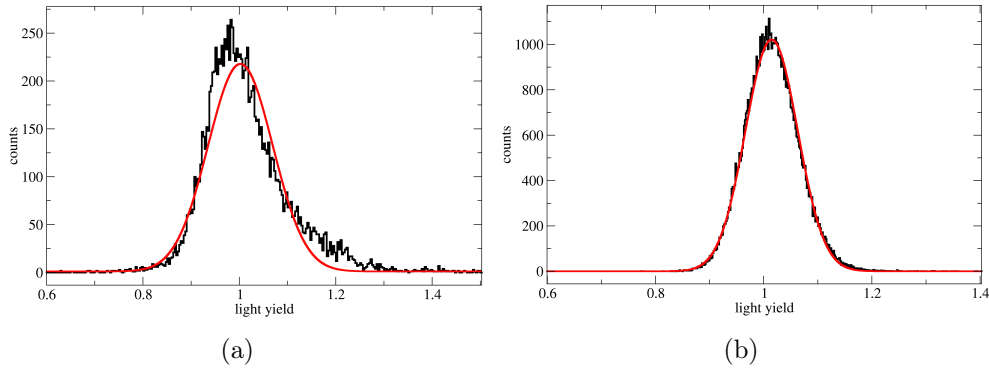

(a)   (b)

Fig. 2.18: Light yield distribution of scintillation events in the ^{212}Pb peak (238 keV) measured with the cylindrical crystal "Rudolf VI" in a cryogenic detector module. In (a) only the crystal surface facing the light detector was roughened while in (b) also the side surface was roughened. The non-Gaussianity of the light yield comes from position dependencies of the light collection which are removed by roughening the side surface. Figure adapted from Ref. [39].

Summary

It was shown that mechanical roughening, as already done in CRESST-II for the crystal surface facing the light detector, leads to a large improvement of the light yield and resolution. We have shown that a larger improvement can in principle be achieved using larger grain sizes, however, the differences are only small. By additional roughening of the side surfaces of a crystal, though, a further improvement of the light yield by ∼20% can be achieved. In addition, this procedure is necessary in crystals with a small absorption

length to reduce the position dependencies which otherwise lead to a non-Gaussian light yield distribution.

By changing the geometry of the crystal from the previously used cylindrical design to a square prism and by additional roughening of the crystal's side surfaces, the light channel of a CRESST detector module showed the following improvement [39]: The light yield increases by ∼50% while the resolution at 122 keV is improved by ∼35% (see Fig. 2.19).
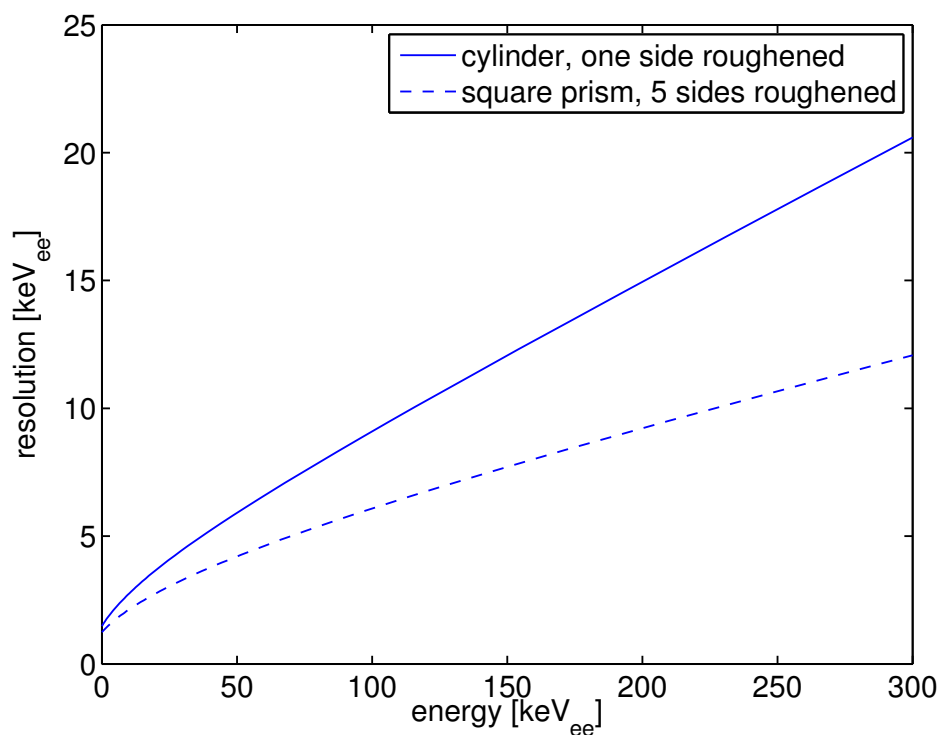
Fig. 2.19: Energy resolution (σ) in the light channel as a function of energy measured with two different low-temperature detectors [39]. The first detector ("Rudolf VI") comprises a cylindrical crystal ($\varnothing$=40 mm, h=40 mm) with one side roughened which has been the standard geometry used in CRESST up to now. The second detector "Wilhelm" consists of a block-shaped crystal ($32\times32\times40$ m^3) with 5 sides roughened. With the second type of detector the energy resolution at 122 keV is improved by ∼35%.

Chapter 3

Crystal Characterization

This section concerns the characterization of the $CaWO_4$ crystals produced at TUM. We often compare these crystals to those that were so far obtained for the CRESST experiment from the following sources:

- General Physics Institute of the Russian Academy of Science (Moscow, Russia); crystals with female names; referred to as "Russian crystals"

- V. Pozdnjakov (Ukraine); crystals with male names; referred to as "Ukrainian crystals"

3.1 Optical Properties

3.1.1 Photoelasticity

Photoelasticity measurements can be used to determine the distribution of stress inside the crystals. Polarized light is transmitted through the crystal and is analyzed with a second crossed polarizer. Deformations of the crystal lattice can induce birefringence where the magnitude depends upon the amount of stresses. When the polarized light passes the sample the light's components along the principal stress directions are phase shifted to each other by δ [85]:

$$\delta = \frac{2\pi d}{\lambda} C(\sigma_1 - \sigma_2) \tag{3.1}$$

where d is the sample thickness, λ is the light wavelength, C is the stress-optic coefficient and σ_1 and σ_2 are the two principal stresses. This phase shift changes the polarization state of the transmitted light which leads to a fringe pattern after the second polarizer. The points along which the difference of the two principal stresses is the same are the so called isochromatics, they appear as areas of constant brightness.

Figure 3.1 shows photoelasticity pictures of several CaWO$_4$ crystals.[1] As can be seen the TUM-grown crystals do show fringe patterns due to internal stresses while this is not the case for the Russian and Ukrainian crystals. The isochromatic lines form concentric rings as well as two hyperbolically shaped areas. The naturally shaped crystal "Rudolf I" (see Fig. 3.1(d)) shows that the directions of the latter are aligned with the a-axes of the crystal lattice (see Fig. 1.15). A likely explanation of the internal stresses in the TUM crystals could be the rather fast growth speed of $\sim$12 mm/h. In contrast to that the Russian crystals, are grown with a much slower speed of 1-2 mm/h. Remaining stress inside the crystal can lead to cleavage during cutting and polishing. Furthermore, it is also likely that a deformed crystal lattice reduces the scintillation efficiency [38].

---

[1]One has to note that CaWO$_4$ is by itself weakly birefringent, therefore the crystals do not appear dark in crossed polarizers.

(a)

(b)

(c)

(d)
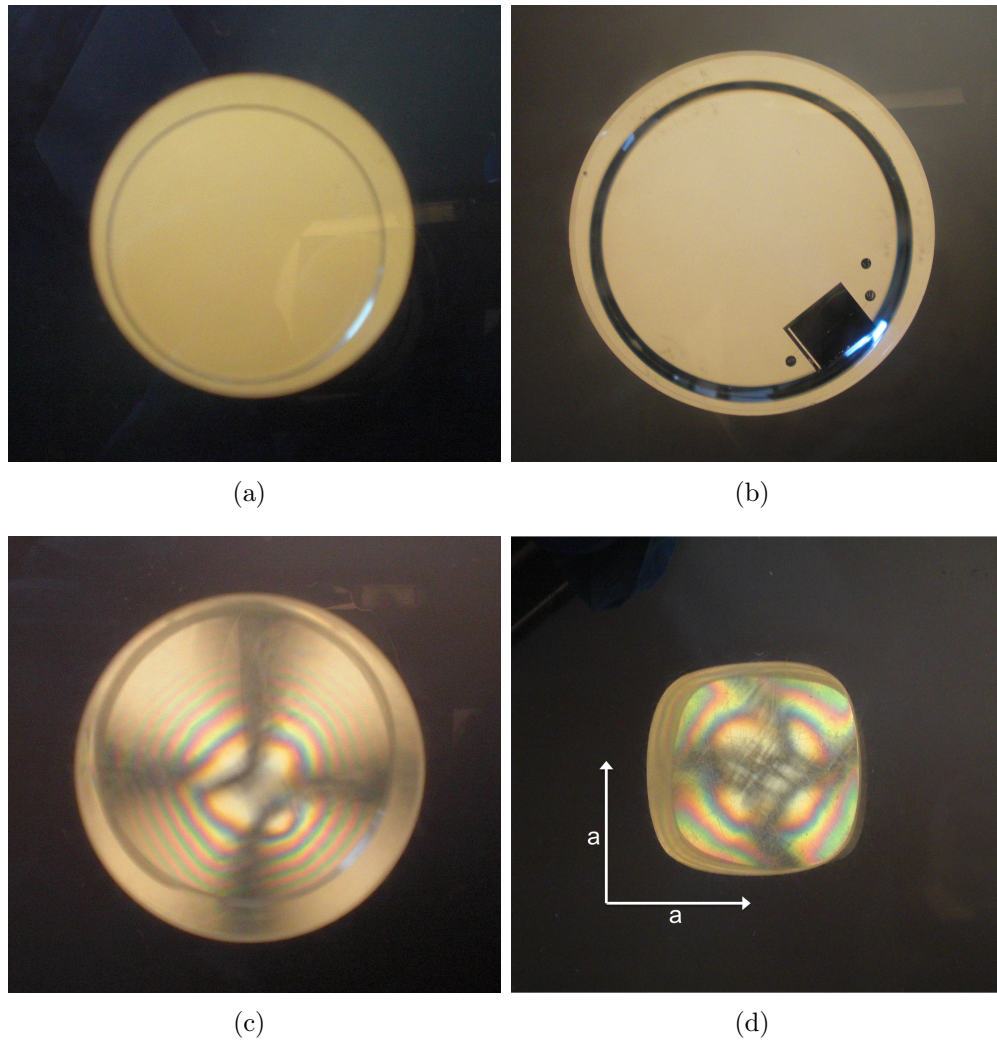
Fig. 3.1: Photoelasticity pictures of the crystals: (a) Boris (Ukraine), (b) Sabine (Russia), (c) Ludwig G. S. (TUM), (d) Rudolf I (TUM). The TUM crystals show internal stresses that lead to fringe patterns under crossed polarizers. In (d) also the a-axes of the crystal lattice are shown. The crystal in (b) has a TES evaporated onto the surface.

3.1.2   Transmittance

The total light output of a scintillating crystal is influenced by the scattering and absorption of light inside the crystal. While the absorption should, of course, be minimized, scattering decreases the fraction of trapped light and increases the light output [56, 72]. The sum of the absorption coefficient α_{abs} and the scattering coefficient α_{scat} is the

attenuation coefficient α_{att}:

$$\alpha_{att} = \alpha_{abs} + \alpha_{scat} \tag{3.2}$$

The inverse of these values are the attenuation length L_{att}, absorption length L_{abs} and scattering length L_{scat}:

$$L_{att}^{-1} = L_{abs}^{-1} + L_{scat}^{-1} \tag{3.3}$$

The attenuation coefficient can be determined in a transmission measurement. As the contributions of scattering and absorption can not be disentangled, α_{att} by itself generally does not provide a quantity to determine the light output of a crystal. However, a transmission measurement gives information about the quality of a crystal as intrinsic defects or impurities often lead to absorption bands or scattering centers. In fact, in Sec. 3.2.2 it will be shown that there is a clear correlation between transmittance and light output of a crystal. In the present section we show the results of transmission measurements that were performed with several $CaWO_4$ crystals produced at the TUM as well as at other institutes.

Experimental Setup

For the transmission measurements a Perkin Elmer LAMBDA 850 UV/VIS spectrophotometer was used. Figure 3.2 shows a schematic picture of the spectrometer. The transmittance was measured for wavelengths from 250-800 nm in steps of 1 nm. The transmittance T is defined as

$$T = I_1/I_0 \tag{3.4}$$

where I_1 and I_0 are the measured intensities with and without the sample in the beam, respectively. The attenuation coefficient was calculated using the following equation

$$T = \frac{(1 - R)^2 \cdot \exp(-\alpha_{att}d)}{1 - R^2 \cdot \exp(-2\alpha_{att}d)} \tag{3.5}$$

Here d is the crystal's thickness, α_{att} its attenuation coefficient, and R its reflectivity. The denominator of this equation accounts for multiple reflections.
$CaWO_4$ is weakly birefringent ($\Delta n \approx 0.017$), however, in the measurements the crystal was usually aligned with the beam of light perpendicular to the surface and parallel to the optical axis of the crystal so that no birefringence occurs. Therefore, the reflectivity can be calculated as

$$R = \frac{(n_o - 1)^2}{(n_o + 1)^2} \tag{3.6}$$

with n_o being the ordinary refractive index which was calculated by the following equation [55]:

$$n_o^2 - 1 = \frac{2.5493 \cdot (\lambda/\mu m)^2}{(\lambda/\mu m)^2 - 0.1347^2} + \frac{0.92 \cdot (\lambda/\mu m)^2}{(\lambda/\mu m)^2 - 10.815^2} \tag{3.7}$$

The error for the attenuation coefficient was calculated from the data of multiple transmission measurements. However, it has to be pointed out that there are some additional uncertainties in the value of α_{att} because the refractive index of the crystal was not directly measured. Furthermore, surface irregularities can cause errors in the measured transmittance in the order of $\sim 20\%$ [72].
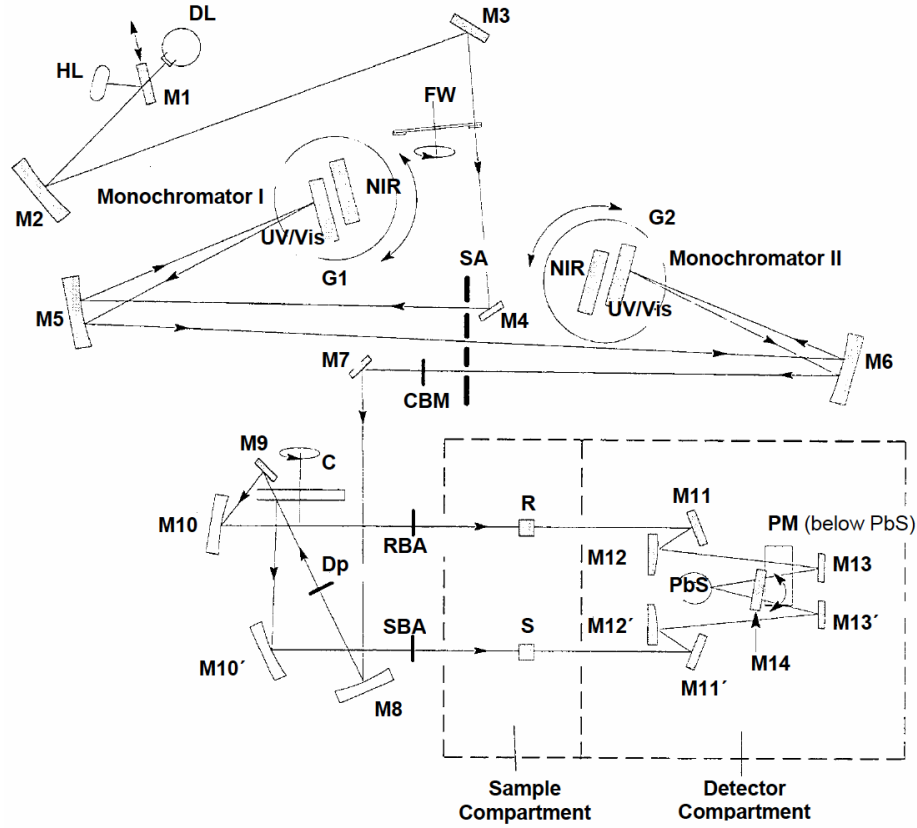
Fig. 3.2: Schematic picture of the Perkin Elmer LAMBDA 850 UV/VIS spectrophotometer [86]. The light sources are a deuterium lamp (DL) and a halogen lamp (HL). The beam is reflected by mirrors (M1-14) and passed through a filter wheel (FW). The light passes two monochromators consisting of grating tables (G1, G2) and a slit assembly (SA). A common beam mask (CBM) restricts the beam to a width and height of about 4.5 mm and 12 mm, respectively. The beam is then split into a reference beam (R) and a sample beam (S). Finally, the light is detected by a R6872 photomultiplier (PM) [86].

Results and Discussion

Figure 3.3(a) shows the mean transmittance measured for several crystals from different suppliers. All crystals had a similar height of ~4 cm, thus their transmittance can directly be compared. The dashed blue line corresponds to the maximum achievable transmittance due to Fresnel reflections. At first, it can be observed that there is a large spread in the transmittance of different crystals. The Russian crystals "Zora" and "Exiton I" show the highest transmittance which almost reaches the Fresnel limit. The by far lowest values were measured for the TUM-grown crystals "Ernst" and "Friedrich V" which are due to inclusions that are also visible by eye and lead to pronounced scattering (see Sec.. 3.1.3 below). The TUM-grown crystals "Karl II", "Ernst" and "Friedrich V" show the absorption band at ~400 nm which was also observed after annealing and attributed to O^--hole centers (see Sec. 2.2). This absorption band is also slightly visible in the other TUM crystals as well as in the Ukrainian crystal "Boris". Two less pronounced absorption bands of unknown origin appear at ~460 nm and ~500 nm in all crystals.[2]

A closer inspection of the transmittance of the two Russian crystals reveals absorption bands at 380 nm, 523 nm, 526 nm and 582 nm (see Fig. 3.3(b)) which can be attributed to Er^{3+} and Nd^{3+} impurities and are caused by the following transitions:

- Er^{3+}: $^4I_{15/2} \rightarrow {}^4G_{11/2}$ (380 nm) [87]

- Er^{3+}: $^4I_{15/2} \rightarrow {}^4H_{11/2}$ (523 nm) [87]

- Nd^{3+}: $^4I_{9/2} \rightarrow {}^2K_{13/2} + {}^4G_{7/2} + {}^4G_{9/2}$ (526 nm) [88]

- Nd^{3+}: $^4I_{9/2} \rightarrow {}^4G_{5/2} + {}^2G_{7/2}$ (582 nm) [88]

These absorption bands have also been observed in other Russian crystals that were obtained for CRESST-II [82]. Rare earth ions are a commonly used dopants for scintillators and laser materials [89, 90]. The contamination observed in the Russian crystals is most likely an accidental one caused by using the same facilities as for the production of other materials doped with rare earth ions. It was also speculated if the rare earth impurities are at least partially responsible for the high transmittance of these crystals [82] since such an improvement especially in the low-wavelength region was observed for doping of $PbWO_4$ [91] and also for La doping of $CaWO_4$ [92]. However, the concentration of rare earth ions in the Russian crystals is typically <5ppm [82, 93] which is probably too low to have a significant influence on the transmittance as, e.g. for $PbWO_4$, doping concentrations of few hundreds of ppm were used [91].

---

[2]These absorption bands are not visible by eye in Fig. 3.3(a) but were found after close inspection of the transmission curves.
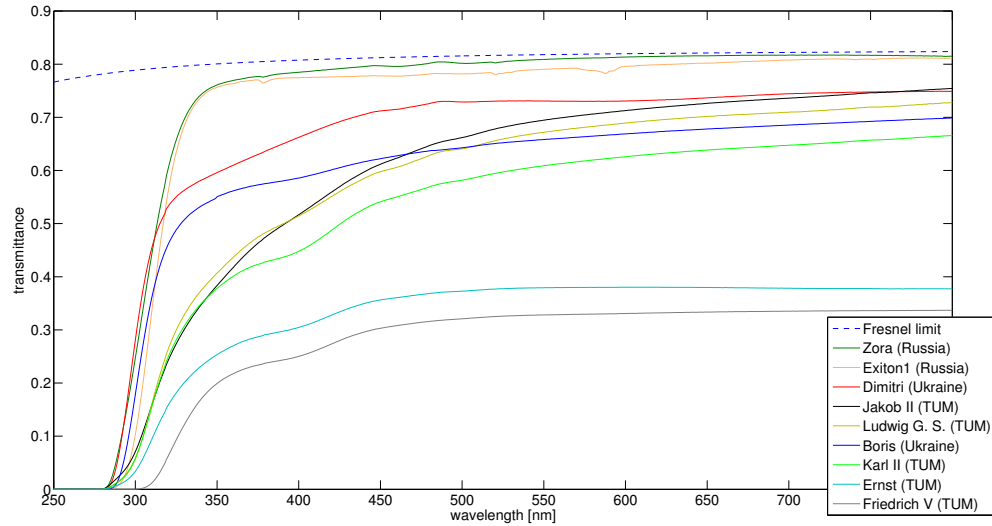
(a)
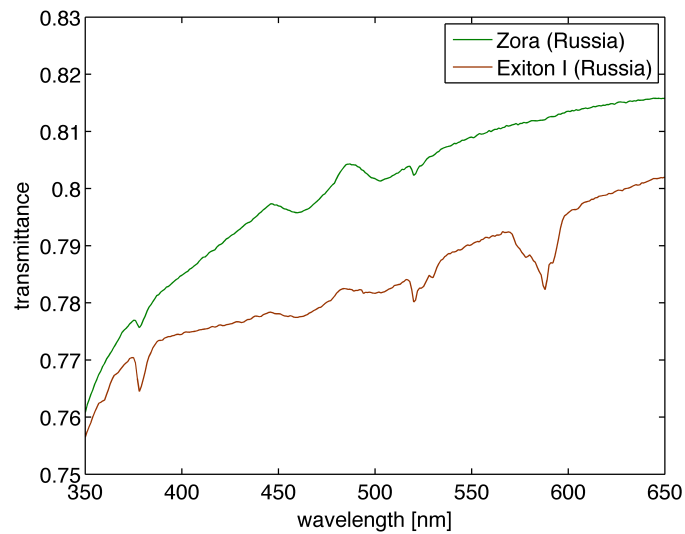
(b)

Fig. 3.3: (a): Transmittance of several crystals from different suppliers. All measured crystals had a length of ~4 cm. The dashed blue line shows the maximum achievable transmittance due to Fresnel reflections. (b): Zoom into the transmission curves of the Russian crystals. The absorption bands at 380 nm, 523 nm, 526 nm and 582 nm are caused by Er^{3+} and Nd^{3+} impurities.

65

From the measured transmittance of all crystals the attenuation coefficient at 430 nm was calculated[3] using Eq. 3.5. The values are shown in Tab. 3.1. It can be seen that the attenuation coefficient of the Russian crystals is about one order of magnitude lower than that of the TUM crystals. If this difference were only due to scattering it would be unproblematic because this would not reduce the light output of the crystals. However, as will be seen in Sec. 3.2.2, crystals with a smaller attenuation coefficient also show a higher light output suggesting that they also have a smaller absorption coefficient. Another possible explanation is that the defects causing the low transmittance can also trap charge carriers which then can not participate in the generation of scintillation light. Another point worth noticing is that the attenuation coefficient determined for the TUM-grown crystal described in Sec. 2.2 is about a factor of 2 lower than that of the TUM crystals investigated here (see Tab. 2.5). The main difference between these crystals is their size. In this section we used cylindrical crystals with 40 mm height and 40 mm diameter that were produced from an ingot with a mass of $\sim$700-800 g while the crystal in Sec. 2.2 was only $18 \times 18 \times 18$mm^3 and produced from a 250 g ingot. A possible explanation for the higher transmittance of the smaller crystal might be that the annealing is more efficient. Another reason could be the smaller growth rate for crystals with a smaller diameter.

Trying to decrease the attenuation coefficient should be one of the main efforts for further improvement of the crystals.

crystal	α_{att} [cm^{-1}] at 430 nm
Boris (Ukraine)	0.070±0.001
Dimitri (Ukraine)	0.041±0.003
Zora (Russia)	0.005±0.001
Exiton I (Russia)	0.013±0.004
Jakob II (TUM)	0.087±0.003
Ludwig G. S. (TUM)	0.088±0.001
Karl II (TUM)	0.115±0.003
Ernst (TUM)	0.165±0.050
Friedrich V (TUM)	0.246±0.007

Tab. 3.1: Values for the attenuation coefficient at the approximate peak position of the CaWO$_4$ emission spectrum for different crystals. The values were calculated from the measured transmittance in Fig. 3.3(a). The errors were obtained from the repetition of several measurements.

---

[3]This wavelength corresponds to the approximate peak position of the CaWO$_4$ emission spectrum.

3.1.3   Scattering Centers

In the previous section the attenuation coefficient of the crystals was determined. It was, however, not possible to discriminate between the scattering and absorption of light. In this section we study the role of scattering in a qualitative way for different crystals. For this we use the simple method of examining the crystals under irradiation with a laser beam. If scattering centers are present in the crystal the laser will become visible in the direction perpendicular to the beam direction and the brightness of the beam gives information on the amount of scattering centers. For this we used a standard commercial red laser pointer (650 nm). Figure 3.4 shows the light scattering of the laser beam in different crystals. All investigated TUM crystals show scattering centers. In the crystal "Ernst" a pronounced scattering center is visible in the center which is responsible for the low transmittance (see Fig. 3.3(a)). The Ukrainian crystal "Boris" also shows very pronounced scattering which was already observed in Ref. [72]. The fact that this crystal has a similar attenuation coefficient as the TUM crystals "Jakob II" and "Ludwig G. S." but shows more scattering suggest that it has a smaller absorption coefficient. In all of the investigated Russian crystals (e.g. "Sabine") as well as in some Ukrainian crystals (e.g. "Alexej II") no scattering centers were visible. This again confirms the good optical quality of the Russian crystals.

In principle, scattering centers are not harmful but actually can lead to an increase of the light output [56]. However, the same defects which cause scattering can also lead to absorption or charge trapping and therefore decrease the light output.

In Ref. [94] it was found that the formation of scattering centers can be prevented by the addition of 1-2 at.% WO_3 to the melt balancing the increased evaporation rate of WO_3 compared to CaO. In this scope, the crystal "Friedrich V" was grown with the addition of 1 at.% of WO_3 (see Tab. 2.3). However, the crystal still shows inclusions and light scattering. In fact the transmittance of the crystal is lower than of those grown from a stoichiometric melt (see Fig. 3.3(a)).

(a)   (b)

(c)   (d)
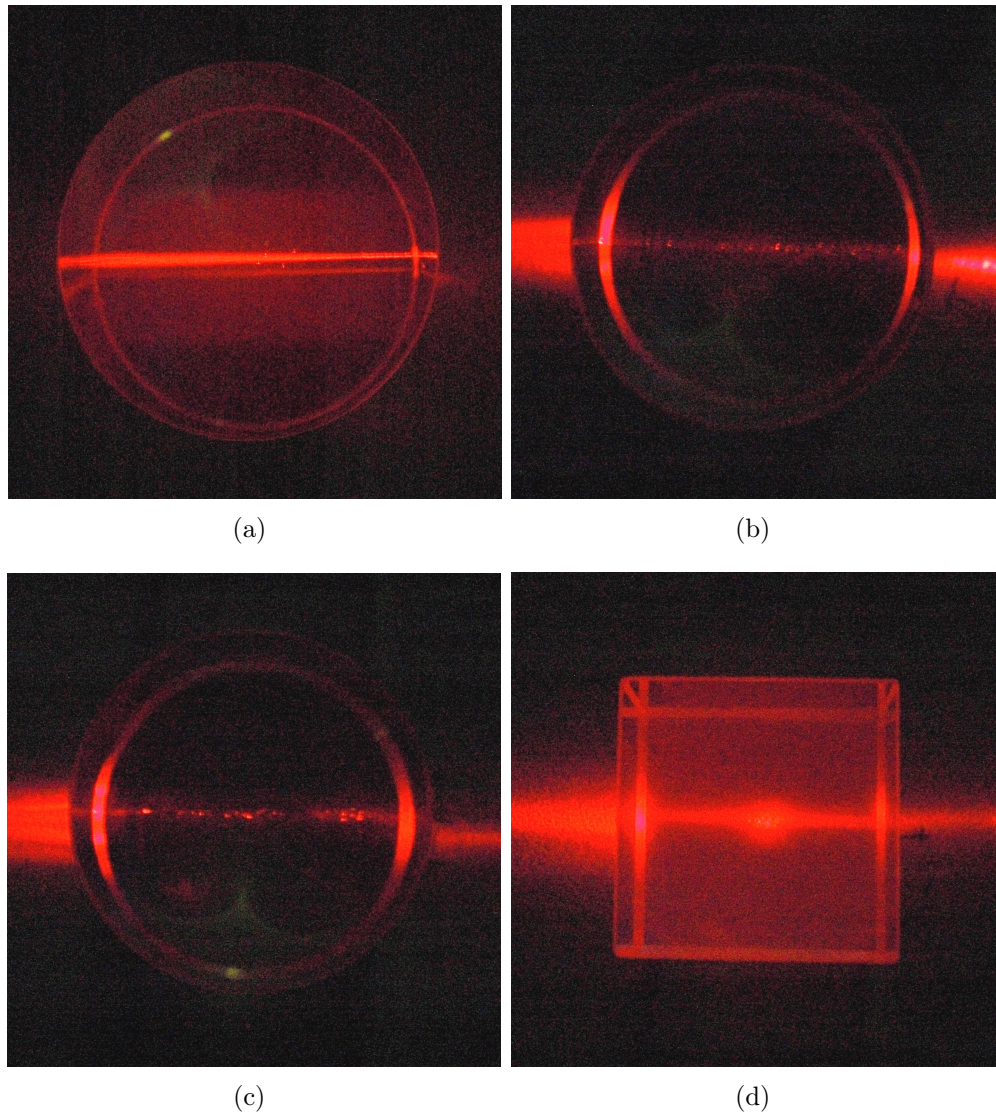
Fig. 3.4: Scattering of a a laser beam inside the Ukrainian crystals "Boris" (a) and the TUM crystals "Jakob II" (b), "Ludwig G. S." (c) and "Ernst" (d). In the latter pronounced scattering from an inclusion in the center can be observed.

Figure 3.5 shows transmission microscopy images of defects found in some of the TUM-grown crystals that are responsible for light scattering. We have identified cavities (Fig. 3.5(a)) and dislocations (Fig. 3.5(b)) to be present in the crystals.
Cavities are believed to be gaseous inclusions that result from oxygen separation from WO_4^{2-} complexes caused by chemical reactions with impurities [95]. In some crystals these inclusions appear more excessively (see Fig. 3.6). They always originate near the

center of the crystal and follow the local growth direction [96]. The occurrence of these cavities was found to be much more frequent in the crystals grown from the powders by MV Labs. This could point to a higher impurity concentration in the powders. However, the powders from MV Labs were graded with the same purity as the powders by Alfa Aesar. In addition, no noticeable difference was found in the ICP-MS analysis of the crystals grown from the different powders (see Sec. 3.3.1). Another explanation might be a deviation from stoichiometry of the synthesized $CaWO_4$ powder. Furthermore, the cause could be the growth process, e.g., due to changes in the temperature gradients.

The occurrence of dislocations is correlated with those of inclusions [97]. In addition, they can be formed by temperature gradients in the cooling crystal [75] and could be decreased by slower cooling rates after growth or during annealing.

In general the formation of defects could be reduced by a slower growth speed.
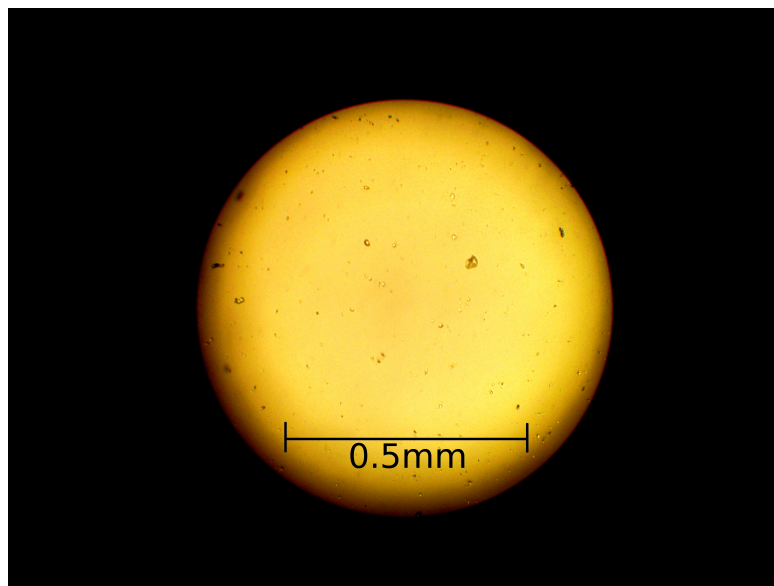
(a)
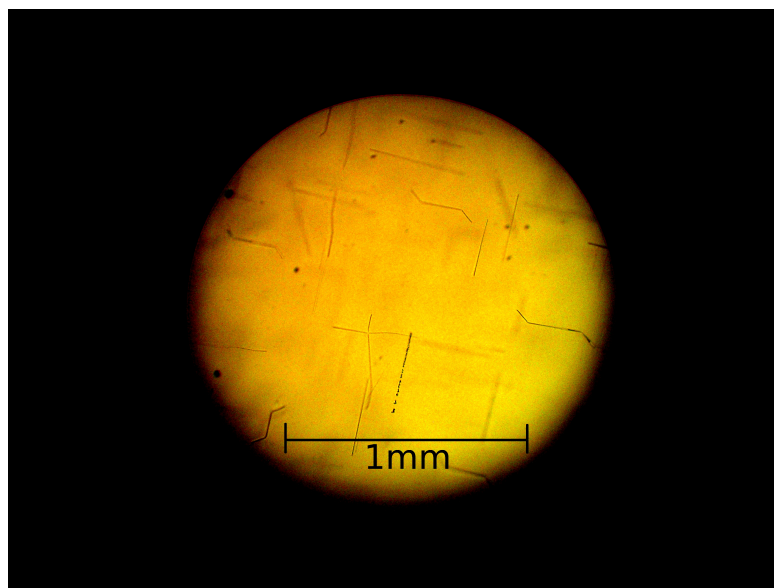
(b)

Fig. 3.5: Transmission microscopy images of some defects found in the TUM-grown CaWO$_4$ crystals. (a) cavities in the crystal "Ernst"; (b) dislocations in the crystal "Ludwig G. S."

Fig. 3.6: Photograph of the crystal "Georg Friedrich" which shows a high concentration of inclusions (shaded area along the central axis).

3.2 Scintillation Properties

3.2.1 Luminescence Spectra

In the following section we investigate the emission and excitation spectra of various $CaWO_4$ crystals under UV excitation at room temperature (RT). These spectra can give information about intrinsic defects and impurities in the crystal.

Experimental Setup

The measurements were performed using a Cary Eclipse fluorescence spectrometer by Agilent Technologies. A schematic picture of the spectrometer can be seen in Fig. 3.7. All emission spectra were corrected for the wavelength dependent response of the photomultiplier in the region 200-600 nm.
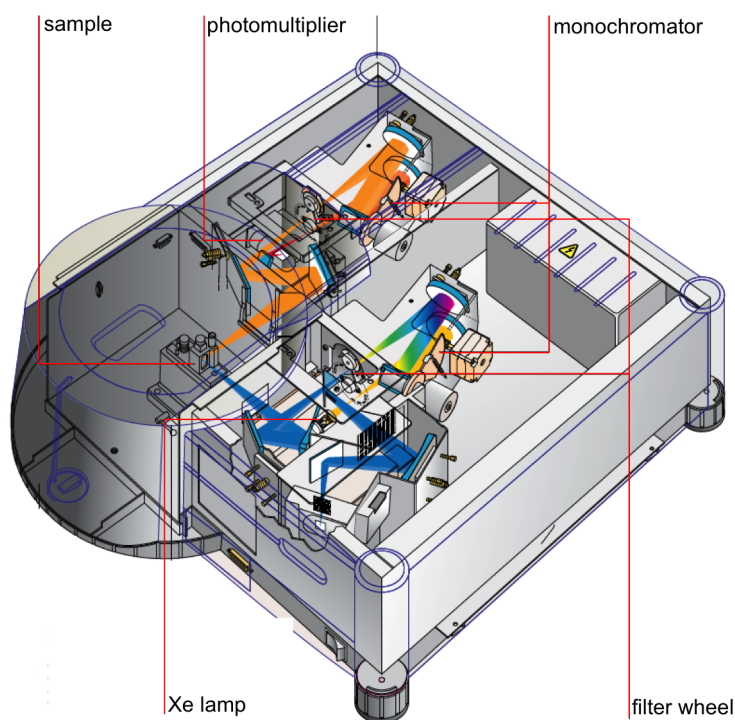

Fig. 3.7: Schematic setup of the Cary Eclipse fluorescence spectrometer. The light from a xenon flash lamp is passed through a filter wheel, a grating monochromator and then directed onto the sample. The fluorescence light emitted by the sample is passed through another filter wheel and grating monochromator and then detected by a photomultiplier tube [98].
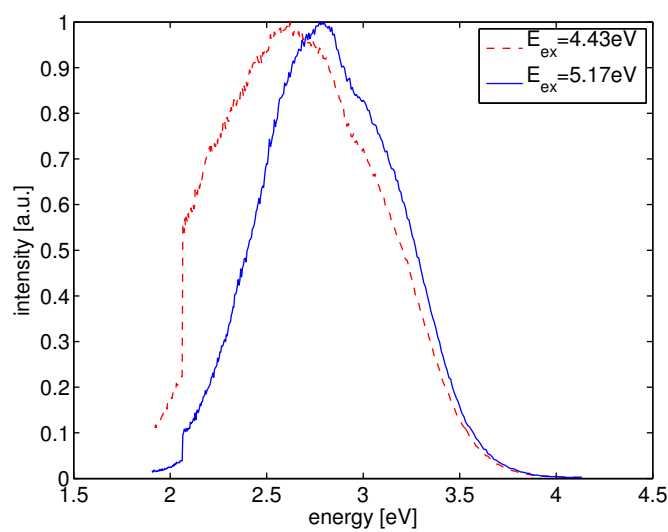
Emission Spectra

Different emission spectra have been reported for $CaWO_4$: The main intrinsic (blue) emission is centered at $\sim$2.9 eV (430 nm). It is attributed to the radiative decay of self-trapped excitons located at the WO_4^{2-} anion [59]. In addition, a green emission band at $\sim$2.3 eV (530 nm) is observed in many crystals and usually ascribed to oxyanions with oxygen vacancy - WO_3 Schottky defects [59]. The relative intensity of this emission band gives information on the concentration of these defects. While the intrinsic blue emission is mainly excited for energies >5 eV above the band gap the extrinsic green emission can also be excited for lower energies. At RT there is an overlap of the onsets for excitation of the blue and green emission and a separate excitation of the two bands is only possible at temperatures <10 K [59]. Excitation with energies <5 eV at RT will lead to a superposition of the blue and green emission bands.

Figure 3.8 shows the emission spectra of the Ukrainian crystals "Boris" and "Alexej I" under excitation at 4.43 eV and 5.17 eV. The kink in the emission spectra slightly below 3 eV is most likely an instrumental effect. The sudden drop at $\sim$2.1 eV comes from the wavelength correction which is only available for higher energies. The shift of the maximum of the emission spectrum can be attributed to the increase of the relative intensity of the blue emission with increasing excitation energy. The plots also show that the crystal "Alexej I" has a higher concentration of oxygen vacancies as the emission spectrum under excitation at 4.43 eV is clearly enhanced at low energies. Figure 3.9 shows the same emission spectra for the TUM crystals "Rudolf VI"[4] and the Russian crystal "Sabine". Here no shift of the emission spectrum can be observed which indicates a negligible contribution of the green emission center. This behaviour was observed for all investigated crystals produced in Russia and at TUM. Therefore, it can be concluded that the crystals grown at the TUM as well as the Russian crystals have a lower density of oxygen vacancies (WO_3 Schottky defects) compared to the Ukrainian crystals. A possible explanation for this observation might be that Ukrainian crystals are grown without addition of oxygen in the growth atmosphere or that they were not annealed in oxygen after growth.

---

[4]The sharp peak at $\sim$2.2 eV in the emission spectrum of "Rudolf VI" comes from a higher order maximum of the light used for excitation.
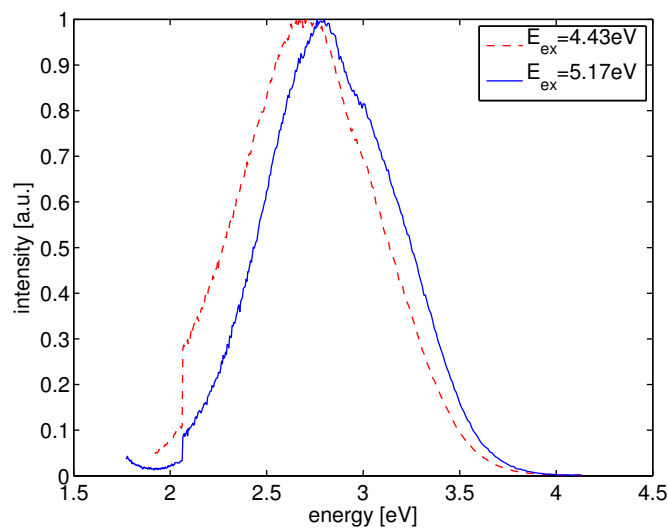
(a)

(b)

Fig. 3.8: Emission spectra of the Ukrainian crystals "Boris" (a) and "Alexej I" (b) under different excitation energies. The shift of the emission spectra under different excitation energies can be attributed to the presence of a defect emission band.
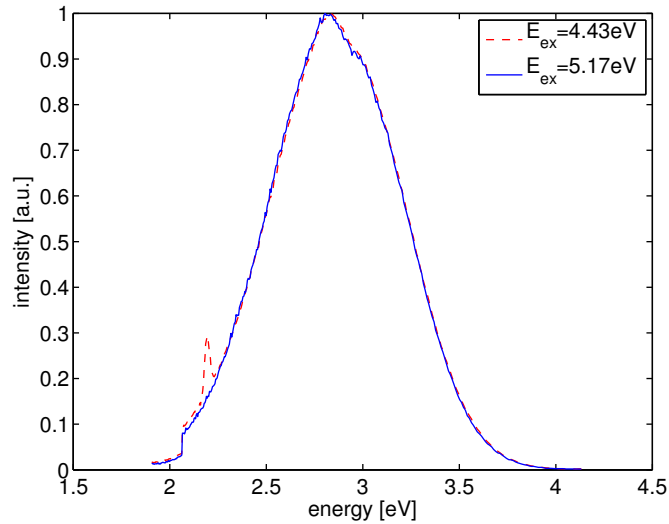
(a)
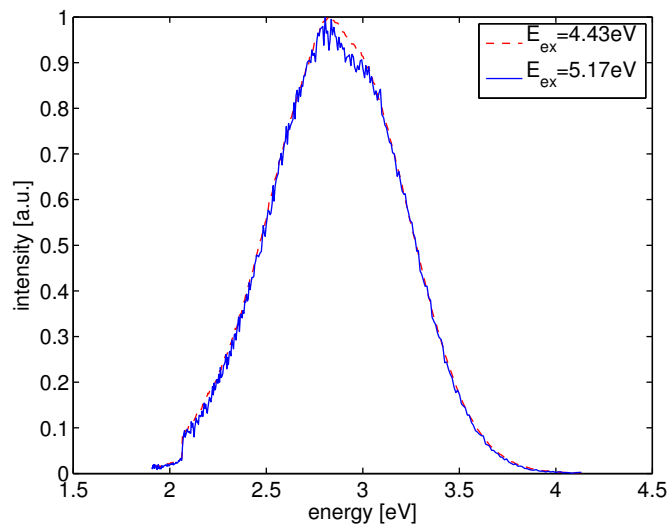
(b)

Fig. 3.9: Emission spectra of the TUM crystal "Rudolf VI" (a) and the Russian crystal "Sabine" (b) under different excitation energies. The identical spectra at different excitation energies indicate a negligible emission from defect centers.

3.2.2   Light Yield

Besides the radiopurity the most important property of a crystal is its light yield. It is defined by the number of detected photons for a certain energy deposition. The light yield is one of the parameters which determine the resolution of the light channel in a cryogenic detector module. Since the region of interest in CRESST-II is at very low energies ($<40\,\mathrm{keV}$) it is important that crystals have a high light yield. In this section we describe measurements where the light yield of a crystal is measured at room temperature (RT) with a photomultiplier (PMT) and compared to the Ukrainian crystal "Boris" which serves as a reference. In Sec. 3.4 we will show results for the light yield measured at low temperatures in a cryogenic detector module.

Experimental Setup

For the measurements the crystals were mounted in an aluminum housing which was covered with the specular reflecting VM2002 foil[5] on the inside. The crystals were held by small Teflon clamps. The reflective housing was then placed onto a PMT (see Fig. 3.10). In this configuration there is a small gap between the crystal and the side walls of the reflective housing as well as between the crystal and the PMT window. In this way the geometry is similar to that of a CRESST-II detector module. In addition, if not stated otherwise the crystal surface that was facing the PMT had been mechanically roughened like it is done for CRESST-II detectors (see Sec. 2.4). The crystal was irradiated with a ^{137}Cs ($662\,\mathrm{keV}$) or a ^{22}Na ($511\,\mathrm{keV}$) gamma source. For the measurements we used a 3" ETL9305KB and a 2" ETL9214KB PMT. To determine the light yield two different measurement techniques were applied: For the first method the PMT signal was directly recorded with a 10bit ADC (Acqiris DC282) with a sampling frequency of $1\,\mathrm{GHz}$ and the light yield was obtained by single photon counting as described in Ref. [56]. For the second method the PMT signal was amplified and integrated over $12\,\mathrm{\mu s}$ using a Canberra model 2020 spectroscopy amplifier. In this case pulses were recorded with a lower sampling frequency of $20\,\mathrm{MHz}$ and the light yield was determined from the pulse height. Concerning the light yield both measurement techniques were found to deliver consistent results. The advantage of the photon counting technique is that it gives a better resolution. However, it produces a large amount of data and requires a more extensive analysis that is prone to errors, e.g. due to double counting.

---

[5]The VM2002 foil (3M, Radiant Mirror Film) is the same reflector that is used for the cryogenic detector modules in CRESST-II.
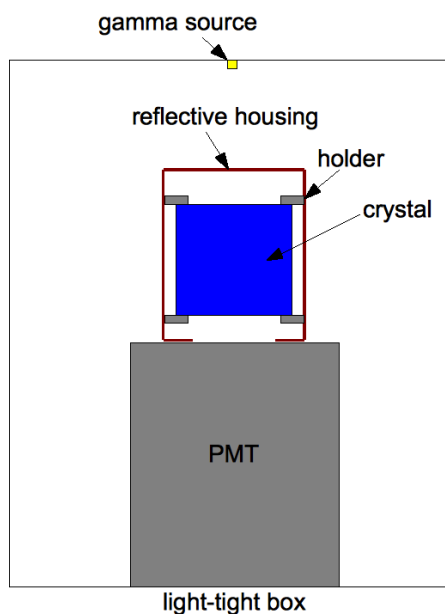
Fig. 3.10: Experimental setup of the light-yield measurements. The crystal was mounted in a reflective housing and placed onto a PMT. This resembles the geometry of a CRESST-like detector module.

Results and Discussion

Figure 3.11 shows the spectrum of the CRESST-II reference crystal "Boris" measured with a ^{137}Cs source, where the photopeak was fitted by a Gaussian. For each crystal the light yield was quantified by the normalized light yield (NLY) defined as the position of the photopeak in comparison to the reference crystal "Boris". The uncertainty of NLY as determined from the repetition of several measurements is about 1-2%.
The results of all light yield measurements are summarized in Tab. 3.2. The normalized light yield of all TUM-grown crystals ranges between ∼85-100%. The lower than average light yield of the two block-shaped (square prism) crystals "Wilhelm" and "Ludwig W." is most likely due to a different geometry of the holder that was used for the measurements. In particular, the opening to the PMT window was smaller than in the holder used for the cylindrical crystals. For the block-shaped crystal "Ernst" the holder was modified so that the opening to the PMT window has the same area as for the cylindrical crystals. The Ukrainian crystal "Dimitri" and especially the Russian crystal "Zora" show a higher light yield than the TUM crystals. Figure 3.12 shows that the value of NLY is correlated with the attenuation coefficient of the crystals determined in Sec. 3.1.2. The higher NLY of "Jakob II" in comparison to "Ludwig G. S." could be explained by its slightly smaller dimensions (see Tab. 2.4). These results suggests that the higher light yield is due to less self-absorption by the crystals. Another possibility is that the defects which lead to

a larger attenuation coefficient can also trap charge carriers. Light yield measurements on other Russian crystals have shown that most of them have values of NLY between ~130-150% [99]. This means that the light yield of the crystals grown at TUM can still be significantly improved. Our measurements suggest that this improvement can most probably be achieved by reducing the attenuation coefficient.
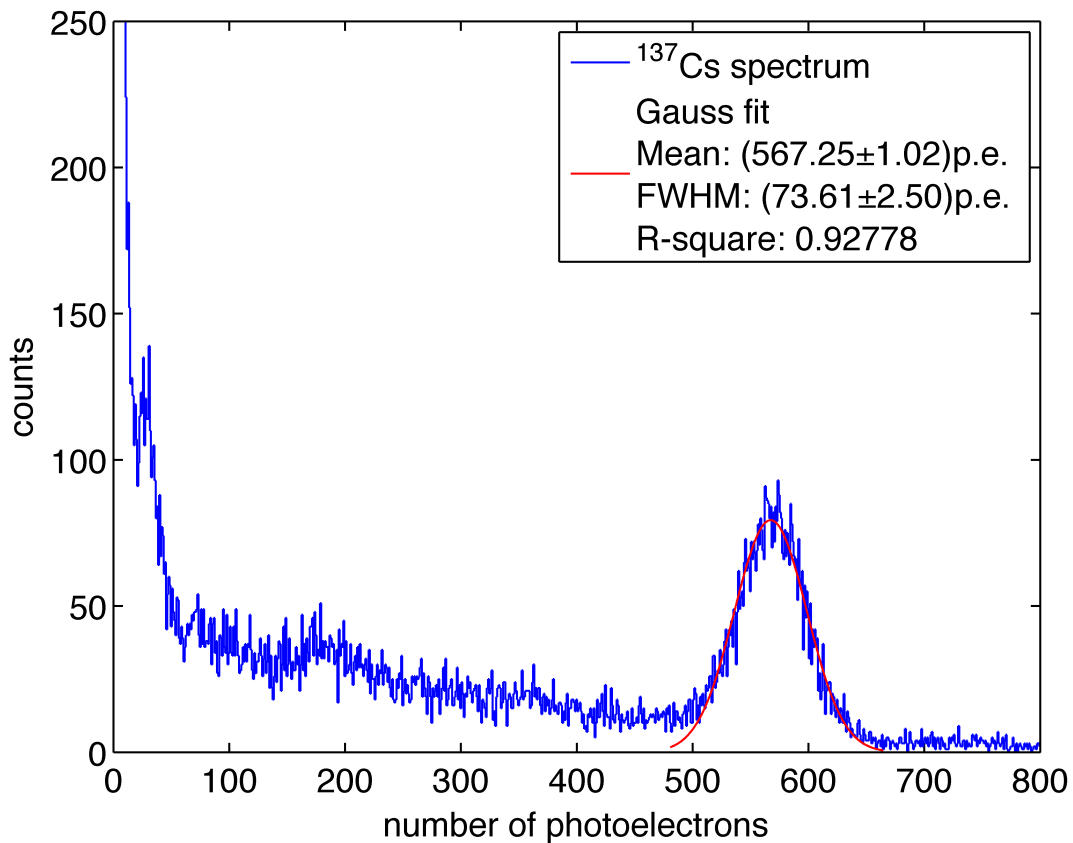
Fig. 3.11: ^{137}Cs spectrum (662keV) measured with the CRESST-II reference crystal Boris. To determine the light yield and resolution the photopeak was fitted by a Gaussian.

crystal	shape	surfaces	NLY (%)
Boris (Ukraine)	cylinder	polished	100±0.2
Zora (Russia)	cylinder	1 side roughened	130.9±1.0
Dimitri (Ukraine)	cylinder	1 side roughened	110.8±0.5
Rudolf VI (TUM)	cylinder	1 side roughened	100.0±0.1
Bernhard I (TUM)	cylinder	1 side roughened	99.9±0.2
Philibert (TUM)	cylinder	1 side roughened	92.2±0.1
Jakob II (TUM)	cylinder	1 side roughened	100.0±0.1
Philipp II (TUM)	cylinder	1 side roughened	95.7±0.1
Wilhelm (TUM)	square prism	5 sides roughened	84.9±0.3
Ludwig W. (TUM)	square prism	5 sides roughened	85.3±0.3
Ernst (TUM)	square prism	1 side roughened	91.3±0.1
Ludwig G. S. (TUM)	cylinder	1 side roughened	88.9±0.2

Tab. 3.2: Results of the light yield measurements of the different crystals. The last column shows the normalized light yield (NLY) with respect to the reference crystal Boris. The quoted uncertainties are the statistical uncertainties (at 95% CL) derived from the fit.
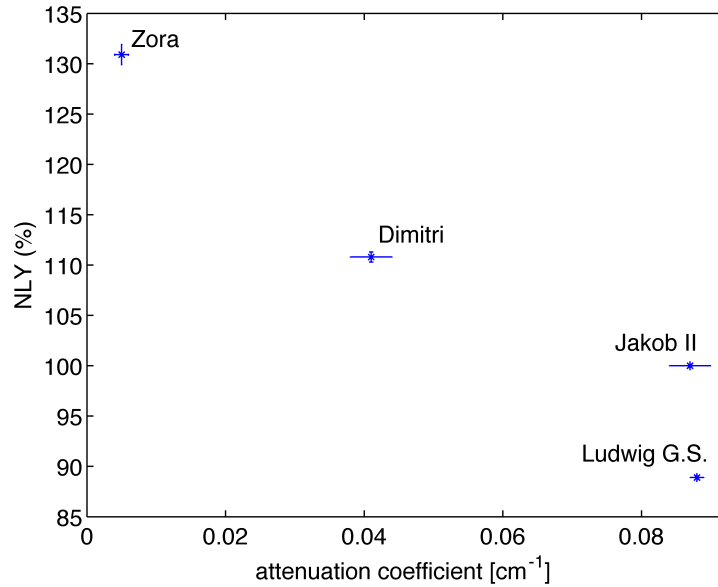
Fig. 3.12: Normalized light yield (NLY) versus the attenuation coefficient as determined in Sec. 3.1.2 for different crystals. It can be seen that a higher light yield is correlated with a smaller attenuation coefficient.

3.2.3   Temperature Dependence of Scintillation Properties

In the previous sections we have described our investigations concerning the optical and scintillation properties at room temperature. However, in CRESST-II the $CaWO_4$ crystals are operated at mK temperatures which is known to have a large influence on, e.g., the light yield and decay times [100]. In this section, we study the scintillation properties as a function of temperature for a $CaWO_4$ crystal produced at TUM and compare them to a Russian crystal.

Experimental Setup

The experiments were carried out at Queen's University in Canada in collaboration with the group of Prof. Dr. Philippe Di Stefano. The setup used for the measurements is described in detail in Ref. [101]. It is based on an optical cryostat from Cold Edge Technologies. The cooling is provided by a cryogen-free Gifford-McMahon cryostat with a closed circuit of helium. It can reach a base temperature of 3.2 K in about 3.5 hours. The main advantage of this setup is the compact geometry where about 40% of the solid angle is covered by two photomultiplier tubes (PMTs) mounted outside of the cryostat, leading to an improved light collection compared to most optical cryostats (see Fig. 3.13). Inside the cryostat a collimated ^{241}Am source is placed which emits α particles as well as γ-rays of 60 keV. A measurement of the α spectrum from the source with a silicon detector showed that the α peak appears at a lower energy of 4.7 MeV compared to the expected energy of 5.5 MeV and is broadened to a FWHM of 0.5 MeV [102]. These are degradation effects that result from a thin window protecting the source. In some measurements we recorded also spectra using an external ^{57}Co γ-ray source (122 keV). The scintillation light is detected by two 1" Hamamatsu R7056 PMTs with a maximum quantum efficiency of QE≈25% at 420 nm. This is well matched to the scintillation spectrum of $CaWO_4$ peaking at about 430 nm. The PMT pulses are recorded by a National Instruments PXI 5154 8-bit digitizer with a sampling rate of 1 GHz. In an online analysis based on Labview only samples that exceed a certain threshold above the baseline are then saved to disk. The used acquisition window was varied between 200 μs at room temperature and 3 ms at the lowest temperature according to the expected change of the decay times. The range between 5%-15% of this acquisition window was used as a pre-trigger. The trigger was provided by a hardware coincidence logic which requires that both PMTs trigger within a coincidence window of 20 μs. The measurement is based on the Multiple Photon Counting Coincidence (MPCC) technique which allows the simultaneous measurement of the light yield and decay time [58]. To obtain the spectrum, the sum of each scintillation event is calculated while the pulse shape is built using the arrival time and amplitude of every recorded sample in an event. In order to reject spurious events such as pile-up and pre-trigger events some data selection cuts are applied. Pile-up (two scintillation events within the same acquisition window) can be identified by comparing the mean arrival time of a scintillation event to the most likely mean arrival time of all of the events. Pre-trigger events (events containing photons during the defined pre-trigger time) are rejected by a cut on the distribution of the first photon of each event. For the construction of the

average pulse shapes, only events from the full-energy peaks of the α and γ particles are used.

As samples we used the TUM-grown CaWO$_4$ crystal "Philibert" and the Russian crystal "Olga". Both crystals had dimensions of $5\times5\times1\,\text{mm}^3$ where one of the $5\times5\text{mm}^2$ surfaces was optically polished and the opposite surface was mechanically roughened to reduce light trapping.

(a) (b)
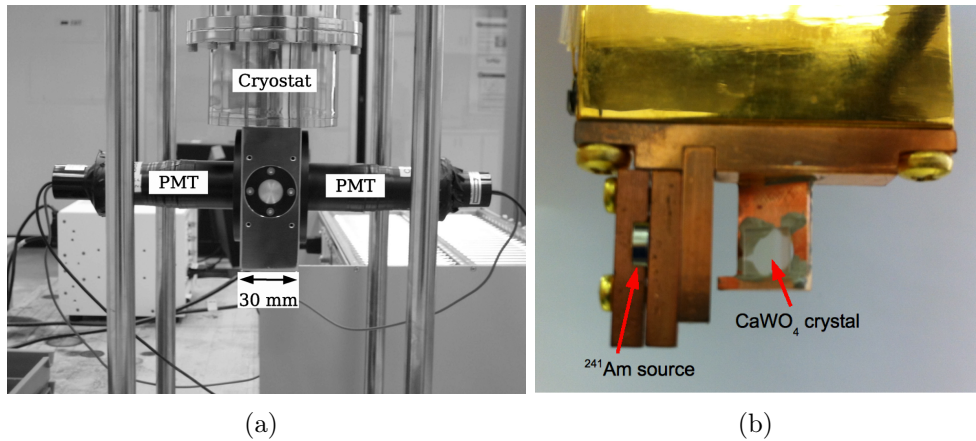
Fig. 3.13: (a): Photograph of the optical cryostat. The compact geometry with a diameter of only $30\,\text{mm}$ allows $\sim 40\%$ of the solid angle to be covered by the PMTs. (b): Picture of the crystal sample mounted inside the cryostat together with the ^{241}Am source.

Results and Discussion

Light Yield As an example, Fig. 3.14 depicts two spectra that were recorded with the TUM crystal at $77\,\text{K}$. One spectrum was obtained only with the internal ^{241}Am source while the other one was taken using the additional ^{57}Co source. The ^{241}Am only spectrum shows the photopeak from the $60\,\text{keV}$ γ-rays and a broader peak from the degraded α particles with an energy of $4.7\,\text{MeV}$. In the spectrum with the additional ^{57}Co source another peak is visible which results mainly from the $122\,\text{keV}$ γ-rays. The also emitted $136\,\text{keV}$ γ quanta with a factor of ~ 8 smaller intensity cannot be separated due to the limited resolution.

The results for the light yield as a function of temperature for both crystals are shown in Fig. 3.15. The light yield for the individual particles was always normalized to the value at $295\,\text{K}$. For the TUM crystal "Philibert" we recorded a full sweep at 22 different temperatures while for the Russian crystal "Olga" we recorded only spectra at 5 different temperatures. Investigating the pulse shapes we discovered that below $20\,\text{K}$ the acquisition window of $3\,\text{ms}$ was not sufficiently long to capture the whole pulse. Therefore, the light yield in those measurements was corrected using a fit to the average pulse shapes

by a sum of exponentials (see Eq. (3.8) below). According to the semi-empirical model in Ref. [103] and a recently developed comprehensive microscopic model of the scintillation mechanism in $CaWO_4$ [38] the temperature dependence of the light yield can be explained in the following way. Below 300 K the light yield increases due the decreasing probability for non-radiative decays of the intrinsic emission centers. At temperatures below ∼200 K nearly all intrinsic emission centers decay radiatively and the light yield curve flattens. Below ∼50 K the migration of excitons to defect centers decreases leading to another increase in light yield. Finally, at ∼10 K the excitons become immobile and the light yield stays approximately constant. For the TUM crystal, the total increase of the light yield at 3.4 K is a factor of ∼1.63 and ∼1.76 for α particles and γ quanta, respectively. Although both samples have the same size and geometry there can be variations when the crystals are mounted into the holder of the cryostat. Therefore, it is not possible to compare the absolute light yield. However, after normalization to the room temperature light yield it is possible to compare the relative increase in both crystals. For the sample "Olga" we found that the total increase of the light yield is a factor of ∼1.43 (∼1.68) for α (γ) events and therefore slightly lower than for the TUM crystal. According to the semi-empirical model in Ref. [103] one cause for the increase of light yield at low temperatures is the reduction of energy transferred to defect centers in the crystal that are responsible for non-radiative decays. We therefore surmise that a different concentration of such defects may be responsible for the different gains of the light yield. The total increase of light yield of α particles at 9 K compared to 295 K quoted in Ref. [103] is 1.82. This is well compatible with the value of 1.77±0.04 we found at 10 K for the TUM crystal. In general the temperature dependence of the light yield of the 60 keV γ-rays from the [241]Am source agrees with that of the 122 keV γ quanta from the external [57]Co source except for a slight difference at 77 K.

]htpb]
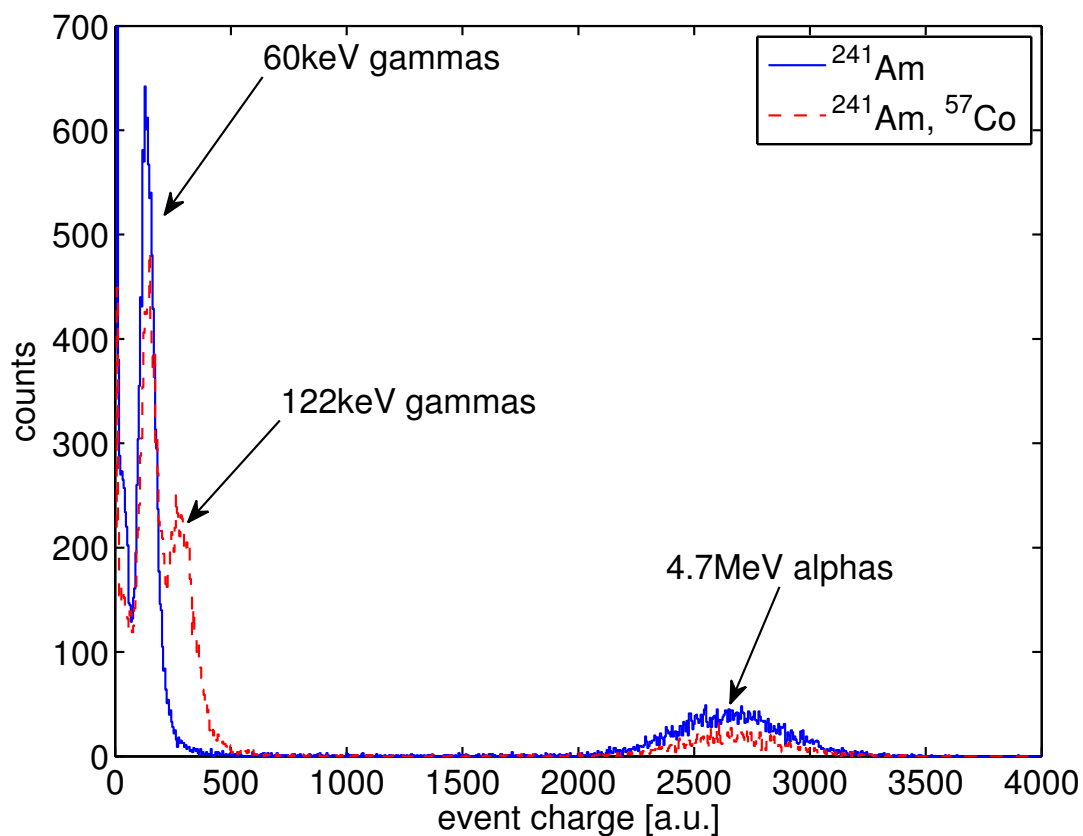
Fig. 3.14: Spectra measured with the TUM crystal "Philibert" using the built-in ^{241}Am source (blue solid line) and an additional external ^{57}Co source (red dashed line). The ^{241}Am spectrum shows a narrow peak originating from the 60 keV γ-rays plus a broad peak due to degraded α particles with a mean energy of 4.7 MeV. With the ^{57}Co source an additional peak from the 122 keV γ-rays is visible.
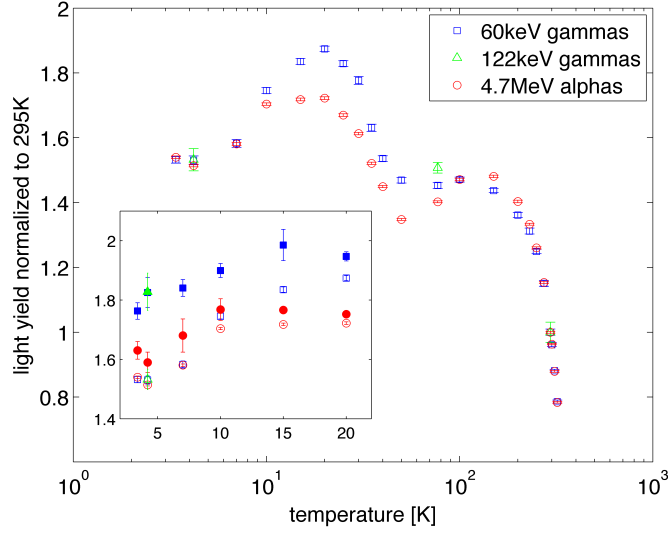
(a)
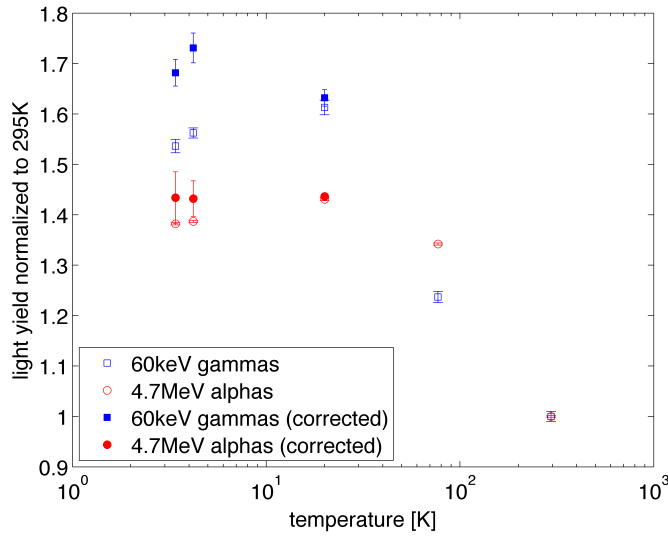
(b)

Fig. 3.15: Light yield normalized to the value at 295 K versus temperature for different particles for the TUM crystal "Philibert" (a) and for the Russian crystal "Olga" (b). The measurements were carried out with an ^{241}Am source emitting 60 keV γ-rays and degraded α particles with an energy of 4.7 MeV. In some measurements an additional ^{57}Co γ-ray source (122 keV) was used. The inset in (a) shows the values at low temperatures after correction for the limited acquisition window (filled markers, for details see main text).

84

An important quantity of a scintillator is the α/γ-ratio of the light yield. We define this ratio as the light yield per unit energy of a ^{241}Am α event (LY$_\alpha$) to that of a 60 keV or 122 keV γ event (LY$_\gamma$). This is similar to the definition of the quenching factor used in CRESST which is, however, taken as the ratio of the light yield for α and γ events of the same energy (see Sec. 1.2.2). Fig. 3.16 shows the α/γ-ratio of the light yield versus temperature. Depicted are the data points before and after the correction of the light yield for the limited acquisition window. For the TUM crystal the value of the α/γ-ratio at 295 K is 0.256±0.003. This is compatible with the value of 0.23±0.02 which we have calculated for α particles of this energy from the equation quoted in Ref. [48]. We observe that as temperature decreases down to 200 K, the α/γ-ratio increases. For temperatures <150 K, it then decreases and stays approximately constant below 30 K. At 3.4 K the value is 0.236±0.005 and therefore significantly smaller than that at room temperature. Such a temperature dependence is predicted by the microscopic model describing the quenching mechanism in CaWO$_4$ that was developed in Ref. [38].

In general, both crystals show a similar variation of the α/γ-ratio with temperature. While the value first increases with decreasing temperature it then decreases again. With values of 0.292±0.003 at 295 K and 0.249±0.005 at 3.4 K the α/γ-ratio of the Russian crystal is systematically higher than that of the TUM crystal.

Within errors the values for the α/γ-ratio determined from the 60 keV peak and 122 keV peak are compatible. This indicates that the light yield of the crystal is approximately linear in this energy region.
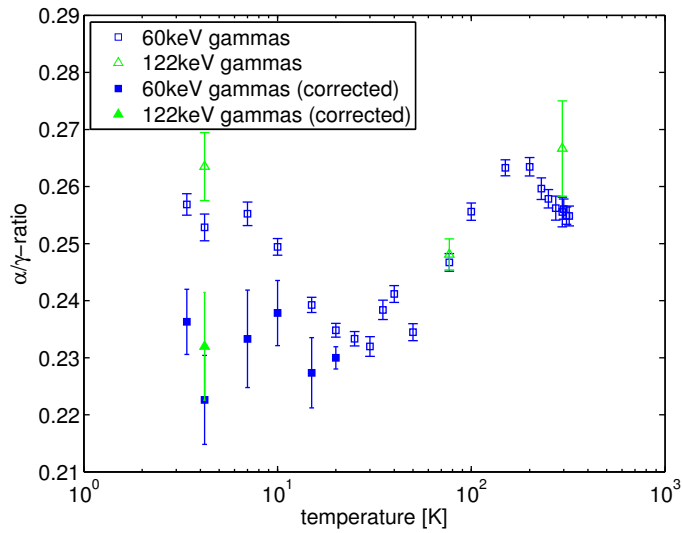
(a)
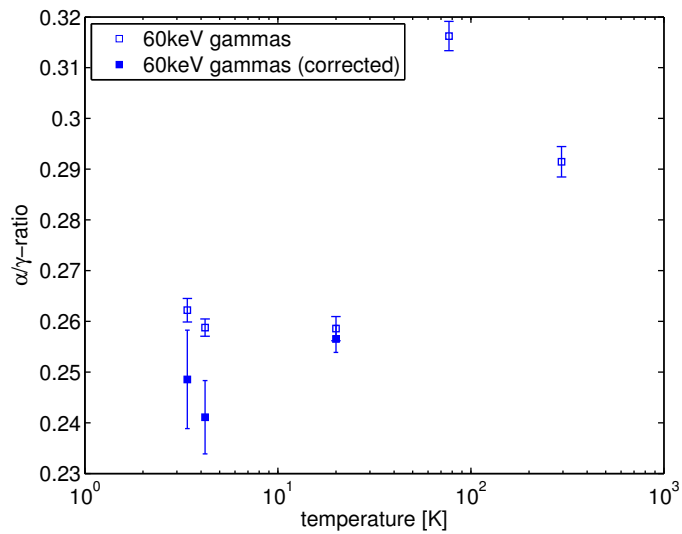
(b)

Fig. 3.16: Temperature dependence of the α/γ-ratio for the TUM crystal "Philibert" (a) and the Russian crystal "Olga" (b). For the low-temperature measurements the correction of the light yield due to the limited acquisition window has to be taken into account (filled markers).

Scintillation Decay Times   Fig. 3.17 shows the average pulse shapes at different temperatures for α and γ events recorded with the TUM crystal. It has to be pointed out that the first photon was always taken as the start of a scintillation event since the real start time is unknown. However, this leads to an overestimation of the first bin in the average pulse shape. To obtain the scintillation decay times τ_i each pulse was fitted with a sum of exponentials and, if necessary, an additional constant background:

$$f(t) = \sum_i \frac{n_i}{\tau_i} \exp(-t/\tau_i) + c \tag{3.8}$$

The values obtained from the fits at different temperatures are shown in Tab. 3.3. In comparison to the decay times in Ref. [100] we have found an additional long component in the ms range that starts to become significant for temperatures $\lesssim 40\,\mathrm{K}$. In general, a lengthening of the observed decay times could be caused by pileup events. However, such a long component was also observed in measurements at mK temperature using low-temperature light detectors [104, 105]. The scintillation decay times of $\tau_1=0.3\pm0.1\,\mathrm{ms}$, $n_1=70\pm15\%$ and $\tau_2=2.5\pm1\,\mathrm{ms}$ reported in Ref. [104] at a temperature of $\sim 20\,\mathrm{mK}$ are in good agreement with the values found at $4.2\,\mathrm{K}$ in this work (see Tab.3.3). Furthermore, we note that also in the isostructural $PbWO_4$ crystals a ms decay component was observed below $50\,\mathrm{K}$ [106]. This might point to some common trapping mechanism for both materials at that temperature range.

It is known that there is a noticeable difference between the decay curves of α and γ events that allows pulse shape discrimination [100, 107]. In general it was found that α pulses have a shorter decay time. This is confirmed by our data where pulses from α events show an additional short component in the average pulse shape. A detailed description of the scintillation pulse shape in $CaWO_4$ and of the physical processes in involved is given in Ref. [38]. According to this model the short component of the decay time is a quenching effect due to the interaction between excitons.

At low temperatures we have observed variations of the long component for α and γ events where that of α events is significantly shorter. In contrast to Ref. [100] we need up to four exponentials to fit our pulse shapes instead of just two.

Comparing the pulse shapes of the two different samples under study we find that the TUM crystal has systematically longer decay times than the sample from Russia. The emission kinetics and especially the long decay component are influenced by trapping centers in the crystal. We therefore assume that a different defect density might account for the varying pulse shapes as we suspect it is also responsible for the different temperature dependences of the light yield.
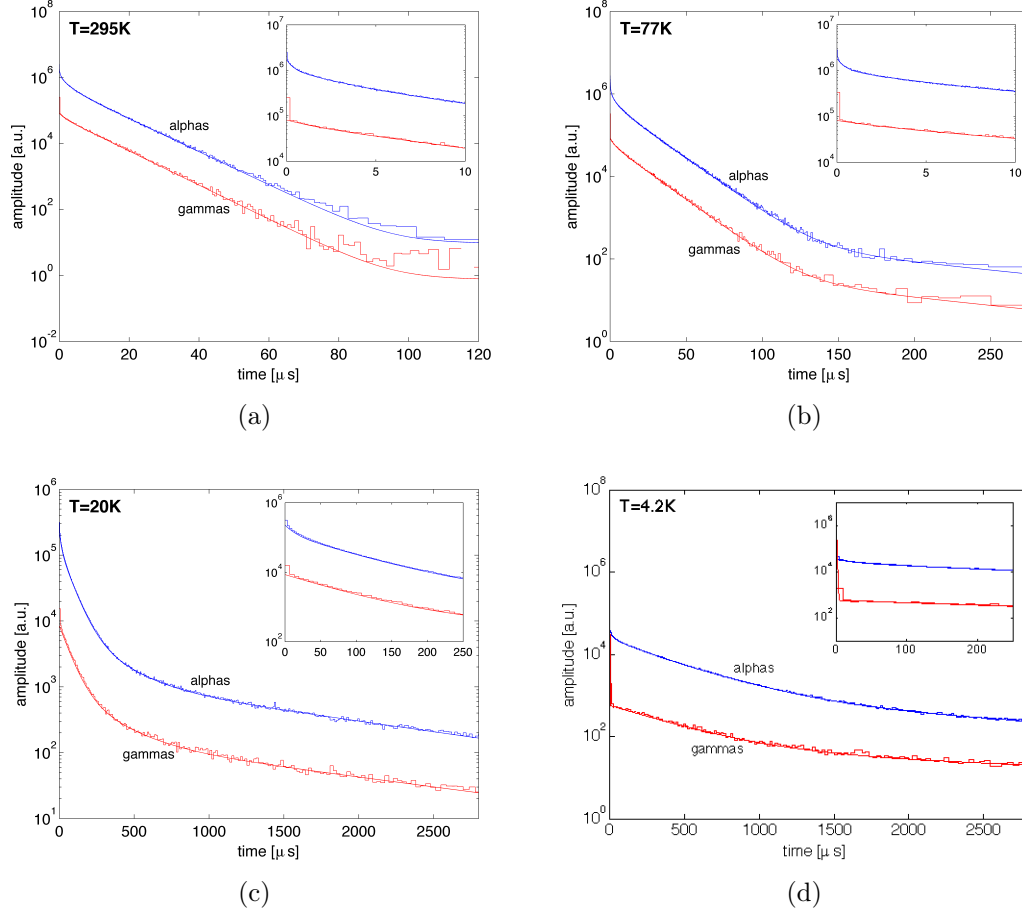
Fig. 3.17: Average pulse shapes for ^{241}Am α (in blue) and γ events (in red) at various temperatures measured with the TUM crystal. The inset shows a zoom into the region of the beginning of the pulse. All pulses were fitted by a sum of exponentials plus an optional constant (see Eq. (3.8)). The fit values are shown in Tab. 3.3.

Figure. 3.18(a) shows the temperature dependence of the decay times obtained for γ events measured with the TUM crystal. The fraction of the light yield that is contained in each component is proportional to the area of the symbols in the plot. To obtain a good fit at low temperatures we had to use 4 exponentials for the α pulses and 3 exponentials for those from the γ events. However, not all of the exponentials comprise a significant fraction of the whole pulse. In Fig. 3.18(a) we have, thus, omitted data points which contribute less than 1% to the total light yield. From the plot one can identify the main component of the pulse shape which comprises the largest fraction of the light yield at all temperatures. For temperatures between 320-40 K the pulse shape

		Philibert (TUM)		Olga (Russia)		Ref. [100]	
		τ (μs)	n (%)	τ (μs)	n (%)	τ (μs)	n (%)
295 K	α particles	0.32±0.01	3.1±0.5	1.61±0.04	12.3±2	-	-
		2.29±0.03	18.2±2	5.77±0.19	35.4±11	1.0±0.2	7
		8.64±0.01	78.7±0.9	9.45±0.09	52.3±20.3	8.6±0.3	93
	γ quanta	1.42±0.1	4.4±1.6	0.99±0.18	3.4±8.2	1.4±0.2	6
		8.39±0.02	95.6±0.3	8.05±0.02	96.6±0.2	9.2±0.3	94
77 K	α particles	0.39±0.01	2.5±0.3	0.54±0.01	3.5±0.3	-	-
		3.77±0.05	15.1±1.4	3.94±0.04	20.2±1.4	3.2±0.3	16
		16.44±0.02	82.0±0.6	15.11±0.02	74.5±0.9	16.6±0.4	84
		115±6	0.5±0.2	98.4±1.5	1.8±0.4	-	-
	γ quanta	2.97±0.13	6.0±1.3	2.7±0.1	7.9±1.4	2.1±0.3	15
		16.17±0.05	93.2±0.4	14.47±0.07	88.6±0.7	17.6±0.3	85
		113±10	0.7±0.5	46±1	3.5±1.9	-	-
4.2 K	α particles	1.7±0.8	2.0±0.3	17.9±0.6	2.0±0.3	1.0±0.2	13
		151±10	10±6	124±4	13±2	-	-
		370±6	69±7	351±3	72±3	330±40	87
		2051±90	19±6	1995±77	13±4	-	-
	γ quanta	-	-	13±3	0.6±0.5	0.9±0.2	>27
		366±5	56±1	353±3	67.9±0.8	480±60	73
		2827±200	44±6	2425±152	31.5±5.6	-	-

Tab. 3.3: Decay times at various temperatures for α and γ events from the ^{241}Am source. The values were determined by fitting the average pulse shapes with a sum of exponentials (see Eq. (3.8)). For comparison, we show the values from Ref. [100] measured for γ quanta and α particles using a ^{60}Co and a ^{241}Am source, respectively.

consists of an additional short component while for lower temperatures we observe a long component that contributes significantly to the light yield. We further note that an intermediate component appears between 15-35 K which was also found in Refs. [100, 58] under excitation with α particles and assigned to the delayed luminescence from recombination processes.
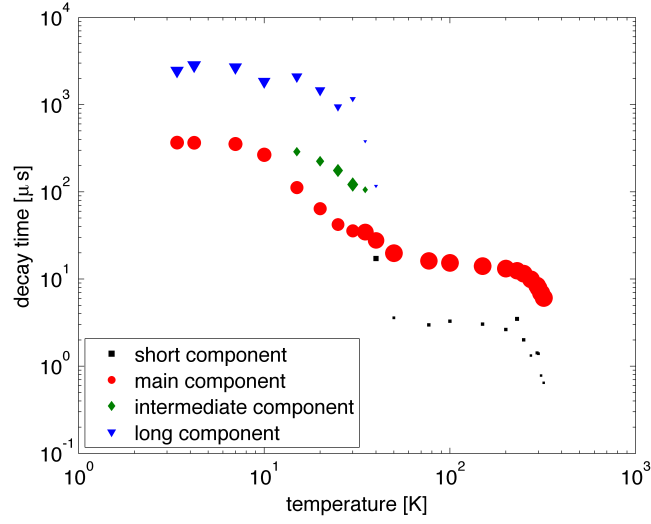
(a)
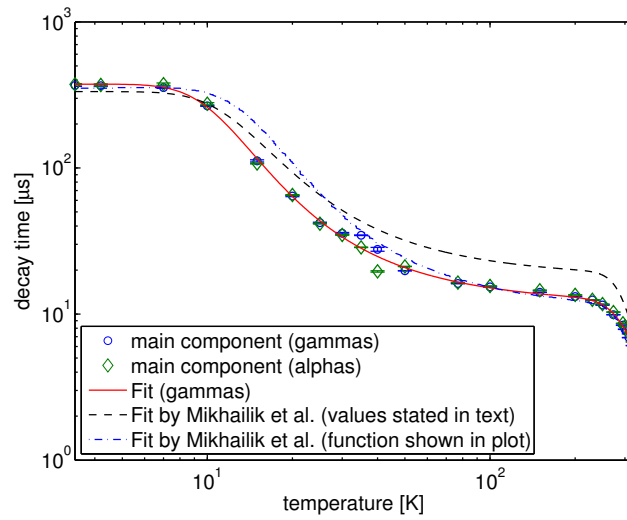
(b)

Fig. 3.18: (a): Decay times versus temperature measured for the TUM crystal under excitation with 60 keV γ-rays. The area of the markers corresponds to the fraction of photons that are contained within each component.

(b): Main decay times versus temperature for excitation with 60 keV γ-rays (blue circles) and 4.7 MeV α particles (green diamonds) measured for the TUM crystal. The red solid line shows the best fit to the data from the γ quanta according to Eq. (3.9). In Ref. [100] there is some inconsistency. The black dashed line shows the fit result from Ref. [100] with the fit parameters that are quoted in the text. However, this function does not agree with the one shown in their plot (blue dashed-dotted line).

It is established that the temperature dependence of the main decay time in $CaWO_4$ can be described with a simple three-level model [100]. In addition, the model was used to describe the decay times and emission intensities as a function of temperature in $PbWO_4$ [77]. The increase of the decay time is here ascribed to a metastable level which can be thermally depopulated at high temperatures but slows down the emission process at lower temperatures. The key parameters of this model are the probabilities for radiative decay from the two excited levels denoted by k_1 and k_2, respectively, and the energy splitting D of the two levels. Furthermore, the model includes a term for non-radiative quenching to the groundstate described by the decay rate K and the energy barrier ΔE. The decay time τ as a function of temperature T can then be calculated by the following equation:

$$1/\tau = \frac{k_1 + k_2 \exp(-D/k_B T)}{1 + \exp(-D/k_B T)} + K \exp(-\Delta E/k_B T) \qquad (3.9)$$

where k_B denotes the Boltzmann constant. We have used Eq. (3.9) to fit the temperature evolution of the main decay time that was obtained for the γ events in the TUM crystal (see Fig. 3.18(b)). From this fit we have obtained the following parameters:

k_1=(2.67±0.02)·10^3 Hz
k_2=(1.702±0.003)·10^5 Hz
D=4.26±0.01 meV
K=(3.1±0.2)·10^8 Hz
ΔE=226±2 meV

The value of the energy splitting D is in good agreement with the value of 4.4 meV quoted in Ref. [100]. However, for the energy barrier for non-radiative quenching ΔE we find a substantially lower value than those given in Refs. [100, 108] (320 meV and 340 meV). This difference might be explained by the inconsistency in Ref. [100] (see Fig. 3.18(b)). In comparison to the fit for the decay time obtained from Ref. [100] there is some difference to our data for temperatures between 10-30 K. This discrepancy is unlikely to be caused by the different excitation (60 keV γ quanta in the present work compared to 5.5 MeV α particles in Ref. [100]) as we have found only slight variations in the temperature dependence of the main decay time for α and γ events. However, this is the temperature region where the intermediate component from recombination processes appears (see Fig. 3.18(a)) which can influence the accuracy of the determination of the main decay time. In addition, the difference could be explained by a sample dependency.

3.3 Radiopurity

The region of interest (ROI) in CRESST-II comprises the nuclear recoil bands at energies <40 keV. As explained in Sec. 1.2.2 the discrimination ability between electron and nuclear recoils decreases with decreasing energy. The lower energy bound of the ROI is defined by accepting a certain number (typically one) of leakage events from the electron recoil band. Therefore, a lower discrimination threshold can be achieved if the electron recoil band below 40 keV is less populated. The intrinsic contamination of the $CaWO_4$ crystals does currently dominate the background rate in this region. A better radiopurity of the crystals that leads to a lower discrimination threshold would greatly increase the sensitivity of the detectors since the expected rate of WIMPs rises exponentially towards lower energies.

In this chapter we study the radiopurity of the $CaWO_4$ crystals grown at TUM as well as of the raw materials used for their production. The results will be compared to the intrinsic contaminations of crystals from other suppliers. The measurements were carried out using different methods including ultra low-background γ-ray spectrometry, trace impurity analysis and low-background scintillation spectroscopy.

3.3.1 Raw Materials for Crystal Growth

The raw materials that are used for the production of $CaWO_4$ crystals are powders of $CaCO_3$ and WO_3. For crystal growth, high purity materials are needed to minimize the amount of defects due to impurities in the crystals and to obtain crystals of high structural perfection. This is important for the optical quality of the crystals as impurity-related defects can, e.g., induce absorption bands or act as scattering centers. A high purity of the starting materials is of course also the first step to minimize the radioactive contamination of the crystals.

Different batches of $CaCO_3$ were obtained from the companies Alfa Aesar, Ube Material Industries, Ltd. and MV Laboratories, Inc.. From Alfa Aesar several batches (1-2 kg each) were obtained between 2006-2010, all with a specified purity of 5N. From MV Laboratories a single batch (10 kg) was bought in 2012 with a specified purity of 5N while from Ube Material Industries a batch (1 kg) of unknown purity was received in 2007.

Concerning the WO_3 powder, we bought several batches from Alfa Aesar (1-2 kg each) between 2006-2012 with a purity specified as 4N8 excluding molybdenum (<100ppm). Molybdenum is usually the main impurity in tungsten compounds and vice versa due to their chemical similarity. Furthermore, two batches of WO_3 (5.5 kg, 10 kg) with a specified purity of 4N8 (including Mo) were obtained in 2012 from MV Laboratories.

Results of Trace Impurity Analysis

The materials ordered from MV Laboratories were delivered with a certificate of analysis regarding the impurities. Fig. 3.19 shows the results for the batch of $CaCO_3$ powder. In

this case the trace impurities were determined by Inductively Coupled Optical Emission Spectroscopy (ICP-OES). The total amount of impurities that was found in the measurement adds up to 3.2ppm, thus the purity of this batch can be graded as 5N. The impurities found in this batch originate from Cd, Cr, Fe, Sr and Ti. For all other investigated elements the concentration is below the sensitivity that can be reached with this method. Regarding the radioactive contamination induced by the found impurities only Cd and Cr have naturally occurring radioactive isotopes. For Cd these are ^{113}Cd and ^{116}Cd with natural abundances of 12.2% and 7.5%, respectively. ^{113}Cd decays via β^- decay with a half-life of $7.7 \cdot 10^{15}$ y and a Q-value of 316 keV [109] while ^{116}Cd can only decay via double beta decay where the half-life is $2.6 \cdot 10^{19}$ y and the Q-value is 2805 keV [110]. The activity of ^{113}Cd in the $CaCO_3$ powder based on the measured concentration of 0.8ppm is only $1.5\,\mu$Bq/kg while the one due to ^{116}Cd is even four orders of magnitude smaller. Therefore, the radioactive contamination introduced by the Cd impurity is negligible. For Cr the isotope ^{50}Cr (natural abundance 4.3%) can decay via double beta decay, however, so far only a lower limit for the half-life of this decay of $>1.8 \cdot 10^{17}$ y could be determined. Sr is known to be responsible for some of the radioactive contamination in $CaWO_4$ crystals due to the isotope ^{90}Sr [111]. However, the origin of this isotope is anthropogenic and stems from radioactive fallout. Therefore, its concentration is in general not correlated to the concentration of natural Sr.

Ag	< 0.3		Cu	< 0.4		K	< 0.6		Pt	< 1		Tl	< 0.6
Al	< 0.6		Dy	< 0.8		La	< 0.3		Re	< 0.4		Tm	< 0.7
As	< 1		Er	< 0.9		Lu	< 0.1		Rh	< 1		V	< 0.3
Au	< 1		Eu	< 0.2		Mg	< 0.2		Ru	< 1		W	< 2
Ba	< 0.3		Fe	0.6		Mn	< 0.1		Sc	< 0.1		Y	< 0.3
Be	< 0.1		Ga	< 2		Mo	< 0.2		Sn	< 0.3		Yb	< 0.2
Bi	< 2		Gd	< 1		Na	< 1		Sr	0.8		Zn	< 0.2
Cd	0.8		Ge	< 1		Nb	< 0.6		Ta	< 1		Zr	< 0.3
Ce	< 2		Hf	< 0.7		Ni	< 0.2		Tb	< 1			
Co	< 0.2		Ho	< 1		Pb	< 0.5		Te	< 2			
Cr	0.4		Ir	< 0.7		Pd	< 1		Ti	0.6			

Fig. 3.19: Results from the analysis of trace impurities in the $CaCO_3$ powder LOT D0712CAA3 obtained from MV Laboratories, Inc.. The concentrations of impurities were determined by ICP-OES. The analysis was carried out by the chemistry laboratory of MV Labs. All values are given in ppm. Values below the limit of quantitation are listed as upper limits.

The analysis results for the two batches of WO_3 powder obtained from MV Laboratories are shown in Fig. 3.20. The impurities of LOT D0912WA1 were determined with High Resolution Inductively Coupled Plasma Mass Spectrometry (HR-ICP-MS) while those of LOT D0113WB1 were determined with Glow Discharge Mass Spectrometry (GD-MS). The total amount of impurities adds up to 11.47ppm and 10.46ppm for LOT D0912WA1

and LOT D0113WB1, respectively, thus the purity of both batches can be graded as 4N8.

In the WO_3 powder LOT D0912WA1 the found impurities are due to As, B, Li, Nb, Re, Th and V. Of those elements only Re, Th and V have naturally occurring radioisotopes. ^{187}Re with a natural abundance of 62.6% undergoes β^- decay with a half-life of $4.35 \cdot 10^{10}$ y and a very low Q-value of 2.66 keV [109]. The activity of ^{187}Re due to the measured concentration of 7ppm is 7.2 Bq/kg and therefore very high. However, because of its low Q-value it does not pose as a background for Dark Matter search where the energy region of interest is typically between $\sim$10-40 keV. This contamination could only be problematic for a low-threshold analysis. The radioactive isotope ^{50}V has a natural abundance of 0.25%, it decays with a half-life of $1.4 \cdot 10^{17}$ y either by electron capture (branching ratio 83%, Q-value 2208 keV) or by β^- decay (branching ratio 17%, Q-value 1037 keV) [109]. Due to the long half-life and the small natural abundance the activity of ^{50}V is in the range of a few nBq/kg and therefore negligible. The Th impurity found in the analysis will lead to a serious radioactive contamination as ^{232}Th has a natural abundance of 100% and a half-life of $1.4 \cdot 10^{10}$ y. It decays by α-decay with a Q-value of 4083 keV and is at the top of a natural decay series that ends with ^{208}Pb [109]. Therefore the presence of ^{232}Th will also lead to the presence of every other radioisotope in the decay chain. The measured concentration of 0.09ppm for Th corresponds to an activity of 370 mBq/kg for ^{232}Th which is rather high. To confirm this contamination a small sample of the batch was also analyzed with HR-ICP-MS at the chemistry laboratory of the Laboratori Nazionali del Gran Sasso (LNGS) in Italy. In this measurement no Th contamination was found and an upper limit of <10ppb could be derived (see Tab. 3.5). This seems to refute the result of the analysis from MV Laboratories. In addition, a screening measurement of the batch using γ-ray spectrometry could also not confirm the Th contamination (see next section). A possible explanation for the Th impurity found in the HR-ICP-MS analysis from MV Laboratories could be the identical mass of ^{232}Th and WO_3. This leads to an isobaric interference in the mass spectrometry measurement and thus to an overestimation of the concentration of Th in the sample.

The impurities found in the WO_3 powder LOT D0113WB1 are due to Al, As, B, Cr, Fe, Na, Nb, Sb, Ti and V. None of these elements has naturally occurring radioisotopes apart from Cr and V. As already shown these only lead to negligible activities. The analysis results are in particular useful as upper limits for the concentration of U and Th of 5ppb, respectively, have been obtained.

Ag	< 0.5		Cs	< 0.5		K	< 5		Pd	< 0.5		Tb	< 0.05
Al	< 2		Cu	< 1		La	< 0.5		Pr	< 0.05		Te	< 0.5
As	1		Dy	< 0.05		Li	0.3		Pt	< 0.5		Th	0.09
B	2		Er	< 1		Lu	< 0.05		Rb	< 0.5		Ti	< 1
Ba	< 0.5		Eu	< 0.05		Mg	< 0.5		Re	7		Tl	< 0.05
Be	< 0.5		Fe	< 1		Mn	< 0.5		Rh	< 0.5		Tm	< 0.05
Bi	< 0.5		Ga	< 2		Mo	< 1		Ru	< 0.5		U	< 0.05
Ca	< 2		Gd	< 0.05		Na	< 5		Sb	< 0.1		V	1
Cd	< 0.1		Ge	< 0.05		Nb	0.08		Sc	< 0.1		Y	< 0.1
Ce	< 0.05		Hf	< 1		Nd	< 0.05		Sm	< 0.05		Yb	< 0.05
Co	< 1		Ho	< 0.05		Ni	< 5		Sr	< 0.5		Zn	< 5
Cr	< 5		In	< 1		Pb	< 0.1		Ta	< 0.5		Zr	< 0.1

(a)

Ag	< 0.05		Cs	< 5		La	< 0.05		Pr	< 0.05		Te	< 0.1
Al	0.07		Cu	< 0.1		Li	< 0.05		Pt	< 0.5		Th	< 0.005
As	1.8		Dy	< 0.05		Lu	< 0.05		Rb	< 0.05		Ti	0.04
B	2.7		Er	< 0.05		Mg	< 0.05		Re	< 1		Tl	< 0.05
Ba	< 0.05		Eu	< 0.5		Mn	< 0.1		Rh	< 0.5		Tm	< 0.05
Be	< 0.01		Fe	0.44		Mo	< 1		Ru	< 0.5		U	< 0.005
Bi	< 0.01		Ga	< 0.1		Na	1.2		Sb	0.14		V	3.8
Ca	< 0.5		Gd	< 0.05		Nb	0.08		Sc	< 0.01		Y	< 0.05
Cd	< 0.5		Ge	< 0.5		Nd	< 0.05		Sm	< 0.05		Yb	< 0.05
Ce	< 0.05		Hf	< 0.05		Ni	< 0.1		Sn	< 0.5		Zn	< 0.1
Co	< 0.05		Ho	< 0.05		Pb	< 0.05		Sr	< 0.05		Zr	< 0.05
Cr	0.19		K	< 0.5		Pd	< 0.05		Tb	< 0.05			

(b)

Fig. 3.20: Results from the analysis of trace impurities in the WO_3 powders LOT D0912WA1 (a) and LOT D0113WB1 (b) obtained from MV Laboratories, Inc.. The concentrations of impurities were determined by HR-ICP-MS (a) and GD-MS (b). The analysis was carried out by the chemistry laboratory of MV Labs. All values are given in ppm. Values below the limit of quantitation are listed as upper limits.

In addition to the measurements described above several samples of $CaCO_3$, WO_3 and $CaWO_4$ powder were analyzed by HR-ICP-MS at the chemistry laboratory of the LNGS at Gran Sasso. The $CaWO_4$ powder was synthesized at the Technische Universität München (see Sec. 2.1.2) from the $CaCO_3$ powder LOT D0712CAA3 and the WO_3 powder LOT D0912WA1 by the following solid state reaction:

$$CaCO_3 + WO_3 \rightarrow CaWO_4 + CO_2 \qquad (3.10)$$

For the trace impurity analysis the $CaCO_3$ samples were dissolved in $0.25\,ml$ HNO_3 solution and diluted. The sample of WO_3 was etched with $2\,ml$ of NH_4OH solution in a

sonic bath for 12 hours and diluted. The $CaWO_4$ was dissolved in 1 ml HF in a sonic bath at 70°C for 10 hours and diluted. Due to the acid-resistance of $CaWO_4$ the final solution was slightly cloudy. The concentrations were determined for U and Th (and Pb in case of the $CaCO_3$ powders) while the instrument was calibrated using a reference standard solution. The results are shown in Tabs. 3.4 and 3.5. The reached sensitivity for the WO_3 and $CaWO_4$ powders is limited due to their resistance towards dissolution and due to the isobaric interference between ^{232}Th and WO_3. Therefore, only upper limits of <5ppb and <10ppb for U and Th, respectively, could be derived for both samples. For the $CaCO_3$ powders the better sensitivity allowed measuring the actual U and Th concentrations in the samples. It shows that the powder from MV Labs contains a higher amount of U and Th. For the latter the concentration is about 3 times higher. An even larger difference was found for Pb where the concentration is more than one order of magnitude higher in the powder by MV Labs. As MV Labs is also the supplier of $CaCO_3$ for Alfa Aesar the different impurity concentrations can not be assigned to a different production process but are most probably the result of different raw materials used in the production.

material	$CaCO_3$ powder	
supplier	Alfa Aesar	MV Labs
	(LOT 610011709B)	(LOT D0712CAA3)
element	**concentration (ppb)**	
U	0.5	0.8
Th	0.4	1.3
Pb	14	230

Tab. 3.4: Results of the HR-ICP-MS analysis performed for different $CaCO_3$ powders by the chemistry laboratory of the LNGS. The concentrations refer to the solid samples and are blank subtracted. The uncertainty is about 30% of the given values.

material	WO_3 powder	$CaWO_4$ powder
supplier	MV Labs	MV Labs1
	(LOT D0912WA1)	
element	**concentration (ppb)**	
U	<5	<5
Th	<10	<10

Tab. 3.5: Results of the HR-ICP-MS analysis performed for different powders by the chemistry laboratory of the LNGS. Other details as in Tab. 3.4.

Results of γ-ray Spectrometry

The analysis of trace impurities presented in the previous section can only be performed for natural elements but can not provide direct information about the presence of radioactive isotopes. Therefore, an investigation of the radiopurity is only possible for radioisotopes with a natural abundance like e.g. ^{40}K, ^{238}U and ^{232}Th. A different method which can directly determine the concentration of radionuclides in a sample is provided by γ-ray spectrometry.

From the $CaCO_3$ and WO_3 powders one sample of each batch provided by the different suppliers as well as the synthesized $CaWO_4$ powders were screened with ultra-low background γ-ray spectrometry. The measurements were performed with a HPGe detector at the Canfranc Underground Laboratory (LSC) located at a depth of 2450 m.w.e. [112]. The detector, operating underground for more than 20 years [113], is currently shielded with an inner layer of 10 cm of old lead and 15 cm of normal lead.

For the WO_3 powders only upper limits on the activities could be derived (see Tab. 3.6) showing their good radiopurity. The samples of $CaCO_3$ from Alfa Aesar and Ube Material do show a contamination with ^{226}Ra while the sample from MV Labs does not (see Tab. 3.7). The presence of radium can be explained by the similar chemical properties of calcium and radium. In the sample obtained from MV Labs an activity due to ^{228}Ra and ^{228}Th was measured. Under the assumption of radioactive equilibrium this activity would correspond to a Th concentration of ∼1.3ppb which is in excellent agreement with the value determined by the HR-ICP-MS analysis (see tab:HR-ICP-MS).

Tab. 3.8 shows the results for the activity of the $CaWO_4$ powders synthesized at the TUM from the powders by Alfa Aesar and MV Labs by solid state reaction (see Eq. (3.10)): The batches denoted by MV Labs1 and MV Labs2 were produced from the WO_3 powders LOT D0912WA1 and LOT D0712CAA3, respectively.[6] In general, the measured activities are not compatible with the contaminations found in the $CaCO_3$ and WO_3 powders which indicates that there is some additional contamination during the synthesis. All $CaWO_4$ powders show an increased activity of ^{226}Ra. The values for ^{228}Ra and ^{228}Th in the batches MV Labs1 and MV Labs2 also hint towards a further contamination but are compatible on a 2 sigma level with the ones found in the $CaCO_3$. The activities of the batch MV Labs1 point towards the introduction of ^{238}U. Furthermore, an additional contamination with ^{40}K is clearly observed.

For comparison Tab. 3.8 includes the data of a specially purified $CaWO_4$ powder from Ref. [114] produced by the NeoChem company which also shows a contamination with ^{226}Ra.

It should be noted that all results obtained by γ-ray spectrometry are consistent with those determined by HR-ICP-MS. An important finding is that for $CaCO_3$ powder a better sensitivity for U and Th can be achieved by HR-ICP-MS. This is not the case for WO_3 and $CaWO_4$ powders due to their resistance towards dissolution and due to the isobaric interference between ^{232}Th and WO_3.

---

[6]Unfortunately, it could not be retraced which batches of the powders by Alfa Aesar were used to synthesize the $CaWO_4$ powder.

It is currently unknown how the additional contamination with radionuclides during the $CaWO_4$ synthesis can be avoided. This, however, will be important to improve the radiopurity of the crystals in the future. An alternative synthesis process is possible via chemical precipitation from a solution. This synthesis can, e.g., be carried out via the following reaction:

$$Ca(NO_3)_2 + WO_3 + 2NH_4OH \rightarrow CaWO_4 + 2NH_4(NO_3) + H_2O \qquad (3.11)$$

The starting materials for this process can be obtained with a high purity of at least 4N8. The advantage is that impurities which are soluble in the NH_4OH solution can be removed. In addition, the stoichiometry of the precipitated $CaWO_4$ powder is guaranteed. In first tests this synthesis was successfully carried out by the chemistry lab of the MV Laboratories company.

material		WO_3 powder	
supplier	Alfa Aesar	MV Labs	MV Labs
	(LOT 23922)	(LOT D0113WB1)	(LOT D0912WA1)
sample mass	83 g	400 g	100 g
isotope		**activity [mBq/kg]**	
^{228}Ra	< 23	< 2.1	< 6.7
^{228}Th	< 6	< 1.6	< 7.4
^{238}U	< 400	< 68	< 350
^{226}Ra	< 10	< 2.2	< 13
^{227}Ac	< 36	< 5.6	-
^{40}K	< 43	< 20	< 69
^{137}Cs	< 7	< 1.2	< 2.6
^{60}Co	< 2	< 0.68	< 1.7

Tab. 3.6: Activities of radionuclides determined by ultra-low background γ-ray spectrometry for the WO_3 powders from different suppliers. The measurements were performed with a HPGe detector at the LSC. Upper limits are given with 95% CL, uncertainties at 1 sigma.

material	CaCO$_3$ powder		
supplier	Alfa Aesar	MV Labs	Ube Material
	(LOT 610011709B)	(LOT D0712CAA3)	
sample mass	35 g	500 g	100 g
isotope	activity [mBq/kg]		
^{228}Ra	< 27	4.3 ± 1.1	< 11
^{228}Th	< 33	6.0 ± 0.6	< 15
^{238}U	< 260	< 23	< 110
^{226}Ra	26 ± 6	< 0.9	58 ± 5
^{227}Ac	< 31	< 3.1	< 17
^{40}K	< 83	< 13	< 81
^{137}Cs	< 7	< 1.0	< 4
^{60}Co	< 6	< 0.6	< 2

Tab. 3.7: Activities of radionuclides determined by ultra-low background γ-ray spectrometry for the CaCO$_3$ powders from different suppliers. Other details as in Tab. 3.6.

material	CaWO$_4$ powder			
supplier	Alfa Aesar	MV Labs1	MV Labs2	Ref. [114]
sample mass	57 g	600 g	600 g	50 g
isotope	activity [mBq/kg]			
^{228}Ra	< 17	2.7±1.0	3.5±0.1	< 19
^{228}Th	< 10	4.6±1.0	4.1±0.9	< 7
^{238}U	< 450	52±11	<52	< 31
^{226}Ra	28 ± 6	5.5±0.7	8.3±0.8	19 ± 5
^{235}U	-	2.2±0.5	<2.7	-
^{227}Ac	<36	<4.1	<4.8	-
^{40}K	< 65	23±5	22±5	< 120
^{137}Cs	< 5.5	<1	<1.3	-
^{60}Co	< 2.6	<0.5	<0.7	< 7

Tab. 3.8: Activities of radionuclides determined by ultra-low background γ-ray spectrometry for the CaWO$_4$ powder synthesized at the TUM from the powders by Alfa Aesar and MV Labs. The batches denoted by MV Labs1 and MV Labs2 were produced from the WO$_3$ powders LOT D0912WA1 and LOT D0712CAA3, respectively. For comparison the data of CaWO$_4$ powder from Ref. [114] is shown. Other details as in Tab. 3.6

3.3.2 Grown Crystals

Segregation of Impurities

An important effect in crystal growth is the segregation of impurities due to their different solubilities in the solid and liquid phase. The equilibrium segregation coefficient s_0, which neglects the influence of the growth speed, is hereby defined as the ratio of the impurity concentration in the crystal c_{crys} and in the melt c_{melt}:

$$s_0 = c_s/c_l \tag{3.12}$$

In most cases the impurity species leads to a reduction of the melting temperature and therefore to a value $s_0 < 1$, which means that the crystallization process leads to a purification. In general, the effective segregation coefficient s_{eff} depends on the growth speed since it takes a finite time for rejected impurities to diffuse back into the melt. In case of $s_0 < 1$ this leads to a liquid layer below the crystallization interface with a higher impurity concentration than the rest of the melt. The effective segregation coefficient s_{eff} then depends on the thickness d of this diffusion boundary layer, the growth speed v and the diffusion coefficient D of the impurity species in the melt [115]:

$$s_{eff} = \frac{s_0}{s_0 + (1 - s_0)\exp\left(-vd/D\right)} \tag{3.13}$$

Figure 3.21 shows the effective segregation coefficient versus the normalized growth rate vd/D. For very large normalized growth rates the effective segregation coefficient approaches a value of 1. In addition, the relative change of s_{eff} is larger for smaller values of s_0.
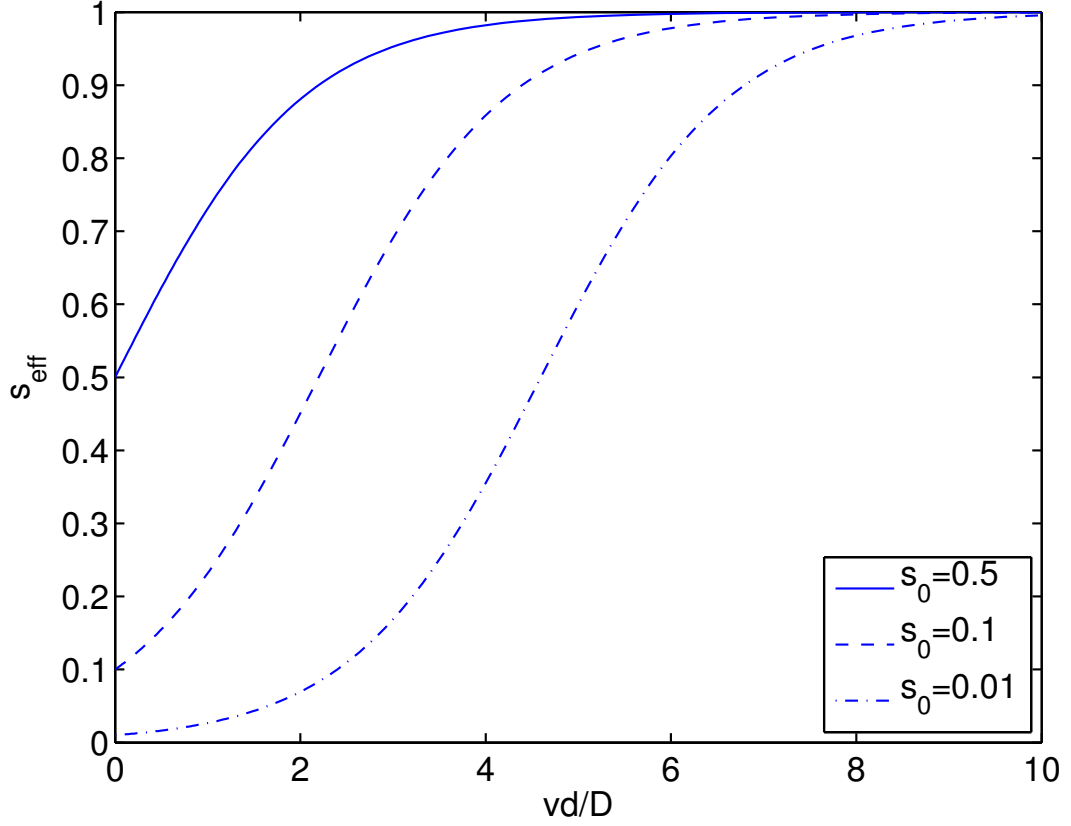
Fig. 3.21: Effective segregation coefficient s_{eff} in dependence of the normalized growth rate vd/D. For large values of vd/D the effective segregation coefficient approaches a value of 1.

Since in the case of $s_{eff}<1$ the impurity concentration in the melt increases during crystal growth there is an impurity gradient in the crystal. Hereby, the concentration of an impurity species in the crystals c_{crys} can be described by the following equation [115]:

$$c_{crys} = c_{melt}s_{eff}(1-g)^{(s_{eff}-1)} \tag{3.14}$$

Here, c_{melt} is the initial impurity concentration in the melt and g represents the fraction of solidified melt. The ratio c_{crys}/c_{melt} as a function of g can be seen in Fig. 3.22. It shows that the impurity gradient in the crystal is larger for smaller values of s_{eff}.
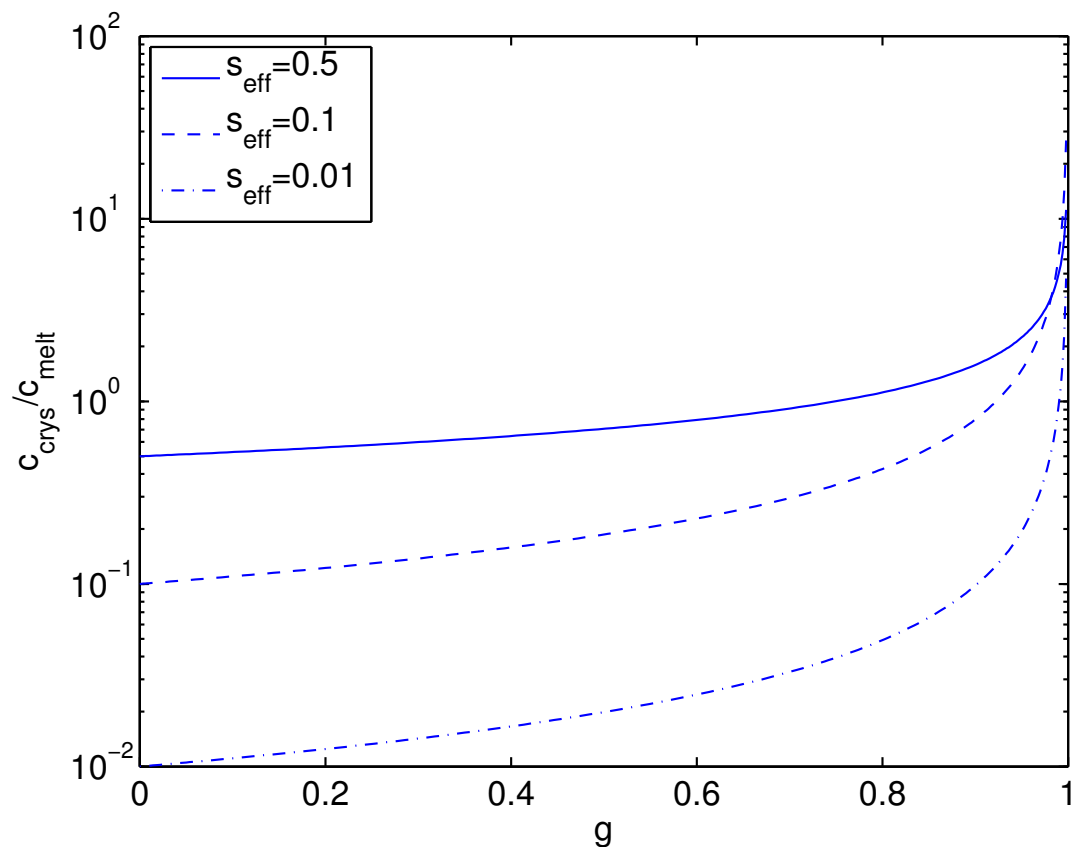
Fig. 3.22: Ratio of the impurity concentration in the crystal c_{crys} to the initial impurity concentration in the melt c_{melt} in dependence of the fraction g of solidified melt. The impurity gradient in the crystal is larger for smaller values of s_{eff}.

Usually, only $\sim$50% of the melt is extracted in each growth. The residual melt is then reused together with new $CaWO_4$ powder to refill the crucible to the same charge.[7] In this case also the concentration of impurities with $s_{eff}<1$ will increase after every growth as illustrated in Fig. 3.23. The plot shows the average impurity concentration in the crystal in dependence on the growth number for different values of the segregation coefficient s. Here s is defined as the ratio between the average impurity concentration in the crystal and the melt. As can be seen the relative increase in impurity concentration after each growth is larger for smaller segregation coefficients.

---

[7]The crucible always has to be refilled to the same charge so that the seed crystal can reach the melt. In addition, the crystal grower can only visually inspect the seeding process if the level of the melt has a certain height.
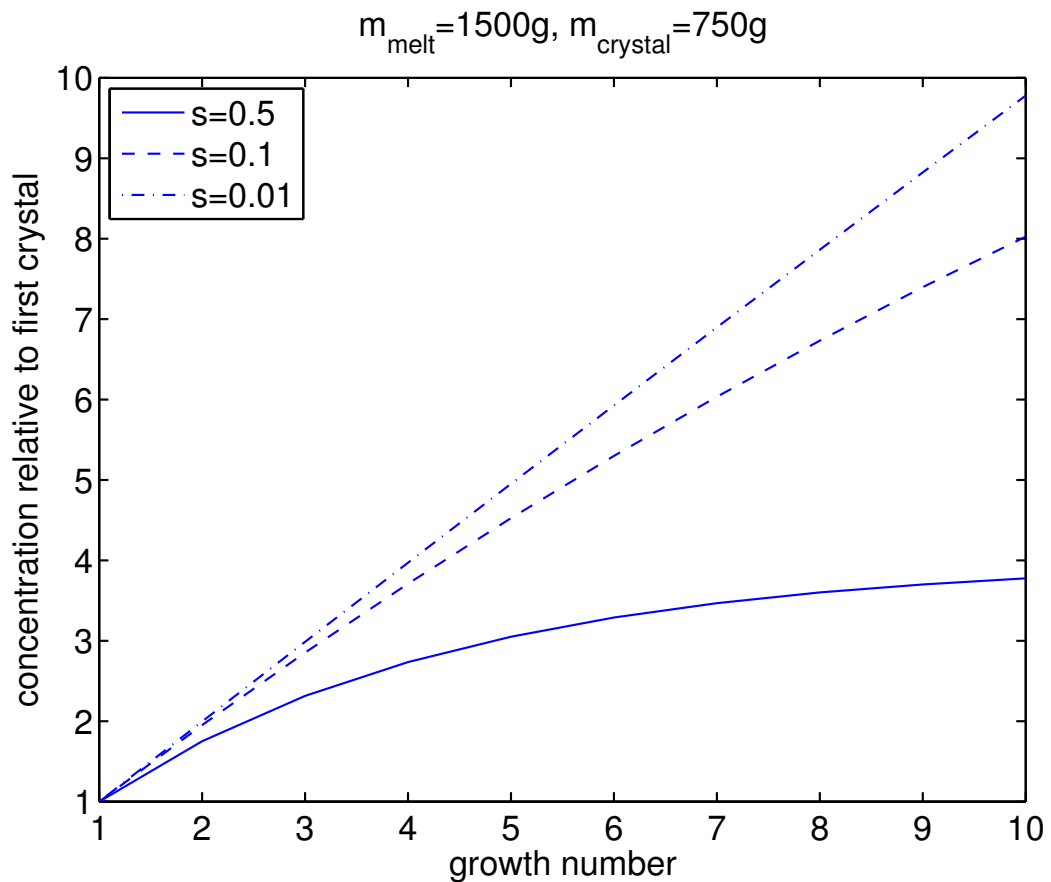
Fig. 3.23: Concentration of impurities in dependence of the growth number under the assumption that 50% of the residual melt is reused after each growth. The relative increase of impurities becomes larger for smaller segregation coefficients s.

Results of ICP-MS Analysis

The purity of the crystals grown at TUM was investigated with ICP-MS analysis at the chemistry lab of the LNGS. The crystals were dissolved in 3 ml of ultra-pure HF. Because $CaWO_4$ is rather resistant to acids the resulting solution was not clear but a powder suspension was present. This suspension was mixed and diluted for the ICP-MS analysis. A multi-element analysis was performed where the instrument was calibrated using a reference standard solution containing four elements over a wide mass range (Li, Y, Ce, Tl). The analysis was performed for the crystals TUM-20, TUM-52 and TUM-54. The crystal TUM-20 was produced from the raw materials by Alfa Aesar while TUM-52 and TUM-54 were produced from powders by MV Labs. TUM-20 and TUM-54 were both the first successful growths after having cleaned the crucible while the crystal TUM-52

was grown as the 5th crystal from the same melt (compare Tab. 2.3). The latter crystal showed a pink coloration and inclusion which first appeared after having increased the oxygen content in the growth atmosphere from 1% to 3% (see Fig. 2.8(a)). The analyzed crystal samples were small pieces ($\sim$1-2 g) that were cut directly below the seed crystal. Tab. 3.9 summarizes the results of the impurity analysis. The crystal TUM-52 shows a smaller concentration for nearly all impurities in comparison to TUM-54. This is opposite to our expectations since TUM-54 was the first growth from a fresh melt while for TUM-52 the melt was reused several times. Although care was taken that the samples do not get mixed up it can not be excluded with absolute certainty. Another but less likely explanation would be a segregation coefficient >1 for all impurities. The largest impurity found in the crystals is due to Mo which is a known contaminant in the WO_3 powders due to its chemical similarity to W. Other impurities are Sr and Mg which originate from the $CaCO_3$ powder since they are in the same chemical group as Ca. It can be seen that the Sr concentration is about a factor of 3 lower in the crystals produced from the powder by MV Labs which was (among other reasons) selected due to the low Sr content. The Sr concentration determined for the $CaCO_3$ powder (0.8ppm) implies a segregation coefficient of $\sim$1[8] which is consistent with the findings in Ref. [114]. A small concentration of Rh from the crucible is also present in all crystals. The values, however, argue against the assumption that Rh is responsible for the pink coloration of the crystal TUM-52 (see Sec. 2) as it shows the smallest Rh concentration of the three crystals. Finally, all crystals show a contamination with U in the range of a few ppb. This concentration can not be explained by the U content of the $CaCO_3$ powder and requires some additional contamination of the WO_3 powder or in one of the production steps. As shown above a possible introduction of U could happen during synthesis of the $CaWO_4$ powder. In general, the contamination with U is confirmed by the radiopurity measurements in Sec. 3.3.4 and 3.4 which show that the activity of the crystals is dominated by ^{238}U and ^{234}U. Also the fact that the crystals from the powders by MV Labs show a U concentration which is a factor of $\sim$3-5 larger was observed in the activity measurements (see Sec. 3.4). However, the absolute values for the U concentration found in the ICP-MS analysis are about one order of magnitude higher than the typical values of the activity measurements. An explanation could be the systematic error related to the incomplete dissolution of the crystals. This is supported by the large spread of concentrations obtained by different dissolving procedures for $CaWO_4$ crystals in Ref. [82] (see also crystal "Elena" in Tab. 3.9). In addition, the U concentration could be overestimated due to an unidentified isobaric interference. Otherwise it would mean that the impurities are not uniformly distributed in the melt so that there is a higher concentration near the seed crystal.

Table 3.9 also shows the results of an ICP-MS analysis of the Russian crystal "Elena" taken from Ref. [82]. In addition, the results for a $CaWO_4$ crystal produced at the Scientific Research Company CARAT (Lviv, Ukraine) [114] are shown. It can be seen that the Russian crystal and also the CARAT crystal have a much larger concentration of impurities. Especially concentrations of the elements Sr and Ba which belong to the Ca

---

[8]This takes into account the mass fraction of $\sim$0.3 used for the synthesis of $CaWO_4$.

group are about one order of magnitude higher. This suggests that the lower transmittance and lower light yield of the TUM crystals (see Sec. 3.1.2, 3.2.2) are rather due to intrinsic defects than impurities. The measurements also confirm the contamination of the Russian crystals with the rare earth elements Gd, Er and Nd that was observed in the transmission measurements (see Sec. 3.1.2).

crystal		TUM-54	TUM-20	TUM-52	Elena [82]	Ref. [114]
element	**unit**					
Li	ppb	<3	<2	<2	11	-
B	ppb	<250	<250	<250	5200	-
Na	ppm	<5	<5	<5	16-170	-
Mg	ppb	319	333	222	1500	-
Al	ppb	<250	<200	<300	4600	-
K	ppm	<50	<30	<30	-	<3
Sc	ppb	<500	<200	<200	15	-
Ti	ppm	<2	<1	<1	0.1	-
Cr	ppb	<600	<250	<300	300	-
Mn	ppb	<100	<100	<100	150	-
Fe	ppm	<25	<25	<25	60	3.5
Ni	ppb	<500	<500	<500	435-5600	-
Cu	ppb	<100	<50	<50	62-2250	-
Zn	ppb	<500	<150	<200	600-5640	-
Ga	ppb	<5	<5	<5	62	-
As	ppb	<60	<50	<50	<28	-
Se	ppm	<50	<50	<50	0.1	-
Rb	ppb	<10	<5	<5	-	<5
Sr	ppb	286	714	200	2100-24480	2500
Y	ppb	17	171	<10	850-8510	-
Zr	ppb	<150	<100	<100	125-230	-
Mo	ppm	5.5	0.9	1.0	0.04-8.0	-
Ru	ppb	<15	<10	<10	-	-
Rh	ppb	33	19	9.5	-	-
Sb	ppb	<25	<10	<10	-	-
Te	ppb	<150	<100	<100	<56-520	-
Cs	ppb	<5	<2	<2	-	-
Ba	ppb	<25	<15	<15	2600-35350	250
La	ppb	<10	18	<10	44-50	-
Ce	ppb	<100	<50	<50	25-50	-
Pr	ppb	<5	<10	<10	1.3-10	-
Nd	ppb	<10	<10	20	780-1100	-
Sm	ppb	<30	<10	<10	<5.8-70	-
Eu	ppb	<5	<2	<2	<1.5-10	-
Gd	ppb	<1	<6	58	1000-5760	-
Er	ppb	<5	<5	<5	940-4170	-
Yb	ppb	<5	<5	<5	62-130	-
Hf	ppb	<50	<50	<50	<2.9	-
Tl	ppb	22	17	19	-	-
Pb	ppb	<15	19	<10	84	300
Bi	ppb	<5	<5	<5	8.2	-
Th	ppb	<70	<50	<50	-	<0.5
U	ppb	8	1.6	4	-	8

Tab. 3.9: Results of the ICP-MS analysis of different CaWO$_4$ crystals. Columns 3-5 show the concentrations of impurities for TUM-grown crystals measured at the chemistry lab of the LNGS. The concentrations refer to the solid samples and they are blank subtracted. The uncertainty is about 30% of the given values. The sixth column shows the analysis results for the Russian crystal "Elena" measured at LNGS and at Durham University (UK) [82]. The different values for the impurity concentrations were obtained by different dissolving procedures. The last column shows the concentrations of a crystal produced by SRC CARAT (Ukraine) that was measured at LNGS [114].

Results of γ-ray Spectrometry

Several of the crystals grown at TUM were screened with HPGe detectors at the low-background facility STELLA (SubTerranean Low Level Assay) [116] of the Gran Sasso Underground Laboratory (LNGS). These crystals were all produced from the raw materials provided by Alfa Aesar. For the screening measurements we used the upper part ("shoulder") that was cut from the raw ingot after annealing.

Tab. 3.10 shows the results for the activities of the TUM crystals denoted by their growth number (compare Tab. 2.4). The limit of $< 1.6\,\mathrm{mBq/kg}$ for the activity of ^{226}Ra in the $CaWO_4$ crystal TUM-20 which was grown from a fresh melt (see Tab. 2.3) in comparison to the much higher activity of $28 \pm 6\,\mathrm{mBq/kg}$ in the $CaWO_4$ powder (see Tab. 3.8) suggests that ^{226}Ra is rejected by the crystal during growth with an estimated segregation coefficienct $s_{Ra} < 0.12$ (90%CL). The segregation of radium has also been observed in Ref. [114] and can be explained by the larger ionic radius of Ra^{2+} which disfavors its accommodation at the site of the Ca^{2+} ion.

Only the crystals TUM-13 and TUM-16 that were produced with a high growth number and no intermittent cleaning of the crucible (see Tab. 2.3) do show a measurable contamination with ^{228}Th and ^{226}Ra. This can also be ascribed to the segregation of these nuclides during crystal growth. As was already shown, radium is rejected by the crystal and accumulated in the melt while a similar behavior is expected for thorium [114]. Therefore, the concentration of these impurities in the crystals will increase with increasing growth number if the residual melt is reused after each growth (see also Fig. 3.23). This becomes more obvious from Fig. 3.24 which shows the activity of ^{228}Th and ^{226}Ra of the crystals versus the growth number. It can be seen that the activity of both isotopes increases with increasing growth number until the crucible is cleaned.

In the case of ^{238}U no clear conclusions can be drawn from the measurements. A measurable contamination with ^{238}U was found in the crystals TUM-22 and TUM-16. However, within errors the values are compatible with the limits determined for the other crystals. Other measurements have shown that ^{238}U is rejected by the crystal with an estimated segregation coefficient of $s_U \approx 0.3$ [114]. As in the case of ^{228}Th and ^{226}Ra one would therefore expect a larger contamination with ^{238}U in the crystals TUM-13 and TUM-16 which is not observed.

The crystal TUM-13 shows a contamination of ^{40}K with a value of $32 \pm 9\,\mathrm{mBq/kg}$. As no such contamination was found for the crystal TUM-16 produced at a later growth it is unlikely that this nuclide was already present in the raw materials and is accumulated in the melt. An accidental contamination during or after production of the crystal might be an explanation.

A small contamination ($\sim 1\,\mathrm{mBq/kg}$) with ^{137}Cs can be found in all crystals. ^{137}Cs is an anthropogenic nuclide produced in nuclear fission that can be found in dust. It is possible that ^{137}Cs was already present in the raw materials which can not be excluded from the determined limits on the activities shown in Tab. 3.6 and Tab. 3.7. In this case the similar activities in the crystals with different growth numbers would point to a segregation coefficient with a value of ~ 1. On the other hand, as the crystal growth did not take place in a clean-room environment a contamination during the production

process is also conceivable.

For comparison Tab. 3.10 shows also the data of CaWO$_4$ crystals produced by SRC Carat (Lviv, Ukraine) from Refs. [114, 48]. For most isotopes of the U/Th chains these crystals show a similar contamination in comparison to those produced at TUM. However, CARAT crystals usually have a very high activity due to ^{210}Pb and ^{210}Po in the order of 100 mBq/kg [114, 48].

crystal	TUM-13	TUM-16	TUM-20	TUM-22	Ref. [114]	Ref. [48]
sample mass	155 g	191 g	214 g	310 g	-	-
isotope			**activity [mBq/kg]**			
^{228}Ra	< 2.7	< 3.4	< 1.4	< 0.96	< 6	0.7 ± 0.1
^{228}Th	3 ± 1	4 ± 1	< 1.8	< 1.2	< 7	0.6 ± 0.2
^{238}U	< 110	60 ± 30	< 47	40 ± 20	< 165	14.0 ± 0.5
^{226}Ra	7 ± 1	13 ± 1	< 1.6	< 3.4	4 ± 2	5.6 ± 0.5
^{235}U	< 3.7	< 3.2	< 2.9	< 1.1	-	1.6 ± 0.3
^{40}K	32 ± 9	< 14	< 8.7	< 13	< 36	< 12
^{137}Cs	0.9 ± 0.4	0.9 ± 0.4	1.6 ± 0.5	1.0 ± 0.4	-	< 0.8
^{60}Co	< 1.9	< 0.38	< 0.3	< 0.22	< 4	-

Tab. 3.10: Activities of radionuclides determined by ultra-low background γ-ray spectrometry for the crystals produced at the TUM. The measurements were performed with HPGe detectors at the LNGS. The crystals are named by their growth number that indicates the order in which they were produced. For comparison the data of crystals from Refs. [114, 48] are also shown. Upper limits from this work, Ref. [114] and Ref. [48] are given with 90%, 95% and 68% CL, respectively. All uncertainties are given at 1 sigma.
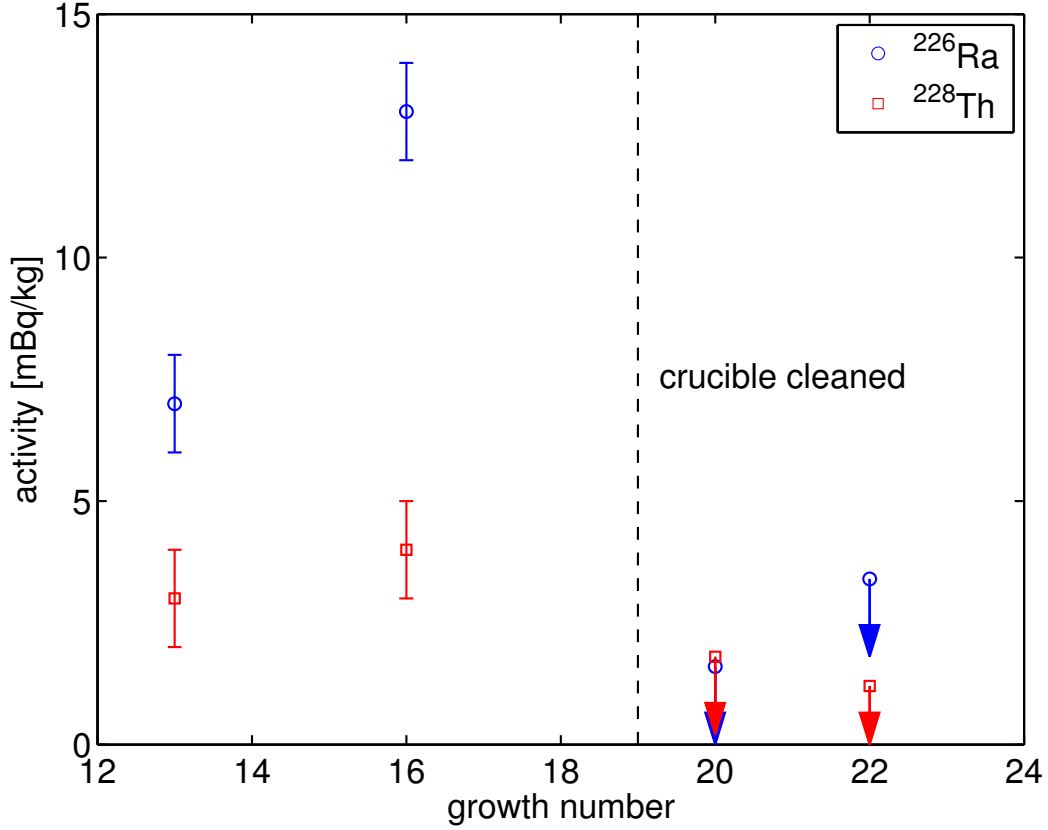
Fig. 3.24: The plot shows the activity of ^{228}Th and ^{226}Ra in the crystals listed in Tab. 3.10 versus the growth number. Upper limits are indicated by downward arrows. The activity increases with increasing growth number if the residual melt is reused and goes down after the crucible has been cleaned.

3.3.3   Residual Melt

An additional information about which radionuclides are rejected during crystal growth can be obtained from the residual melt. Therefore, we have screened the residual melt after growth nr. 56 with low-background γ-ray spectrometry. The raw material of the melt comes from the powders provided by MV Labs and was used to grow 3 crystals of ~740 g each. The screening measurements were performed with a HPGe detector in the Garching underground lab [117]. The results in Tab. 3.11 show that the activities of ^{228}Th, ^{228}Ra and ^{226}Ra are a factor of ~5-8 higher than in the CaWO$_4$ powders (see Tab. 3.8). This confirms that Ra and Th are rejected during crystal growth and accumulated in the melt.

sample	CaWO$_4$ melt
sample mass	672 g
isotope	**activity [mBq/kg]**
Ra-228	20±6
Th-228	23±9
U-238	< 337
Ra-226	42±4
K-40	< 71
Cs-137	< 3.5
Co-60	< 2.3

Tab. 3.11: Activities measured for a sample of residual CaWO$_4$ melt with low-background γ-ray spectrometry. The measurement was performed with a HPGe detector at the Garching underground lab. Limits are given at 90%CL, uncertainties at 1 sigma.

3.3.4 Low-Background Scintillation Spectroscopy

The following section describes a low-background screening setup which was built in the Garching Underground Laboratory (UGL) to investigate the radiopurity of $CaWO_4$ crystals. The general idea behind the setup is to use a crystal as scintillation detector for its intrinsic radioactive decays. Thus the crystal acts simultaneously as sample and detector. The advantage of this technique is that detection efficiencies of 100% are achieved for intrinsic alpha and beta decays. To reduce the background originating from external radioactivity and cosmic radiation the setup contains a passive shielding and an active muon veto. Furthermore, care was taken to use only radiopure materials in the construction. With the help of pulse shape discrimination it is possible to disentangle contaminations from alpha and beta emitters. In addition, a coincidence search can be used to tag decays from short-lived isotopes of the natural decay chains.

Setup

A schematic picture and photograph of the setup is shown in Figs. 3.25(a) and 3.25(b). For the detection of the scintillation light a 2" ETL9214 photomultiplier tube (PMT) is used. Photomultiplier tubes, especially the parts made from glass, are known to contain a rather large amount of radioactive isotopes. The window of the ETL9214 PMT is made from a low-background glass which contains 300ppm K, 250ppm Th and 100ppb U [118]. Nevertheless, the rate of gammas with energies $>100\,\text{keV}$ emitted by the PMT is $\sim 0.5\,\text{Hz}$ [119] which is quite high. Therefore, a 22cm long light guide is used to shield the $CaWO_4$ crystal from the PMT. The light guide is made from synthetic quartz (Suprasil B) which has a very high purity. The concentration of K, e.g., is typically <10ppb. For optical coupling of the light guide to the PMT silicon oil (DC 200) was used. In addition, the light guide was wrapped with a reflective foil (VM2002) to maximize the light collection. The shielding consists of high-purity copper (NO58) and low-activity lead ($<5\,\text{Bq/kg}$ ^{210}Pb). The minimum thickness of the shielding corresponds to $16\,\text{cm}$ of copper which shields 99.6% of 2.6 MeV gammas.[9] On the top, the shielding consists of 10 cm copper and 5 cm low-activity lead. The whole setup is surrounded by an air-tight PVC box which can be flushed with nitrogen to suppress background due to radon. On the top and on all sides (except bottom) plastic scintillator (BC408) panels which are read out by 2" PMTs (EMI9266) are used as muon veto.

---

[9]This corresponds to the most intense gamma line at high energies of the natural decay chains which is emitted in the decay of ^{208}Tl.
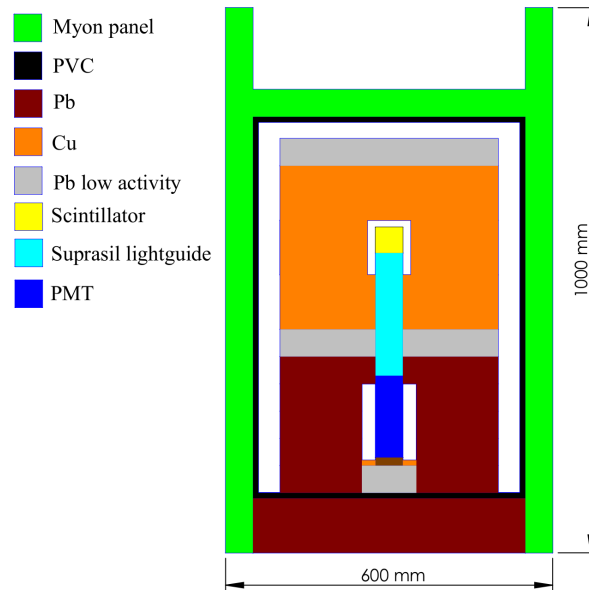
(a)

(b)

Fig. 3.25: Schematic picture (a) and photograph (b) of the setup for low-background scintillation spectroscopy. The scintillator is coupled to the photomultiplier via a quartz light guide. The setup is shielded against ambient radioactivity by lead and copper. Plastic scintillator panels serve as muon veto.

A scheme of the read-out electronics based on NIM modules is shown in Fig. 3.26. Its main purpose is to set up an anti-coincidence between the signal PMT (detecting the scintillation light of the $CaWO_4$ crystal) and the muon veto PMTs. The individual parts are explained in the following:

- Fast Amp: Fast Amplifier Phillips Scientific 776; the signal from the muon veto PMTs is amplified 10x

- TFA: Timing filter amplifier Ortec 474; the signal of the PMT detecting the scintillation light of the $CaWO_4$ crystal is amplified 20x and integrated over 100 ns

- FIFO: Linear Fan In Fan Out LeCroy 428F; the signal is split into two parts; one output is digitized by the ADC, the other one is used to generate a trigger

- Discr.: Discriminator LeCroy 623; a trigger signal is generated for the signal PMT and each of the muon veto panels

- OR: Logical FIFO LeCroy 429A; this module is used as an OR gate to pass on a trigger if any of the muon veto panels has triggered

- Gate: Gate generator Phillips Scientific 794; generates a gate with a length of 100 µs that is used as veto signal

- Delay: Delay generator Phillips Scientific 794; delays the trigger from the signal PMT so that it falls into the veto gate

- Coinc. Logic: Logic unit Caen N455; sets up an anti-coincidence between the delayed trigger of the signal PMT and the veto gate

- ADC: Acqiris DC282; digitizes the amplified PMT pulse with a sampling rate of 25 MHz and a vertical resolution of 10bit
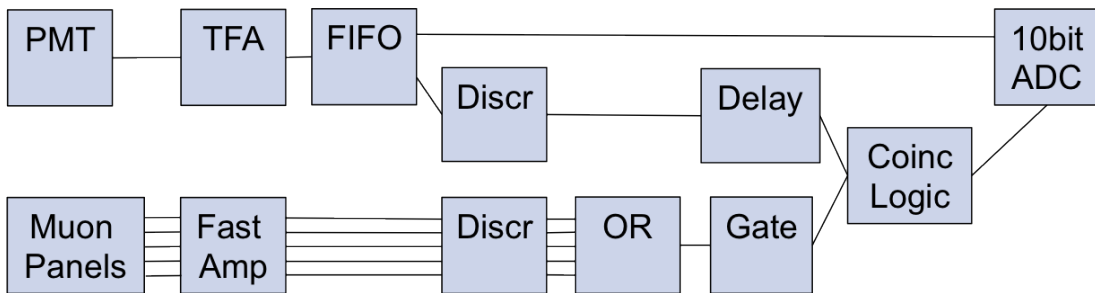
Fig. 3.26: Schematic picture of the read-out electronics. A hardware anti-coincidence is set up between the signal PMT and the PMTs of the muon veto panels. For details see text.

Background Spectra

To investigate the efficiency of the shielding and of the muon veto several background spectra were recorded (see Fig. 3.27). For these measurements the crystal "Karl II" was used which was optically coupled to the light guide with G608N index matching gel. The first spectrum was recorded with open shielding and without muon veto. Several broad lines, e.g., at 662 keV (^{137}Cs), 1461 keV (^{40}K) and 2615 keV (^{208}Tl) can be seen. The integral count rate between 100-2700 keV is ~11 Hz. The second spectrum was recorded without muon veto but with closed shielding which reduces the integral rate to ~0.8 Hz. The spectrum is featureless except for a narrow peak at ~145 keV which results from Cherenkov light produced by muons in the light guide. In the final spectrum recorded with closed shielding and muon veto a count rate of 0.06 Hz was achieved. This value is similar to the integral count rate of the low-background γ-ray spectrometry setup "GEM" which is 0.07 Hz in the same energy interval (100-2700 keV) [117]. It is obvious that the peak originating from Cherenkov events has almost completely vanished with the muon veto. The efficiency of the muon veto defined by the reduction of the number of Cherenkov events is $\gtrsim$96%.
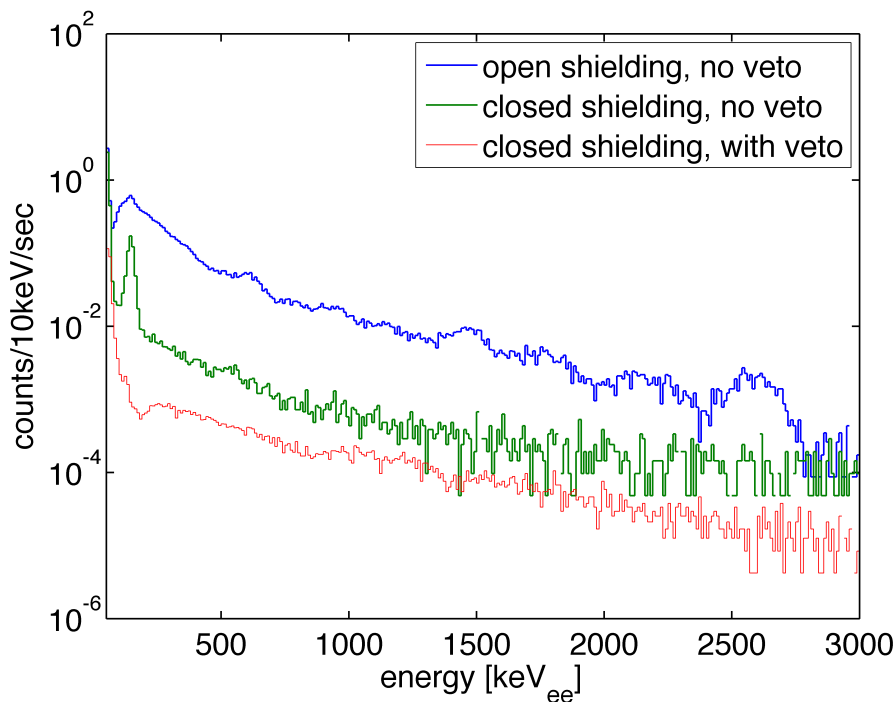
Fig. 3.27: Background spectra with different shielding and veto configurations. The peak at ~145 keV in the middle spectrum is due to Cherenkov events produced by muons in the light guide.

An interesting feature appears when the setup is flushed with nitrogen to suppress radon. As shown in Fig. 3.28 an additional peak appears in the spectrum next to the Cherenkov events. It was found that this peak arises from N_2 fluorescence which is heavily quenched in normal air but increases by a factor of ~ 14 in pure nitrogen [120]. Due to this additional background and because the radon activity was estimated to be negligible in the small volume inside the shielding it was decided to abandon the nitrogen flushing in further measurements.
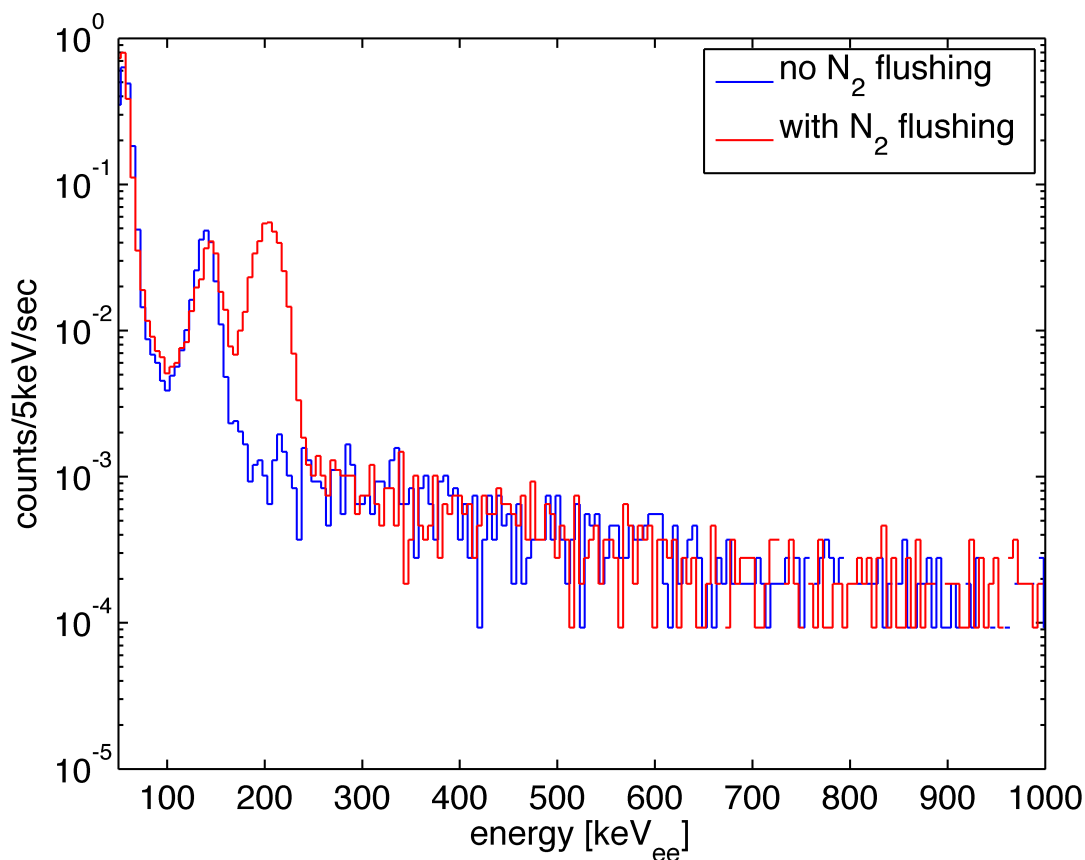
Fig. 3.28: Background spectra measured with and without N_2 flushing. The peak at ~ 145 keV in both spectra arises from Cherenkov events produced by muons in the light guide. With N_2 flushing an additional peak from N_2 fluorescence is visible.

Energy Calibration

An energy calibration of the detector was performed at the beginning and at the end of each measurement with gamma sources of the isotopes ^{241}Am (60 keV), ^{133}Ba (80 keV, 356 keV), ^{22}Na (511 keV, 1275 keV) and ^{228}Th (2615 keV). The energy of a scintillation

event was derived from the integral over the pulse. The pulse integral x versus energy E was fitted by a power law:

$$E = ax^b + c \qquad (3.15)$$

Figure 3.29 shows the energy calibration of the crystal "Karl II". One can see that the energy response is fairly linear. The energy resolution (FWHM) at $511\,\mathrm{keV}$ is 15%. The long term stability of the energy calibration over a measurement time of several weeks is in the range of $\sim$5% and therefore below the typical energy resolution [121]. The energy detected as scintillation light is only a fraction of the deposited energy. Furthermore, this fraction differs for alpha and gamma events. Therefore, we denote the energy in units of electron equivalent (subscript *ee*) which corresponds to the amount of scintillation light detected for gamma radiation of this energy.
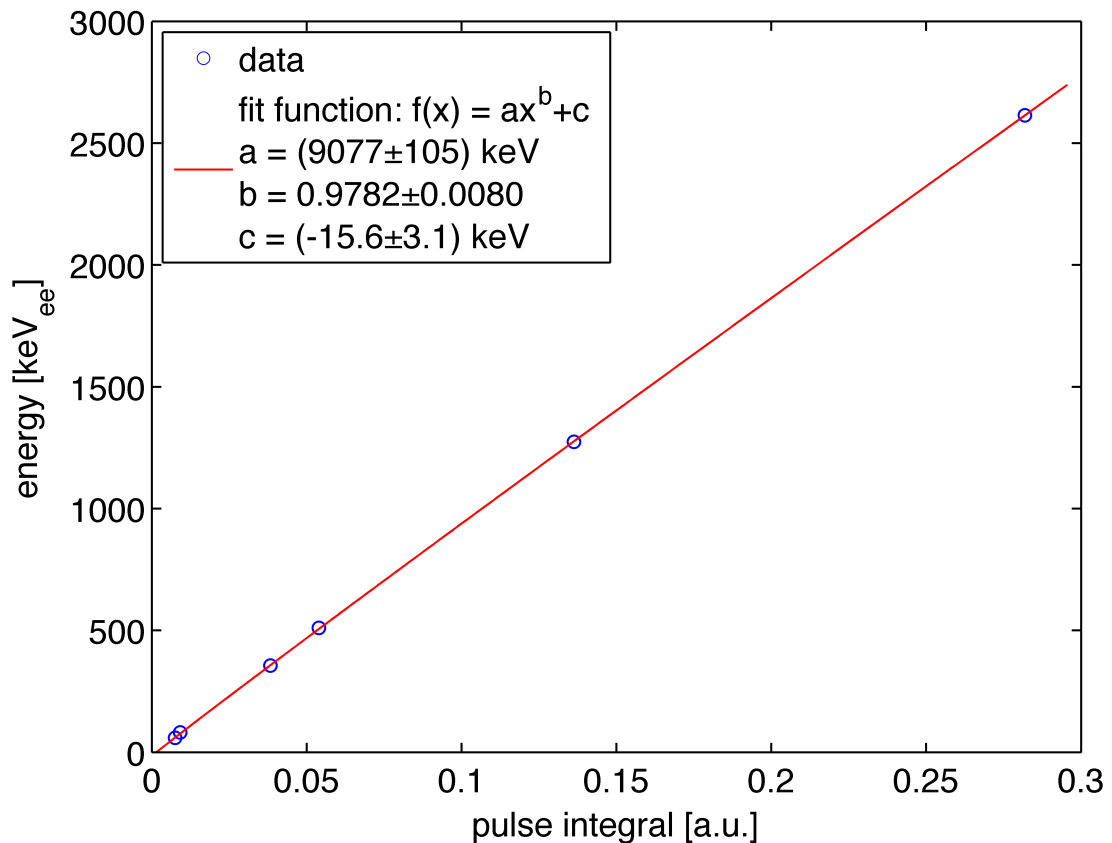
Fig. 3.29: Energy calibration for the crystal "Karl II" performed with different gamma sources. The red line shows a fit to the data with Eq. (3.15).

Pulse Shape Discrimination

It is known that scintillation events from alpha particles and gamma quanta have different timing characteristics [107, 100] (see also Sec. 3.2.3). This effect can be used to discriminate between alpha and gamma events [107]. In order to test the discrimination ability the crystal "Karl II" was irradiated with an ^{241}Am alpha source. The source emits alphas with an energy of 5.5 MeV which are, however, degraded due to a thin window protecting the source so that their exact energy is unknown. The scintillation pulses of the alpha source were averaged and compared to the average scintillation pulse of 1275 keV gammas from a ^{22}Na source which have approximately the same pulse integral. As can be seen in Fig. 3.30(a) the pulses from alpha events have a shorter decay time which is related to their higher ionization density [38]. To discriminate between alpha and gamma events different parameters were tested like the mean arrival time, the integral/height ratio, the ratio of the Root-Mean-Squared-Errors (RMSEs) of fits with average pulses and the "optimum" linear filter. The best results were obtained with the "optimum" linear filter adapted from Ref. [122]. For every pulse a shape indicator (SI) is calculated in the following way:

$$SI = \frac{\sum_i p(i) \cdot w(i)}{\sum_i p(i)} \tag{3.16}$$

Hereby p(i) is the ith sample of the pulse and w is a weight function defined by:

$$w = \frac{p_\alpha - p_\gamma}{p_\alpha + p_\gamma} \tag{3.17}$$

where p_α and p_γ are the average pulses from alpha and gamma events, respectively, normalized to the same integral. A histogram of the shape indicator obtained from the 1275 keV gamma and ^{241}Am alpha pulses is shown in Fig. 3.30(b). The small population on the right side of the shape indicator of alpha events comes from gamma background during the measurement with the alpha source. The discrimination power between alphas and gammas can be defined by:
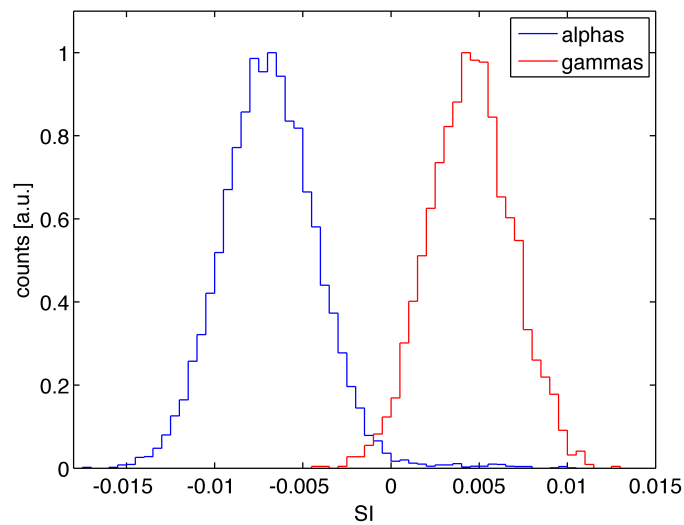
$$D = \frac{m_\alpha - m_\gamma}{\sqrt{\sigma_\alpha{}^2 + \sigma_\gamma{}^2}} \tag{3.18}$$

where m and σ are the mean and standard deviation, respectively, derived from a Gaussian fit to the shape indicator distribution. With this definition[10] we obtain a value of D=3.4.

---

[10]The discrimination power defined in this way is commonly used to compare different discrimination parameters but has no direct probabilistic meaning.
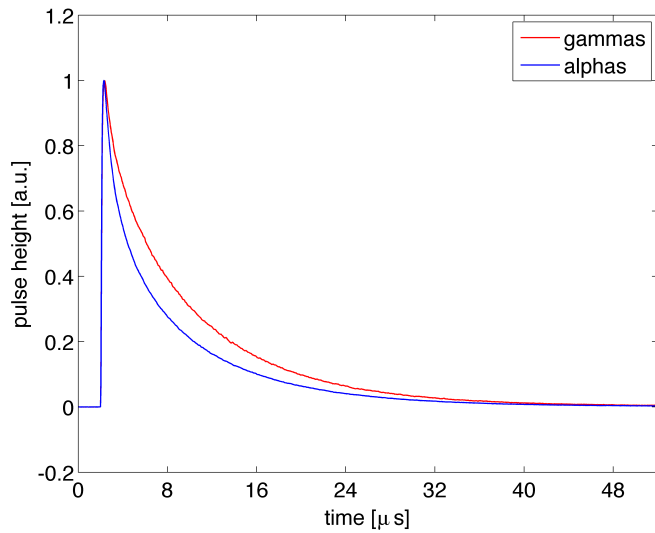
(a)

(b)

Fig. 3.30: (a): Averaged scintillation pulses for ^{241}Am alpha events ($\sim$5.5 MeV) and gamma events from a ^{22}Na source (1275 keV). (b): Histogram of the shape indicator (SI) defined by Eq. 3.16 for alpha and gamma events from the calibration sources.

It has to be noted that the discrimination ability between alphas and gammas decreases with decreasing energy of the pulses. However, most of the alpha events appear

117

at high energies $\gtrsim 800\,\mathrm{keV}_{ee}$ where the discrimination works efficiently enough. Figure 3.31 shows a 2D-histogram of the energy versus the shape indicator (SI) from a background measurement with full shielding and muon veto. In the plot different populations originating from alpha and gamma events can be distinguished. Besides that Cherenkov events are well separated from scintillation pulses due to their very short pulse length (see Fig. 3.32). In addition, we found the presence of "mixed" pulses from the simultaneous detection of Cherenkov and scintillation light (see Fig. 3.32(c)). These events form a band which can leak down to the region of alpha events. However, their contribution to the total number of alpha events was estimated to be $\lesssim 1\%$ [121].
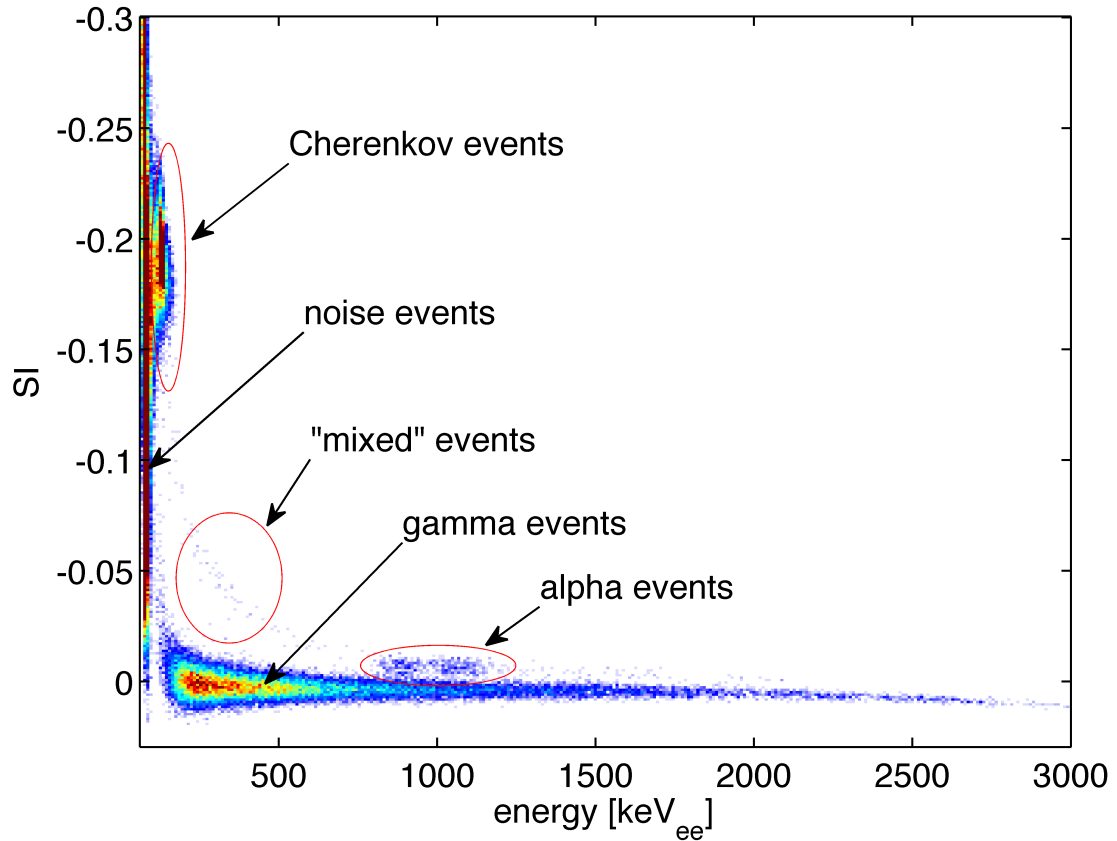
Fig. 3.31: The plot shows a 2D-histogram of energy versus shape indicator (SI) in a recorded background spectrum. Different populations from alpha, gamma, Cherenkov and "mixed" events can be distinguished. For details see text.
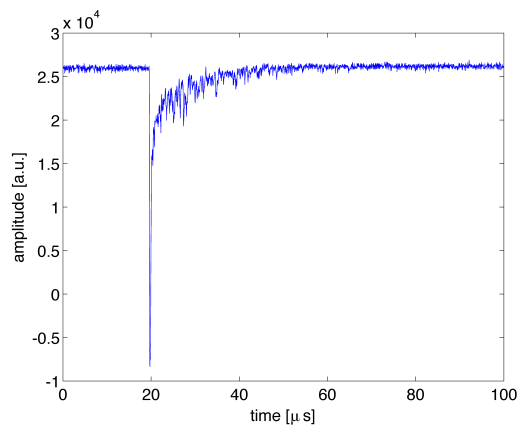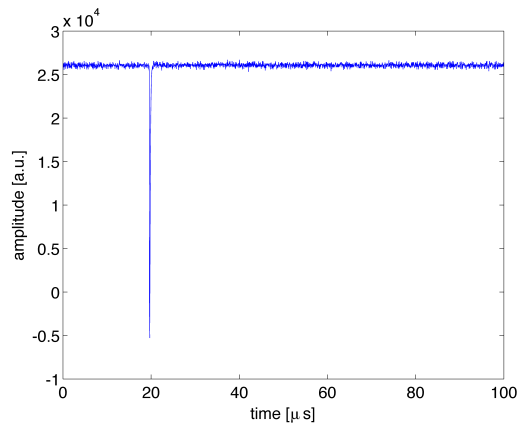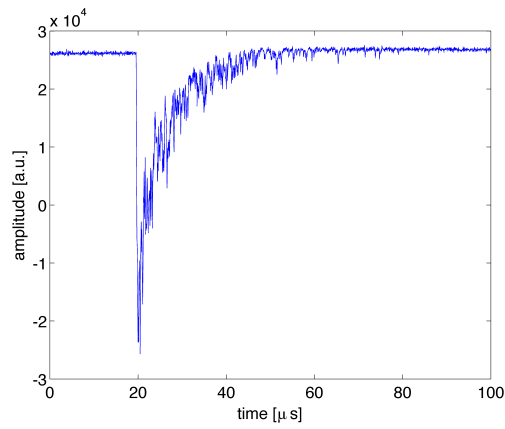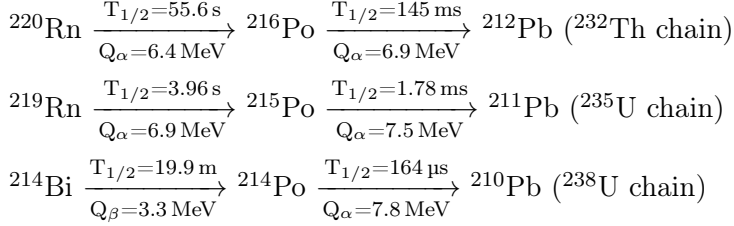
Fig. 3.32: Typical pulses from scintillation events (a), Cherenkov events (b), and "mixed" events (c) where Cherenkov and scintillation light are detected simultaneously.

119

Coincidence Search

To identify the decays from short-lived isotopes and their mother isotopes in the natural decay chains it is possible to search for coincidences. This technique was also applied to $CaWO_4$ crystal scintillators in Ref. [123]. The coincidences that can be searched for are:

$$^{220}\mathrm{Rn} \xrightarrow[\mathrm{Q}_\alpha = 6.4\,\mathrm{MeV}]{\mathrm{T}_{1/2} = 55.6\,\mathrm{s}} {}^{216}\mathrm{Po} \xrightarrow[\mathrm{Q}_\alpha = 6.9\,\mathrm{MeV}]{\mathrm{T}_{1/2} = 145\,\mathrm{ms}} {}^{212}\mathrm{Pb} \; (^{232}\mathrm{Th\ chain})$$

$$^{219}\mathrm{Rn} \xrightarrow[\mathrm{Q}_\alpha = 6.9\,\mathrm{MeV}]{\mathrm{T}_{1/2} = 3.96\,\mathrm{s}} {}^{215}\mathrm{Po} \xrightarrow[\mathrm{Q}_\alpha = 7.5\,\mathrm{MeV}]{\mathrm{T}_{1/2} = 1.78\,\mathrm{ms}} {}^{211}\mathrm{Pb} \; (^{235}\mathrm{U\ chain})$$

$$^{214}\mathrm{Bi} \xrightarrow[\mathrm{Q}_\beta = 3.3\,\mathrm{MeV}]{\mathrm{T}_{1/2} = 19.9\,\mathrm{m}} {}^{214}\mathrm{Po} \xrightarrow[\mathrm{Q}_\alpha = 7.8\,\mathrm{MeV}]{\mathrm{T}_{1/2} = 164\,\mathrm{\mu s}} {}^{210}\mathrm{Pb} \; (^{238}\mathrm{U\ chain})$$

In the coincidence search all pairs of events are tagged that fall into a certain range regarding their energy, time difference and shape indicator (see Tab. 3.12). For the α-α coincidences ($^{220}\mathrm{Rn} \longrightarrow {}^{216}\mathrm{Po}$ and $^{219}\mathrm{Rn} \longrightarrow {}^{215}\mathrm{Po}$) the requirements for the energy and shape indicator are the same for the first and the second event. Both intervals were chosen conservatively so that they cover all alpha events. For the β-α coincidence of $^{214}\mathrm{Bi} \longrightarrow {}^{214}\mathrm{Po}$ the parameters are different for the first and the second event. In particular, only a threshold of 100 keV is required for the first event. In addition, no requirement is made for the shape indicator of the first event since for low-energy pulses the shape indicator might be misidentified.

The time window was chosen to minimize the interference with the other coincidences. Nevertheless, e.g., the search for the $^{214}\mathrm{Bi} \longrightarrow {}^{214}\mathrm{Po}$ coincidence also tags the $^{219}\mathrm{Rn} \longrightarrow {}^{215}\mathrm{Po}$ coincidence with an efficiency of 0.136. Therefore, the activities have to be corrected for this effect. As $^{214}\mathrm{Po}$ has the shortest half-life of the three coincidences the lower limit of the time window should be as small as possible. The used value of 106.5 µs is determined by the length of the acquisition window (100 µs) and the dead time of the data acquisition (6.5 µs). The latter was determined by simulating scintillation events with a known time difference using a pulse generator [121]. To obtain the number of accidental coincidences the coincidence window was simply shifted by 10 s where no real coincidences are expected.

Using the half-lifes of $^{216}\mathrm{Po}$, $^{215}\mathrm{Po}$ and $^{214}\mathrm{Po}$ efficiencies of 0.715, 0.803 and 0.517, respectively, are obtained by integrating over the corresponding time window. For the $^{214}\mathrm{Bi} \longrightarrow {}^{214}\mathrm{Po}$ coincidence an additional factor has to be taken into account due to the energy threshold for the beta decay. This efficiency was determined to be 0.956 from a simulation of the spectrum of the $^{214}\mathrm{Bi}$ decay using Geant4 [121].

coincidence	energy [keV]	time difference	shape indicator	efficiency
^{220}Rn$\longrightarrow^{216}$Po	1200-2400	10-300 ms	-0.02-0.003	0.715
^{219}Rn$\longrightarrow^{215}$Po	1400-2600	0.5-10 ms	-0.02-0.003	0.803
^{214}Bi$\longrightarrow^{214}$Po	>100 1400-2600	106.5-500 µs	- -0.02-0.003	0.494

Tab. 3.12: Parameters used in the search for coincidences of short-lived isotopes of the natural decay chains. All events are tagged that fall within a certain range regarding their energy, time difference and shape indicator.

Results

The setup was used to determine the intrinsic contaminations of the crystal "Karl II". The first 851 h of the measurement were recorded with incomplete muon veto because one panel was still missing. Another 208 h of measurement time were recorded with full muon veto. For the live-time calculation the dead time from the muon veto, read out electronics and data quality cuts was taken into account [121]. The total dead time amounts to less than 5%.

For the determination of alpha activities only the measurement with full muon veto was used as otherwise the leakage from "mixed" events as described above can probably not be neglected anymore. To determine the total alpha activity a histogram of the shape indicator for all events in the energy range 700-2500 keV$_{ee}$ was plotted. This histogram was fitted by a sum of two Gaussians (see Fig. 3.33) and the area of the Gaussian that corresponds to the alpha events was used to calculate the activity. The total alpha activity in the energy range 700-2500 keV$_{ee}$ determined with this method is 7.03±0.58 mBq/kg. This value is slightly higher than the activity of 5.16±0.52 mBq/kg determined for the crystal by a low-temperature detector measurement (see Sec. 3.4). The difference could be explained by additional systematic errors like a non-Gaussian distribution of the shape indicator. In addition, because of the limited time resolution ($\mathcal{O}(\text{ms})$) of low-temperature detectors some short-lived decays can not be identified which leads to an underestimation of the activity.
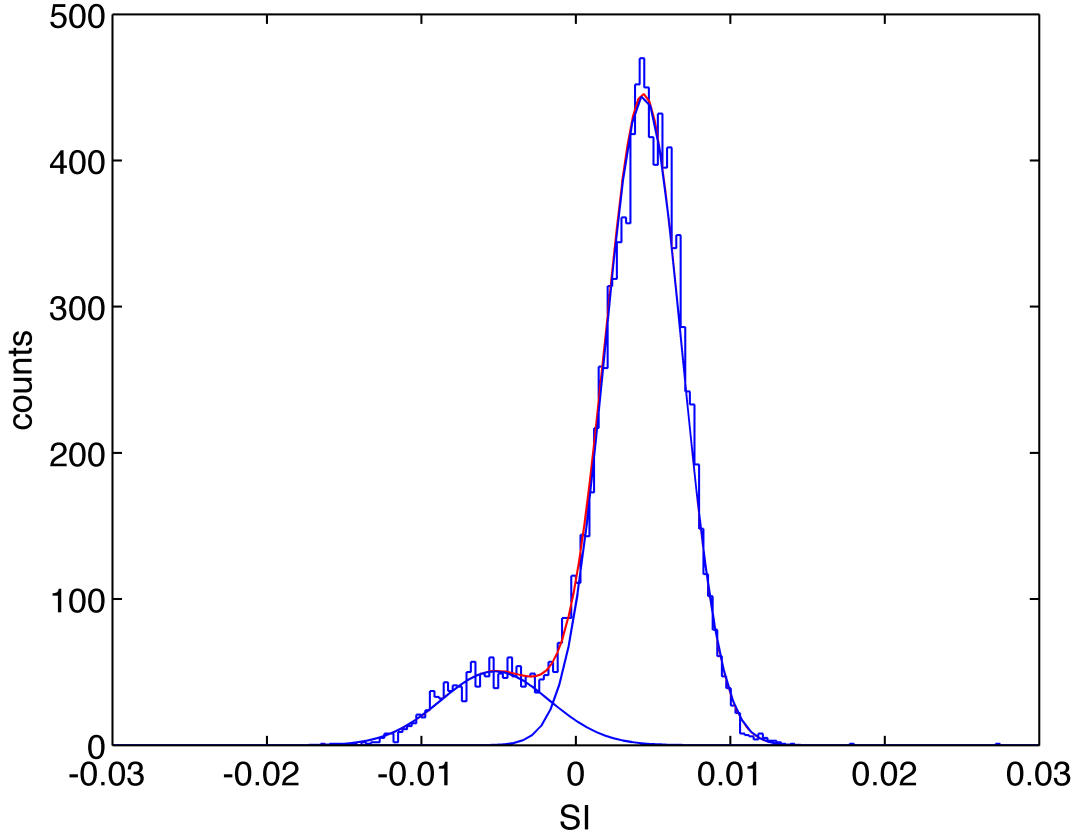
Fig. 3.33: Histogram of the shape indicator (SI) in the energy range 700-2500 keV$_{ee}$. The two Gaussian distributions arise from alpha (left distribution) and gamma events (right distribution), respectively. A fit with the sum of two Gauss functions was used to determine the total alpha activity.

To determine the spectrum of alpha events an energy dependent cut on the shape indicator value was performed. Hereby, the energy dependence of the shape indicator was directly derived from the data [121]. Figure 3.34 shows the obtained spectrum of alpha events. It can be seen that the activity is dominated by two peaks arising from ^{238}U with an activity of 2.0±0.3 mBq/kg and from the sum of ^{234}U, ^{230}Th and ^{226}Ra with an activity of 2.7±0.3 mBq/kg. It can not be excluded that there is also a contribution from the alpha peak of ^{232}Th to the ^{238}U peak. However, ^{232}Th is usually not far from equilibrium with ^{228}Th. The activity of the latter was determined to be 0.04±0.01 mBq/kg from the coincidence search (see Tab. 3.14), therefore the contribution to the ^{238}U peak is ≲2%. In addition, a peak from ^{235}U is expected between the two peaks. Its activity can be estimated from that of ^{238}U to be ∼0.09 mBq/kg and contributes, therefore, also only

~2% to the total activity of the two peaks.
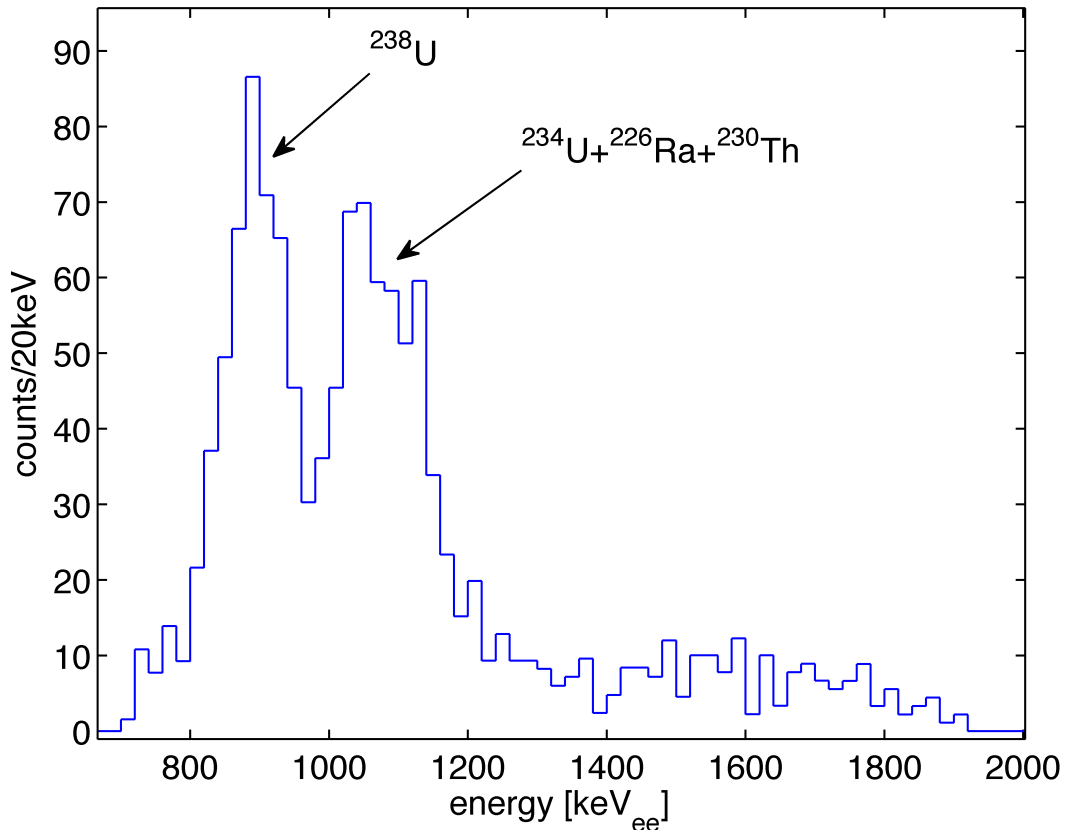
Fig. 3.34: Spectrum of alpha events obtained by pulse shape discrimination. It can be seen that the activity is dominated by two peaks arising from ^{238}U and from the sum of ^{234}U, ^{230}Th and ^{226}Ra.

The results of the coincidence search are shown in Tab. 3.13. The signal-to-background ratio is ~4 for the coincidence search of ^{220}Rn$\longrightarrow$^{216}Po with the longest time window. For the other two coincidences the number of accidentals is almost negligible. Figure 3.35(a) shows the spectra obtained from the ^{219}Rn$\longrightarrow$^{215}Po coincidence search. Despite the low statistics the two alpha peaks are clearly visible. In Fig. 3.35(b) we have plotted the time difference between the two events. The half-life of T$_{1/2}$=1.49±0.42 ms derived from an exponential fit to the data is in agreement with the literature value of T$_{1/2}$=1.78 ms for the half-life of ^{215}Po.

The activities derived from the coincidence search and the alpha spectrum are summarized in Tab. 3.14. Since ^{238}U and ^{234}U as well as ^{214}Bi/^{214}Po and ^{226}Ra have to be in radioactive equilibrium their activities can be used to determine the activity of ^{230}Th

from the combined peak in Fig. 3.34.

Another quantity which can be extracted from the data is the α/γ-ratio. We define this quantity as the ratio of the energy between γ and α events producing the same amount from scintillation light. This quantity is similar to the quenching factor as used in CRESST which is defined as the ratio of the light yield for α and γ events of the same energy (see Sec. 1.2.2). In fact, the α/γ-ratio and quenching factor are the same if either the scintillation signal from α particles or that from γ-quanta is linear in the corresponding energy range (0.9-7.7 MeV). The α/γ-ratio for all alpha peaks as a function of energy is depicted in Fig. 3.36. It is observed that the ratio increases with increasing energy which is consistent with the findings of Ref. [123].

coincidence	counts	accidentals	activity [µBq/kg]
^{220}Rn$\longrightarrow^{216}$Po	41	9	43±12
^{219}Rn$\longrightarrow^{215}$Po	97	1	138±14
^{214}Bi$\longrightarrow^{214}$Po	56	1	112±18

Tab. 3.13: Results from the coincidence search for short-lived isotopes in the natural decay chains. The number of accidental coincidences was determined by shifting the coincidence window by 10 s.
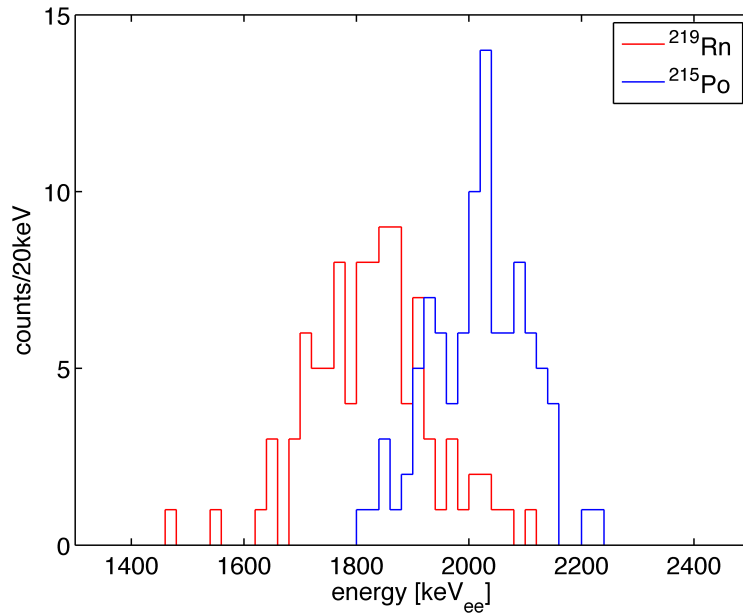
(a)
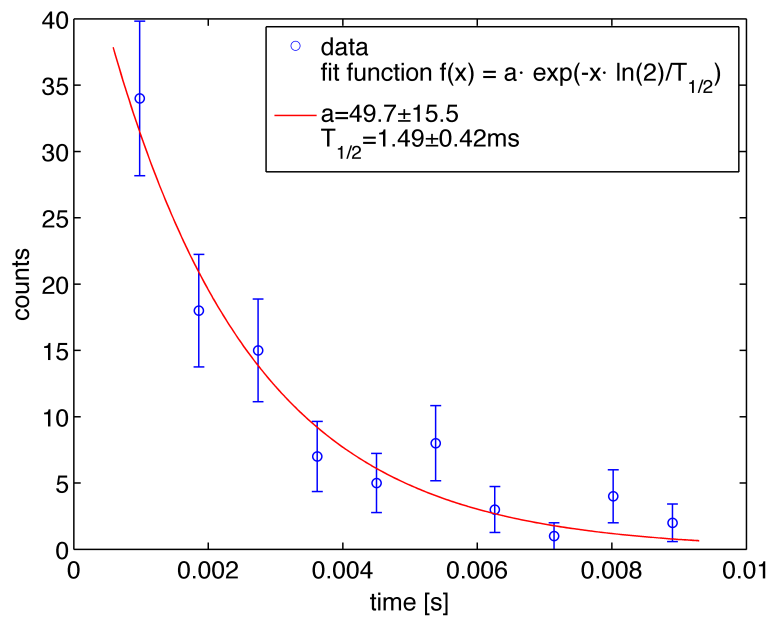
(b)

Fig. 3.35: Results from the ^{219}Rn⟶^{215}Po coincidence search. (a): Energy spectrum with the alpha peaks from ^{219}Rn and ^{215}Po. (b): Time difference between the two events. The exponential fit is in agreement with the literature value of $T_{1/2}$=1.78 ms for the half-life of ^{215}Po.

125

isotope	activity [mBq/kg]
^{238}U	2.01±0.25
^{230}Th	0.59±0.39
^{226}Ra	0.11±0.02
^{227}Ac	0.14±0.01
^{228}Th	0.04±0.01
total α-activity (700-2500 keV$_{ee}$)	7.03±0.58

Tab. 3.14: Final results of the activities determined for the crystal "Karl II" by low-background scintillation spectroscopy. Shown are the activities of long-lived isotopes in the natural decay chains as well as the total alpha activity.
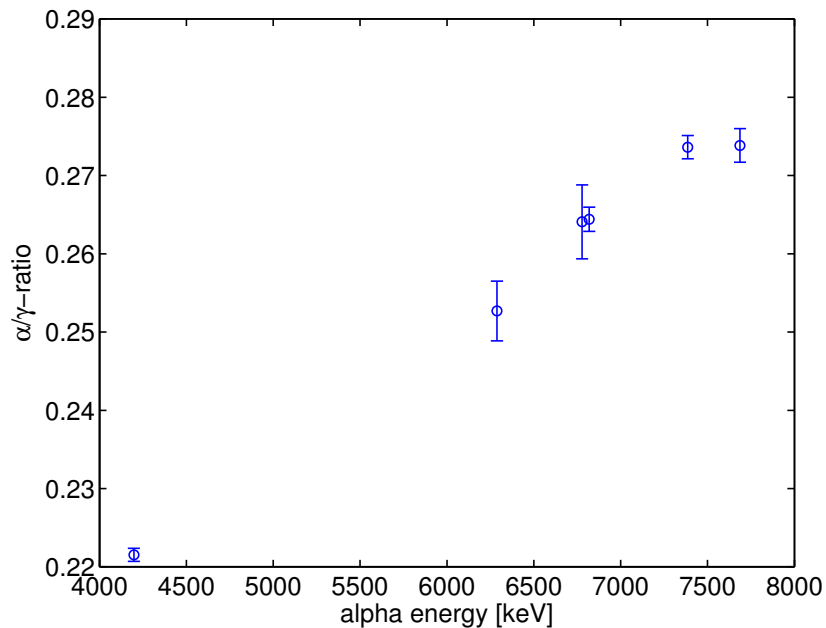
Fig. 3.36: α/γ-ratio for different alpha energies. An increase of the ratio with increasing energy is observed.

3.4 Low-Temperature Detectors

Several of the crystals produced at TUM were operated as low-temperature detectors. The crystal TUM-27 ("Rudolf VI"), TUM-40 ("Wilhelm") and TUM-49 ("Karl II") were used for measurements at the CRESST test cryostat at the LNGS to determine their light yield at mK temperatures and their radiopurity. Because of the promising results especially concerning their good radiopurity the crystals TUM-29 ("Bernhard I"), TUM-38 (Philipp II"), TUM-40 ("Wilhelm") and TUM-45 ("Ludwig W.") have been installed as Dark Matter detectors in run33 of the CRESST-II experiment. In this section we will describe the different detector designs that were used and the performance of the detectors.

3.4.1 Detector Fabrication

As explained in Sec. 1.2 a crystal operated as low-temperature detector measures the temperature rise (phonon signal) from a particle interaction. In CRESST-II this phonon signal is read out by a tungsten transition edge sensor (W-TES). The W-TESs used for the measurements were fabricated at the Max Planck Institut für Physik (MPI) in Munich. In the so called composite detector design the TES is not directly deposited on the absorber crystal but onto small $CaWO_4$ carrier substrates by sputtering and evaporation processes and photolithography. The carrier substrates with the TES are then glued onto the larger absorber crystal using an epoxy resin. For the evaporation process it is necessary to heat up the crystal under vacuum which can partially reverse the effects of oxygen annealing (see Sec. 2.2). Therefore, the composite detector design prevents a degradation of the light yield of the absorber crystal.

A photograph of a W-TES is shown in Fig. 3.37. It consists of a 200 nm thin W film with an area of $6\times8\,mm^2$. A gold film across the W structure is used as thermal contact and to inject heater pulses used for calibration and stabilization of the operating point. Electrical contacts are provided by aluminum pads. The connections are made by thin bond wires.
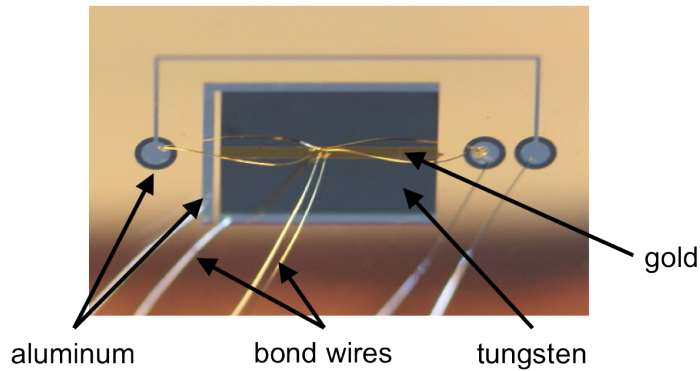
127

Fig. 3.37: Photograph of a tungsten transition edge sensor (W-TES) used to measure the phonon signal of the low-temperature detectors.

For the low-temperature detectors different designs were realized:

- standard design:
  For the measurements of the cylindrical crystals TUM-27 and TUM-49 at the CRESST test cryostat the standard detector module design was used (see Fig. 3.38). The size of the carrier with the W-TES that was glued onto the crystal was $20 \times 10 \times 2 \, \text{mm}^3$. The crystal was paired with a silicon-on-sapphire (SOS) light detector and mounted in a copper holder. The crystal surface facing the light detector had been roughened (see Sec. 2.4). The crystal is held by silver coated bronze clamps were used. Crystal and light detector are surrounded by a reflective and scintillating foil (3M radiant mirror film VM2002).
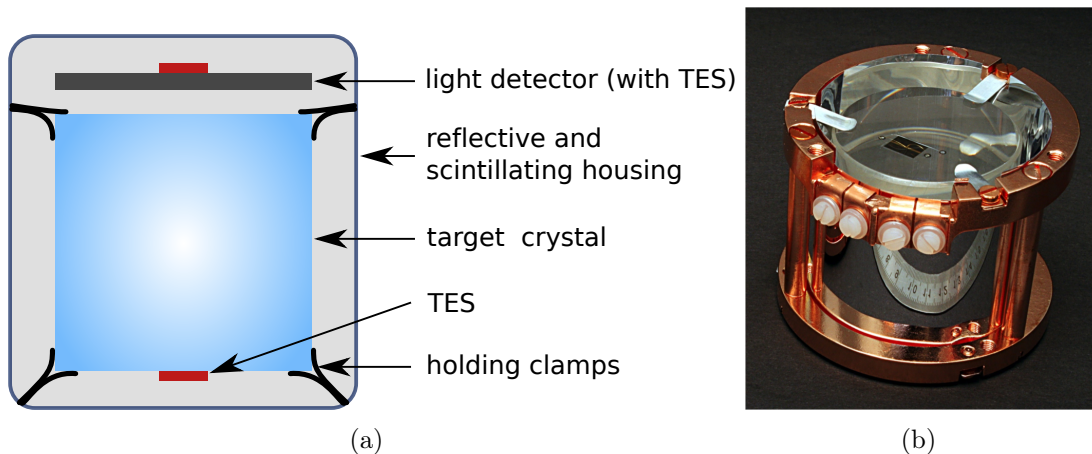
Fig. 3.38: Schematic picture (a) of the standard CRESST-II detector design. In (b) a photograph of the detector module without the light detector is shown.

- stick holder design:

  For the crystals TUM-40 and TUM-45 that were installed in CRESST-II a block-shaped geometry was chosen as suggested in Sec. 2.3. In addition, a special holder design was developed in Ref. [39] where the crystal is held by $CaWO_4$ sticks (see Fig. 3.39). This has the advantage that the crystal is only surrounded by scintillating materials which is crucial in order to reject the background from surface alpha decays. In this module five surfaces of the crystal had been roughened. Only the top surface where the carrier is glued and the spots where the sticks touch the crystal remain polished. Otherwise the module is similar to the standard design and only slight changes have been made to accommodate for the rectangular shape of the reflector foil and to hold the $CaWO_4$ sticks.

(a)   (b)
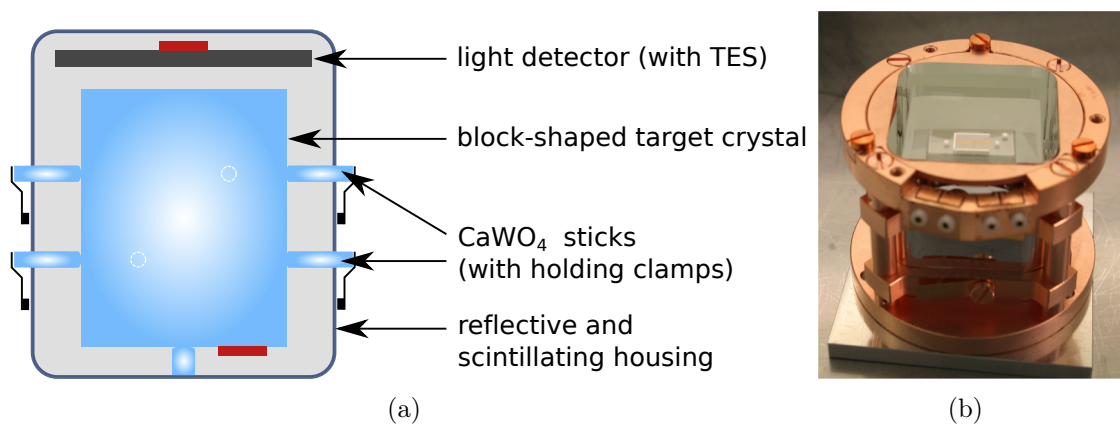
Fig. 3.39: Stick holder design used for the crystals TUM-40 and TUM-45 installed in run33 of CRESST-II. The block shaped crystal is held by $CaWO_4$ sticks which avoids non-scintillating surfaces inside the detector housing.

129

- K-14 type design:
  The cylindrical crystals TUM-29 and TUM-38 that were also installed in CRESST-
  II were equipped with a cylindrical carrier of 40 mm diameter and 7 mm thickness.
  In this design bronze clamps coated with scintillating parylene hold the crystal
  at the carrier substrate (see Fig. 3.40). It was shown that organic scintillators in
  contact with the crystal surface can lead to stress relaxation events [124]. However,
  as they will happen in the carrier crystal and not in the main absorber they can
  be identified by pulse shape discrimination. Here also the curved lateral surface of
  the crystal was roughened in addition to the surface facing the light detector. In
  all other regards the module design is again similar to the standard one.

(a)   (b)
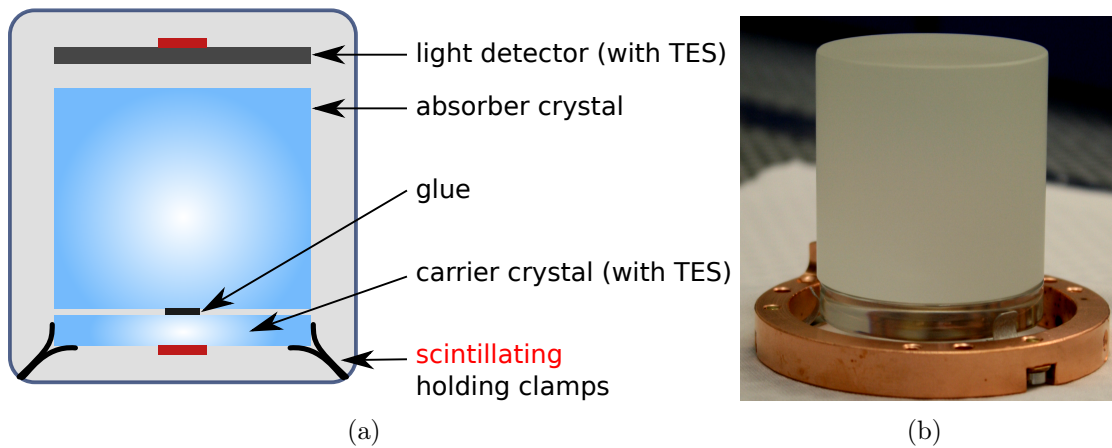
Fig. 3.40: K-14 type design: For the crystals TUM-29 and TUM-38 installed
in run33 of CRESST-II a detector design based on a large carrier crystal was
developed. Scintillating clamps are holding the crystal at the large carrier substrate
on the bottom.

A summary of all low-temperature detectors is given in Tab. 3.15.

crystal name	crystal geometry	module design	site of operation
TUM-27	cylinder, d=40 mm, h=40 mm	standard	CRESST test cryostat
TUM-29	cylinder, d=40 mm, h=40 mm	K-14 type	CRESST-II (run33)
TUM-38	cylinder, d=40 mm, h=40 mm	K-14 type	CRESST-II (run33)
TUM-40	square prism, s=32 mm, h=40 mm	stick holder	CRESST test cryostat, CRESST-II (run33)
TUM-45	square prism, s=32 mm, h=40 mm	stick holder	CRESST-II (run33)
TUM-49	cylinder, d=40 mm, h=40 mm	standard	CRESST test cryostat

Tab. 3.15: Low-temperature detectors made from TUM crystals. The table shows the crystal geometry, the module design and where it was operated.

3.4.2 Experimental Setups

Recently, a test setup for CRESST-II detectors was installed at the Gran Sasso underground lab (LNGS) [124]. In this setup a single detector module can be operated in a ^{3}He/^{4}He-dilution refrigerator (MINIKELVIN 400-TOF, Leiden Cryogenics). The readout electronics are similar to the CRESST setup. A shielding of 10 cm low-activity lead is used to reduce the background from ambient radioactivity. However, as there is no copper and polyethylen shielding and the dilution refrigerator itself is not shielded from the detectors the background rate is typically a factor of 100 higher than in CRESST. Three of the TUM crystals were operated as low-temperature detectors at the test cryostat (see Tab. 3.15) with a typical measurement time of 1-2 weeks. Energy calibrations were performed with a ^{57}Co gamma source (122 keV, 136 keV). The light detector was calibrated with a ^{55}Fe source. This allows to determine the light yield defined as the fraction of energy deposited in the CaWO$_4$ crystal which is detected by the light detector. As the extrinsic gamma background is rather high no information about the radiopurity

of the CaWO$_4$ crystals concerning gamma and beta emitters could be obtained. However, intrinsic alpha decays can be easily separated from electron/gamma events using the phonon-light technique due to their lower light yield (see Sec. 1.2.2). As CRESST detectors are optimized for low energies in the keV range a precise energy calibration for alphas in the MeV range is difficult. Furthermore, the resolution is in this energy range suffers from the saturation of the pulses. Therefore, with the limited statistic of the short measurement time only the total alpha activity could be obtained. Details of the alpha analysis can be found in Refs.[39, 93].

Four of the TUM crystals were installed in the current data taking campaign (run33) of the CRESST-II experiment (see Tab. 3.15) which started in July 2013. Here we present preliminary data from the first ∼20 kg days of net exposure. Unfortunately, the detector TUM-45 was not usable because of its poor energy resolution due to very small pulse heights. This is probably caused by the read-out electronics and not an effect of the crystal or detector design.

3.4.3   Results

Light Yield

The values for the light yield at low temperatures of several CaWO$_4$ detectors are summarized in Tab. 3.16. The light yield of the TUM-grown crystals ranges between ∼1.3-1.8% while that of the Russian crystals is between ∼1.5-2.4%. This confirms the observations made by the measurements at room temperature where the light yield of the Russian crystals can be up to ∼30% higher due to their higher transmittance. As for the Russian crystals only the bottom surface was roughened an even larger light yield can be expected by roughening also the side surfaces.

The values for the crystals "Rita", "Wibke" and "Maja" were determined from data of run32 with a slightly different method [125]. Therefore, an additional systematic error between the values can not be excluded.

crystal	roughened surfaces	light yield (%)
TUM-27	bottom+sides	1.31
TUM-29	bottom+sides	1.76
TUM-38	bottom+sides	1.57
TUM-40	bottom+sides	1.62
TUM-49	bottom	1.66
VK34	bottom	1.56
Lise	bottom	2.11
Rita	bottom	2.44
Wibke	bottom	1.48
Maja	bottom	1.70

Tab. 3.16: Light yield at low temperatures of several $CaWO_4$ detectors. The light yield is given as the fraction of the energy deposited in the $CaWO_4$ crystal that is detected by the light detector. The values for the crystals "Rita", "Wibke" and "Maja" were taken from Ref. [125].

Radiopurity

The total alpha activity of several crystals is shown in Tab. 3.17. The alpha activity of the TUM-grown crystals ranges between ∼1-5 mBq/kg [39, 126, 93]. This is within the range of the Russian and Ukrainian crystals with the best radiopurity like "Daisy" which shows a total alpha activity of 3.05±0.02 mBq/kg [93]. However, most crystals from Russia and Ukraine have alpha activities in the range of ∼15-35 mBq/kg [93] and their radiopurity is thus one order of magnitude worse.

crystal	total alpha activity [mBq/kg]	background rate (10-40 keV) [cpd/kg/keV]
TUM-27	1.23±0.06	-
TUM-29	-	3.4
TUM-38	-	3.1
TUM-40	3.07±0.11	3.5
TUM-49	5.16±0.52	-
VK31	-	30.8
Frederika	-	6.9
Daisy	3.05±0.02	6.4
Verena	14.44±0.05	-
Wibke	33.09±0.07	-
K07	23.93±0.06	-
Rita	14.41±0.04	-

Tab. 3.17: Radiopurity of several $CaWO_4$ detectors. The total alpha activity was obtained from measurements at the CRESST test cryostat [39, 126, 93] and from data of run32 [93]. The background count rate in the energy region of interest was calculated from preliminary data of run33.

The radiopurity of the detector TUM-40 was studied in detail using internal alpha lines [126]. The activities of all long-lived alpha emitters of the natural decay chains derived from 20.7 kg days of exposure are summarized in Tab. 3.18. It is obvious that the total activity is dominated by ^{238}U with a value of about 1 mBq/kg. This was also observed in the screening measurements using low-background scintillation spectroscopy (see Sec. 3.3.4). As it was shown in Sec. 3.3.1 the $CaCO_3$ powder used for crystal production shows a U concentration of 0.5ppb. This would correspond to a ^{238}U activity of 2.2 mBq/kg in the $CaWO_4$ powder and can therefore explain the activity in the crystal assuming some additional segregation during crystal growth. However, the measurements in Sec. 3.3.1 also suggest that an additional contamination occurs during the synthesis of the $CaWO_4$ powder. The clear identification of the origin of the U contamination will be important to further improve the radiopurity of the TUM grown crystals.
For comparison we have also shown the alpha activities derived from ∼90 kg days of run32 data for the Russian crystals "Rita" and "Daisy" [93]. The crystal "Rita" shows an at least 10 times higher activity for all isotopes except ^{238}U. "Daisy" is one of the radiopurest Russian crystals, however, for most isotopes its activity is still a factor of ∼3 higher than that of TUM-40.

crystal	TUM-40	Rita	Daisy
isotope	**activity [µBq/kg]**		
^{238}U	1010±20	41±2	42±2
^{230}Th	56±5	1422±13	90±3
^{226}Ra	43±10	948±11	82±4
^{210}Po	18±4	3420±21	144±4
^{235}U	40±4	-	-
^{231}Pa	23±4	222±5	22±24
^{227}Ac	105±4	1594±145	338±26
^{232}Th	9±2	284±6	49±3
^{228}Th	15±4	556±8	50±3

Tab. 3.18: Radioactive contamination obtained from internal alpha lines. The activities of the crystal TUM-40 were determined from 20.7 kg days of run33 data [126]. For "Rita" and "Daisy" an alpha analysis was done with 92.8 kg days and 90.1 kg days of data from run32 [93].

In Fig. 3.41(a) the background spectrum in the energy region of interest (ROI) of the detector TUM-40 is shown together with that of the Russian crystal VK31. It illustrates the superior radiopurity of the TUM-grown crystal. The background rate of the Russian crystal is dominated by ^{227}Ac which is a long-lived isotope in the ^{235}U chain. As depicted in Fig. 3.41(b) it can decay via β-decay (Q-value 44.8 keV) to excited states of ^{227}Th at 9.5 keV and 24.5 keV which leads to the structures indicated in Fig. 3.41(a). As shown in Tab. 3.17 the background rate of the TUM crystals in the ROI is about one order of magnitude lower than that of the Russian crystal VK31. In comparison to the Russian crystals "Daisy" and "Frederika" with the best radiopurity the background rate of the TUM crystals is still a factor of $\sim$2 lower. This is in agreement with the lower activity from isotopes that appear in the region of interest like ^{227}Ac in the TUM crystals (see Tab. 3.18).
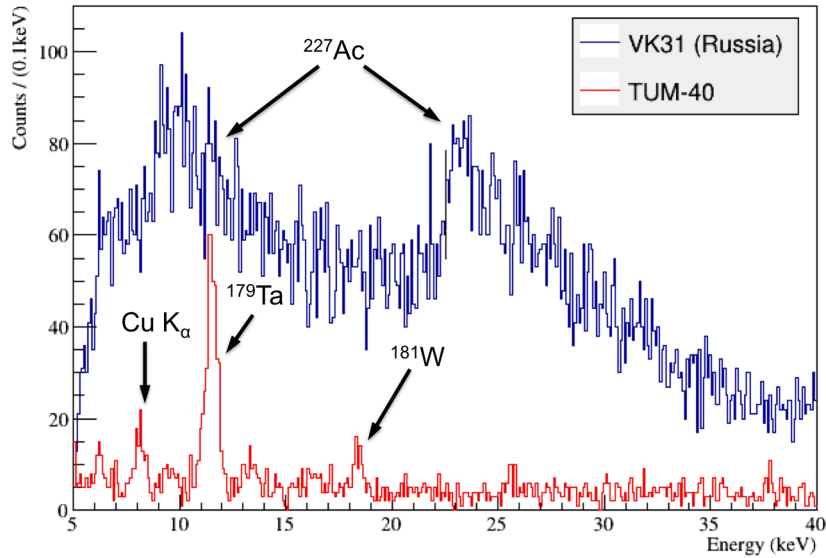
(a)
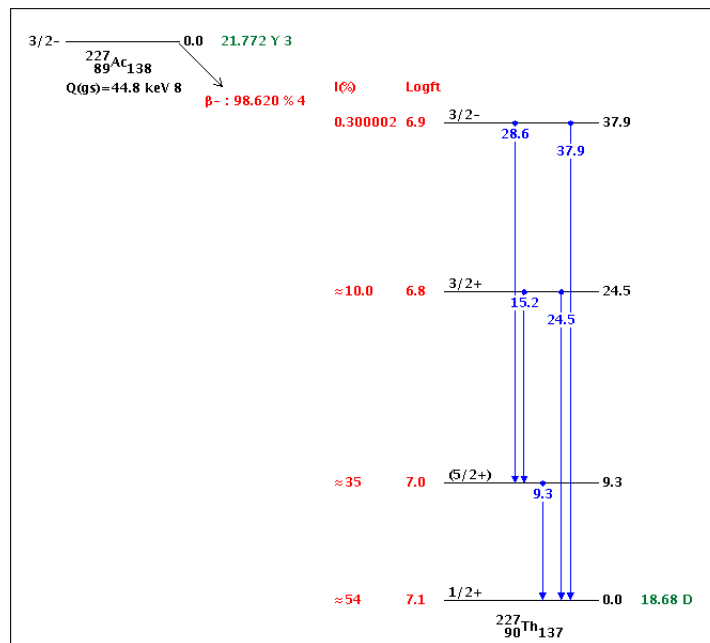
(b)

Fig. 3.41: (a): Background spectrum in the region of interest of the detector TUM-40 in comparison to the Russian crystal VK31. The Russian crystal shows a ~10 times higher background dominated by an internal ^{227}Ac contamination. (b): Decay scheme of the ^{227}Ac beta decay taken from Ref. [109].

Cosmogenic Activation

The combined spectrum of all three TUM crystals is depicted in Fig. 3.42. It shows some lines from external contaminations with ^{234}Th, ^{210}Pb and copper fluorescence as well as weak lines at 13.3 keV and 77 keV which could not yet be identified. The other peaks are internal contaminations and originate from the cosmogenic isotopes ^{179}Ta and ^{181}W. These nuclides were already observed in previous data and clearly identified by their half-lifes [111]. The isotope ^{179}Ta ($T_{1/2}$=1.82 y) can be produced by a (p,α) reaction on ^{182}W while ^{181}W ($T_{1/2}$=121 d) can originate from a (p,t) reaction on ^{183}W. Both decay via electron capture while ^{181}W does mainly decay to an excited state at 6.2 keV (see Fig. 3.43). The visible energy of the ^{179}Ta decay is the binding energy of the atomic shell of Hf which leads to lines at 65.4 keV (K-capture) and 11.3 keV (L-capture). For ^{181}W the detected energy is the sum of the energies of the atomic shell of Ta and the 6.2 keV gamma-ray leading to lines at 73.6 keV (K-capture) and 17.9 keV (L-capture).
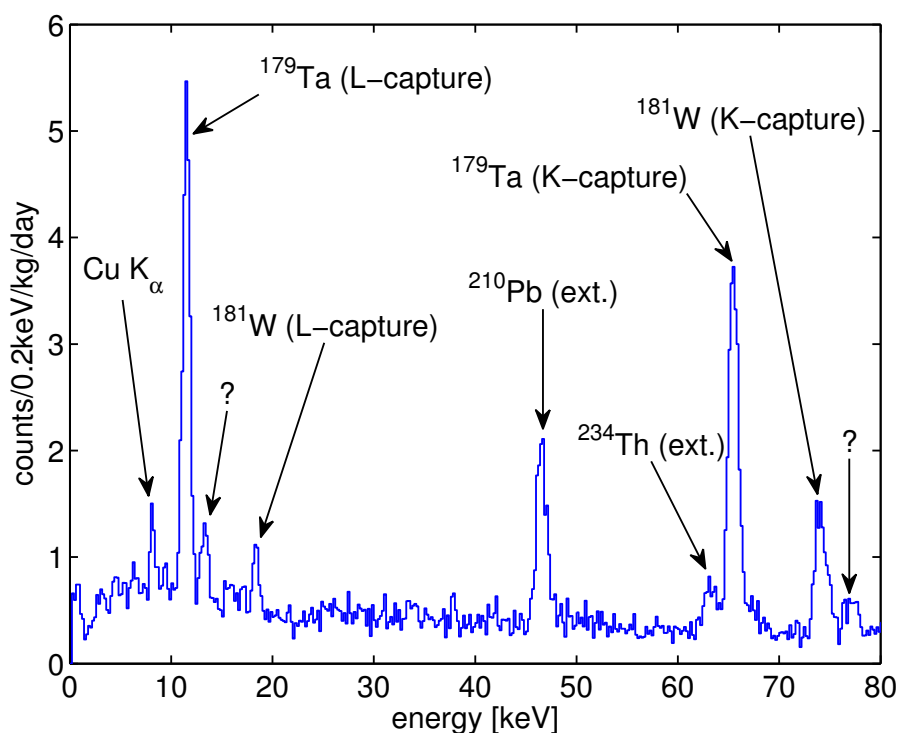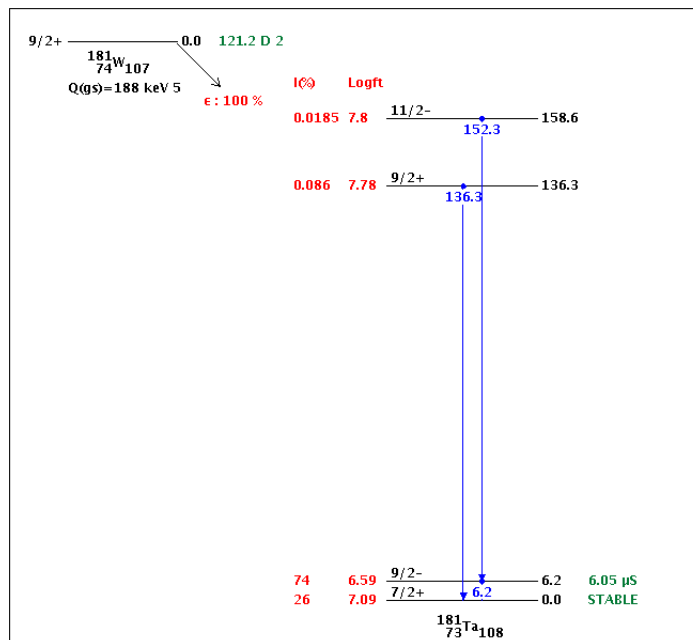

Fig. 3.42: Combined background spectrum of the detectors TUM-29, TUM-38 and TUM-40. The observed lines are due to the cosmogenic isotopes ^{179}Ta and ^{181}W, external contaminations from ^{210}Pb, ^{234}Th and copper fluorescence. In addition, yet unidentified lines at 13.3 keV and 77 keV are visible.
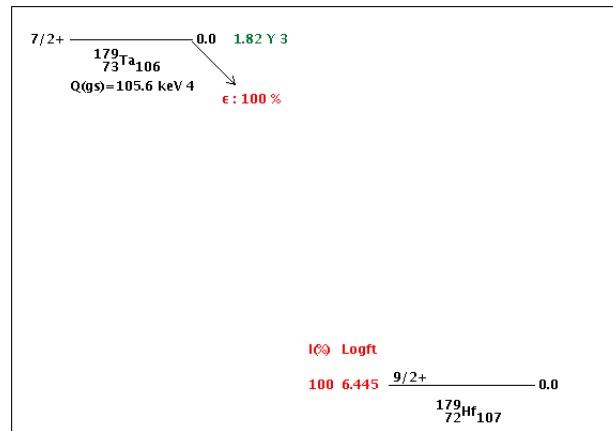
(a)

(b)

Fig. 3.43: Decay scheme of the isotopes ^{179}Ta and ^{181}W taken from Ref. [109].

In Tab. 3.19 we summarize the activities of the cosmogenic isotopes for several run33 detectors. The crystals "Daisy" and "Frederika" were delivered together in July 2002. "Daisy" was already installed in previous CRESST runs and has therefore been stored underground at the LNGS for most of the time since September 2002. This was not the case for "Frederika" which explains their different activities.The higher activity of the TUM crystals can be explained from the fact that they were produced only recently

138

and have not been stored underground for more than a few months. We also suspect a larger activation of the raw materials used for crystal growth since the WO_3 powder was shipped by air mail from the US. In addition, if ^{179}Ta is segregated during crystal growth, a larger concentration is expected in the TUM crystals which were produced with a much higher growth speed (see Sec. 3.3.2). This could also explain the dominance of the activity of ^{179}Ta over ^{181}W in the TUM crystals why it is opposite for the Russian crystals. A higher activity of ^{179}Ta is also expected for long exposures of >600 days to cosmic radiation (see Fig. 3.44). A summary of all radioactive isotopes produced by cosmogenic activation of tungsten and calcium is given in App. A.1.

	activity [µBq/kg]	
crystal	^{179}**Ta (K-capture)**	^{181}**W (K-capture)**
TUM-29	205±18	113±20
TUM-38	214±19	136±25
TUM-40	285±20	102±24
Daisy	17±28	86±23
Frederika	70±22	109±24

Tab. 3.19: Activity of cosmogenic isotopes in some of the detectors of run33.

The reduction of the cosmogenic background in the crystals will be one of the most important issues in the future. Since the isotopes are rather long-lived this requires to minimize the activation in the first place. Therefore, the raw materials and grown crystals should be stored underground. In addition, shipping of the WO_3 powder should not be carried out by air mail. Preferably, one would already like to have influence on the production of the WO_3 powder to assure that its exposure to cosmic radiation is minimized.

Figure 3.44 depicts the activity of the cosmogenic isotopes in dependence of the time of exposure to cosmic rays at sea level. The curves were obtained from the ACTIVIA simulation described in App. A.1. Limiting the exposure to cosmic rays to less than 100 days should decrease the activity of ^{179}Ta by one order of magnitude.
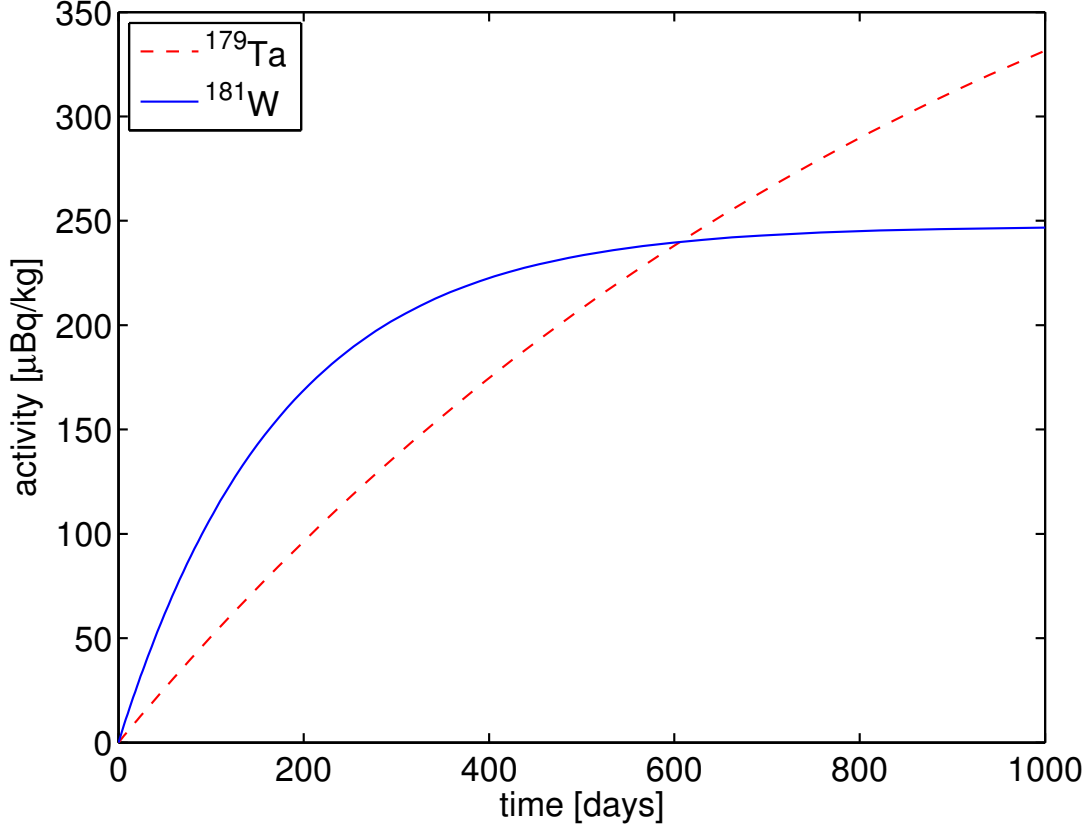
Fig. 3.44: Activity of ^{179}Ta and ^{181}W in CaWO$_4$ in dependence of the exposure to cosmic rays at sea level. The curves were calculated from the production rate obtained from the ACTIVIA simulation (see App. A.1).

Dark Matter Results

The detector TUM-40 shows one of the best performances of all crystals employed in the current CRESST data taking campaign. In addition to the low background count rate due to the excellent radiopurity it also exhibits a very low energy threshold of 600 eV. Furthermore, the stick holder design does efficiently veto backgrounds from surface alpha decays. Using an exposure of 29 kg-live days collected in 2013 with this detector it has been possible to set the currently best limit on spin-independent WIMP-nucleon scattering for WIMPs lighter than 3 GeV/c^2 (see Fig. 3.45) [127]. It also rules out part of the parameter space of the excess reported in the previous run of CRESST.
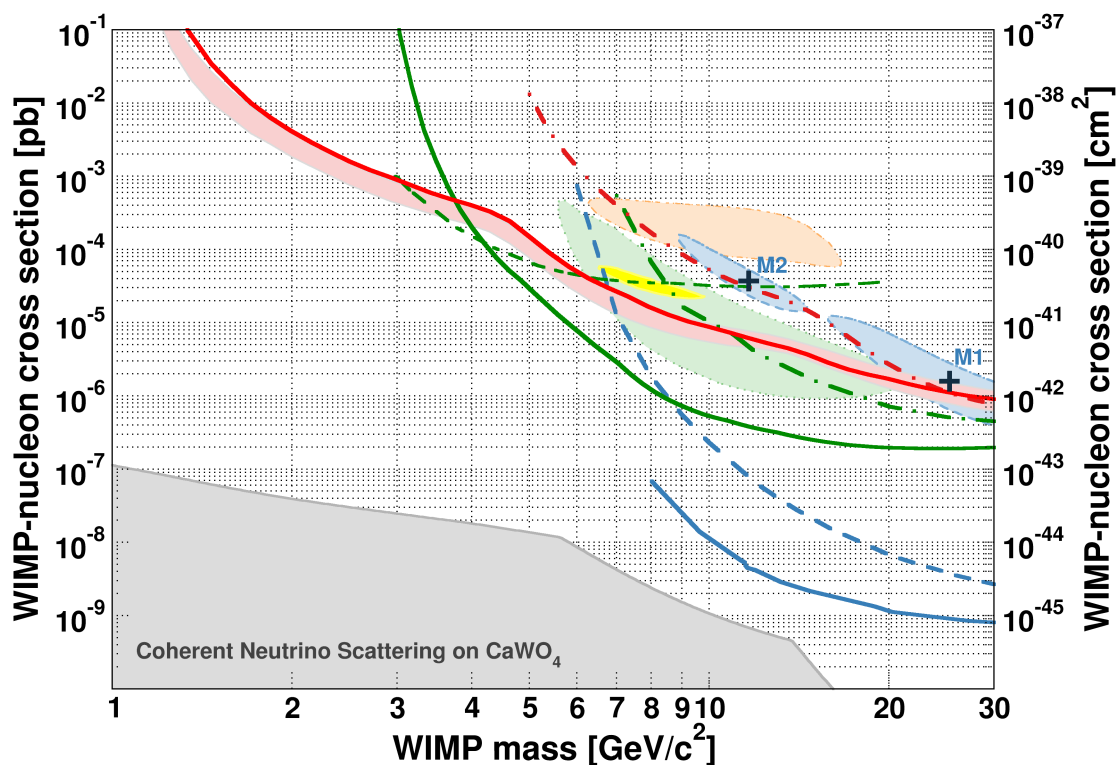
Fig. 3.45: Limit for spin-independent WIMP-nucleon scattering derived with the detector TUM-40 using 29 kg-live days of data [127]. The 90% C.L. upper limit (solid red) is depicted together with the expected sensitivity (1σ C.L.) from the background-only model (light red band). Also shown are the 2σ contour of the previous CRESST run [27] (light blue), the reanalyzed data from the CRESST commissioning run [128] (dash-dotted red line), limits from Ge-based experiments: SuperCDMS [31] (solid green line), CDMSlite [35] (dashed green line) and EDEL-WEISS [129] (dash-dotted green line), the parameter space favored by CDMS-Si [26] (light green), CoGeNT [130] (yellow) and DAMA/Libra [131] (orange), exclusion curves from liquid Xenon experiments LUX [29] (solid blue), XENON100 [30] (dashed blue). Marked in grey is the limit for a background-free $CaWO_4$ experiment arising from coherent neutrino scattering.

Chapter 4

Conclusion and Outlook

The aim of this work was to develop the production line of scintillating $CaWO_4$ single crystals that can be used as a multi-element target material in the direct Dark Matter search experiments CRESST and EURECA. In the scope of this work over 50 $CaWO_4$ crystals were grown using a dedicated Czochralski furnace at the crystal laboratory of the TUM. Through optimization of the growth process it is now possible to grow $\sim$700 g ingots that can be used to produce $\sim$300 g detector crystals. These crystals have the size and mass currently needed for CRESST detectors. To realize the total target mass of up to 500 kg that is planned for the future EURECA experiment it might be preferable to increase the mass of a single detector crystal to $\sim$1 kg to decrease the number of read-out channels.

The influence of high-temperature oxygen annealing, different crystal shapes and surface roughening on the optical properties was investigated to optimize the scintillation performance. The annealing process was found to significantly improve the transmittance and thereby increase the light output by up to $\sim$40%. Through further optimization of the annealing it might be possible to also reduce internal stresses that have been observed in photoelasticity measurements. Regarding the crystal shape we have suggested a block-shaped design instead of the formerly used cylindrical crystals. It was shown that this reduces position dependencies of the light collection and therefore improves the energy resolution of the light channel. There is also evidence that a higher light output can be achieved with block-shaped crystals which, however, needs further investigation. The surface roughening procedure was optimized by additional roughening of the crystal's side surfaces. This improves the light output by up to $\sim$20% and also leads to a further reduction of position dependencies.

The temperature dependence of the scintillation properties was studied down to 3.4 K. We have measured an increase of the light output by a factor of $\sim$1.7 at low temperatures compared to room temperature which is compatible with previous measurements by others. In addition, we have observed the appearance of a scintillation component with a long decay time of $\sim$2 ms that has only been suggested by low-temperature detector measurements before. For the first time we have directly measured the temperature dependence of the α/γ-ratio of the light yield. It was observed that this ratio decreases

by ∼10% at 3.4 K compared to room temperature.

Several measurements were conducted to compare the optical and scintillation properties as well as the radiopurity of the crystals grown at TUM to those produced at other institutes in Russia and Ukraine. We found that the optical properties of the TUM crystals can still be improved. The typical attenuation length of ∼10 cm is about one order of magnitude lower than those of the best Russian crystals. This is correlated with a ∼30% lower light yield of the TUM crystals. The origin of this relatively low attenuation length was found in the presence of inclusions and dislocations. In the future, an improvement of the optical properties could most probably be achieved by decreasing the growth speed of the crystals.

To assure a good radiopurity of the crystals we have used powders of $CaCO_3$ and WO_3 with a high purity of 5N and 4N8, respectively, for production. We have tested powders (from different suppliers) that were selected by trace impurity analysis and screened with low-background γ-ray spectrometry. It was found that the radioactive contamination of all WO_3 powders is below the detection limit. Some of the $CaCO_3$ powders show an activity of ^{226}Ra between ∼30-60 mBq/kg. This impurity can be explained by the similar chemical properties of calcium and radium. In addition, we found that the $CaCO_3$ powders contain about 1ppb of U and Th.

First measurements of the grown crystals that were operated as low-temperature detectors at the CRESST test cryostat showed a very good radiopurity. The total alpha activity was determined to be between ∼1-3 mBq/kg which is about one order of magnitude better than those of typical Russian and Ukrainian crystals.

To determine the individual activities of specific isotopes in the grown crystals a setup for low-background scintillation spectroscopy was installed in the Garching underground laboratory. With this setup it is now possible to determine the radioactive contamination of scintillators at the µBq/kg level. We have found that the activity is dominated by ^{238}U. This contamination can partially be explained by the U content in the $CaCO_3$ powder. However, an additional U contamination is probably introduced during the synthesis of the $CaWO_4$ powder from $CaCO_3$ and WO_3. First tests have shown that an alternative synthesis could be carried out by chemical precipitation from a solution which is likely to reduce the radioactive contamination.

Because of their good radiopurity, 4 TUM-grown crystals were installed in the current Dark Matter run of the CRESST-II experiment in the scope of this work. In the energy region of interest between 10-40 keV an unprecedented low background count rate of ∼3 cpd/kg/keV was achieved with these new crystals. This is an order of magnitude better than that of a typical Russian crystal and about a factor of 2 better than the best crystals obtained so far. The remaining background in this region is dominated by the cosmogenic activation of tungsten. Therefore, in the future the exposure to cosmic radiation has to be minimized, e.g., by underground storage of the raw materials and crystals.

By comparing the activities of the raw materials, grown crystals and residual melt we have observed that impurities like radium and thorium are rejected during crystal growth. This offers the possibility to further improve the crystals' radiopurity by multiple crys-

tallization steps which are foreseen in the near future.

Using one of the TUM CaWO$_4$ detectors, CRESST has been able to set the current best limit for spin-independent WIMP-nucleon scattering for WIMP masses below $\sim$3 GeV/c^2. Due to these promising results it is planned that in the next run of CRESST all crystals from other suppliers will be replaced by TUM-grown crystals.

Appendices

Appendix A

Additional Measurements and Simulations

A.1 Simulation of Cosmogenic Activation

The activation of a tungsten and calcium target with natural isotopic composition was simulated using the ACTIVIA code [132]. An exposure of 100 days to cosmic rays at sea level with energies between $0\text{-}10^4$ MeV in steps of 100 MeV was simulated. The results are shown in Tabs. A.1 and A.2. For tungsten the largest activity originates from ^{178}W ($T_{1/2}$=22 d) which is in equilibrium with ^{178}Ta ($T_{1/2}$=9.31 m). The K-capture lines of these isotopes at 67.4 keV and 65.4 keV are indistinguishable from those of ^{179}Ta and ^{181}W which are clearly observed in the background spectra of the CaWO$_4$ detectors (see Sec. 3.4). For ^{178}Ta, however, an additional line at 158.5 keV would be expected but is not observed. As the half-life of ^{178}W is only 22 days and the detectors have been stored underground for several months the activity is probably too low to be seen by the detectors. The β^--decay of ^{185}W with an endpoint at 432.5 keV is expected to contribute to the continuous background in the region of interest. Other lines like those from ^{175}Hf or ^{169}Yb are not observed in the spectra.

For calcium the largest activity results from ^{37}Ar which leads to a K-capture line at 2.8 keV. In the background spectrum of the detector TUM-40 a line at 2.69 keV is observed. This line is attributed to the M-capture of ^{179}Ta (2.60 keV) as it would fit the expected capture ratio [133]. Whether there is a contribution from ^{37}Ar to this line can be tested with future data by looking at the time dependence of the activity. A small contribution to the continuous background in the detectors is expected from the β^--decay of ^{35}S with a low Q-value of 167.3 keV.

isotope	half-life [days]	production rate [kg^{-1} day^{-1}]	activity [µBq kg^{-1}]	decay mode	energy deposit [keV]
^{159}Dy	144	2.9	13	EC	110 (26.6%) 52.0 (73.4%)
^{169}Yb	32	10.1	104	EC	375.5 (6.1%) 532.3 (12.3%) 438.7 (81.1%)
^{173}Lu	500	14.3	22	EC	412.1 (22.1%) 240.7 (20.9%) 139.9 (50%)
^{172}Hf	683	14.5	16	EC	254.9 (58%) 243.2 (19%)
^{175}Hf	70	25.1	182	EC	496.1 (17%) 406.7 (80%)
^{179}Ta	665	69.3	80	EC	65.4
^{182}Ta	115	10.8	57	β^-	1373.8-1814.3 (20.1%) 1289.1-1814.3 (43.2%) 1553.2-1814.3 (29.2%)
^{178}W/ ^{178}Ta	22	62.7	694	EC	67.4 65.4 (62%) 158.5 (34%)
^{181}W	121	33.5	169	EC	73.6 (74%) 67.4 (26%)
^{185}W	75.1	9.0	63	β^-	0-432.5
^{183}Re	70	4.5	32	EC	361.2 (14.1%) 278.3 (64.9%)
^{184}Re	38	2.6	25	EC	1075.5 (17.8%) 972.8 (76.5%)

Tab. A.1: Cosmogenic activation of tungsten with natural isotopic composition simulated with the ACTIVIA code. The activity was calculated assuming 100 days of exposure to cosmic rays at sea level. Only radionuclides with a half-life >10 days and an activity >1 kg^{-1} day^{-1} are shown. The energy deposit for EC decay is only listed for K-capture.

isotope	half-life [days]	production rate [kg^{-1} day^{-1}]	activity [µBq kg^{-1}]	decay mode	energy deposit [keV]
^{7}Be	53.3	3.0	25	EC	0.05 (89.6%) 477.6 (10.4%)
^{32}P	14.28	11.7	135	β^-	0-1710.7
^{33}P	25.3	1.8	20	β^-	0-248.5
^{35}S	87.4	5.8	37	β^-	0-167.3
^{37}Ar	35	202.4	2019	EC	2.8

Tab. A.2: Cosmogenic activation of calcium with natural isotopic composition simulated with the ACTIVIA code. Other details as in Tab. A.1

A.2 Simulation of the Light Collection in a CRESST Detector Module

This section describes Mont-Carlo (MC) simulations to study the light collection in CRESST-like detector modules. A similar simulation was carried out in Ref. [56] to study different crystal shapes. We have improved this simulation by implementing a more sophisticated model for the surface roughening. In addition, we did a more systematic study of the influence of roughening different crystal surfaces.

Geometry

For the Monte-Carlo simulations we used the GEANT4 (version 4.9.4p02) software [134]. The implemented geometry is a simplified model of a CRESST-II detector module. It includes a CaWO$_4$ crystal and a silicon-on-sapphire (SOS) light detector which are surrounded by vacuum and enclosed together in a reflective housing[1] (see Fig. A.1). We have tested three different geometries for the crystal and the reflective housing: a cylindrical shape (module a)), a square prism (module b)) and a hexagonal prism (module c)). The dimensions of the different modules are shown in Tab. A.3. All simulated crystals have the same volume and, in addition, the side that is facing the light detector has the same surface area. The positions of the objects were always changed so that the distances depicted in Fig. A.1 stayed constant. Furthermore, the dimensions of the disc-shaped SOS light detector, which has a diameter of 4 cm and a thickness of 430 µm, were always kept unchanged.

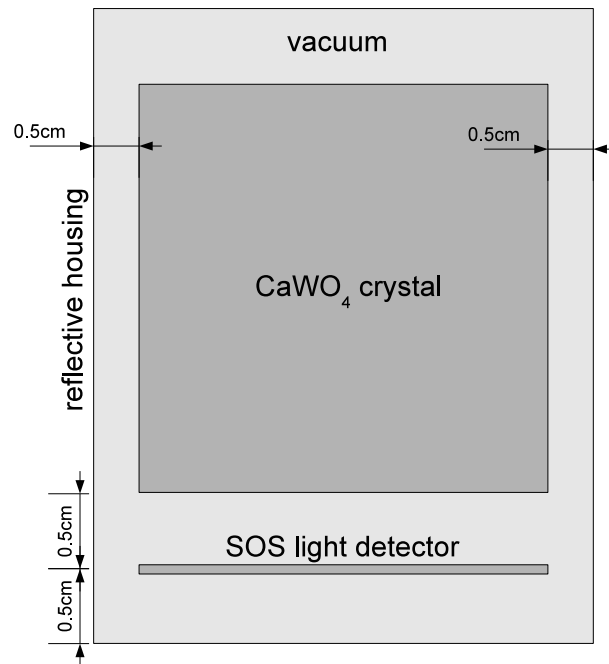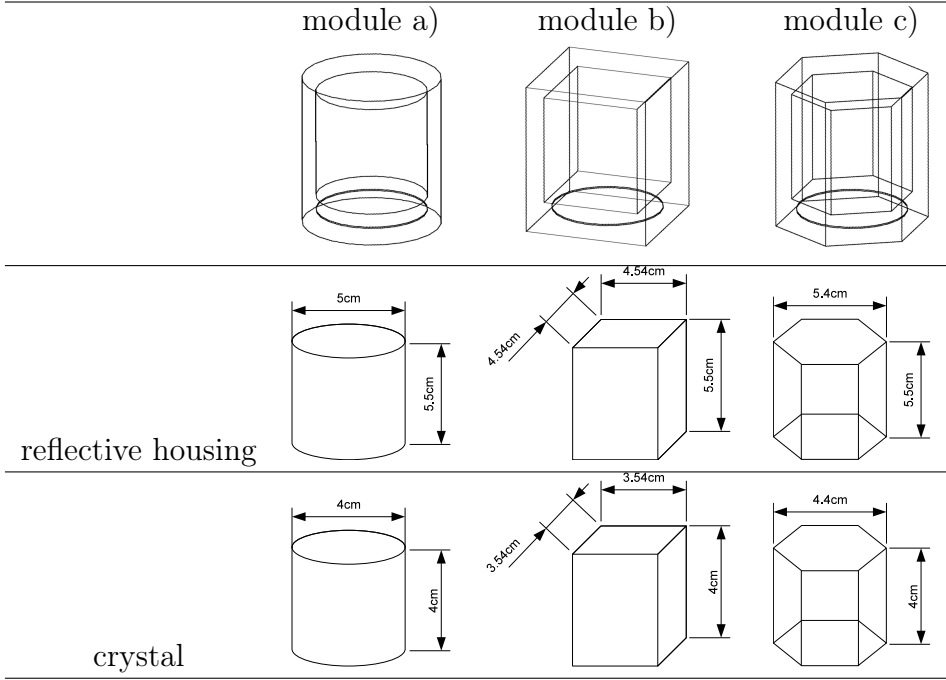[1]The scintillating properties of the VM2002 foil were not implemented in the simulation.

Fig. A.1: Schematic drawing of the simulation of a CRESST-like detector module. The simulation includes a $CaWO_4$ crystal and a silicon-on-sapphire (SOS) light detector that are enclosed together in a reflective housing.

Tab. A.3: Geometries and dimensions of the crystal and reflective housing in the different simulated modules.

Physics Implementation

Running the simulation, 5000 scintillation events are generated at random positions inside the crystal. In each scintillation event 10,000 photons with random linear polarizations and an isotropic angular distribution over a solid angle of 4π are produced. The scintillation spectrum was implemented as a single Gaussian with a mean of $2.8\,\mathrm{eV}$ and a FWHM of $0.56\,\mathrm{eV}$ which was taken from the measurement of a $CaWO_4$ crystal under photoexcitation at $8\,\mathrm{K}$ [59]. At the surface of the light detector and the reflective housing the photons can either be reflected or absorbed. The reflection spectra which were entered into the simulation are shown in Fig. A.2. The reflectivity of the housing was taken from a room temperature measurement of the VM2002 foil [135]. The absorption of the light detector (LD) is different for the two sides and was taken from room temperature measurements of a SOS waver [136]. In the simulation the sapphire side of the light detector is facing the $CaWO_4$ crystal. At the surface of the $CaWO_4$ crystal photons can either be reflected or refracted according to the Fresnel equations and the entered refractive indices of the materials. For the vacuum a refractive index of $n_{vac} = 1$ was entered in the simulation. The refractive index n_{CaWO_4} of the $CaWO_4$ crystal was calculated by the following dispersion formula [55]:

$$n_{CaWO_4}^{2} - 1 = \frac{2.5493 \cdot (\lambda/\mu m)^2}{(\lambda/\mu m)^2 - 0.1347^2} + \frac{0.92 \cdot (\lambda/\mu m)^2}{(\lambda/\mu m)^2 - 10.815^2} \qquad \text{(A.1)}$$

where λ is the photon wavelength. It should be noted that CaWO$_4$ (crystal class: 4/m) is weakly birefringent ($\delta \approx 0.017$ [52]), however, GEANT4 is not capable of simulating birefringent materials. The used refractive index is that for the ordinary beam.

Photons that travel inside the CaWO$_4$ crystal can also undergo bulk absorption and Rayleigh scattering. For the absorption length L_{abs} and scattering length L_{scat} the values $L_{abs} = 27.9\,\text{cm}$ and $L_{scat} = 278.6\,\text{cm}$ were used. These were determined in Sec. 2.2 for a CaWO$_4$ crystal grown by the Crystal Laboratory of the Technische Universität München. It should be noted that the absorption and scattering lengths can show large variations in different crystals. In Ref. [61], e.g. the values $L_{abs} = 15.4\,\text{cm}$ and $L_{scat} = 16.4\,\text{cm}$ were determined for a CaWO$_4$ crystal that was produced by SRC Carat (Lviv, Ukraine). We have measured values for the attenuation length that range between $\sim$10-150 cm for different CaWO$_4$ crystals from different suppliers (see Sec. 3.1.2).
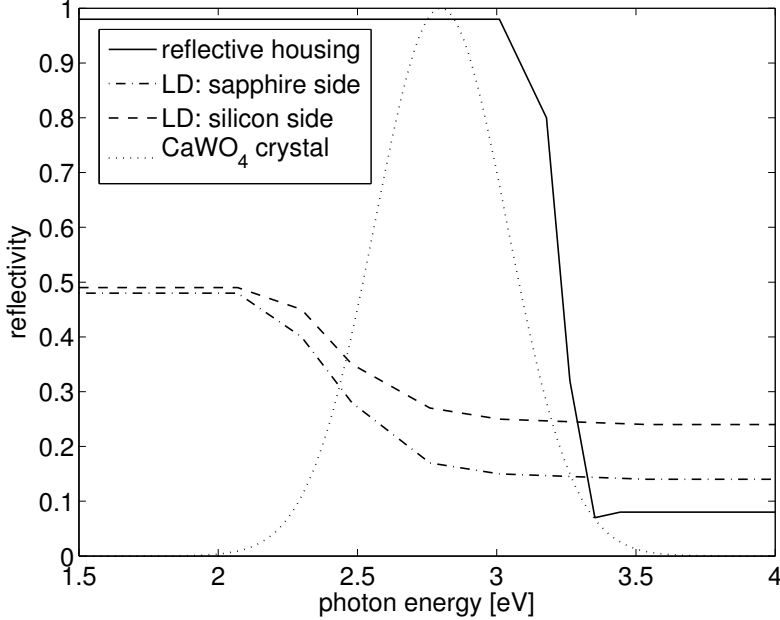
Fig. A.2: Wavelength dependent reflection spectra of the reflective housing and the light detector (LD) that were used for the simulations of a CRESST-like detector module. For comparison the implemented emission spectrum of the CaWO$_4$ crystal is also shown.

In the simulations, different surfaces of the CaWO$_4$ crystal were implemented as non-specular reflecting. This was done using the UNIFIED model, which assumes that a rough surface is a collection of micro-facets [137]. In this model the angle α between a micro-facet normal and the average surface normal will follow a Gaussian distribution with standard deviation σ_α. To determine the value of σ_α the surface profile of a CaWO$_4$ crystal that was mechanically roughened using 800B$_4$C powder was measured with a

TENCOR P10 Surface Profiler (see Sec. 2.4). From the differentiation of the surface profile in steps of $2\,\mu m$ the distribution of the micro-facet slopes α was obtained. A Gaussian fit to this distribution leads to a value of $\sigma_\alpha = 6.7°$ (see Tab. 2.9) that can be used in the simulation. In addition, the simulation model offers the possibility to specify the probabilities for specular reflection, Lambertian reflection, backscattering and reflection according to the facet slope distribution. These are given by the specular spike constant c_{ss}, the diffuse lobe constant c_{dl}, the backscattering constant c_{bs}, and the specular lobe constant c_{sl}, respectively. The values of these constants depend on the photon wavelength λ in comparison to the standard deviation of the height distribution σ_h of the surface. According to Ref. [84] the specular spike vanishes and the reflection is dominated by the specular lobe as soon as $\sigma_h/\lambda > 1.5$. From the measured surface profile we have obtained $\sigma_h/\lambda = 1.65$ for a wavelength of $\lambda = 430\,nm$ (see Tab. 2.9) and we thus set $c_{sl} = 1$.

Validation of the Simulation

To test if the simulation of a roughened surface does correctly reproduce experimental results a dedicated measurement was performed. For this measurement a cylindrical $CaWO_4$ crystal with a diameter of $16\,mm$ and a height of $20\,mm$ was used. The crystal was placed on the window of a 2" ETL9214 photomultiplier tube (PMT) (see Fig. A.3). As a spacer between crystal and PMT we used a thin wire of $40\,\mu m$ thickness which provides a well defined gap without blocking much light. The window of the PMT around the crystal was covered with a black cap ensuring that only light transmitted through the crystal surface facing the PMT is detected. The whole setup is surrounded by a light-tight box where the inner walls have been covered in black. As there are no reflective surfaces except for the crystal, the PMT window and the PMT cathode the setup is easy to simulate. As input parameters for the simulation the refractive index of the PMT window (n=1.49) and the quantum efficiency of the PMT ($\sim 25\%$ at $430\,nm$) specified in the datasheet were used. For the $CaWO_4$ the emission spectrum entered in the simulation was measured under UV excitation ($280\,nm$) with a Cary Eclipse fluorescence spectrophotometer by Agilent Technologies. The maximum of the emission spectrum was found at $\sim 430\,nm$ which agrees with the position expected for the intrinsic emission band in $CaWO_4$ [59]. In addition, the attenuation length of the crystal was determined with a Perkin Elmer LAMBDA 850 UV/Vis spectrophotometer. The attenuation length at $430\,nm$ was found to be $\sim 10\,cm$. Under the assumption that scattering can be neglected in the crystal the measured wavelength dependent attenuation length was adapted as the crystal's absorption length in the simulation. Furthermore, the wavelength dependent refractive index of the crystal for the simulation was calculated by Eq. (A.1).

In both measurement and simulation the crystal was irradiated from the top with an [241]Am gamma source ($59.5\,keV$). The spectrum was obtained by the single photon counting method and the light yield was determined from the position of the $59.5\,keV$ photopeak. The reproducibility of the measurement was tested by the repetition of multiple measurements and found to be $\sim 2\%$. The first measurement was performed with all

surfaces of the crystal optically polished. Using the measured light yield and the light collection efficiency which is obtained from the simulation of the setup the intrinsic light yield of the crystal can be deduced. The so obtained value was found to be 18,500 ph/MeV which agrees well with literature values ranging between 16,000 ph/MeV~23,000 ph/MeV [57, 60, 61].

In addition, two measurements were performed where one of the crystal's planar surfaces had been roughened as described above. In the first measurement the roughened surface (surface 1) was facing the PMT while in the second measurement it was placed opposite to the PMT (surface 2). The results of the measured light yield normalized to that of the polished crystal together with the simulation of the setup for all three measurements is shown in Fig. A.4. It can be seen that the results of the simulation which uses the value σ_α=6.7° that was obtained from the measured surface profile do not match the results of the measurements. However, agreement between measurement and simulation can be achieved by setting σ_α=45°. The mismatch between the value of σ_α obtained from the measured surface profile and the one that correctly matches the results from the measurements may have several reasons. In Ref. [138] it was found that the surface profile can deviate from the angular distribution of the measured optical reflectance although the deviation was much smaller than in our case. In addition, it was found that the reflection probability constants c_{sl}, c_{ss}, c_{bs} and c_{dl} actually depend on the incidence angle [138]. One might consider that the condition that the reflection is dominated by the specular lobe may not be fully fulfilled in our case. However, by testing different combinations for the values of the reflection probability constants no agreement between simulation and measurement could be achieved. Since the value of σ_α=45° does reasonably describe our measurements we adapt this value for the following simulations.
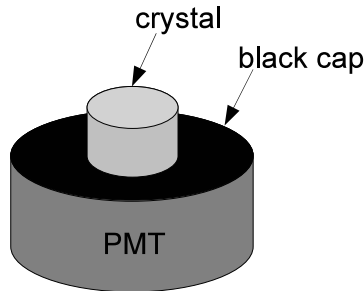

Fig. A.3: Setup for the light yield measurements to validate the simulation. A CaWO$_4$ crystal is placed onto the window of a photomultiplier tube (PMT). The PMT window around the crystal is covered with a black cap so that only light transmitted through the crystal surface facing the window can be detected.
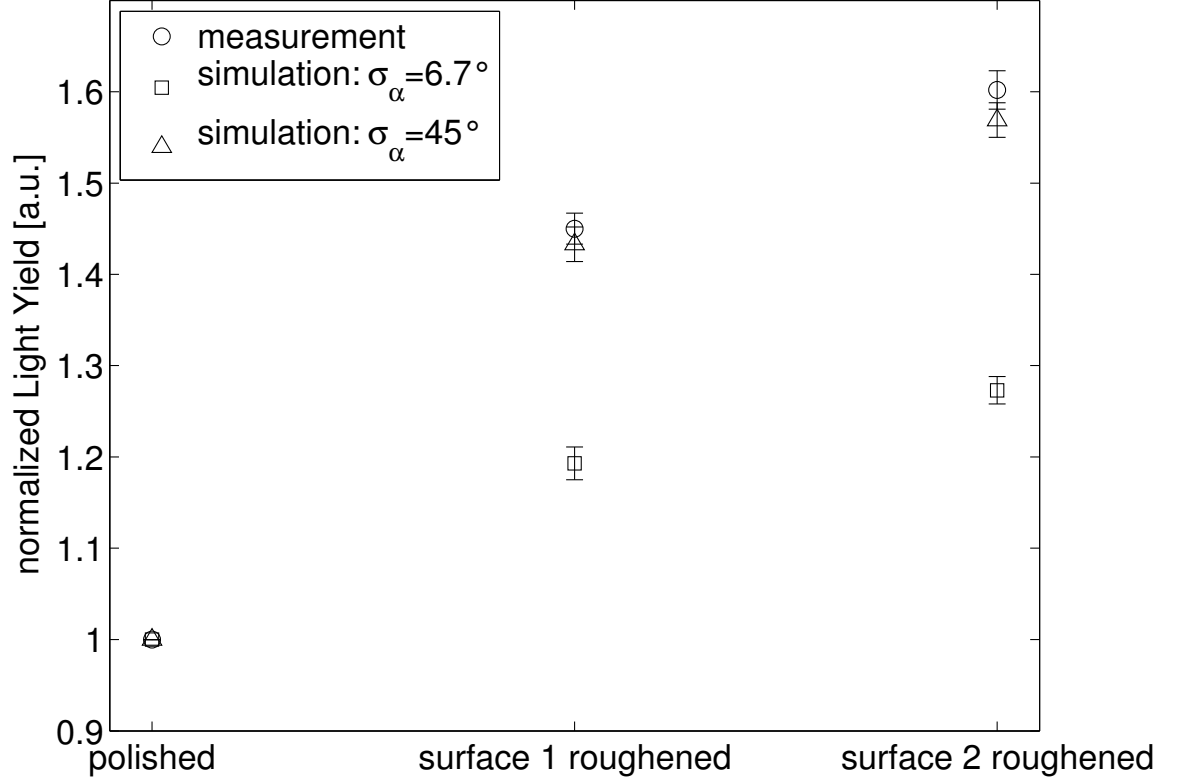
Fig. A.4: Comparison of the measured and simulated light yield of the setup shown in Fig. A.3. The setup was tested with all crystal surfaces optically polished, the surface facing the PMT (surface 1) roughened and the surface opposite to the PMT (surface 2) roughened. Simulations were carried out with different values for the facet slope distribution σ_α. Reasonable agreement between measurement and simulation is found for a value of $\sigma_\alpha=45°$.

Results and Discussion

Tab. A.4 shows the results of the simulation of the different modules. For each module the CaWO$_4$ crystal was simulated with different surfaces roughened. Here p denotes the simulation with all surfaces polished, r_a with the surface facing the light detector roughened, r_b with the surface opposite to the light detector roughened, r_c with all side surfaces roughened, r_d with the surface facing the light detector and all side surfaces roughened, r_e with the surface opposite to the light detector and all side surfaces roughened, and r_f with all surfaces roughened. In each simulation the mean fraction of photons η_{LD} that is absorbed by the light detector, the reflective housing η_{hsg} and the crystal η_{crys} was

determined.

The simulation of module a) with the surface facing the light detector roughened (r_a) reflects the configuration that is currently used in the CRESST-II experiment. The value of η_{LD}=22.6% is a bit lower than the values which were determined experimentally for several CRESST-II detector modules that range between 28%-36% [125]. These differences can be explained by the different absorption lengths of different crystals. The influence of different absorption lengths on the simulated light collection is shown in Fig. A.5. The measured light collection of 28%-36% corresponds to absorption lengths of ∼50-100 cm. This is well compatible with the attenuation lengths of ∼10-150 cm measured for $CaWO_4$ crystals used in CRESST-II (see Sec. 3.1.2).

It is worth noticing is that the hexagonal crystal in module c) with all surfaces polished (p) shows a ∼10% higher light collection efficiency compared to the other two modules. This can be explained by the multi-faceted surface which prevents that a photon is internally reflected infinitely. By contrast in the cylindrical and rectangular crystal ∼50% of the photons are trapped inside the crystal due to infinite total internal reflection [79, 139]. Regarding the surface roughening the best light collection in all modules is achieved with all side surfaces of the crystal roughened (r_c) which offers an improvement of a factor of ∼2 compared to the polished crystal. In this configuration there are only small differences in the light collection between the differently shaped modules of ∼5%. The best result is achieved with module b) where the crystal is shaped like a square prism.

We like to point out that apart from increasing the light collection surface roughening does also reduce position dependencies of the light collection. This is especially true for the cylindrical crystal where otherwise a large dependency upon the radial position of the scintillation event is present resulting from a radial dependence of the fraction of trapped light [79]. To illustrate this Fig. A.6 shows the relative difference $\Delta\eta_{LD}$ of the light collection against the position of the scintillation events. For the polished cylindrical crystal the light collection in the center near the symmetry axis is ∼75% larger than near the curved surface (see Fig. A.6(a)). After roughening of the curved surface the maximum difference between the light collection is reduced to ∼10% (see Fig. A.6(b)). A similar radial position dependence of the light collection appears in the hexagonal crystal of module c) when all surfaces remain polished (see Fig. A.6(e)) albeit not as pronounced as in the cylinder. This can be ascribed to the fact that on average photons emitted near the center have to undergo fewer internal reflections before they can leave the crystal. For a rectangular crystal like in module b) it can be shown that the fraction of trapped photons is actually independent of the position of the scintillation event [139] that is why it shows the smallest position dependence of the light collection (see Fig. A.6(c)). After roughening of all side surfaces the maximum difference in the light collection in dependence of the position of the scintillation event is ∼10% for all modules. A small position dependence is desirable as it also influences the resolution of the detectors.

Similar studies have been carried out in Refs. [140, 141] where the light collection of differently shaped $CaWO_4$ and $ZnWO_4$ crystals was compared using MC simulations and measurements with a PMT. The results show that the highest light collection was achieved with the side surfaces of the crystal roughened which is consistent with our

findings. However, they find that the light collection increases from a cylinder over a hexagonal to a rectangular crystal. This difference could result from the different dimensions and optical properties of the crystals in Refs. [140, 141]. In addition, the geometry of the simulations and measurements with a PMT as light detector are slightly different, in particular, because it has only a single surface for light detection. According to Ref. [141] the best light collection is achieved with a triangular prism.
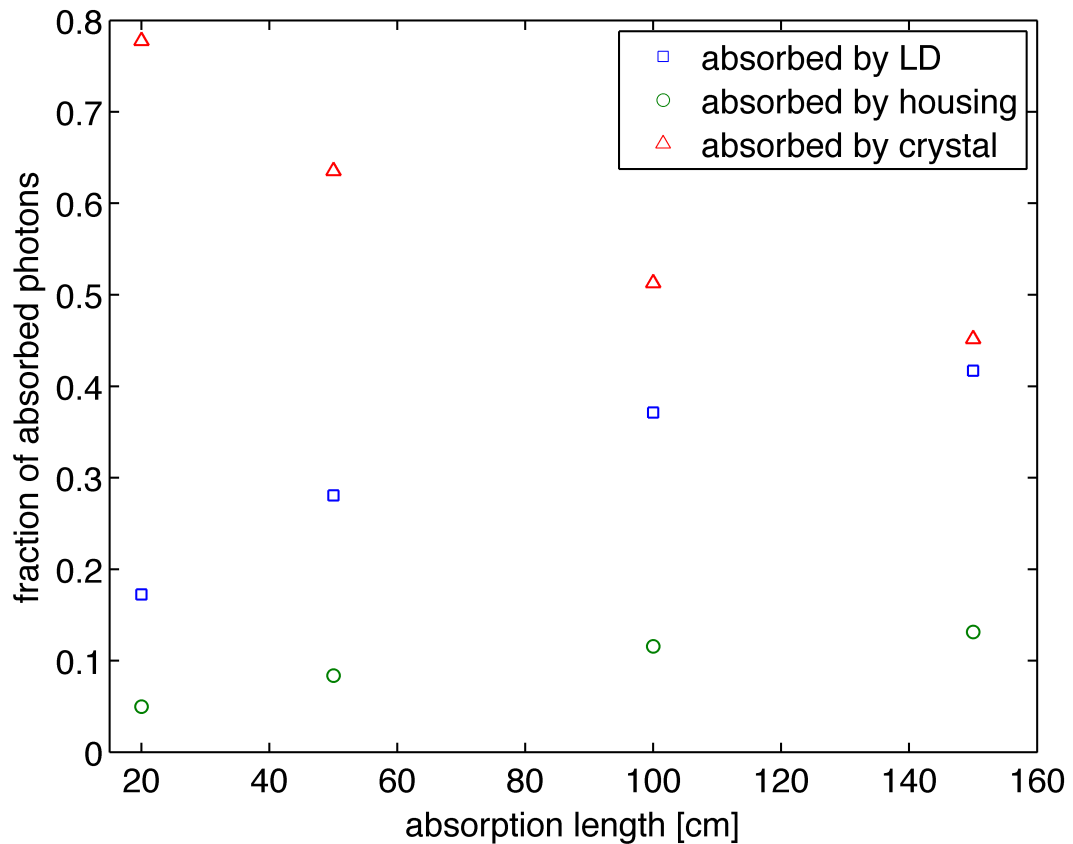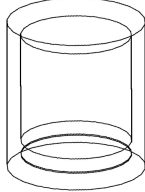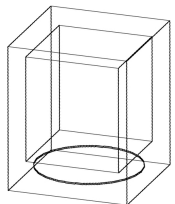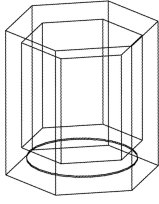
Fig. A.5: Simulated light collection of module a) with the surface facing the light detector roughened (r_a) for different absorption lengths of the CaWO$_4$ crystal. The scattering of scintillation light by the crystal was neglected in the simulation.

	surfaces	η_{LD} (%)	η_{crys} (%)	η_{hsg} (%)
module a)	p	18.3	76.8	4.9
	r_a	22.6	70.0	7.4
	r_b	20.7	71.6	7.7
	r_c	36.0	57.1	6.9
	r_d	31.0	61.3	7.7
	r_e	32.3	60.2	7.5
	r_f	29.3	62.6	8.1
module b)	p	18.8	75.1	6.1
	r_a	22.8	67.9	9.3
	r_b	21.6	68.9	9.6
	r_c	37.8	53.0	9.2
	r_d	32.3	57.5	10.2
	r_e	33.9	56.1	10.0
	r_f	30.6	58.5	10.9
module c)	p	20.4	72.9	6.8
	r_a	23.7	66.5	9.8
	r_b	22.2	67.8	10.0
	r_c	37.4	54.6	8.0
	r_d	31.9	59.2	8.9
	r_e	33.4	57.9	8.7
	r_f	30.1	60.4	9.5

Tab. A.4: Results of the simulation of a CRESST-like detector module. The values show the mean fraction of photons absorbed by the light detector η_{LD}, the CaWO$_4$ crystal η_{crys} and the reflective housing η_{hsg}. The crystal was simulated with different surface properties: all surfaces polished p; surface facing the light detector roughened r_a; surface opposite to the light detector roughened r_b; all side surfaces roughened r_c; surface facing the light detector and all side surfaces roughened r_d; surface opposite to the light detector and all side surfaces roughened r_e; all surfaces roughened r_f.
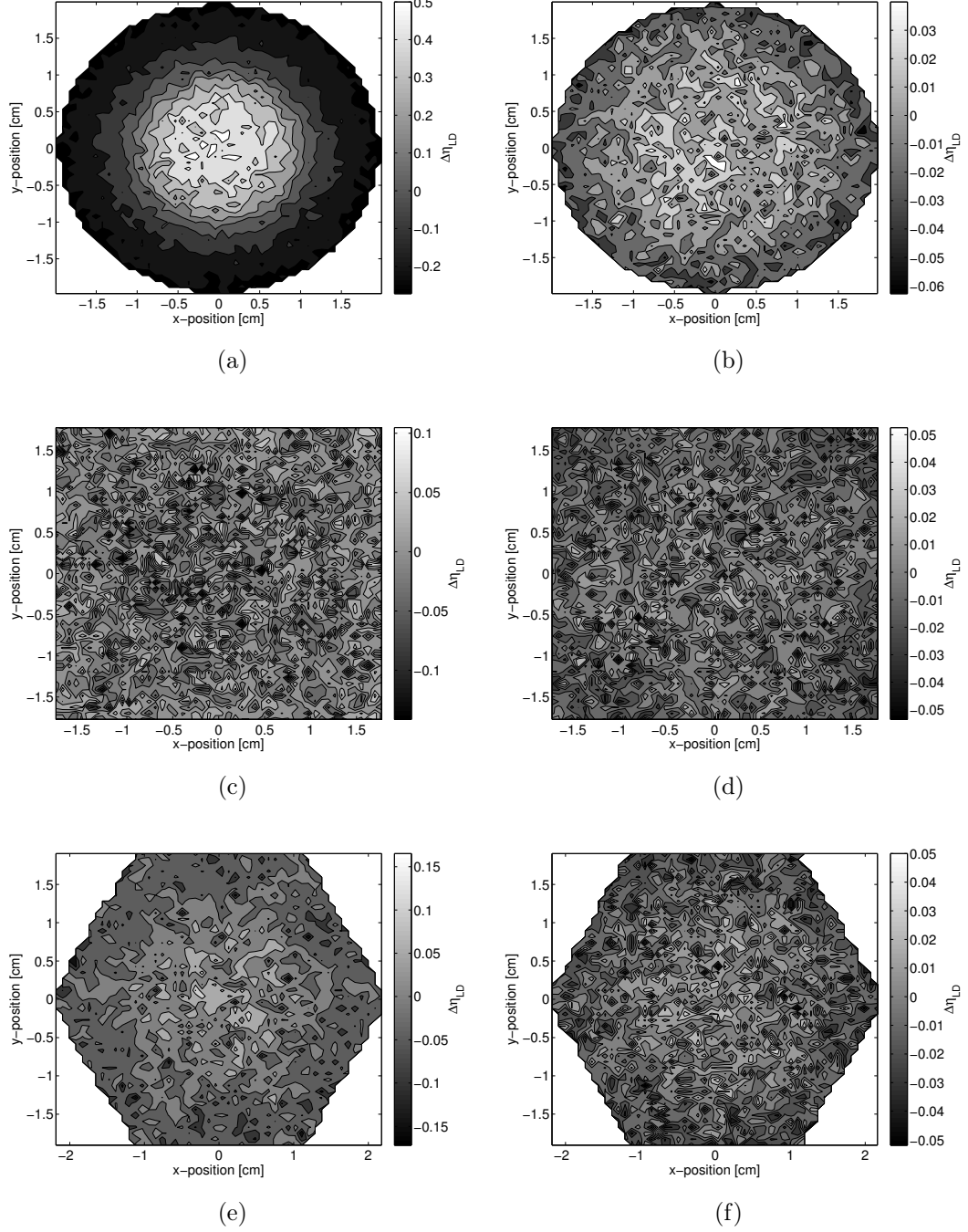
Fig. A.6: Relative difference $\Delta\eta_{LD}$ of the light collection for different positions inside the crystal. (a): module a) with all surfaces polished (p); (b): module a) with the curved surface roughened (r_c); (c): module b) with all surfaces polished (p); (d): module b) with all side surfaces roughened (r_c); (e): module c) with all surfaces polished (p); (f): module c) with all side surfaces roughened (r_c).

161

A.3 Low-Temperature Reflectivity Measurements of the VM2002 Foil

This section describes a measurement of the reflection spectrum of the VM2002 foil carried out at temperatures down to $\sim$20 K. The foil is used as reflector surrounding the CRESST detector modules (see Sec. 1.2). To maximize the light collection it is important that the foil has a high reflectivity at mK temperatures where CRESST detectors are operated. However, the reflectivity of the foil is only known at room temperature [142]. The measurements we have conducted do not allow to determine the absolute reflectivity of the foil but only the approximate trend of the reflection spectrum. Since the room temperature reflectivity has a cutoff at $\sim$385 nm which is already very close the maximum of the emission spectrum of $CaWO_4$ (see Fig. A.7) it is important to check whether this cutoff changes at low temperatures.

A schematic picture of the setup for the measurements is shown in Fig. A.8. As light source we used a tungsten halogen lamp. The foil is attached to a copper block which is connected to the cold finger of a cryocooler (Edwards Cryodrive 3.0). The sample is placed in a vacuum chamber with optical windows. The light reflected from the foil is collected by an optical fiber and detected by a Maya2000 Pro (Ocean Optics) UV/Vis spectrometer. The temperature at the copper holder was measured with a PT100.

Results of the reflection spectrum measured at room temperature and at the base temperature of the cryocooler of $\sim$20 K are shown in Fig. A.9. The apparent decrease in reflectivity at low temperatures is caused by slight changes in the alignment of the foil due to thermal contraction of the copper holder. Therefore the reflectivity values at different temperatures can not be directly compared. However, the plot shows that the cutoff of the reflectivity at $\sim$385 nm does not change at low temperatures.
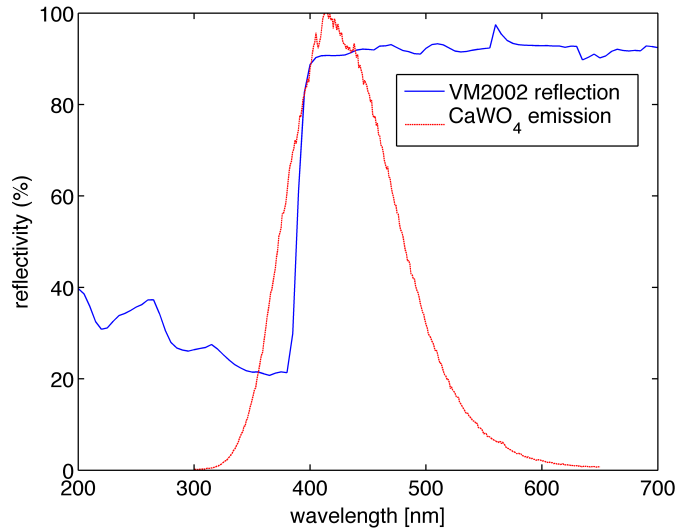
Fig. A.7: Reflectivity of the VM2002 foil measured with a Perkin Elmer LAMBDA 900 UV/Vis spectrophotometer and an Ulbricht sphere. The reflectivity is normalized to that of Spectralon®. The red dashed line shows the emission spectrum of $CaWO_4$ measured under UV excitation at $280\,nm$ as described in Sec. 3.2.1.
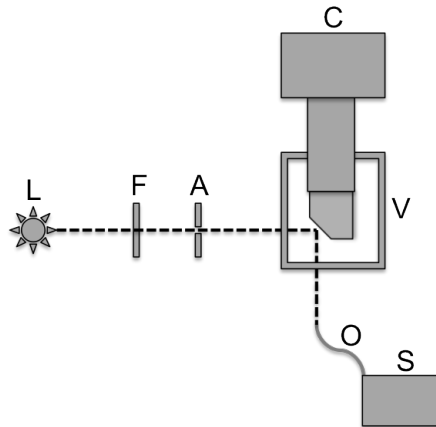

Fig. A.8: Setup for the reflectivity measurements of the VM2002 foil at low temperatures. A tungsten halogen lamp (L) is used as light source. The lamp spectrum is filtered (F) to wavelength between ∼360-590 nm and passes an aperture (A); The foil is placed in a vacuum chamber (V) with optical windows and attached to the cold finger of a cryocooler (C). The light is collected by an optical fiber (O) and detected by a UV/Vis spectrometer (S).
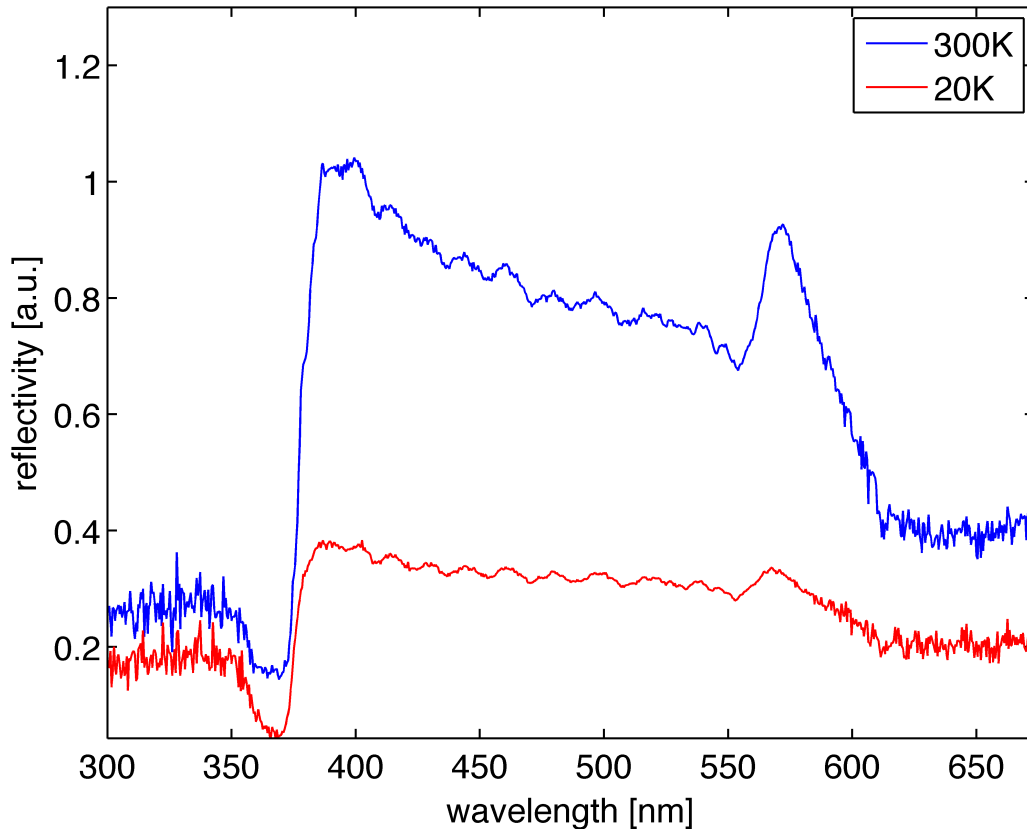
Fig. A.9: Reflectivity spectra of the VM2002 foil at 300K and ∼20 K. Due to slight changes in the alignment of the foil at low temperatures the absolute reflectivity values can not be directly compared. The spectra show that the cutoff of the reflectivity around ∼385 nm does not change at low temperatures.

A.4 Low-Background γ-Ray Spectrometry Measurements

This section present the results of screening measurements carried out for various samples in the context of the $CaWO_4$ crystal production and the CRESST experiment. The measurements were performed with HPGe detectors at the underground lab Garching. A detailed description of the setups is given in Ref. [117].

A.4.1 Brass Sample

This section presents the results for a screening measurement of a brass sample. The material was used to produce screws for the detector holders of run33 of the CRESST-II experiment. The screening measurement was performed with a HPGe detector at the underground lab Garching [117]. The results are presented in Tab. A.5. As only upper limits for the activities were obtained the material could be installed in CRESST.

sample	brass
mass	631 g
isotope	**activity [mBq/kg]**
^{228}Ra	<21
^{228}Th	<5.3
^{238}U	<102
^{226}Ra	<4.5
^{210}Pb	<653
^{40}K	<47
^{137}Cs	<2.2
^{60}Co	<2.9

Tab. A.5: Activities of a sample of brass that was used to produce screws for the detector holders of CRESST-II run33. The measurement was performed with a HPGe detector at the underground lab Garching. Limits are given at 90%CL, errors at 1 sigma.

A.4.2 Powders for Crystal Roughening

As mentioned in Sec. 2.4 the surfaces of the $CaWO_4$ crystals are mechanically roughened to improve the light collection. Here we present the screening measurements for three different powders that can be used for roughening.

The first column of Tab. A.6 shows the results of a 600SiC powder that is usually used by the crystal laboratory of the Technische Universität München (TUM) for roughening. The second column shows a sample of 600SiC paper as used by the crystal laboratory. The last column shows a special batch of $800B_4C$ powder that was ordered by the Max-Planck-Institut für Physik (MPI) München.

The B_4C powder has the lowest radioactive contamination and is henceforth used for roughening. The SiC paper can be used alternatively as the powder is attached to the paper so there is a smaller danger of contaminating the crystal surface.

sample	600SiC powder	600SiC paper	800B$_4$C powder
mass	94.0 g	9.7 g	79.4 g
isotope	**activity [mBq/kg]**		
^{228}Ra	2656±318	1099±324	243±78
^{228}Th	2511±181	673±127	411±48
^{238}U	8356±1020	1434±368	517±108
^{226}Ra	604±53	257±95	161±28
^{210}Pb	1581±360	<663	<160
^{40}K	951±509	8071±5675	<484
^{137}Cs	117±23	<111	<32
^{60}Co	54±15	173±73	<24

Tab. A.6: Activities of three different powders that can be used for roughening the crystal surfaces. The measurements were performed with a HPGe detector at the underground lab Garching. Limits are given at 90%CL, errors at 1 sigma.

A.5 Radiopurity of Raw Materials for ZnMoO$_4$ Crystals

Because of the promising results regarding the radiopurity of the CaWO$_4$ crystals produced at TUM a feasibility study for the growth of ZnMoO$_4$ crystals was initiated. This was done in collaboration with the Lumineu project [143, 144] which concerns the development of low-temperature detectors based on scintillating ZnMoO$_4$ to search for the neutrinoless double beta decay ($0\nu\beta\beta$) of ^{100}Mo.

The raw materials for the growth of ZnMoO$_4$ are powders of ZnO and MoO$_3$. Batches of ZnO with a purity of 5N and MoO$_3$ with a purity of 3N8 were obtained from MV laboratories, Inc.. The analysis certificates summarizing the impurities in the powders are shown in Fig. A.10.

The powders were also screened with low-background γ-ray spectrometry in the underground lab Garching [117]. The results are shown in Tab. A.7.

The screening measurement of the ZnO powder showed an increased count rate at the 93 keV line of ^{234}Th which would correspond to a ^{238}U activity of 176±70 mBq/kg. However, as no increased count rate was measured for the 63 keV peak of ^{234}Th the result may just be a statistical fluctuation of the background. For the MoO$_3$ powder an activity of 153±47 mBq/kg of ^{40}K was measured. This contamination is confirmed by the trace impurity analysis which shows a concentration of 12ppm of K. This would correspond to an activity of 372 mBq/kg which is a factor of $\sim$2 higher than that determined from the γ-ray spectrometry.

However, neither ^{238}U or ^{40}K do pose as background for $0\nu\beta\beta$ of ^{100}Mo. The only important contributions to the background come from ^{208}Tl (^{228}Th chain), ^{214}Bi and ^{210}Tl

(^{226}Ra chain) [144] for which only upper limits could be derived.

Ag	< 1		Cd	3		In	< 1		Pb	6		Sr	< 1
Al	< 1		Co	< 1		K	< 1		Re	< 1		Th	< 1
As	< 1		Cr	< 1		Li	< 1		Rh	< 1		Ti	< 1
B	< 1		Cu	< 1		Mg	< 1		Ru	< 1		Tl	< 2
Ba	< 1		Fe	< 1		Mn	< 1		Sb	< 1		V	< 1
Be	< 1		Ga	< 1		Mo	< 1		Sc	< 1		W	< 1
Bi	< 2		Ge	< 1		Na	< 1		Se	< 1		Zr	< 1
Ca	< 1		Hf	< 1		Ni	< 1		Sn	< 1			

Ce	< 1		Eu	< 1		La	< 1		Pr	< 1		Tm	< 1
Dy	< 1		Gd	< 1		Lu	< 1		Sm	< 1		Yb	< 1
Er	< 1		Ho	< 1		Nd	< 1		Tb	< 1			

(a)

Ag	< 0.1		Cs	< 0.5		K	12		Rb	< 0.5		Tl	< 0.1
Al	3		Cu	2		La	< 0.1		Re	6		Tm	< 0.1
As	18		Dy	< 0.5		Li	< 1		Rh	< 0.1		U	< 0.1
Au	< 0.1		Er	< 0.5		Lu	< 0.1		Ru	< 0.1		V	0.3
B	< 0.5		Eu	< 0.1		Mg	< 0.5		Sb	0.5		W	50
Ba	< 0.5		Fe	11		Mn	< 0.1		Sc	< 0.1		Y	< 0.1
Be	< 0.1		Ga	< 0.5		Na	* < 1		Sn	0.3		Yb	< 0.1
Bi	< 0.1		Gd	< 0.1		Nb	0.4		Sr	< 0.5		Zn	0.2
Ca	< 0.5		Ge	< 0.1		Ni	< 5		Ta	< 0.1		Zr	< 0.1
Ce	1		Hf	< 0.1		Pb	1		Tb	< 0.1			
Co	0.1		Ho	< 0.1		Pd	< 0.1		Th	< 0.1			
Cr	3		In	< 0.5		Pt	< 0.5		Ti	1			

(b)

Fig. A.10: Trace impurity analysis of the ZnO powder LOT R907ZNA1R (a) and MoO$_3$ powder LOT R1207MOA1R4 (b) obtained from MV Laboratories, Inc.. All values are given in ppm and were determined by ICP-OES (a) and HR-ICP-MS (b) except for Na which was determined by ICP-OES. The analysis was carried out by MV laboratories, Inc..

sample	ZnO	MoO$_3$
	LOT R907ZNA1R	LOT R1207MOA1R4
mass	394 g	437 g
isotope	**activity [mBq/kg]**	
^{228}Ra	<104	<8.9
^{228}Th	<30	<11
^{238}U	176±70	<349
^{226}Ra	<14	<14
^{210}Pb	<326	-
^{40}K	<201	153±47
^{137}Cs	<4.5	<4.6
^{60}Co	<6.6	<4.9

Tab. A.7: Activities of ZnO and MoO$_3$ powders measured with HPGe detectors at the underground lab Garching. Limits are given at 90%CL, errors at 1 sigma.

Bibliography

[1] F. Zwicky, "Die Rotverschiebung von extragalaktischen Nebeln," *Helv. Phys. Acta* **6** (1933) 110–127.

[2] D. Clowe, *et al.*, "A Direct Empirical Proof of the Existence of Dark Matter," *Astrophys. J. Lett.* **648** (Sept., 2006) L109–L113, arXiv:astro-ph/0608407.

[3] V. Springel, C. S. Frenk, and S. D. M. White, "The large-scale structure of the universe," *Nature* **440** no. 7088, (04, 2006) 1137–1144.

[4] K. G. Begeman, A. H. Broeils, and R. H. Sanders, "Extended rotation curves of spiral galaxies - Dark haloes and modified dynamics," *Mon. Not. R. Astron. Soc.* **249** (Apr., 1991) 523–537.

[5] **Planck** Collaboration, P. Ade *et al.*, "Planck 2013 results. XVI. Cosmological parameters," arXiv:1303.5076 [astro-ph.CO].

[6] D. H. Weinberg, J. S. Bullock, F. Governato, R. K. de Naray, and A. H. G. Peter, "Cold dark matter: controversies on small scales," arXiv:1306.0913 [astro-ph.CO].

[7] S. Trippe, "The "Missing Mass Problem" in Astronomy and the Need for a Modified Law of Gravity," arXiv:1401.5904 [astro-ph.CO].

[8] S. S. McGaugh, "A Tale of Two Paradigms: the Mutual Incommensurability of LCDM and MOND," arXiv:1404.7525 [astro-ph.CO].

[9] E. W. Kolb and M. S. Turner, *The early universe.* Addison-Wesley, Reading, 1990.

[10] R. Catena and L. Covi, "SUSY dark matter(s)," arXiv:1310.4776 [hep-ph].

[11] L. Bergstrom, "Dark Matter Candidates," *New J. Phys.* **11** (2009) 105006, arXiv:0903.4849 [hep-ph].

[12] **CMS** Collaboration, T. Miceli, "A search for dark matter appearing as missing transverse energy at CMS," *J. Phys. Conf. Ser.* **485** (2014) 012030.

[13] **ATLAS** Collaboration, G. Aad, *et al.*, "Search for Dark Matter in Events with a Hadronically Decaying W or Z Boson and Missing Transverse Momentum in pp Collisions at $\sqrt{s} = 8$ TeV with the ATLAS Detector," *Phys. Rev. Lett.* **112** (Jan, 2014) 041802.

[14] V. C. Spanos, "The Price of a Dark Matter Annihilation Interpretation of AMS-02 Data," `arXiv:1312.7841 [hep-ph]`.

[15] T. Linden and S. Profumo, "Probing the Pulsar Origin of the Anomalous Positron Fraction with AMS-02 and Atmospheric Cherenkov Telescopes," *Astrophys. J.* **772** (2013) 18, `arXiv:1304.1791 [astro-ph.HE]`.

[16] D. Hooper and L. Goodenough, "Dark Matter Annihilation in The Galactic Center As Seen by the Fermi Gamma Ray Space Telescope," *Phys. Lett.* **B697** (2011) 412–428, `arXiv:1010.2752 [hep-ph]`.

[17] T. Daylan, *et al.*, "The Characterization of the Gamma-Ray Signal from the Central Milky Way: A Compelling Case for Annihilating Dark Matter," `arXiv:1402.6703 [astro-ph.HE]`.

[18] E. Bulbul, *et al.*, "Detection of An Unidentified Emission Line in the Stacked X-ray spectrum of Galaxy Clusters," `arXiv:1402.2301 [astro-ph.CO]`.

[19] A. Boyarsky, O. Ruchayskiy, D. Iakubovskyi, and J. Franse, "An unidentified line in X-ray spectra of the Andromeda galaxy and Perseus galaxy cluster," `arXiv:1402.4119 [astro-ph.CO]`.

[20] **IceCube** Collaboration, M. Aartsen *et al.*, "Evidence for High-Energy Extraterrestrial Neutrinos at the IceCube Detector," *Science* **342** no. 6161, (2013) 1242856, `arXiv:1311.5238 [astro-ph.HE]`.

[21] B. Feldstein, A. Kusenko, S. Matsumoto, and T. T. Yanagida, "Neutrinos at IceCube from Heavy Decaying Dark Matter," *Phys. Rev.* **D88** no. 1, (2013) 015004, `arXiv:1303.7320 [hep-ph]`.

[22] **DAMA/LIBRA** Collaboration, R. Bernabei *et al.*, "New results from DAMA/LIBRA," *Eur. Phys. J.* **C67** (2010) 39–49, `arXiv:1002.1028 [astro-ph.GA]`.

[23] D. Hooper, J. I. Collar, J. Hall, D. McKinsey, and C. M. Kelso, "Consistent dark matter interpretation for CoGeNT and DAMA/LIBRA," *Phys. Rev. D* **82** (Dec, 2010) 123509.

[24] **CoGeNT** Collaboration, C. E. Aalseth, *et al.*, "Results from a Search for Light-Mass Dark Matter with a P-type Point Contact Germanium Detector," `arXiv:1002.4703 [astro-ph.CO]`.

[25] **CoGeNT** Collaboration, C. Aalseth *et al.*, "Search for An Annual Modulation in Three Years of CoGeNT Dark Matter Detector Data," `arXiv:1401.3295 [astro-ph.CO]`.

[26] **CDMS** Collaboration, R. Agnese, *et al.*, "Silicon Detector Dark Matter Results from the Final Exposure of CDMS II," *Phys. Rev. Lett.* **111** (Dec, 2013) 251301.

[27] **CRESST** Collaboration, G. Angloher, *et al.*, "Results from 730 kg days of the CRESST-II Dark Matter search," *Eur. Phys. J.* **C72** (2012) 1–22.

[28] K. Petraki and R. R. Volkas, "Review of asymmetric dark matter," *Int. J. Mod. Phys.* **A28** (2013) 1330028, `arXiv:1305.4939 [hep-ph]`.

[29] **LUX** Collaboration, D. Akerib *et al.*, "First results from the LUX dark matter experiment at the Sanford Underground Research Facility," *Phys. Rev. Lett.* **112** (2014) 091303, `arXiv:1310.8214 [astro-ph.CO]`.

[30] **XENON100** Collaboration, E. Aprile *et al.*, "Dark Matter Results from 225 Live Days of XENON100 Data," *Phys. Rev. Lett.* **109** (2012) 181301, `arXiv:1207.5988 [astro-ph.CO]`.

[31] **SuperCDMS** Collaboration, R. Agnese *et al.*, "Search for Low-Mass WIMPs with SuperCDMS," `arXiv:1402.7137 [hep-ex]`.

[32] N. Chen, *et al.*, "Exothermic isospin-violating dark matter after SuperCDMS and CDEX," `arXiv:1404.6043 [hep-ph]`.

[33] G. B. Gelmini, A. Georgescu, and J.-H. Huh, "Direct Detection of Light "Ge-phobic" Exothermic Dark Matter," `arXiv:1404.7484 [hep-ph]`.

[34] S. Scopel and K. Yoon, "A systematic halo-independent analysis of direct detection data within the framework of Inelastic Dark Matter," `arXiv:1405.0364 [astro-ph.CO]`.

[35] **SuperCDMS** Collaboration, R. Agnese, *et al.*, "Search for Low-Mass Weakly Interacting Massive Particles Using Voltage-Assisted Calorimetric Ionization Detection in the SuperCDMS Experiment," *Phys. Rev. Lett.* **112** (Jan, 2014) 041302.

[36] M. Aglietta, *et al.*, "Single muon angular distributions observed in the LVD particle astrophysics experiment," *Astropart. Phys.* **2** (May, 1994) 103–116.

[37] S. Roth, "Sputtered tungsten thin films and composite detectors for the application in the dark matter experiments cresst and eureca," diploma thesis, Technische Universität München, 2007.

[38] S. Roth, *The Potential of Neganov-Luke Amplified Cryogenic Light Detectors and the Scintillation-Light Quenching Mechanism in CaWO4 Single Crystals in the Context of the Dark Matter Search Experiment CRESST-II.* PhD thesis, Technische Universität München, 2013.

[39] R. Strauss, *Energy-Dependent Quenching Factor Measurements of CaWO4 Crystals at mK Temperatures and Detector Prototypes for Direct Dark Matter Search with CRESST.* PhD thesis, Technische Universität München, 2013.

[40] **EURECA** Collaboration, G. Angloher, *et al.*, "EURECA conceptual design report," *Phys. Dark Univ.* **3** (2014) 41–74.

[41] **EDELWEISS** Collaboration, E. Armengaud, *et al.*, "Final results of the EDELWEISS-II WIMP search using a 4-kg array of cryogenic germanium detectors with interleaved electrodes," *Phys. Lett. B* **702** no. 5, (2011) 329 – 335.

[42] **XENON1T** Collaboration, E. Aprile, "The XENON1T Dark Matter Search Experiment," `arXiv:1206.6288 [astro-ph.IM]`.

[43] **DEAP** Collaboration, P. Gorel, "Search for Dark Matter with Liquid Argon and Pulse Shape Discrimination: Results from DEAP-1 and Status of DEAP-3600," `arXiv:1406.0462 [astro-ph.IM]`.

[44] J. Lewin, "Review of mathematics, numerical factors, and corrections for dark matter experiments based on elastic nuclear recoil," *Astropart. Phys.* **6** no. 1, (December, 1996) 87–112.

[45] S. Bilenky and C. Giunti, "Neutrinoless double-beta decay: A brief review," *Mod. Phys. Lett.* **A27** (2012) 1230015, `arXiv:1203.5250 [hep-ph]`.

[46] A. P. Meshik, C. M. Hohenberg, O. V. Pravdivtseva, and Y. S. Kapusta, "Weak decay of ^{130}Ba and ^{132}Ba: Geochemical measurements," *Phys. Rev. C* **64** (Aug, 2001) 035205.

[47] Z. Sujkowski and S. Wycech, "Neutrinoless double electron capture: A Tool to search for Majorana neutrinos," *Phys. Rev.* **C70** (2004) 052501, `arXiv:hep-ph/0312040 [hep-ph]`.

[48] Y. G. Zdesenko, *et al.*, "CARVEL experiment with ^{48}CaWO$_4$ crystal scintillators for the double β decay study of ^{48}Ca," *Astropart. Phys.* **23** no. 2, (2005) 249–263.

[49] R. Hazama, *et al.*, "Challenge on Ca-48 enrichment for CANDLES double beta decay experiment," `arXiv:0710.3840 [nucl-ex]`.

[50] D.-L. Fang, *et al.*, "Evaluation of the resonance enhancement effect in neutrinoless double-electron capture in 152Gd, 164Er and 180W atoms," *Phys. Rev.* **C85** (2012) 035503, `arXiv:1111.6862 [hep-ph]`.

[51] V. I. Tretyak private communication.

[52] "mindat.org - the mineral and locality database."
`http://www.mindat.org/min-3560.html`.

[53] T. Edison *Nature* **53** no. 1377, (1896) 470.

[54] M. Nikl, V. V. Laguta, and A. Vedda, "Complex oxide scintillators: Material defects and scintillation performance," *Phys. Status Solidi B* **245** no. 9, (2008) 1701–1722.

[55] O. S. O. America, *Handbook of Optics*, vol. 2. McGraw-Hill Professional, Columbus, 2 ed., 1994.

[56] M. v. Sivers, "Optimizing Detectors for Dark Matter Search," Diploma thesis, Technische Universität München, 2010.

[57] M. Moszyński, *et al.*, "Characterization of $CaWO_4$ scintillator at room and liquid nitrogen temperatures," *Nucl. Instrum. Meth.* **A553** (Nov., 2005) 578–591.

[58] H. Kraus, V. B. Mikhailik, and D. Wahl, "Multiple photon counting coincidence (MPCC) technique for scintillator characterisation and its application to studies of $CaWO_4$ and $ZnWO_4$ scintillators," *Nucl. Instrum. Meth.* **A553** (Nov., 2005) 522–534.

[59] V. B. Mikhailik, *et al.*, "One- and two-photon excited luminescence and band-gap assignment in $CaWO_4$," *Phys. Rev. B* **69** no. 20, (May, 2004) 205110.

[60] M. v. Sivers, *et al.*, "Influence of annealing on the optical and scintillation properties of CaWO single crystals," *Opt. Mater.* **34** (Sept., 2012) 1843–1848, `arXiv:1206.1588 [physics.optics]`.

[61] D. Wahl, V. B. Mikhailik, and H. Kraus, "The Monte-Carlo refractive index matching technique for determining the input parameters for simulation of the light collection in scintillating crystals," *Nucl. Instrum. Meth.* **A570** (Jan., 2007) 529–535.

[62] A. Erb and J.-C. Lanfranchi, "Growth of high-purity scintillating $CaWO_4$ single crystals for the low-temperature direct dark matter search experiments CRESST-II and EURECA," *CrystEngComm* **15** (2013) 2301–2304.

[63] J. Czochralski, "Ein neues Verfahren zur Messung der Kristallisationsgeschwindigkeit der Metalle," *J. Phys. Chem.* **92** (1918) 219–221.

[64] K. Nassau and L. G. van Uitert, "Preparation of Large Calcium-Tungstate Crystals Containing Paramagnetic Ions for Maser Applications," *J. Appl. Phys.* **31** (Aug., 1960) 1508.

[65] A. J. Valentino and C. D. Brandle, "Diameter control of czochralski grown crystals," *J. Cryst. Growth* **26** (1974) 1–5.

[66] W. Bardsley, G. W. Green, C. H. Holliday, and D. T. J. Hurle, "Automatic control of czochralski crystal growth," *J. Cryst. Growth* **16** (1972) 277–279.

[67] Z. Shao, Q. Zhang, T. Liu, and J. Chen, "Computer study of intrinsic defects in $CaWO_4$," *Nucl. Instrum. Meth.* **B266** (Mar., 2008) 797–801.

[68] V. Yakovyna, A. Matkovskii, D. Sugak, C. Solskii, and S. Novosad, "Effects of annealing on calcium tungstate crystals," *Radiat. Meas.* **38** (2004) 403–406.

[69] V. Yakovyna, *et al.*, "Effect of thermo-chemical treatments on the luminescence and scintillation properties of $CaWO_4$," *Opt. Mater.* **30** (June, 2008) 1630–1634.

[70] W. Zhu, X. Feng, Z. Wu, and Z. Man, "On the annealing mechanism in $PbWO_4$ crystals," *Physica B* **324** (Nov., 2002) 53–58.

[71] I. Bavykina, *et al.*, "Development of cryogenic phonon detectors based on $CaMoO_4$ and $ZnWO_4$ scintillating crystals for direct dark matter search experiments," *Opt. Mater.* **31** (Aug., 2009) 1382–1387.

[72] D. Wahl, *Optimization of light collection in inorganic scintillators for rare event searches.* PhD thesis, St Catherine's College, Oxford, 2005.

[73] R. Kesavamoorthy and A. K. Arora, "Light scattering by decorated dislocations in alkali halide crystals," *J. Phys. C: Solid State Phys.* **16** (May, 1983) 2611–2618.

[74] H. J. Levinstein, G. M. Loiacono, and K. Nassau, "Calcium Tungstate. II. Observation of Dislocations," *J. Appl. Phys.* **34** (Dec., 1963) 3603–3608.

[75] B. Cockayne, D. S. Robertson, and W. Bardsley, "Growth defects in calcium tungstate single crystals," *Br. J. Appl. Phys.* **15** (Oct., 1964) 1165–1169.

[76] M. Nikl, K. Nitsch, J. Hybler, J. Chval, and P. Reiche, "Origin of the 420 nm absorption band in $PbWO_4$ single crystals," *Phys. Status Solidi B* **196** (July, 1996) K7–K10.

[77] M. Nikl, *et al.*, "Radiation induced formation of color centers in $PbWO_4$ single crystals," *J. Appl. Phys.* **82** (Dec., 1997) 5758–5762.

[78] W. Jost, *Diffusion in solids, liquids, gases.* Academic Press, 1960.

[79] C. Carrier and R. Lecomte, "Trapping of fluorescent light in cylindrical scintillators," *Nucl. Instrum. Meth.* **A278** (June, 1989) 622–624.

[80] U. Thalhammer, "Light Yield Measurements of Differently Shaped $CaWO_4$ Crystals." Diploma thesis, 2012.

[81] D. Strul, J. Sutcliffe-Goulden, P. Halstead, and P. K. Marsden, "Optimization of fiber-optic readout of LSO scintillation crystals with acid etching," *IEEE Trans. Nucl. Sci.* **49** (June, 2002) 619–623.

[82] J. Ninkovic, *Investigation of CaWO4 Crystals for Simultaneous Phonon-Light Detection in the CRESST Dark Matter Search*. PhD thesis, Technische Universität München, 2005.

[83] M. Nieto-Vesperinas and J. A. Sanchez-Gil, "Light scattering from a random rough interface with total internl reflection," *J. Opt. Soc. Am. A* **9** no. 3, (1992) 424–436.

[84] S. Nayar, K. Ikeuchi, and T. Kanade, "Surface reflection: physical and geometrical perspectives," *IEEE Trans. Pattern Anal. Machine Intell.* **13** no. 7, (Jul, 1991) 611–634.

[85] J. Dally and W. Riley, *Experimental Stress Analysis*. McGraw-Hill Inc., 3 ed., 1991.

[86] *Perkin Elmer LAMBDA 850 Hardware Guide*.

[87] F. Cornacchia, *et al.*, "Growth and spectroscopic characterization of Er^{3+}:$CaWO_4$," *J. Appl. Phys.* **101** no. 12, (2007) .

[88] Y. Huang, *et al.*, "Growth and spectra properties of Nd^{3+}-doped PbWO4 single crystal," *Solid State Commun.* **127** no. 1, (2003) 1 – 5.

[89] M. Nikl, *et al.*, "The doping of $PbWO_4$ in shaping its scintillator characteristics," *Radiat. Meas.* **33** no. 5, (2001) 705 – 708.

[90] A. Kenyon, "Recent developments in rare-earth doped materials for optoelectronics," *Prog. Quant. Electron.* **26** no. 4–5, (2002) 225 – 284.

[91] M. Kobayashi, *et al.*, "Significant improvement of $PbWO_4$ scintillating crystals by doping with trivalent ions," *Nucl. Instrum. Meth.* **A434** no. 2–3, (1999) 412 – 423.

[92] S. Baccaro, *et al.*, "Effect of La Doping on Calcium Tungstate ($CaWO_4$) Crystals Radiation Hardness," *Phys. Status Solidi B* **178** no. 2, (2000) 799–804.

[93] A. Münster, "Absolute Alpha-Radioactivity Determination of Scintillating $CaWO_4$ Crystals for Direct Dark Matter Search," Diploma thesis, Technische Universität München, 2013.

[94] A. Blistanov, *et al.*, "Defects in calcium tungstate crystals," *Cystallogr. Rep.* **51** no. 4, (2006) 661–663.

[95] R. Oeder, "Distribution coefficients, cavity formation and cellular structures in Czochralski CaWO4 crystals," *J. Cryst. Growth* **36** (Nov., 1976) 1–3.

175

[96] K. Nassau and A. M. Broyer, "Calcium Tungstate: czochralski Growth, Perfection and Substitution," *J. Appl. Phys.* **33** (Oct., 1962) 3064–3073.

[97] A. R. Chaudhuri and L. E. Phaneuf, "Grown-In Dislocations in Calcium Tungstate Crystals Pulled from the Melt," *J. Appl. Phys.* **34** (Aug., 1963) 2162–2167.

[98] Agilent Technologies, *Cary Eclipse Fluorescence Spectrometer Brochure.*

[99] K. Schäffner private communication.

[100] V. B. Mikhailik, H. Kraus, S. Henry, and A. J. B. Tolhurst, "Scintillation studies of CaWO$_4$ in the millikelvin temperature range," *Phys. Rev. B* **75** no. 18, (May, 2007) 184308.

[101] M.-A. Verdier, P. C. F. Di Stefano, E. Mony, P. Nadeau, and W. Rau, "Setup for Low Temperature alpha / gamma Scintillation Measurements," *IEEE Trans. Nucl. Sci.* **59** (Oct., 2012) 2324–2327.

[102] P. Nadeau private communication.

[103] V. B. Mikhailik and H. Kraus, "Performance of scintillation materials at cryogenic temperatures," *Phys. Status Solidi B* **247** no. 7, (2010) 1583–1599.

[104] P. C. F. di Stefano, *et al.*, "Textured silicon calorimetric light detector," *J. Appl. Phys.* **94** (Nov., 2003) 6887–6891, `arXiv:physics/0307042`.

[105] W. Westphal, *Development and Characterization of Cryogenic Detectors for the CRESST Experiment.* PhD thesis, Technische Universität München, 2008.

[106] L. L. Nagornaya, *et al.*, "Tungstate and Molybdate Scintillators to Search for Dark Matter and Double Beta Decay," *IEEE Trans. Nucl. Sci.* **56** (Aug., 2009) 2513–2518.

[107] Y. G. Zdesenko *et al.*, "Scintillation pulse shape discrimination with CaWO4, ZnWO4 and CdWO4 crystal," *FM* **12** no. 2, (2005) 269.

[108] G. B. Beard, W. H. Kelly, and M. L. Mallory, "Temperature Dependent Luminescence of CaWO$_4$ and CdWO$_4$," *J. Appl. Phys.* **33** (Jan., 1962) 144–147.

[109] National Nuclear Data Center, "information extracted from the Chart of Nuclides database." `http://www.nndc.bnl.gov/chart/`.

[110] F. A. Danevich, *et al.*, "New results of ^{116}Cd double β decay study with ^{116}CdWO$_4$ scintillators," Phys. Rev. C **62** no. 4, (Oct., 2000) 045501, `nucl-ex/0003001`.

[111] **CRESST** Collaboration, R. Lang, *et al.*, "Electron and gamma background in CRESST detectors," *Astropart. Phys.* **32** no. 6, (2010) 318 – 324.

[112] A. Bettini, "Underground laboratories," *Nucl. Instrum. Meth.* **A626–627, Supplement** no. 0, (2011) S64 – S68.

[113] A. Morales, *et al.*, "Results of a search of the neutrinoless decay of 76Ge to the first excited state of 76Se in the Canfranc tunnel," *Nuovo Cim.* **104** no. 10, (1991) 1581–1585.

[114] F. A. Danevich, *et al.*, "Effect of recrystallisation on the radioactive contamination of $CaWO_4$ crystal scintillators," *Nucl. Instrum. Meth.* **A631** (Mar., 2011) 44–53.

[115] K. Wilke and J. Bohm, *Kristallzüchtung.* No. Bd. 1 in Kristallzüchtung. VEB Deutscher Verlag der Wissenschaften, 1973.

[116] C. Arpesella, "A low background counting facility at laboratori nazionali del Gran Sasso," *Appl. Radiat. Isot.* **47** no. 9–10, (1996) 991 – 996.

[117] M. Hofmann, T. Mannel, and M. v. Sivers, "Low-background gamma-ray spectrometry in the Garching underground laboratory," *AIP Conf. Proc.* **1549** no. 1, (2013) 38–41.

[118] ET Enterprises Ltd., *9214B series data sheet.*

[119] R. McAlpine, "photomultipliers for low background applications," tech. rep., Electron Tubes Ltd.

[120] T. Dandl, T. Heindl, and A. Ulrich, "Fluorescence of nitrogen and air," *JINST* **7** no. 11, (2012) P11005.

[121] R. Kneissl Master's thesis, Technische Universität München, 2014. in preparation.

[122] E. Gatti and F. D. Martini, "A new linear method of discrimination between elementary particles in scintillation counters," *Nucl. Electr.* **2** (1961) 265–276.

[123] Y. G. Zdesenko, *et al.*, "Scintillation properties and radioactive contamination of $CaWO_4$ crystal scintillators," *Nucl. Instrum. Meth.* **A538** (2005) 657–667.

[124] K. Schäffner, *Study of Backgrounds in the CRESST Dark Matter Search.* PhD thesis, Technische Universität München, 2013.

[125] M. Kiefer, *Improving the Light Channel of the CRESST-II-Dark Matter Detectors.* PhD thesis, Technische Universität München, 2012.

[126] R. Strauss private communication.

[127] R. Strauss (on behalf of the CRESST collaboration), "New Results from the CRESST Experiment." Talk at IDM conference, June, 2014.

[128] A. Brown, S. Henry, H. Kraus, and C. McCabe, "Extending the CRESST-II commissioning run limits to lower masses," *Phys. Rev.* **D85** (2012) 021301, arXiv:1109.2589 [astro-ph.CO].

177

[129] **EDELWEISS** Collaboration, E. Armengaud *et al.*, "A search for low-mass WIMPs with EDELWEISS-II heat-and-ionization detectors," *Phys. Rev.* **D86** (2012) 051701, `arXiv:1207.1815 [astro-ph.CO]`.

[130] **CoGeNT** Collaboration, C. Aalseth *et al.*, "CoGeNT: A Search for Low-Mass Dark Matter using p-type Point Contact Germanium Detectors," *Phys. Rev.* **D88** no. 1, (2013) 012002, `arXiv:1208.5737 [astro-ph.CO]`.

[131] C. Savage, G. Gelmini, P. Gondolo, and K. Freese, "Compatibility of DAMA/LIBRA dark matter detection with other searches," *JCAP* **0904** (2009) 010, `arXiv:0808.3607 [astro-ph]`.

[132] J. Back and Y. Ramachers, "Activia: Calculation of isotope production cross-sections and yields," *Nucl. Instrum. Meth.* **A586** no. 2, (2008) 286 – 294.

[133] C. Strandhagen private communication.

[134] S. Agostinelli, *et al.*, "Geant4 - a simulation toolkit," *Nucl. Instrum. Meth.* **A506** no. 3, (2003) 250 – 303.

[135] P. Huff, *The Detector Parameters Determining the Sensitivity of the CRESST-II Experiment.* PhD thesis, Technische Universität München, 2010.

[136] F. Petricca, *Dark Matter Search with Cryogenic Phonon-Light Detectors.* PhD thesis, Ludwig-Maximilians-Universität München, 2005.

[137] C. Levin, A. Moisan, "A more physical approach to model the surface treatment of scintillation counters and its implementation into detect," *IEEE Nucl. Sci. Symp. Conf. Rec.* **2** (November, 1996) 702–706.

[138] M. Janecek and W. W. Moses, "Simulating scintillator light collection using measured optical reflectance," *IEEE Trans. Nucl. Sci.* **57** no. 3, (2010) 964–970.

[139] C. Carrier and R. Lecomte, "Theoretical modelling of light transport in rectangular parallelepipedic scintillators," *Nucl. Instrum. Meth.* **A292** (July, 1990) 685–692.

[140] F. Danevich, *et al.*, "Optimization of light collection from crystal scintillators for cryogenic experiments," *Nucl. Instrum. Meth.* **A744** (2014) 41–47, `arXiv:1402.2241 [physics.ins-det]`.

[141] F. Danevich, *et al.*, "Impact of geometry on light collection efficiency of scintillation detectors for cryogenic rare event searches," `arXiv:1404.7846 [physics.ins-det]`.

[142] M. Janecek and W. W. Moses, "Optical reflectance measurements for commonly used reflectors," *IEEE Trans. Nucl. Sci.* **55** no. 4, (Aug, 2008) 2432–2437.

[143] J. Beeman, *et al.*, "Potential of a next generation neutrinoless double beta decay experiment based on $ZnMoO_4$ scintillating bolometers," *Phys. Lett.* **B710** (2012) 318–323, arXiv:1112.3672 [hep-ex].

[144] J. Beeman, *et al.*, "ZnMoO4: A Promising bolometer for neutrinoless double beta decay searches," *Astropart. Phys.* **35** (2012) 813–820, arXiv:1202.0238 [nucl-ex].

Danksagung